To The Graduate Council:

I am submitting herewith a thesis written by Scott B. Thomas entitled "Qualification of a Steady-State Reactor Core Physics Methodology for Boiling Water Reactor Core Design and Analysis". I have examined the final copy of this thesis for form and content and recommend that it be accepted in partial fulfillment of the requirements for the degree of Master of Science, with a major in Nuclear Engineering.

L. F. Miller, Major Professor

We have read this thesis
and recommend its acceptance:

Accepted for the Council:

Vice Provost
and Dean of The Graduate School

STATEMENT OF PERMISSION TO USE

In presenting this thesis in partial fulfillment of the requirements for a Master's degree at The University of Tennessee, Knoxville, I agree that the Library shall make it available to borrowers under the rules of the Library. Brief quotations from this thesis are allowable without special permission, provided that accurate acknowledgment of the source is made.

Permission for extensive quotation from or reproduction of this thesis may be granted by my major professor, or in his absence, by the Head of Interlibrary Services when, in the opinion of either, the proposed use of the material is for scholarly purposes. Any copying or use of the material in this thesis for financial gain shall not be allowed without my written permission.

Signature Scott B. Thomas

Date 12/1/89

QUALIFICATION OF A STEADY-STATE REACTOR PHYSICS METHODOLOGY FOR BOILING WATER REACTOR CORE DESIGN AND ANALYSIS

A Thesis

Presented for the

Master of Science

Degree

The University of Tennessee, Knoxville

Scott B. Thomas

December 1989

DEDICATION

To my Parents, Henry and Sandy

ACKNOWLEDGMENTS

The author extends his sincerest appreciation to a number of individuals for their assistance and support during the course of this investigation. In particular the author is indebted to Tom Beu for his technical guidance and advice during this project. Without Tom's contributions the completeness of this thesis would not have been possible.

The author also wishes to thank Professors Larry F. Miller, Harold L. Dodds, Thomas W. Kerlin, P. F. Pasqua, and Belle R. Upadhyaya, who served as my director and committee respectively, for their helpful comments on this work.

Thanks are due to Sam L. Forkner, author of the CORE-II core simulator code, for his helpfulness in resolving modeling problems and his review of this thesis.

It was the author's privilege to work with Alan Bruce and Ed Hersperger during this project. Their assistance and patience in answering a multitude of questions are very much appreciated.

The financial support of this research by the Tennessee Valley Authority is gratefully acknowledged.

Finally, I would like to thank my family, Arlene, Emily and Drew for their tremendous support during the course of this work.

ABSTRACT

This thesis presents a reactor core model developed to simulate the Quad Cities-1 reactor core from initial critical through cycle 2 using newly developed reactor core physics methodologies. The reactor core is modeled using a nodal core simulator which includes a coupled neutronic/thermal-hydraulic, three-dimensional representation. Few group cross-sections for use in the core simulator are generated with a two-dimensional, fine mesh lattice physics code. Calculated results are compared with measured data from monthly in-core detector measurements through cycle 2, end-of-cycles 1 and 2 gamma scan measurements, distributed rod pattern startup reactivity, cold condition local criticality experiments, and high power steady-state reactivity. These calculations will be used, in conjunction with other benchmark calculations, to qualify the new reactor physics methodologies for steady-state Boiling Water Reactor design analyses for the Browns Ferry Nuclear Plant.

The results presented in this thesis identify areas in the methodology which are improved and other areas which require further refinements. The new core physics methodologies provide improved predictions of hot operating reactivity and power distributions. However, cold reactivity calculations and simulated traversing in-core probe readings are shown to be less consistent and possible causes are presented.

TABLE OF CONTENTS

LIST OF FIGURES

LIST OF TABLES

TABLE PAGE

LIST OF ABBREVIATIONS

ADF - Assembly Discontinuity Factor

BWR - Boiling Water Reactor

CF - Control Fraction

$\overline{CF}$ - Exposure Averaged Control Fraction

CH - Control History

CPR - Critical Power Ratio

E - Exposure

LHGR - Linear Heat Generation Rate

LPRM - Local Power Range Monitor

NRC - Nuclear Regulatory Commission

PCI - Pellet Clad Interaction

SRM - Source Range Monitor

TIP - Traversing In-core Probe

TVA - Tennessee Valley Authority

U - Water Density

$\overline{U}$ - Exposure Averaged Water Density

UH - Water Density History

1.0 INTRODUCTION

1.1 Overview

Accurate core physics calculations are necessary for the safe and efficient operation of nuclear reactors. Nuclear reactor vendors and nuclear utilities are continually refining existing core physics methodologies and developing improved methodologies to increase the accuracy of core behavior predictions. These advances increase fuel utilization, increase operating efficiency and make advanced fuel management techniques possible.

The Tennessee Valley Authority (TVA) currently performs steady-state core analysis for the Browns Ferry Nuclear Plant using Boiling Water Reactor (BWR) analysis methods based on the LATTICE[1], CORE[2], and FIBWR[3] computer codes. Comparisons with measured data from recent cycles containing high enrichment, high burnable poison (gadolinium) loaded fuel have shown that problems exist in predicting axial power shapes and thermal limits. Although the precise cause is unknown, results from preliminary evaluations indicate a dependence on the predicted burnup rate of gadolinium.

Difficulty in properly predicting power shapes can adversely affect reload core design analyses. Non-optimal loading patterns, increased potential for violation of Technical Specifications and operation at less than rated conditions due to thermal limits problems are a few of the possible consequences. Operational support activities can also suffer due to an inability to accurately locate peak power and

determine limiting Linear Heat Generation Rates (LHGRs) when developing rod patterns.

Due to the axial power and thermal limits mispredictions, it is evident that more refined methods would be beneficial in modeling the high energy fuel assemblies needed for long (18-24 month) cycle lengths. Improved physics methods based on the TGBLA[4], CORE-II[5], and FIBWR computer codes have been developed and are being implemented by TVA.

The CORE-II code is a coupled neutronic/thermal-hydraulic, three-dimensional, nodal reactor core simulator developed by TVA. Steady-state neutronic calculations are made based on a variation of the "QUANDRY" style nodal methods[6]. Unlike the modified one-group CORE code, CORE-II employs a full two-group solution. The explicit modeling of thermal neutron exchange between nodes is expected to benefit the analyses. Other major improvements incorporated in the CORE-II code include the use of Assembly Discontinuity Factors (ADF) to account for nodal heterogenities, explicit modeling of the reflector region, and the use of improved moderator void correlations.

Few group cross-sections for use in the core simulator are generated with TGBLA, a two-dimensional, fine mesh lattice physics code. TGBLA was developed under a cooperative study between General Electric Company and Toshiba Corporation. The methods are based on few group diffusion theory with transport theory corrections. An advanced treatment of the depletion of the gadolinium isotopes is expected to improve the power mispredictions by the core simulator.

Assembly thermal-hydraulic characteristics for use in the core simulator are generated using the FIBWR steady-state thermal-hydraulic simulator code. The FIBWR code incorporates a detailed geometrical representation of the complex flow paths in a BWR fuel assembly. Each assembly design is analyzed to determine data used to describe the interrelationship of assembly flow, pressure drop and power.

Regardless of the theoretical basis of the mathematical models, the usefulness and accuracy of the reactor physics methods can only be determined through benchmark calculations. Extensive comparisons to measured data and higher order calculations will be performed before the TGBLA/CORE-II core physics methods are used for predictive core calculations. The ability to track reactor criticality and power distributions over a wide range of BWR operating states must be verified and the associated uncertainties and biases must be quantified. The results of these benchmark calculations will be documented in a licensing topical report and submitted to the Nuclear Regulatory Commission (NRC) for their review.

To illustrate the need for accurate core physics methods, some example applications are described in section 1.2. Section 1.3 contains a description of the measured data available from the Quad Cities-1 reactor for use in qualifying reactor physics methods. Finally, the objective and summary of this thesis are given in section 1.4.

1.2 Applications of Steady-State Core Physics Methods

Steady-state physics methods are utilized for a wide range of core analyses. Fresh fuel batch sizes and fuel shuffling patterns are investigated for future cycles based on projected cycle energy requirements. This preliminary design is typically performed during the current cycle in order to accommodate a one year lead time for manufacturing of fresh fuel. As a result, the ability to predict fuel assembly characteristics at the completion of the current cycle is vital to determining a safe and efficient reference loading pattern for the future cycle.

Once established, the reference loading pattern is analyzed to demonstrate that sufficient margins to thermal and reactivity limits exist. Shutdown margin calculations, and hot excess reactivity calculations are performed to ensure that the core reactivity can be controlled through the cycle. Simulated core depletions with projected control rod patterns are developed to demonstrate that the core can be operated within thermal limits throughout the cycle.

In addition, safety analyses are performed to ensure that the reference loading pattern can safely withstand postulated transient and accident scenarios. Some events, such as the rod withdrawal error, can be analyzed using steady-state calculations. Other events are modeled using separate transient analysis codes, with cross-sections from the steady-state core simulator. These analyses include the rod drop accident and pressurization transients. The above analyses qualify the loading pattern for operation and set cycle specific operating ranges

and limits. The results of the above design analyses are submitted to the NRC for acceptance before the cycle can be operated.

Steady-state reactor physics methods are also used during plant operation to determine target control rod patterns and investigate alternative operating strategies. Multi-cycle analyses are performed to predict future fuel requirements and efficiently plan transition cycles employing improved refueling patterns and fuel designs.

Finally, steady-state reactor physics methods play a vital role in making advances in fuel management feasible. For BWRs these advances include control cell refueling patterns which mitigate power peaking in fuel adjacent to partially inserted control blades, spectral shift operation to maximize fuel utilization, power coastdown, and the use of increased enrichment fuel with axially zoned burnable poisons for increased burnup and longer cycle lengths.

1.3 Qualification of Physics Methods Using Data From Quad Cities-1

The measured data available for the Quad Cities-1 reactor are extensive and have become a standard benchmark for the qualification of BWR physics methods. Detailed fuel design and operating data are available to model core operation from the initial critical through cycle 2[7,8].

Traversing In-core Probe (TIP) measurements were made on a monthly basis through cycles 1 and 2, yielding 28 sets of steady-state power distribution data. Quad Cities TIP detectors measure the thermal neutron flux at 24 axial positions in 41 radial core locations. These

measurements are useful in evaluating power distribution calculations throughout an operating cycle.

Gamma scan projects were performed at the end-of-cycles 1 and 2 to obtain detailed measurements of the recent power history of individual assemblies[9],[10]. The gamma scan projects involved measuring the La-140 activity of selected assemblies at 12 or 24 axial locations. The gamma scan technique represents the most detailed power measurements available for commercial BWRs. Unlike TIP measurements, which measure the average power of the four fuel assembly segments surrounding the detector, the gamma scan data provides an accurate measure of the power distribution in a single assembly averaged over the last one to two months operation.

The end-of-cycle 1 gamma scan involved 31 assemblies distributed in groups of three to four neighboring assemblies from each octant of the core. Eighty-nine assemblies were scanned following cycle 2. The assemblies encompassed nearly a complete octant of the core and 12 additional symmetric locations. Comparisons to these gamma scan measurements provide a detailed measure of the ability of core physics methods to predict nodal power.

Critical core configuration data are available from distributed (in-sequence) rod pattern startups at various core exposures. These data can be used to determine the uncertainty and bias associated with predicting reactivity at cold conditions. The rod withdrawal sequences used in these criticals were typical of normal reactor startups.

Numerous local critical experiments were performed during cycle 1. These critical experiments involved withdrawing two to four adjacent

control rods producing very peaked neutron flux distributions. Calculated results from these experiments can be used to determine the capability of reactor physics methods to predict criticality induced in very localized regions (typical of stuck rod shutdown margin calculations). Comparing local to in-sequence critical results can be used to demonstrate the capability to calculate the same k-effective for critical conditions with both peaked and uniform neutron flux distributions.

Finally, the capability to predict steady-state criticality throughout a cycle can be quantified by examining the effective multiplication factors from the cycle depletion calculations. Accurate knowledge of this calculational bias is required for calculations performed at near rated power and for accurate cycle length estimates.

1.4 Objective and Project Summary

The objective of this thesis is to develop a Quad Cities-1 reactor core model using the TGBLA/CORE-II physics methods and to compare the calculated results for reactivity and power distributions with measured data. The results contained in this thesis include comparisons of calculated results with data from monthly TIP measurements through cycle 2, end-of-cycles 1 and 2 gamma scan measurements, distributed rod pattern startup reactivity, cold condition local criticality experiments, and high power steady-state reactivity. These results will be used by TVA, in conjunction with other benchmark calculations, to qualify the TGBLA/CORE-II reactor physics methods for steady-state BWR design analyses of the Browns Ferry Nuclear Plant.

This thesis identifies areas in the methodology which are improved and other areas which require further refinements. The results obtained with the new physics methods are compared with previous results for the Quad Cities-1 benchmark data obtained using the LATTICE/CORE physics methods. These comparisons show that the TGBLA/CORE-II methods provide improved predictions of hot operating reactivity and power distributions. However, cold reactivity calculations and simulated TIP readings are shown to be less consistent and possible causes are presented.

The calculations performed during this project were the first full scale application of the TGBLA/CORE-II code system. Only small problem benchmark calculations had previously been performed to check the CORE-II neutronic algorithms. Consequently, unexpected problems were encountered during the model development. This required additional investigations into alternative modeling schemes in both the lattice and core simulator calculations, a detailed examination of the simulated TIP calculations, the resolution of convergence problems with low moderator density TGBLA cases, and the discovery of general coding errors in CORE-II. Due to the evolutionary nature of the core model and computer codes, only the final results are reported in this thesis.

In addition to performing calculations with the TGBLA and CORE-II computer codes, various auxiliary FORTRAN programs were developed during the course of this project. These programs were written to perform comparisons of simulated TIP readings and gamma scan results with measured data. A program was also written to investigate problems in TIP predictions.

The organization of this thesis is as follows. A general description of the methodology used to model the Quad Cities-1 reactor is given in section 2. The core model and simulator input are presented in section 3. The core depletion calculations which tracked the core operation through cycle 2 are described in section 4.0. Comparisons of calculated and measured results are given in sections 5.0, 6.0, and 7.0. Finally, a summary of the comparisons, conclusions about the TGBLA/CORE-II results, and recommendations for future work are given in section 8.0.

2.0 ANALYSIS METHODS

2.1 Overview

Due to the spatial variation of moderator density, control rods, exposure, enrichment, and burnable poison within a BWR, an accurate core simulator requires three-dimensional representation with thermal-hydraulic feedback. The complexity of BWRs makes it impractical to utilize explicit transport theory methods or traditional finite difference methods to model all heterogeneous details in a single step. To achieve a feasible computational algorithm, the analysis is separated into three steps: (1) detailed fuel assembly neutronic modeling, (2) detailed fuel assembly thermal-hydraulic modeling, and (3) nodal core modeling based on input from the assembly modeling.

This section contains an overview of each of the three modeling steps as performed for the Quad Cities-1 benchmarking. The representation of the assembly data for use in the core model is also presented. Inputs specific to the Quad Cities-1 cycles 1 and 2 calculations (assembly designs, core loadings, operating data, etc.) are contained in section 3.

2.2 Assembly Neutronic Modeling

The core simulator represents the core as a three-dimensional array of rectangular nodes, each having homogeneous internal properties. As a result, spatially averaged fuel assembly neutronic properties which incorporate the detailed structure of BWR fuel assemblies must be determined.

Assembly neutronic properties are determined by a large number of variables. These variables can be grouped into three major categories: (1) assembly design, (2) operating history, and (3) current operating environment. The assembly design is determined by the enrichment and burnable poison distribution, number of fuel and water rods, structural material, dimensions, and geometry. The assembly operating history can be described by exposure and exposure-averaged values of control state and moderator density. The current operating environment of a BWR fuel assembly is a function of its core location, control state, moderator density, fuel temperature, power level, and the neutronic properties of adjacent fuel.

It is apparent from the above discussion that a large number of phenomena are to be represented in the core simulator. As described later in this section, the effect of all of these variables, with some compromise in detail, is incorporated in the results of the assembly neutronic analysis.

Assembly separability assumption. The effect of neighboring fuel segments on the neutronic properties is difficult to calculate. This is due to the large number of combinations of different adjacent fuel types, each with different operating histories, within a given core loading pattern. Fortunately the combination of exchannel water gaps and a relatively hard neutron energy spectrum in BWRs tends to neutronically isolate the assemblies. This fact is demonstrated by the success of modified one-group core simulators which ignore thermal neutron transport between assemblies. Consequently, the change in

operating environment due to different neighboring fuel has a relatively small effect on the neutronic properties.

An approximation is made to account for the effect of neighboring assemblies. Each core fuel node is assumed to be located in an infinite, periodic lattice in the radial direction, and uniform and infinitely long in the axial direction. With these assumptions, assemblies can be modeled separately in two dimensions, using zero-leakage boundary conditions.

For large commercial BWRs this is a good approximation for a majority of the fuel assemblies. Assemblies located on the reactor periphery can experience a radial flux gradient that invalidates this assumption. However, small errors in the predictions for peripheral assemblies are acceptable due to their low power. In addition, boundary conditions in the core simulator can be used to compensate for this deficiency.

BWR fuel assemblies typically vary axially in enrichment and burnable poison distributions, therefore it is often necessary to model more than one two-dimensional radial slice (lattice). As a result, further references to assembly modeling and physics data will be made in terms of the lattices within a fuel assembly.

Lattice physics data generation. The assembly neutronic modeling for the Quad Cities-1 fuel assemblies was performed using the TGBLA code. TGBLA is a two-dimensional, fine mesh lattice physics code based on few group diffusion theory with transport theory corrections. The diffusion theory eigenvalue problem uses three-group (fast, epithermal,

thermal) cross sections constructed from the spatially dependent neutron spectra. TGBLA explicitly represents the fuel rods, water rods, fuel cladding, burnable poisons, control rods, channel boxes, in-channel water, and ex-channel water. A description of the solution techniques used in the TGBLA code is beyond the scope of this thesis, but can be found in various references[11],[12].

The core simulator calculations require that the reactor core be modeled under conditions ranging from cold zero power to hot full power. Therefore, a large range of operating conditions was simulated in the assembly neutronic analysis to construct a flexible reactor core model. Lattice physics data for each lattice type were generated as a function of exposure, moderator density, and control state.

To establish a basis for the effect of irradiation and moderator density on lattice physics parameters, uncontrolled base depletions were run using the operating conditions listed in Table 2-1. These cases were run using 23 exposure points, with smaller steps used earlier in the depletion to track the rapid burnup of the gadolinium isotopes. Isotopic concentrations from the base depletions were written to restart files at various exposures during the depletions for later use.

The operating conditions used in base depletions were representative of average conditions in the core. The fuel temperature was set to be representative of the average at rated core power. The base power density corresponded to the core-average rated power. The moderator temperature for hot cases was set to the saturation temperature at rated core pressure.

Table 2-1

Temperature and Water Density Input Used in the Generation of Lattice Physics Data

Steam Conditions	Fuel Temperature (°F)*	Moderator Temperature (°F)	Water Density (g/cc) Ex-Channel	In-Channel
"Cold"	1250	68.0	0.9976	0.9976
0% Voids	1250	546.8	0.7372	0.7372
40% Voids	1250	546.8	0.7372	0.4572
80% Voids	1250	546.8	0.7372	0.1773

*Fuel temperature = 1250°F for all cases except Doppler when the fuel temperature = 68°F/950°F/1500°F/2500°F.

In general, the actual fuel operating histories will not be consistent with those of the base depletion cases. For example, the base depletion cases assume the current and the exposure-averaged moderator density are equal. Instantaneous changes in the base values of moderator density, fuel temperature, and control state can be modeled in the core simulator with a high degree of accuracy if the effects are assumed to be separable. Using this assumption, the effects of deviations from the base conditions were determined by performing a parametric analysis.

TGBLA restart (branch) cases were run by reading the isotopic concentrations from selected exposure points of the base depletions, changing only a selected operating condition, and recalculating the lattice physics parameters. A complete list of cases used in the generation of lattice physics data for the Quad Cities-1 lattices are shown in Table 2-2. Exposure points used in each case are shown in Table 2-3.

The base depletions assume that the fuel was depleted with the control blade withdrawn. Data for controlled fuel were determined by restarting from the base depletions and calculating the lattice physics parameters with the control rod inserted (cases B1-B4 in Table 2-2).

Lattice physics data were generated to quantify the Doppler effect. Both uncontrolled and controlled restarts from the base depletions were run using fuel temperatures different from the base temperature (cases C1-C7 in Table 2-2).

As stated previously, the base depletions are based on the exposure-averaged and current moderator density being equal. Restart

Table 2-2

Definitions of Cases Used in the Generation
of Lattice Physics Data

Case	Fuel Temperature (°F)	Control Rod (I=IN/O=OUT)	Moderator Temperature (°F)	In-Channel Water Density (g/cc)	Restart From Case	Results
A1	1250	0	68.0	0.9976	--	BASE
2	1250	0	546.8	0.7372	--	UNCONTROLLED
4	1250	0	546.8	0.4572	--	DEPLETION
	1250	0	546.8	0.1773	--	
B1	1250	I	68.0	0.9976	A1	
2	1250	I	546.8	0.7372	A2	CONTROLLED
3	1250	I	546.8	0.4572	A3	DATA
4	1250	I	546.8	0.1773	A4	
C1	68	0	68.0	0.9976	A1	DOPPLER DATA
	950	0	68.0	0.9976	A1	
	1500	0	68.0	0.9976	A1	
	2500	0	68.0	0.9976	A1	
C2	68	0	546.8	0.7372	A2	
	950	0	546.8	0.7372	A2	
	1500	0	546.8	0.7372	A2	
	2500	0	546.8	0.7372	A2	
C3	68	0	546.8	0.4572	A3	
	950	0	546.8	0.4572	A3	
	1500	0	546.8	0.4572	A3	
	2500	0	546.8	0.4572	A3	

Table 2-2 (Continued)

Case	Fuel Temperature (°F)	Control Rod (I=IN/O=OUT)	Moderator Temperature (°F)	In-Channel Water Density (g/cc)	Restart From Case	Results
C4	68	0	546.8	0.1773	A4	
	950	0	546.8	0.1773	A4	
	1500	0	546.8	0.1773	A4	
	2500	0	546.8	0.1773	A4	
C5	68	0	68.0	0.9976	A3	
	1500	0	546.8	0.7372	A3	
	1500	0	546.8	0.1773	A3	
D1	1250	0	68.0	0.9976	A2	MODERATOR
	1250	I	68.0	0.9976	A2	DENSITY
	1250	0	546.8	0.4572	A2	HISTORY
	1250	I	546.8	0.4572	A2	DATA
	1250	0	546.8	0.1773	A2	
	1250	I	546.8	0.1773	A2	
D2	1250	0	68.0	0.9976	A3	
	1250	I	68.0	0.9976	A3	
	1250	I	546.8	0.7372	A3	
	1250	0	546.8	0.1773	A3	
	1250	I	546.8	0.1773	A3	
	1250	0	546.8	0.7372	A3	

Table 2-2 (Continued)

Case	Fuel Temperature (°F)	Control Rod (I=IN/O=OUT)	Moderator Temperature (°F)	In-Channel Water Density (g/cc)	Restart From Case	Results
D3	1250	I	68.0	0.9976	A4	
	1250	0	546.8	0.9976	A4	
	1250	I	546.8	0.7372	A4	
	1250	0	546.8	0.7372	A4	
	1250	I	546.8	0.4572	A4	
	1250	0	546.8	0.4572	A4	
E1	1250	I	68.0	0.7372	--	CONTROL
2	1250	I	546.8	0.4572	--	HISTORY
3	1250	I	546.8	0.1772	--	DATA
4	1250	0	68.0	0.7372	E2	
5	1250	0	546.8	0.4572	E3	
6	1250	0	546.8	0.1772	E4	

All cases run at full power and constant xenon conditions.

Table 2-3

Exposure Points (GWd/MT) Used in the Generation of Lattice Physics Data

Base Depletion	Controlled Restart	Doppler Effects	Void History	Control History	Lattice Physics Library
0.0					
0.005	0.005		0.005	0.005	0.005
0.22	0.22	0.22	0.22	0.22	0.22
0.55					0.55
1.1	1.1		1.1	1.1	1.1
1.65					1.65
2.2					2.2
3.3	3.3		3.3	3.3	3.3
4.4					4.4
5.5	5.5		5.5	5.5	5.5
6.6					6.6
7.7	7.7	7.7	7.7	7.7	7.7
8.8					8.8
9.9	9.9		9.9	9.9	9.9
11.0	11.0		11.0	11.0	11.0
12.1					12.1
13.2	13.2		13.2	13.2	13.2
16.5	16.5	16.5	16.5	16.5	16.5
					19.25
22.0	22.0		22.0	22.0	22.0
					24.75
27.5	27.5	27.5	27.5	27.5	27.5
					30.25
33.0	33.0				33.0
38.5					38.5
46.0	46.0				46.0
51.5					

cases were run from the base depletions to calculate lattice physics data describing the history effect of deviations in moderator density. Both uncontrolled and controlled restarts were run with varying moderator densities (cases D1-D3 in Table 2-2).

To determine the history effect of depleting with the control rod inserted, restart cases were run from controlled depletions (cases E1-E3 in Table 2-2) and withdrawing the control rod (cases E4-E5 in Table 2-2).

2.3 Lattice Physics Data Representation

The TGBLA analyses produced homogenized three-group cross-section data for each unique lattice type. This section describes the representation of these data for use in the core simulator and the techniques used to correct the lattice physics data at base conditions to the actual operating conditions.

To accurately describe the neutronic properties of each node, the base lattice physics parameters used in the core simulator are functions of exposure E, moderator density U, and control fraction CF (defined as the fraction of the node height a control rod is inserted). The three group cross-section data were processed with auxiliary programs to produce controlled (CF = 0) and uncontrolled (CF = 1) table sets of two-group lattice physics data at specific E and U values. The core simulator uses multi-variable Lagrangian interpolation of the table sets to obtain the nodal parameters at the current values of E, U and CF. Except for the correction factors described later in this section, values from the uncontrolled base depletion cases and

controlled restart cases were used to construct the uncontrolled and controlled lattice physics table sets, respectively.

The table set representation of the lattice physics data is highly accurate, but is inefficient with respect to storage and processing requirements. Therefore, parameters which have secondary effects and/or have little variation over the range of operating conditions are represented using polynomial fits. Some parameters represented using fits include Doppler reactivity worth, fission yields, and moderator density history corrections to power-to-TIP conversion factors and kinetics parameters.

Due to variations in core operation during the cycle, U and CF will not remain constant. By averaging nodal U and CF values with respect to the nodal E, moderator density history and control history variables can be defined as

$$UH(E) = E\ \overline{U}(E) \tag{2-1}$$

$$CH(E) = E\ \overline{CF}(E) \tag{2-2}$$

Where $\overline{U}$ and $\overline{CF}$ are the exposure-averaged moderator density and exposure-averaged control fraction respectively

$$\overline{U}(E) = \frac{1}{E}\int_0^E U(E)\ dE \tag{2-3}$$

$$\overline{CF}(E) = \frac{1}{E}\int_0^E CF(E)\ dE \tag{2-4}$$

Since the base lattice physics data are taken from the uncontrolled base depletion and controlled restart cases, the assumptions incorporated in the table sets are that $U = \overline{U}$ and CF = 0 with base values of power density (equilibrium xenon) and fuel temperature T_f. Parameters which are not sensitive to deviations from the base conditions of the table sets are determined simply by interpolation. For other variables, in particular the nodal infinite multiplication factor k_∞, corrections to the base values are required to accurately represent the lattice physics data at the actual operating conditions.

Moderator density history correction. The moderator density has a large affect on the neutron spectrum, which in turn, influences the spatial isotopic concentrations resulting from burnup. Since the base table sets assume that $U = \overline{U}$, a correction to the base k_∞ is necessary to account for the change in reactivity due to isotopic concentrations different from those assumed in the table sets. The effect on reactivity is determined for both uncontrolled and controlled nodes at three $\overline{U}$ values and four U values. Moderator density history correction factors are tabulated in table sets for use in the core simulator. The following ratio is used to define the moderator density history effect:

$$C_{uh} = \frac{k_\infty(U=U1,\ \overline{U}=U2)}{k_\infty(U=\overline{U}=U2)} \qquad (2\text{-}5)$$

where U1 is the current moderator density and U2 is the exposure-averaged moderator density. The numerator is the k_∞ from the moderator density history restart cases (cases D1-D3 in Table 2), and the denominator is the base k_∞ from the uncontrolled base depletions (cases A2-A4 in Table 2-2) or the controlled restarts (cases B1-B4 in Table 2-2).

Other variables affected by differences in U and $\overline{U}$ are adjusted using polynomial fits. These parameters include the power-to-TIP conversion factor, delayed neutron fraction, and group average neutron velocities. These corrections have been shown to be insensitive to both enrichment and gadolinium loadings. Therefore, fitting coefficients for Quad Cities-1 lattices were taken from similar Browns Ferry fuel designs.

Control history correction. The spatial isotopic concentrations resulting from burnup are also sensitive to the control rod being inserted or withdrawn during the depletion. Therefore, reactivity adjustments to k_∞ are made in the core simulator to account for control history effects. Since the uncontrolled base table sets assume that the control rod is withdrawn during the depletion ($\overline{CF} = 0$), reactivity adjustments to k_∞ are made to account for control history effects when the uncontrolled node has been operated with the control rod inserted. The control history correction for uncontrolled nodes is defined as:

$$C_{ch} = \frac{k_\infty(CF=1, \overline{CF}=0)}{k_\infty(CF=\overline{CF}=0)} \qquad (2\text{-}6)$$

The controlled k_∞ table sets assume $\overline{CF} = 0$ and $CF = 1$, therefore the k_∞ of controlled nodes are also corrected for control history. The control history correction is similarly defined for controlled nodes:

$$C_{ch} = \frac{k_\infty(CF=\overline{CF}=1)}{k_\infty(CF=0,\overline{CF}=1)} \qquad (2\text{-}7)$$

where

$k_\infty(CF=1,\overline{CF}=0)$ = infinite multiplication factor from the controlled restart cases (cases B1-B4 in Table 2-2),

$k_\infty(CF=\overline{CF}=0)$ = infinite multiplication factor from the uncontrolled base depletion cases (cases A1-A4 in Table 2-2),

$k_\infty(CF=\overline{CF}=1)$ = infinite multiplication factor from the controlled depletion cases (cases E1-E3 in Table 2-2),

$k_\infty(CF=0,\overline{CF}=1)$ = infinite multiplication factor from the control history restart cases (cases E4-E6 in Table 2-2).

The control history corrections are tabulated in controlled and uncontrolled table sets at the four instantaneous moderator densities.

Xenon and samarium concentration correction. The base k_∞ values incorporate the negative reactivity worth of equilibrium xenon and samarium concentrations at the base power density. Because these fission products have extremely high absorption cross sections, deviations from the base concentrations are accounted for. The

correction is related to the fractional change in xenon and samarium concentrations relative to the base concentrations:

$$C_{xs} = 1 - \left[\rho_{xe} \frac{(X - X_o)}{X}\right] - \left[\rho_{sm} \frac{(S - S_o)}{S}\right] \qquad (2\text{-}8)$$

where

X = Xe-135 concentration at the current power density (atoms/barn-cc),

S = Sm-149 concentration at the current power density (atoms/barn-cc),

X_o = Xe-135 concentration at the base power density (atoms/barn-cc),

S_o = Sm-149 concentration at the base power density (atoms/barn-cc),

ρ_{xe} = reactivity worth of base equilibrium Xe-135 concentration,

ρ_{sm} = reactivity worth of base equilibrium Sm-149 concentration.

The current xenon (X) and samarium (S) concentrations for the steady-state depletion modeling of Quad Cities-1 were determined by the core simulator based on the calculated nodal power. Zero nodal xenon concentrations and equilibrium samarium concentrations were used in the Quad Cities-1 cold critical analyses.

To account for changes in the thermal neutron spectrum due to deviations from the base xenon and samarium concentrations, C_{xs} is also used to correct the thermal diffusion area and thermal absorption cross-section.

Fuel temperature correction. Deviations of the nodal fuel temperature T_f from the base value T_f^o affect the nodal multiplication factor through Doppler broadening of the resonances in the fuel. This effect is accounted for by adjusting the base k_∞ in the core simulator using the following correction factor:

$$C_D = 1 + \alpha(\sqrt{T_f} - \sqrt{T_f^o}) \qquad (2\text{-}9)$$

Where the Doppler coefficient (α) is determined from a polynomial fit dependent on U, $\bar{U}$, CF and E. The Doppler fit was generated for each lattice type using data generated in the Doppler restart cases (cases C1-C5 in Table 2-2).

In addition to correcting k_∞, C_D is used to make corrections to other parameters sensitive to changes in resonance absorption. These parameters include the age-to-thermal, the fast absorption plus removal cross-section, and the resonance escape probability.

Combination of correction factors. The effect of deviations from the base fuel temperature, control history, xenon concentration, samarium concentration, and moderator density history are assumed to be independent and separable. The correction factors described in the previous subsections are combined in the core simulator to adjust the base nodal k_∞ values by:

$$k_\infty = k_\infty^o \, C_D \, C_{xs} \, C_{uh} \, C_{ch} \qquad (2\text{-}10)$$

where

k_∞ = the corrected nodal infinite multiplication factor,

k_∞^o = the base k_∞ interpolated from the table sets.

2.4 Assembly Thermal Hydraulic Modeling

Because of the strong coupling between the nodal lattice physics data and moderator density, the CORE-II core simulator includes a thermal-hydraulic model to calculate the core-wide moderator density and flow distributions. A large number of thermal-hydraulic iterations are typically performed in the core simulator to obtain a solution for a particular core configuration. Therefore, to avoid performing repeated calculations of pressure drop and flow for each assembly in the core, the detailed assembly thermal-hydraulic analysis is performed externally to the core simulator using the FIBWR code.

FIBWR calculates single channel flow rates by solving the steady-state one-dimensional equations for continuity, momentum, and energy. The complex geometry and flow paths of BWR thermal-hydraulic channels are explicitly modeled, including the leakage flow to the bypass region. The bypass flow makes up the non-boiling coolant between assemblies and is typically 10% of the total core flow. The bypass flow provides moderation in the core top, cools in-core instruments and control rods, and allows for consistent detector measurements throughout the core by surrounding each detector location with non-boiling water.

Detailed calculations are made for each thermal-hydraulic channel type, which are defined by the fuel assembly geometry and orifice size.

Each thermal-hydraulic channel type is analyzed using a fixed axial power distribution and base values of inlet temperature and core pressure. The channel flow rate is determined using several channel powers at varying channel pressures. The results are input to the core simulator via table sets of channel flows at specific values of channel power and pressure drop.

To account for deviations in the assumed conditions of the channel flow table sets, the base channel flows are corrected in the core simulator for variations of the reactor pressure, inlet temperature and axial power shape. A parametric analysis is performed using FIBWR to determine what the effect of varying these parameters has on the channel flow rate. The corrections are represented as polynomial fits for use in the core simulator.

2.5 Nodal Core Modeling

The three-dimensional core modeling is performed using the CORE-II core simulator code. CORE-II is capable of modeling the inter-relationship of all operating parameters, including power level, control rod position, flow, pressure, exposure, and moderator density. Options are available to calculate thermal limits, simulate in-core detectors, perform core depletions, and track the Ba-140 concentration distribution for gamma scan comparisons. Special fuel management options are also available to calculate the Haling exposure distribution, estimate relative rod worths, and to aid in the development of fuel shuffling patterns.

The core simulator input is based on the detailed assembly neutronic and thermal-hydraulic analysis described in sections 2.2 and 2.3, respectively. The assembly data are combined to form cycle specific input libraries. Nodal operating history data are maintained through the use of restart files.

The control rod configuration is accounted for in the core simulator by using either controlled or uncontrolled lattice physics data for each node. If control rods are only partially inserted, nuclear parameters are determined by interpolating controlled and uncontrolled data.

CORE-II is capable of modeling water nodes based on input cross-section data. With this ability, a core reflector region can be modeled by surrounding the fueled core with water nodes.

Core representation. The CORE-II core simulator represents the reactor core as a three-dimensional array of rectangular nodes. Consistent with the fuel assembly analysis, radial node dimensions in the core modeling represent individual fuel assemblies and surrounding water. Node heights are typically six inches, but can be non-uniform in length to accommodate the axial variation of enrichment and/or burnable poison within fuel assemblies.

Figure 2-1 shows the radial plane of the Quad Cities-1 core with the standard coordinate system used to identify assembly, control rod, and detector locations.

Input arrays are used to assign nuclear and thermal-hydraulic parameters for each core node. Fuel assemblies with similar heat

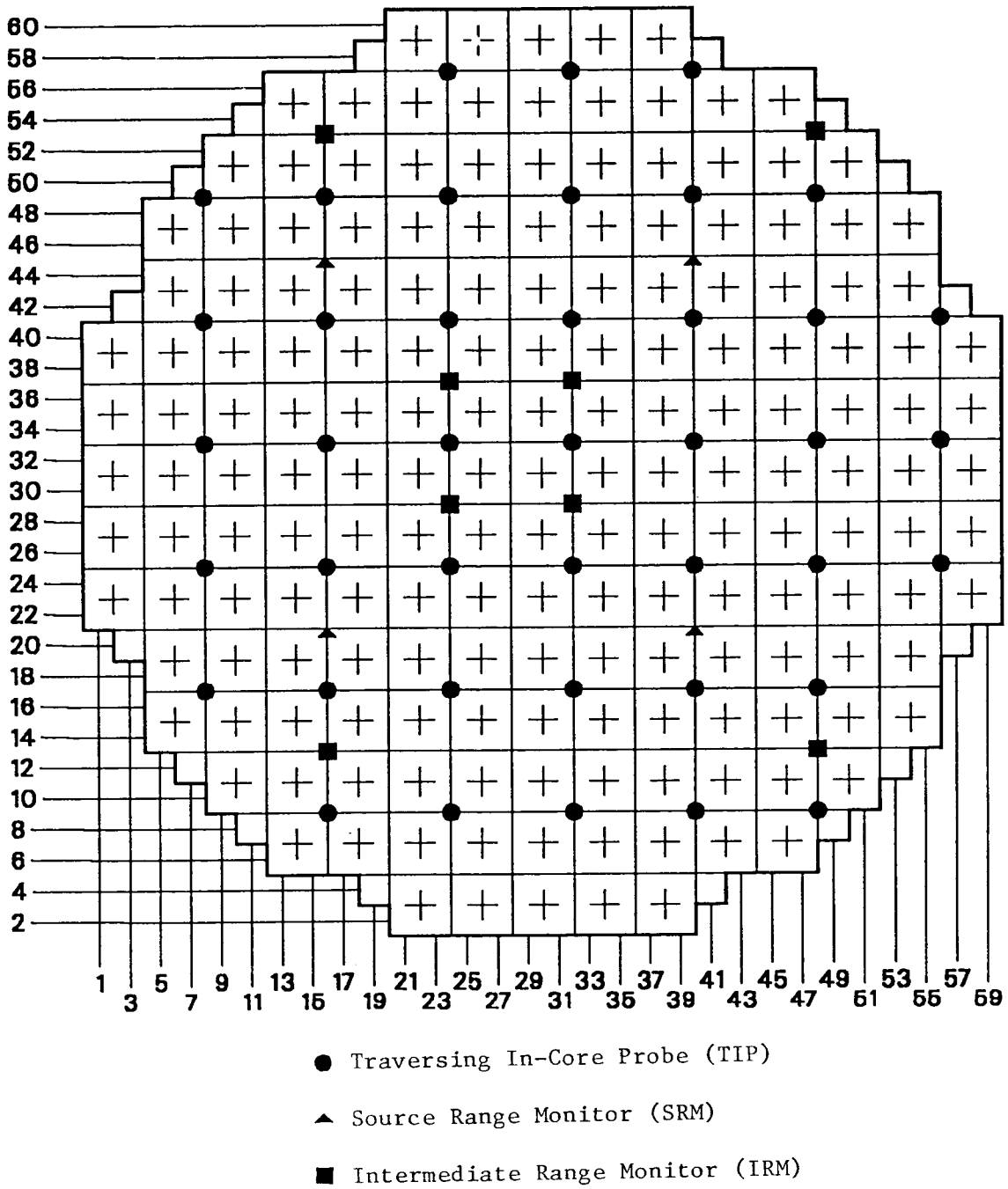

Figure 2-1. Coordinate System and Detector Locations

transfer properties, flow characteristics, and axial variations in nuclear properties are modeled as the same assembly type. The axial variation within an assembly type is defined by assigning different lattice types. Figure 2-2 illustrates the difference between assembly type and lattice type. Character labels signifying assembly types have been used in this figure for illustrative purposes.

Similarly, an orifice type array is used to separately model channels with different orifice sizes. This array was used in the Quad Cities modeling to designate the peripheral channels which contain restricted orifices relative to the channels located in the central core region.

Together, the assembly type, lattice type, and orifice type arrays are used to index the table sets and fitting coefficients contained in the core simulator input library. Thus, each node was explicitly modeled according to its unique neutronic and thermal-hydraulic characteristics.

Neutronic model. The CORE-II core simulator is based on advanced nodal steady-state two-group diffusion theory. Inner and outer iterations are used to solve mesh centered finite difference equations for the node average fluxes. This solution is embedded in an overall iteration algorithm which computes expansion coefficients and discontinuity factors which force agreement with higher order calculations.

Assembly discontinuity factors (ADF) are used to account for the removal of the assembly heterogeneity during the production of the

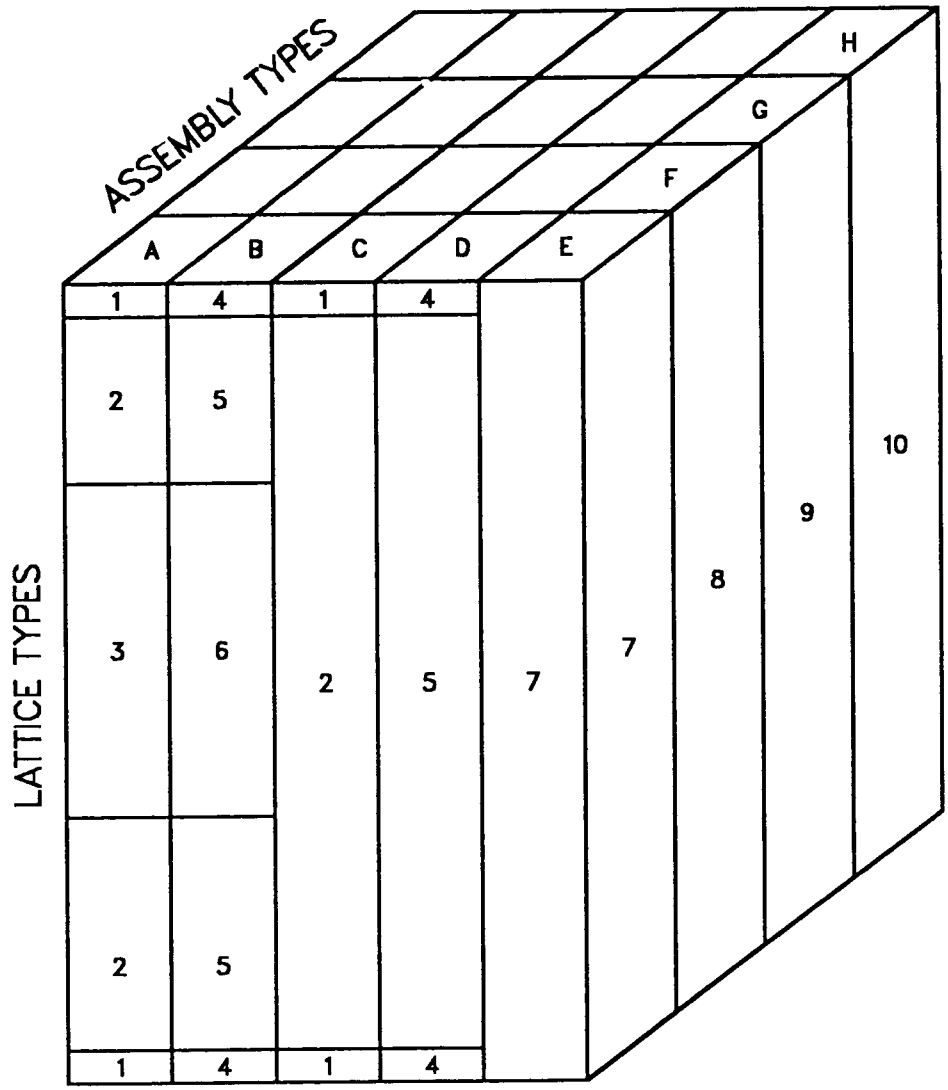

Figure 2-2. Assembly and Lattice Types

cross-section data. These factors are obtained from TGBLA as the ratio of the lattice gap fluxes to lattice average fluxes. The core simulator utilizes these values to estimate the nodal surface flux given the node average flux. Table sets of two group ADF's are input to the core simulator for the wide and narrow gap.

Input values for energy dependent albedoes are applied as boundary conditions to peripheral nodes. The CORE-II neutronics equations were flexibly derived and programmed to avoid the numerical problems associated with modeling water nodes and non-uniform height nodes.

Thermal hydraulic model. Due to the strong coupling of the nodal neutronics data and the nodal operating conditions, the thermal-hydraulic model of the core has a significant effect on the calculation of reactivity and power distributions. Thus, the thermal-hydraulic calculations are equally as important as the neutronics calculations.

The objective of the thermal-hydraulic calculations is to compute the nodal water density, fuel temperature, and moderator temperature distributions based on input or current estimated values of core flow, bypass flow, inlet temperature, core pressure drop, and nodal power distribution. The analysis is based on mass and energy balance equations, together with void correlations which describe the full range of BWR coolant conditions.

The core flow is distributed to the individual channels using an iterative procedure to balance the individual assembly pressure drops with the total core pressure drop. The iterations force the sum of the channel and bypass flows to equal the specified total core flow. The

core pressure drop is adjusted between thermal-hydraulic iterations to equalize the calculated total core flow with the specified total core flow. Channel flows are evaluated based on input table sets of channel flow versus channel power and pressure described in section 2.4. The nodal water density distribution is then calculated based on the flow distribution, nodal power distribution, and core inlet temperature.

The core simulator accounts for the reactivity feedback effects by iterating between the neutronic and thermal-hydraulic calculations. These power-void iterations are continued until the solution is converged or a maximum number of iterations have been performed. The lattice physics parameters remain constant through the neutronic iterations, and are not updated until a new thermal-hydraulic calculation has been performed. Thus, the thermal-hydraulic feedback is accomplished through the re-evaluation of the nodal physics parameters after each thermal-hydraulic calculation.

The Doppler effect is another important reactivity coupling which is dependent on the calculation of effective nodal fuel temperatures. The average nodal fuel temperature is determined in the thermal-hydraulic calculations using correlations which are functions of the nodal bulk moderator temperature, nodal average linear power density and nodal average exposure.

Depletion modeling. Since the lattice physics data are determined as a function of exposure, the detailed accounting of individual isotopic concentrations and their effects on reactivity is incorporated in the core simulator input. The core simulator depletion calculation

needs only to increment the nodal exposures and track operating history dependent variables. A special auxiliary burnup calculation to track Ba-140 for comparison with measured in gamma scan data is described later.

Core depletion calculations which simulate actual reactor operations are performed using the forward step depletion method. The exposure range to be modeled, typically a reactor cycle, is divided into exposure steps during which the operating parameters have minor variations. The operating conditions are assumed to be stepwise constant over the exposure interval. Representative operating parameters describing the exposure step are used to calculate the power distribution at the current core exposure. The new nodal exposure, nodal water density history, and nodal control history distributions are then incremented in proportion to the nodal relative power and core average incremental exposure. Properties of each node are updated by:

$$E_{n+1} = E_n + P\ \Delta E\left(\frac{AWC}{AWN}\right) \tag{2-11}$$

$$UH_{n+1} = UH_n + U\ P\ \Delta E\left(\frac{AWC}{AWN}\right) \tag{2-12}$$

$$CH_{n+1} = CH_n + CF\ P\ \Delta E\left(\frac{AWC}{AWN}\right) \tag{2-13}$$

where

E = nodal exposure (Gwd/Mt),

P = nodal relative power at E(n),

DE = core average exposure increment (Gwd/Mt),

U = nodal water density during exposure step (g/cc),

CF = nodal control fraction during exposure step,

UH = nodal water density history,

CH = nodal control history,

AWC = core average nodal mass of heavy metal (Kg/cc),

AWN = node average mass of heavy metal (Kg/cc).

The core power distribution and effective multiplication factor are recalculated using the updated nodal neutronic parameters evaluated at the new core average exposure. Using this procedure, the fuel is depleted through a reactor cycle in a series of exposure steps.

Ba-140 tracking model. Comparisons to measured gamma scan data requires that the end of cycle Ba-140 distribution be calculated by the core simulator. The rate equation describing the time dependent production and decay of Ba-140 is:

$$\frac{dN_B}{dt} = \gamma_B \Sigma_f \phi - \lambda_B N_B \qquad (2\text{-}14)$$

where

$N_B(t_n)$ = Ba-140 atom density (atoms/barn-cm),

γ_B = effective fission yield of Ba-140,

Σ_f = macroscopic fission cross section (1/cm),

ϕ = neutron flux (neutrons/barn-cm-sec),

λ_B = Ba-140 decay constant (1/sec).

By assuming that each of these variables is stepwise constant over a given time interval, this equation can be recast for use in the core simulator:

$$N_B(t_n) = S_B(t_n)\ P + \left[N_B(t_{n-1}) - S_B(t_n)\ P\right] e^{-(\lambda_B\ \Delta t)} \qquad (2\text{-}15)$$

where

n = 1,2, ,,, m,

$N_B(t_n)$ = end of step nodal Ba-140 atom density (atoms/barn-cm),

P = nodal power calculated by the core simulator (Mw),

Δt = incremental time of depletion step (sec),

and S_B is a pseudo Ba-140 production rate defined by:

$$S_B = \frac{\gamma_B\ C}{\kappa\ \lambda_B} \qquad (2\text{-}16)$$

where

κ = assembly average energy released per fission (Mev),

$C = 1.0 \times 10^{24}$ barns/cm^2.

To accurately account for the variation of the pseudo Ba-140 production rate (S_B) through operation, S_B is calculated during the fuel assembly neutronic analysis and are tabulated in table sets for use in the core simulator. On option, the Ba-140 distribution can be set to the equilibrium concentration by the core simulator.

Simulated TIP Readings. Detailed power distribution measurements in BWRs are made using traversing in-core probes (TIPs). The simulation of TIP readings is included in the core simulator to enable comparisons with measured TIP data. In addition, simulated TIP readings are used to predict detector responses in specific design analyses (e.g. rod withdrawal error).

Instrument tubes in BWRs are located in the narrow gap of four fuel assembly cells. TIP measurements are made by running a small fission chambers through the instrument tubes and averaging the response over six inch intervals. Thus, the TIP readings measure the average power of the four surrounding fuel assembly segments.

The core simulator calculates TIP readings as a function of the power produced in the four surrounding assemblies. Simulated TIP readings are calculated at each radial TIP location, and each axial level as:

$$R = \frac{1}{n} \sum_{i=1}^{n} \frac{P(i)}{J(i)} \qquad (2\text{-}17)$$

where

n = number of assemblies surrounding TIP detector (=4),

R = predicted TIP reading,

P(i) = nodal relative power of adjacent fuel node i,

J(i) = power-to-TIP conversion factor of adjacent of fuel node i.

The nodal relative power is obtained from a power distribution calculation using the core conditions at the time of the measurement. The power-to-TIP conversion factor, J, is defined as the ratio of the assembly fission rate to the fission rate at the detector. Thus, the TIP calculation assumes the variation of the detector response is directly proportional to the nodal relative power.

Power-to-TIP conversion factors are determined by interpolation of input table sets and are obtained from the detailed lattice physics analysis as a function of exposure, water density, and control state. Consistent with measured TIP data, the predicted TIP readings are normalized to the axial average of a user-specified radial TIP location.

3.0 CORE MODEL AND INPUT DATA

3.1 Overview

The spatial representation used to model a BWR core is usually determined by the available computer resources (memory size, computing power) and the desired accuracy. For less accurate calculations, approximations which utilize core symmetry (e.g. quarter core representation), groupings of similar fuel assembly types, and large node sizes can be made to reduce the required computer resources. Approximations can also be made in the core operation modeling by using large depletion steps and relaxing the convergence criteria.

An IBM model 3084-KQ mainframe computer with a virtual memory operating system was used for all calculations reported in this thesis. The memory size and disk storage available on this system was effectively limitless. Due to the significance of the calculated results with respect to qualifying the analysis methods, the computing costs associated with the calculations were of secondary importance. This allowed a relatively high degree of detail to be incorporated in both the core representation and modeling.

This section contains a description of the core model used to simulate Quad Cities-1 cycles 1 and 2 operation. An overview of the reactor design data, fuel assembly design data, and reactor operational parameters used in the modeling is also presented.

3.2 Core Model

All core calculations were performed using full core, three-dimensional representation, with thermal-hydraulic feedback. Standard fuel node sizes used in core simulator and process computer calculations are 6x6x6 inches. A somewhat more detailed representation was used for the Quad Cities-1 core.

Since the CORE-II core simulator is capable of modeling non-uniform node sizes, it was possible to model the unique top and bottom three inch segments of the initial core 7x7 fuel assemblies. This axial zoning was explicitly modeled by splitting the top and bottom fuel nodes to form three inch nodes. The remaining fuel was modeled using the standard 6x6x6 inch node size.

To provide an accurate representation of the true core boundary, reflector nodes were used to completely surround the fueled core. The cross-section data used for the reflector nodes represented the coolant and smeared metal core components located in the corresponding core regions (top, bottom, and periphery). Assembly sized reflector nodes (6x6x6 inch) were placed adjacent to peripheral fuel nodes and larger reflector nodes (12x6x6 inch) were placed along the core top and bottom. Figure 3-1 illustrates the core nodalization, including the reflector region. The fuel and reflector were represented using a total of 25,304 nodes. Actual computer memory requirements were based on a larger (28x32x32 node) problem size.

Boundary conditions. Albedo boundary conditions were applied to the outer edge of the reflector nodes. Since the size of the reflector

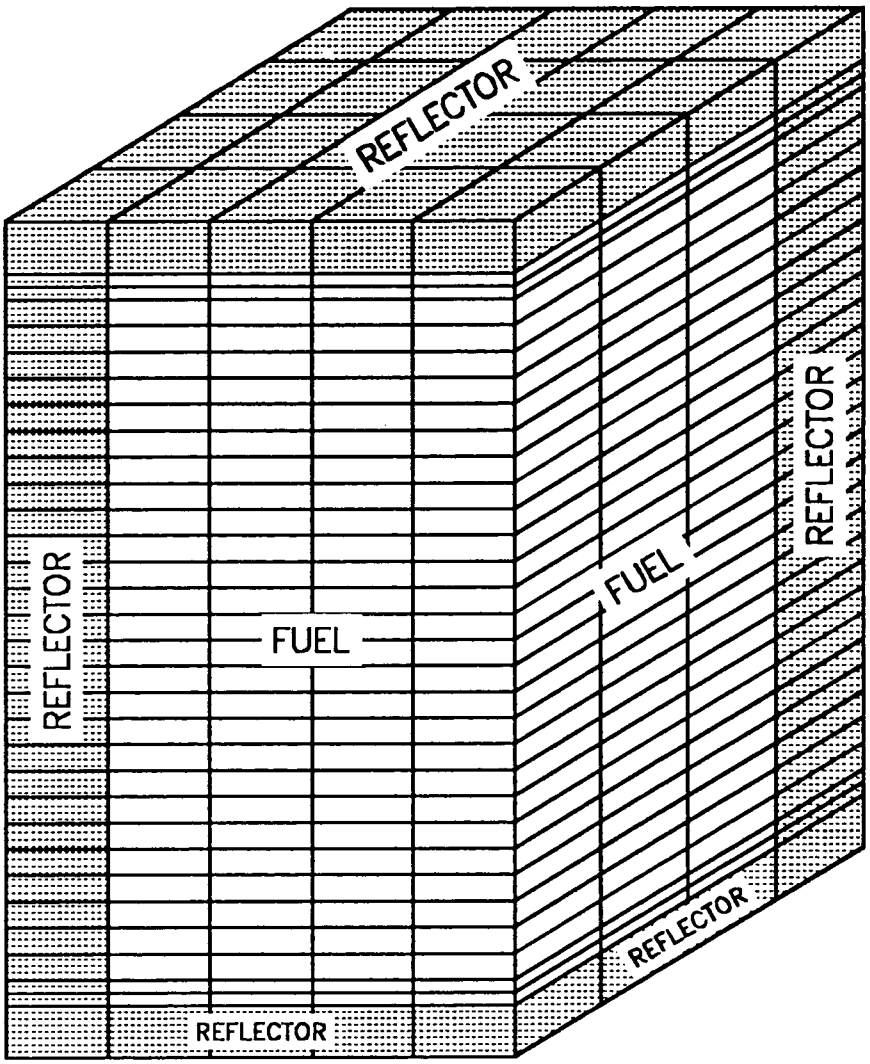

Figure 3-1. Quad Cities-1 Reflected Core Model

nodes are larger than two to three mean-free-paths of fast neutrons in water, a significant number of the neutrons which travel to the edge of reflector nodes do not return to the fueled region. As a result, the core reactivity and power distribution are somewhat insensitive to the choice of albedo values.

Reasonable estimates of the albedo values were calculated analytically. This method was chosen due to its simplicity compared to the alternatives of performing detailed calculations of the flux behavior in the reflector regions, or empirically determining albedo values by matching calculated and measured power distributions.

The two-group, one-dimensional diffusion equation describing a thick reflecting slab was used to calculate energy dependent albedo values $A_{i,j}$ which relate the incident neutron current (J_{in}) and the reflected neutron current (J_{out}).

$$J_{out} = A_{i,j} J_{in} \tag{3-1}$$

The following analytical solution exists for a very thick reflecting slab:

$$A_{i,j} = \frac{(\alpha_{i,j} - 2)}{(\alpha_{i,j} + 2)} \tag{3-2}$$

with

$$\alpha_{1,1} = \frac{L_1}{D_1} \tag{3-3}$$

$$\alpha_{2,2} = \frac{L_2}{D_2} \tag{3-4}$$

$$\alpha_{1,2} = \left[\frac{\Sigma_1^r}{(D_1\ \Sigma_1^a - D_2\ \Sigma_2^a)}\right] (D_1\ \alpha_{1,1} - D_2\ \alpha_{2,2}) \tag{3-5}$$

where

$\alpha_{1,1}$ = albedo for fast neutrons returning as fast neutrons,

$\alpha_{2,2}$ = albedo for thermal neutrons returning as thermal neutrons,

$\alpha_{1,2}$ = albedo for fast neutrons returning as thermal neutrons,

L_1, L_2 = fast and thermal diffusion length, respectively,

D_1, D_2 = fast and thermal diffusion coefficient, respectively,

Σ_1^a, Σ_2^a = fast and thermal absorption cross sections, respectively,

Σ_1^r = fast group removal cross section.

Albedo values for each reflector region were calculated using cross-section data from TGBLA analyses for a base water density. The analytical albedo solution (equation 3-2) and reflector cross-section data at various water densities are used in the core simulator to correct the input albedoes to the actual water density.

Core simulator input. A large amount of core simulator input was required to accurately describe the core configuration, fuel characteristics, and operation of the core. The core simulator input was obtained from a variety of sources.

Core loading patterns, fuel assembly design data, core design data, and operating parameters were obtained from References 7 and 8. Detailed lattice physics data for each lattice type were explicitly generated using TGBLA. Two group cross-section data for the reflector nodes were taken from existing TVA TGBLA results for typical BWR core reflector regions. Thermal hydraulic data were taken from existing TVA analyses of similar Browns Ferry fuel designs.

3.3 Fuel Assembly Design Data

The fuel assembly design data were obtained from Reference 7. This information provided a complete description of the assembly designs for lattice physics calculations including: (1) pellet, clad, and assembly dimensions, (2) enrichment and burnable poison distributions, (3) fissile material and burnable poison weights and densities, and (4) channel dimensions.

Cycle 1 fuel assembly types. The cycle 1 core contained four distinct assembly types. All of the initial core assemblies had a 7x7 rod array, with an average U-235 enrichment of 2.12 w/o. Table 3-1 summarizes fuel assembly information and other pertinent data for cycles 1 and 2.

Table 3-1

Fuel Assembly Data

	Initial Core 7x7				Cycle 2 Reload			
Assembly Type	1	2	3	4	5	6	7	8
Dished Pellets	Yes	No	Yes	No	Yes	No	Yes	No
Assembly Avg Enrichment	2.12	2.12	2.12	2.12	2.30	2.50	2.71	2.51
No. Cycle 1 Assemblies	185	127	276	136	0	0	0	0
No. Cycle 2 Assemblies	164	115	251	130	23	36	4	1
Geometry	7x7	7x7	7x7	7x7	7x7	8x8	7x7	7x7
Fuel Rods per Assembly	49	49	49	49	49	63	49	48
Water Rods per Assembly	0	0	0	0	0	1	0	0
Burnable Poison Rods	3	3	2	2	3	4	5	3
Fuel	UO2	UO2	UO2	UO2	UO2	UO2	MOX	MOX
Total Fuel (Kg-oxide)	218	223	218	223	213	208	211	211

Assembly types 1 and 2 contained two fuel rods with 3.0 w/o gadolinia (Gd^2O^3) along the middle 139 inches, and one fuel rod with 0.5 w/o gadolinia along a 60 inch center segment. Figure 3-2 shows the radial enrichment and burnable poison distribution within assembly types 1 and 2. Figure 3-3 shows the axial zoning of both gadolinia fuel rod types. In this figure, as well as in Figure 3-2, the 0.5 w/o gadolinia concentration is shown as "Type Z", and the 3.0 w/o gadolinia concentration is shown as "Type Y". The only difference between these assembly types was that assembly type 1 contained some fuel rods composed of dished fuel pellets. The dishing of the pellet ends was designed to mitigate pellet clad interactions (PCI).

Assembly types 3 and 4 were similar to assembly types 1 and 2, respectively, but contained only two fuel rods with 3.0 w/o gadolinia along the middle 139 inches. Figure 3-4 shows the radial enrichment and burnable poison distribution within assembly types 3 and 4.

The axial zoning of the initial core fuel required analysis of six distinct lattice types (three dished and three undished). All six lattice types were explicitly modeled with TGBLA to generate lattice physics data for use in the core simulator. Because of the similar neutronic characteristics, the dished and undished lattices could have been accurately modeled using physics data for only one of the pellet designs.

Cycle 2 fuel assembly types. The cycle 2 core contained eight distinct assembly types. In addition to the four assembly types used in cycle 1, the cycle 2 core contained 7x7, 8x8, and two plutonium

2.12 wt% U-235 BUNDLE AVERAGE

WIDE-WIDE CORNER

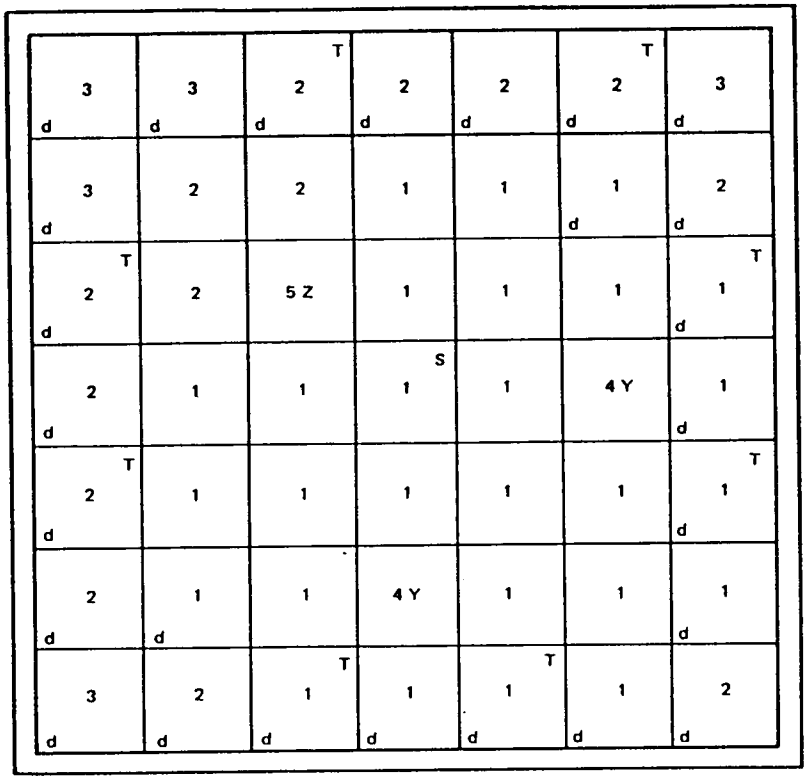

ROD TYPE	U-235 (wt%)	Gd_2O_3 (wt%)	NO. OF RODS
1	2.47	0	27
2	1.70	0	14
3	1.20	0	5
4 Y	2.47	3.0	2
5 Z	2.47	0.5	1

S = SPACER CAPTURE ROD
T = TIE ROD
d = DISHED ROD IN A DISHED BUNDLE

Figure 3-2. Assembly Design for Types 1 and 2 Initial Fuel

Source: "Core Design and Operating Data for Cycles 1 and 2 of Quad Cities 1," EPRI NP-240, Electric Power Research Institute.

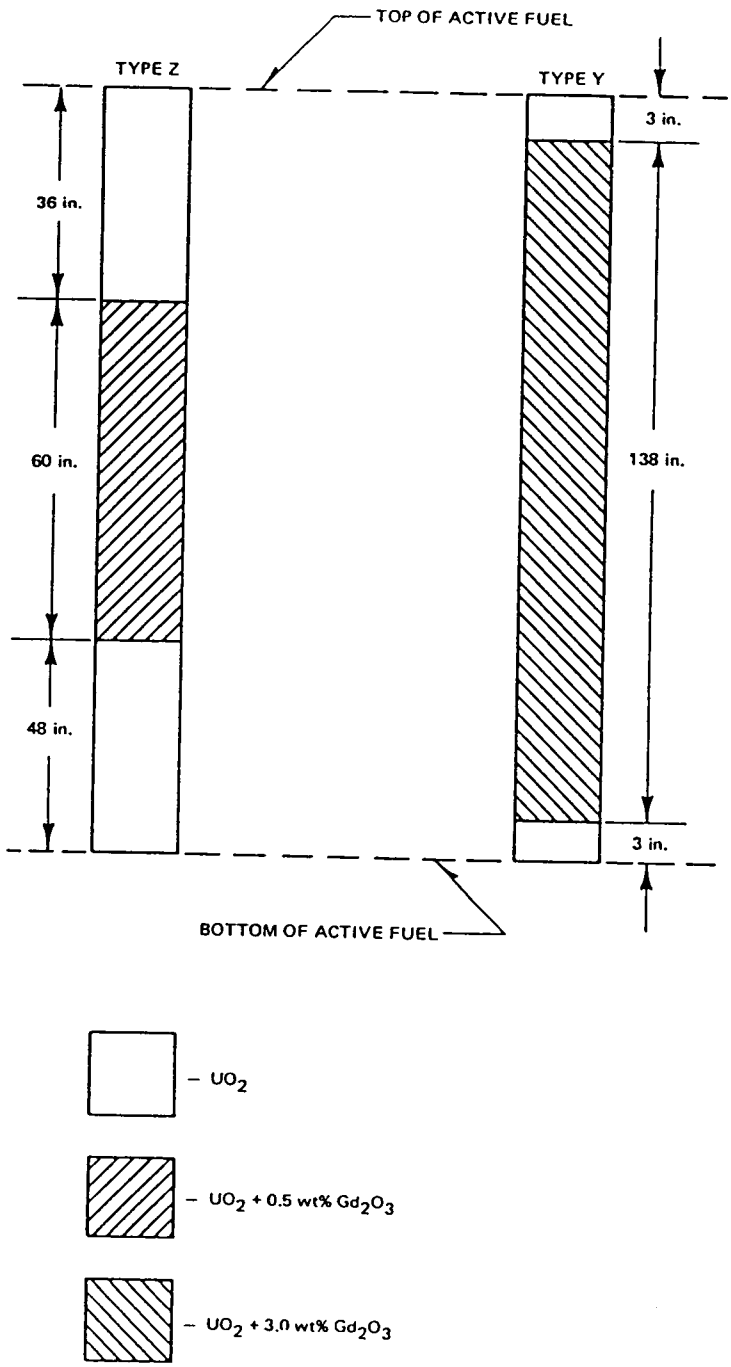

Figure 3-3. Axial Zoning of Initial Core Assembly Types

Source: "Core Design and Operating Data for Cycles 1 and 2 of Quad Cities 1," EPRI NP-240, Electric Power Research Institute.

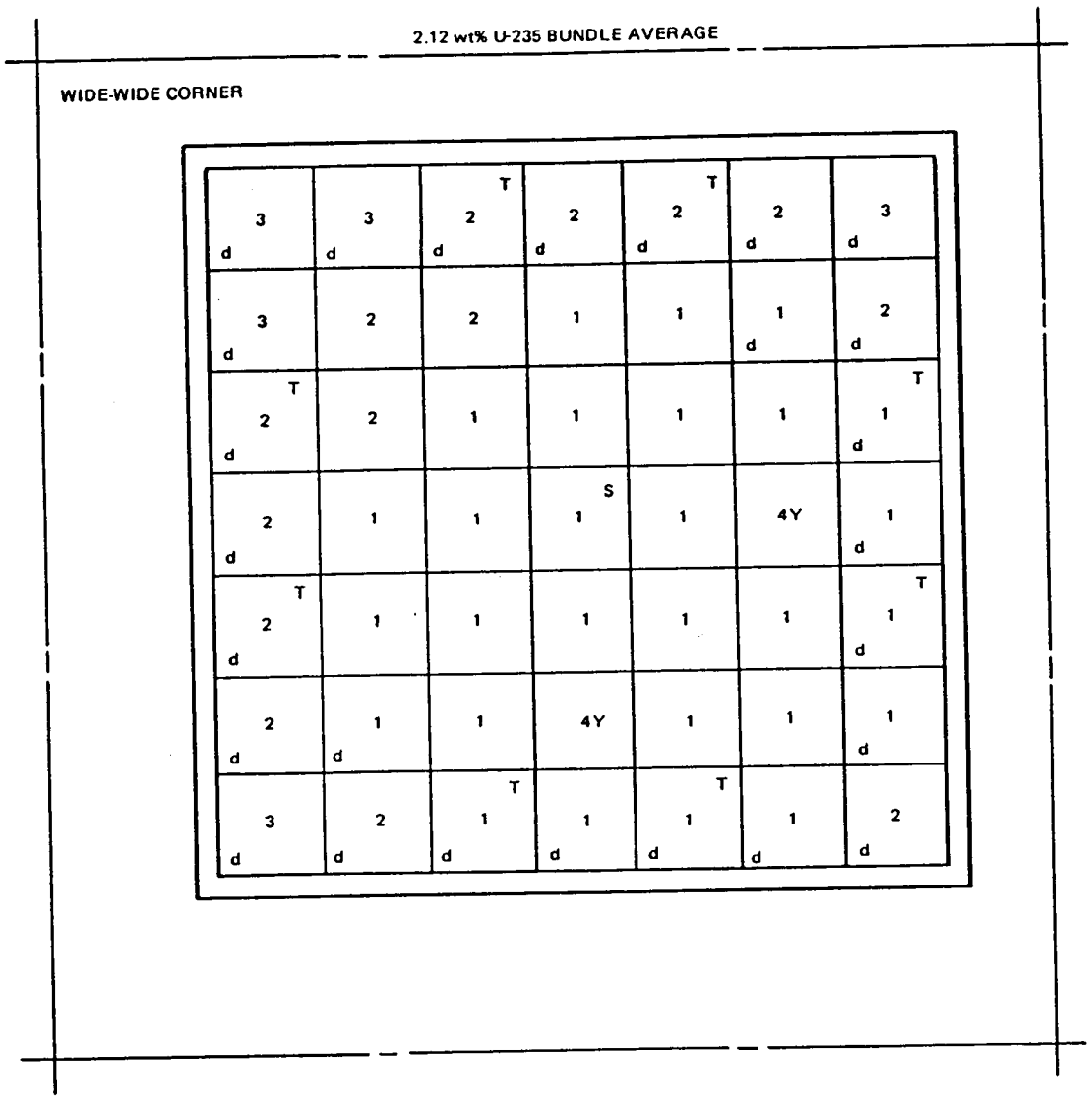

ROD TYPE	U-235 (wt%)	Gd_2O_3 (wt%)	NUMBER OF RODS
1	2.47	0	28
2	1.70	0	14
3	1.20	0	5
4 Y	2.47	3.0	2

S = SPACER CAPTURE ROD
T = TIE ROD
d = DISHED ROD IN A DISHED BUNDLE

Figure 3-4. Assembly Design for Types 3 and 4 Initial Fuel

Source: "Core Design and Operating Data for Cycles 1 and 2 of Quad Cities 1," EPRI NP-240, Electric Power Research Institute.

bearing Mixed Oxide (MOX) reload assembly types. Radial enrichment and burnable poison distributions for the 7x7 and 8x8 reload assembly types are shown in Figure 3-5 and 3-6, respectively. The reload 7x7 assembly type had a higher U-235 enrichment (2.30 w/o) relative to the initial core 7x7 and was not axially zoned. The reload 8x8 assembly type had an average U-235 enrichment of 2.50 w/o and contained one water rod to flatten the assembly power distribution.

The two MOX assembly types were loaded as part of a plutonium recycle demonstration program. The assembly designs for the two MOX assembly types are shown in Figures 3-7 and 3-8. These assemblies are not only unique in that they contain plutonium, but they also have a non-symmetric loading and contain annular fuel pellets. TGBLA is capable of modeling hollow pellets, but assumes that assemblies are symmetric across the diagonal. Therefore, both halves of each assembly design were analyzed and compared to LATTICE results generated with the actual assembly loadings. The assemblies halves with k-infinity behaviors most similar to LATTICE results were used in the core modeling. The error introduced by this approximation is negligible due to the minimal degree of fuel rod asymmetry and the small MOX assembly batch size (5 assemblies).

The reload fuel assemblies were uniform in the vertical direction. Thus, lattice physics data for only four additional lattice types were required to model cycle 2. The cycle 2 core included a total of ten distinct lattice types.

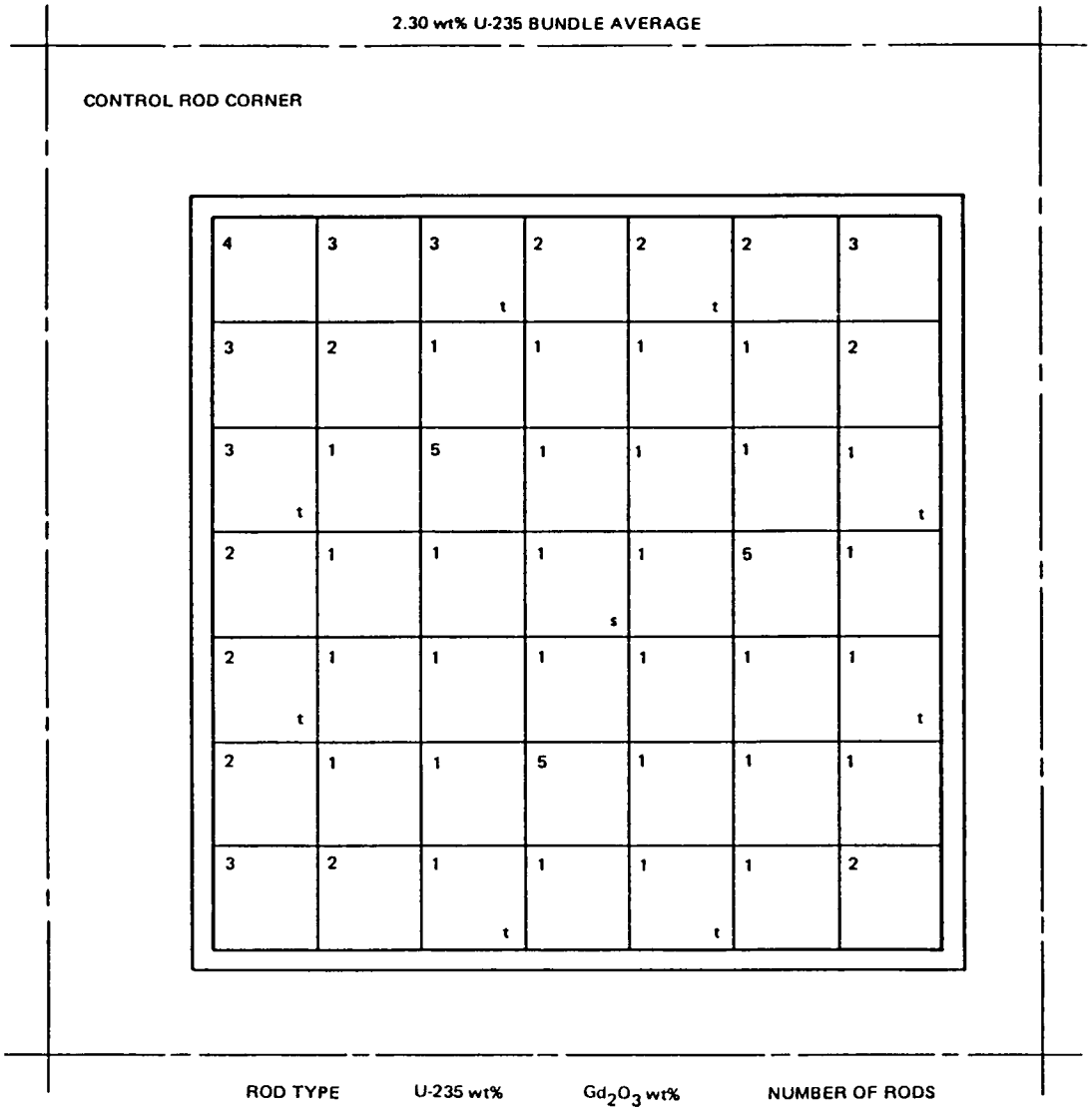

ROD TYPE	U-235 wt%	Gd_2O_3 wt%	NUMBER OF RODS
1	2.56	0	29
2	1.94	0	10
3	1.59	0	6
4	1.33	0	1
5	2.56	2.50	3

t = TIE RODS
s = SPACER CAPTURE ROD

Figure 3-5. Assembly Design for 7x7 Reload Fuel

Source: "Core Design and Operating Data for Cycles 1 and 2 of Quad Cities 1," EPRI NP-240, Electric Power Research Institute.

2.50 wt% U-235 BUNDLE AVERAGE

WIDE-WIDE CORNER

4	3	T 2	2	2	T 2	2	3
3	2	1	1	1	1	1	2
T 2	1	G 5	1	1	1	G 5	T 1
2	1	1	1	1	1	1	1
2	1	1	1	WS	1	1	1
T 2	1	1	1	1	1	1	T 1
2	1	G 5	1	1	1	G 5	1
3	2	T 1	1	1	T 1	1	2

ROD TYPE	ENRICHMENT wt% U-235	Gd_2O_3 wt%	NUMBER OF RODS
1	2.73	0	40
2	2.06	0	14
3	1.80	0	4
4	1.40	0	1
5	2.73	1.5	4
WS	–	0	1

WS – SPACER CAPTURE WATER ROD
T – TIE RODS
G – GADOLINIUM RODS

Figure 3-6. Assembly Design for 8x8 Reload Fuel

Source: "Core Design and Operating Data for Cycles 1 and 2 of Quad Cities 1," EPRI NP-240, Electric Power Research Institute.

WIDE-WIDE WATER GAP
(CONTROL BLADE)

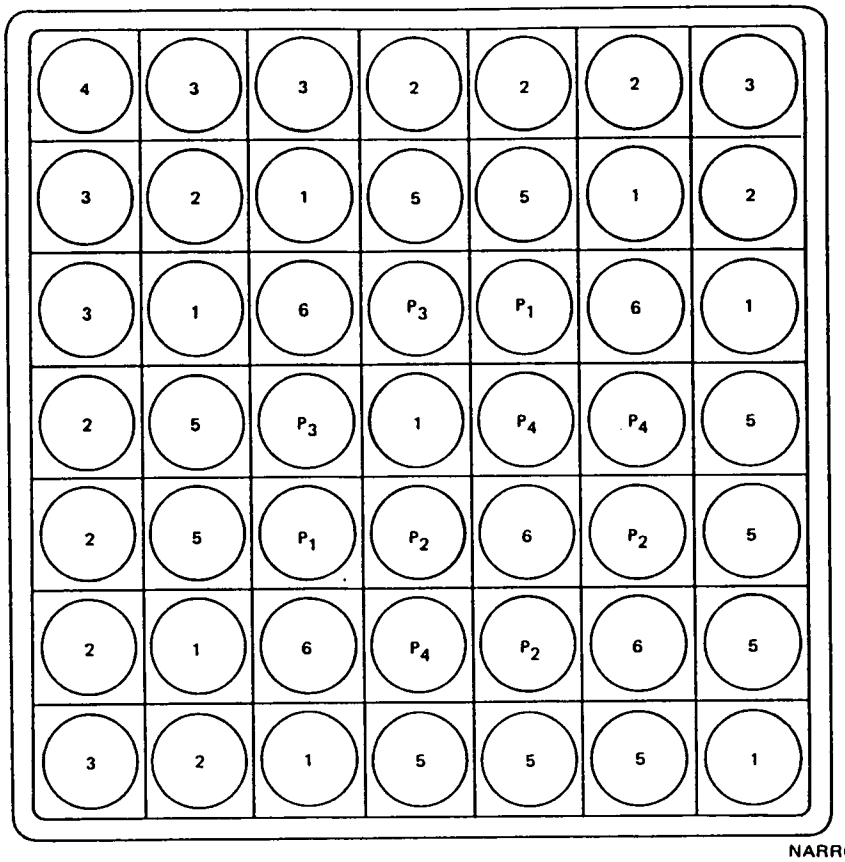

NARROW-NARROW
WATER GAP

URANIUM FUEL
FUEL TYPE 1 – 2.56 wt% U–235 2 – 1.94 3 – 1.69 4 – 1.33 5 – 3.30 6 – 2.56 + 3.0 wt% Gd_2O_3

PLUTONIUM FUEL (NATURAL U, 91% TD)	
HOLLOW PELLETS (0.15 i.d. CORE)	SOLID PELLETS
P_3* – 2.34 wt% FISSILE P_4 – 3.62	P_1* – 2.14% wt% Pu FISSILE P_2 – 3.52

* 80% FISSILE PuO_2. ALL OTHERS 90% FISSILE

STACK DENSITY OF FUEL	
FUEL TYPE	grams/cc
UO_2	10.32
Gd_2O_3-UO_2	10.19
SOLID MO_2	9.89
ANNULAR MO_2	8.94

Figure 3-7. Assembly Design for MOX Reload Fuel, Center Design

Source: "Core Design and Operating Data for Cycles 1 and 2 of Quad Cities 1," EPRI NP-240, Electric Power Research Institute.

WIDE-WIDE WATER GAP
(CONTROL BLADE)

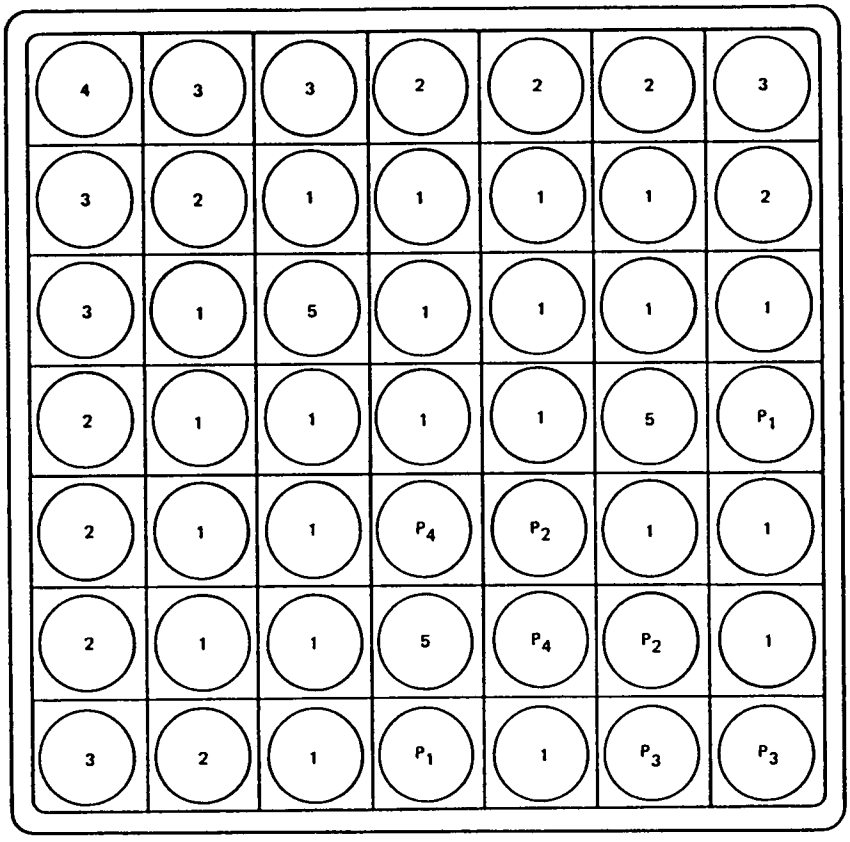

REFLECTOR

URANIUM FUEL	
NO. OF RODS	FUEL TYPE
22	1 – 2.56 wt% U–235
9	2 – 1.94 wt% U–235
6	3 – 1.69 wt% U–235
1	4 – 1.33 wt% U–235
3	5 – 2.56 wt% U–235 + 2.5 wt% Gd_2O_3

(SEE FIGURE 6 FOR DENSITIES)

PLUTONIUM FUEL (NATURAL U, 91% TD)			
HOLLOW PELLETS (0.150 i.d. CORE)		SOLID PELLETS	
NO. OF RODS	FUEL TYPE	NO. OF RODS	FUEL TYPE
2	P_3*–2.34 wt% FISSILE	2	P_1*–2.14 wt% Pu FISSILE
2	P_4 –3.62 wt% FISSILE	2	P_2 –3.52 wt% FISSILE

* 80% FISSILE PuO_2, ALL OTHERS 90% FISSILE

Figure 3-8. Assembly Design for MOX Reload Fuel, Peripheral Design

Source: "Core Design and Operating Data for Cycles 1 and 2 of Quad Cities 1," EPRI NP-240, Electric Power Research Institute.

3.4 Core Design Data

The Quad Cities-1 reactor is a General Electric BWR-3 design, with a rated power of 2511 MWt. The rated core flow at rated power is 98.6 Mlb/hr. A summary of the core design characteristics is shown in Table 3-2. Quad Cities-1 was among the first BWRs to employ fuel assemblies with burnable poisons to control reactivity, replacing the boron curtains which characterized BWR-1 and BWR-2 reactors.

The locations of the 177 cruciform control rods and the 41 TIP thimble tubes are shown in Figure 2-1. The TIP tubes are arranged so that symmetric pairs are formed across the upper-right to lower-left core diagonal. With the fuel loaded symmetrically with respect to this diagonal, the pairing of the TIP locations provides a means of checking the consistency of the TIP readings when the reactor is operated with control rod patterns with similar symmetry.

The cycle 1 core loading is shown in Figure 3-9. This loading is octant symmetric, with fuel assemblies containing dished pellets loaded in a ring around the central core region.

The cycle 2 core was virtually an extension of the initial core, with only 9% of the assemblies being discharged and a large control rod inventory at end-of-cycle. Figure 3-10 shows the core loading for cycle 2. Four MOX fuel assemblies were loaded in the center control cell and a single MOX assembly was loaded in a peripheral location. The cycle 2 core was nearly octant symmetric, with the exception of the peripheral MOX assembly.

Typical of BWR reactors, the peripheral assembly locations contain a smaller fuel support orifice diameter (1.424 inch) relative to the

Table 3-2

Summary of Core Description

Design	BWR-3
Vendor	General Electric
Rated Core Thermal Power, MW	2511
Total Core Flow at Rated Power, Mlb/hr	98.6
Total Number of Fuel Assemblies	724
Total Number of Control Rods	177
Total Number of Radial TIP Locations	41
Active Fuel Height, in	144
Assembly Pitch, in	6

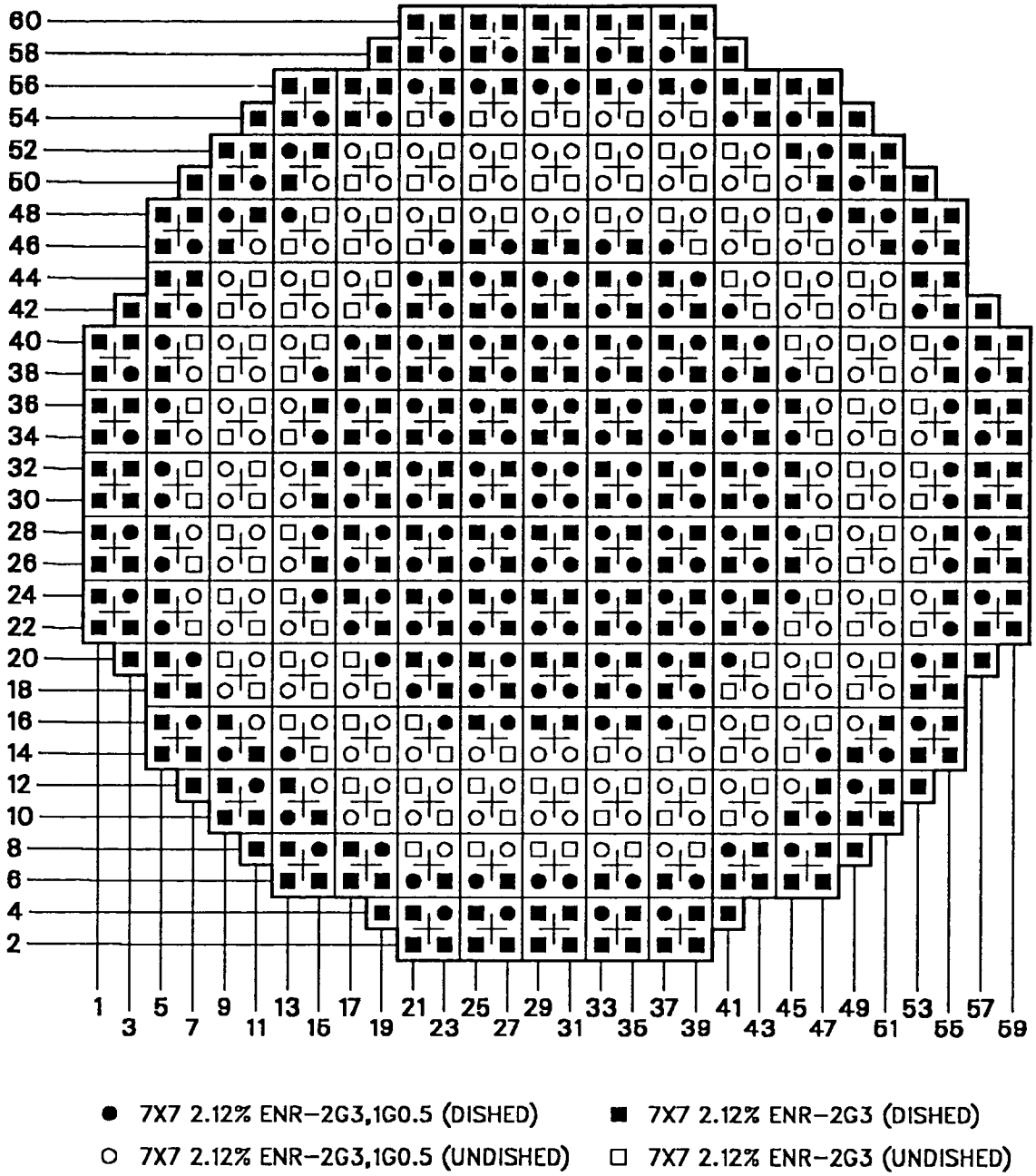

Figure 3-9. Cycle 1 Core Loading Pattern

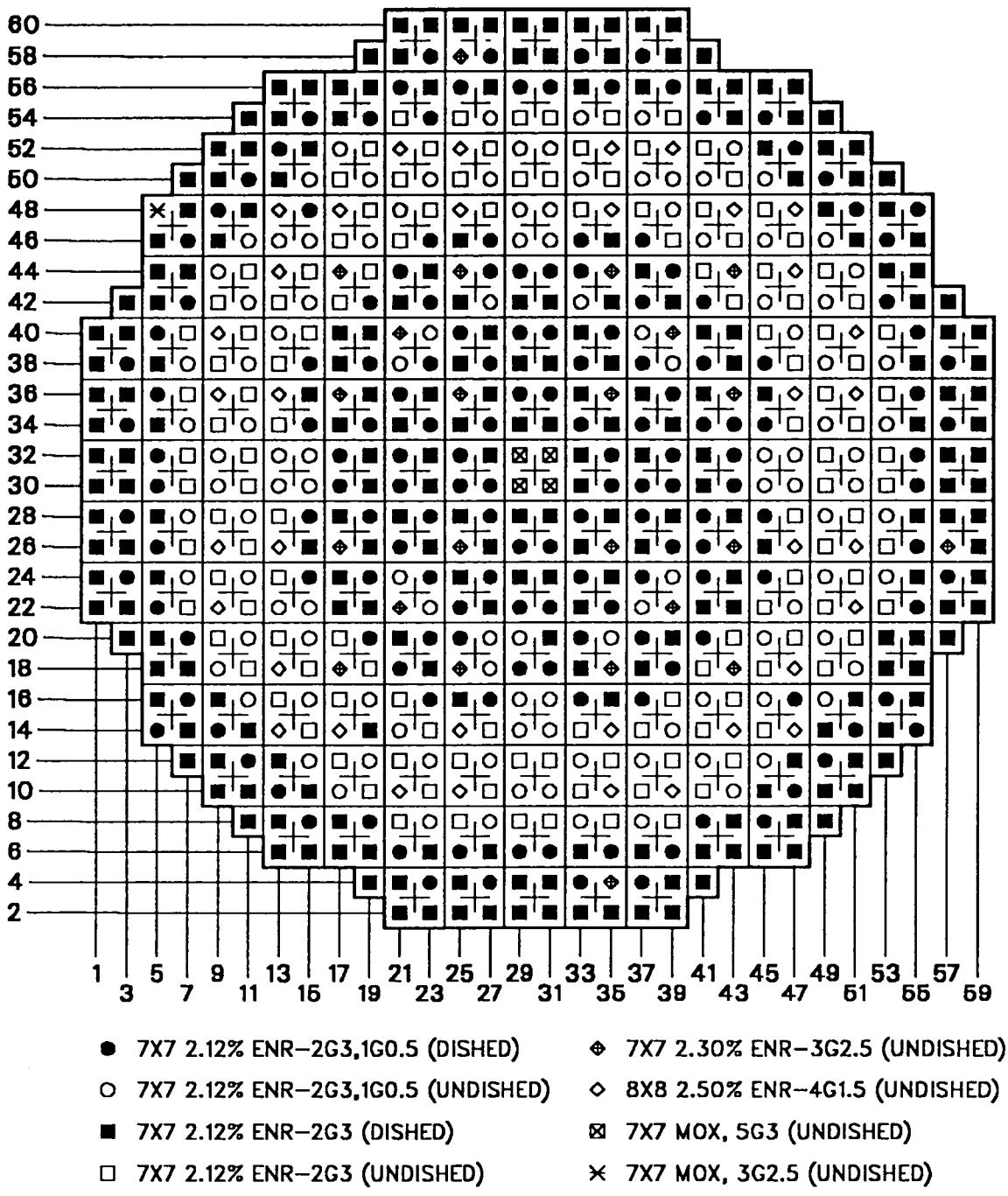

Figure 3-10. Cycle 2 Core Loading Pattern

central assembly locations (2.262 inch). This serves to redirect core flow to the central region and provides increased cooling for the higher powered assemblies. Separate thermal-hydraulic data were input to the core simulator to explicitly model each orifice size.

3.5 Core Operating Data

Core operating parameters needed to simulate the operation of Quad Cities-1 through cycle 2 have been compiled in References 7 and 8. There are 16 sets of operation data which span the entire cycle 1 operation, and 13 sets which span cycle 2 operation. The operating data describes high power core conditions at specific exposure points based on process computer output.

The operating data available at each exposure includes: (1) core average exposure, (2) core thermal power, (3) core flow, (4) inlet subcooling, (5) control rod configuration and (6) complete axial TIP readings for all 41 in-core detector locations. Core bypass flow rate data were published in Reference 8 as a function of the fraction of rated core flow. Tables 3-3 and 3-4 summarize the operating parameters for cycles 1 and 2, respectively.

An example operation data sheet showing the axial TIP distribution for seven of the 41 detectors is shown in Figure 3-11. The measured TIP data for a single string is reported on two lines. The first line of TIP data contains the core X-Y location of the TIP string, followed by 12 TIP readings. The second line contains the remaining 12 TIP readings, with the last reading corresponding to the TIP reading at the core top.

Table 3-3

Cycle 1 Operating Data

Step	Core Ave Exposure (GWd/MT)	Core Power (MW)	Pressure (psia)	Core Flow (Mlb/hr)	Leakage Flow (Mlb/hr)	Inlet Subcooling (BTU/lb)
1	0.000	2184.88	1036.69	84.39	7.19	18.88
2	0.272	2253.25	1028.36	99.61	9.11	21.18
3	0.712	2240.16	1025.01	94.65	8.48	21.98
4	0.882	2240.16	1025.01	94.65	8.48	21.98
5	1.052	2197.06	1039.41	97.58	8.85	21.19
6	1.470	2450.00	1044.75	97.97	8.90	23.34
7	2.239	2450.00	1044.75	97.97	8.90	23.34
8	2.727	2413.91	1039.04	95.30	8.57	23.52
9	3.190	2413.91	1039.04	95.30	8.57	23.52
10	3.749	2197.00	1021.23	94.84	8.51	21.78
11	3.836	2320.16	1032.24	94.72	8.49	22.65
12	4.074	2377.00	1030.52	92.93	8.27	23.58
13	4.737	2337.00	1020.02	90.95	8.02	23.42
14	5.301	2337.00	1020.02	90.95	8.02	23.42
15	5.654	2014.00	1010.17	73.50	5.81	25.14
16	6.031	2225.50	1029.82	97.89	8.89	21.22
17	6.558	2210.00	1025.15	94.14	8.42	21.81
18	6.807	2210.00	1025.15	94.14	8.42	21.81
19	7.205	2267.00	1027.61	95.62	8.61	22.21
20	7.397	2267.00	1027.61	95.62	8.61	22.21
21	7.628	2187.25	1016.16	97.73	8.87	21.08
22	7.659	2203.41	1025.64	95.94	8.65	21.54
22b	7.980	2166.00	1008.00	97.19	8.81	18.91

Source: "Core Design and Operating Data for Cycles 1 and 2 of Quad Cities 1," EPRI NP-240, Electric Power Research Institute.

Table 3-4

Cycle 2 Operating Data

Step	Core Ave Exposure (GWd/MT)	Core Power (MW)	Pressure (psia)	Core Flow (Mlb/hr)	Leakage Flow (Mlb/hr)	Inlet Subcooling (BTU/lb)
23	7.286	1422.73	980.75	49.33	3.44	27.69
24	7.303	2171.47	1024.20	83.83	7.98	24.02
25	7.532	2156.00	1033.90	88.01	8.55	23.98
26	7.964	2156.00	1033.90	88.01	8.55	23.98
27	8.337	2096.69	1008.69	82.07	7.74	23.74
28	8.424	2411.53	1023.69	97.42	9.83	23.02
29	8.790	2500.22	1049.39	96.68	9.73	24.20
30	9.142	2500.22	1049.39	96.68	9.73	24.20
31	9.584	2463.00	1052.66	97.23	9.80	23.74
32	10.174	2463.00	1052.66	97.23	9.80	23.74
33	10.658	2474.00	1015.47	96.02	9.64	22.99
34	11.239	2474.00	1015.47	96.02	9.64	22.99
35	11.593	2155.53	1006.56	98.24	9.94	20.62
36	11.936	2155.53	1006.56	98.24	9.94	20.62
37	12.399	1829.19	962.00	93.87	9.34	18.28
38	12.897	1713.17	960.31	94.10	9.38	17.12
39	13.199	1547.00	952.00	95.70	9.59	15.60
40	13.612	1487.00	953.00	94.90	9.48	15.20

Source: "Core Design and Operating Data for Cycles 1 and 2 of Quad Cities 1," EPRI NP-240, Electric Power Research Institute.

DATASET 02, AUGUST 30, 1972

Reactor Conditions

Core Average Exposure, 646.0 MWd/t
Core Thermal Power, 2253.25 MWT
Core Pressure, P, 1028.36 psia
Core Flow, 99.61 Mlb/hr
Inlet Subcooling at P, 21.18 Btu/lb

Control Configuration

Legend: 48, Full Out; 0, Full In.

48	48	48	48	48	48	48	48	48	48	48	48	48	48	48
48	48	48	48	48	36	48	28	48	36	48	48	48	48	48
48	48	48	48	2	48	8	48	8	48	2	48	48	48	48
48	48	48	36	48	26	48	40	48	26	48	36	48	48	48
48	48	0	48	8	48	0	48	0	48	8	48	0	48	48
48	36	48	26	48	32	48	26	48	32	48	26	48	36	48
48	48	8	48	0	48	0	48	0	48	0	48	8	48	48
48	28	48	40	48	26	48	32	48	26	48	40	48	28	48
48	48	8	48	0	48	0	48	0	48	0	48	8	48	48
48	36	48	26	48	32	48	26	48	32	48	26	48	36	48
48	48	0	48	8	48	0	48	0	48	8	48	0	48	48
48	48	48	36	48	26	48	40	48	26	48	36	48	48	48
48	48	48	48	2	48	8	48	8	48	2	48	48	48	48
48	48	48	48	48	36	48	28	48	36	48	48	48	48	48
48	48	48	48	48	48	48	48	48	48	48	48	48	48	48

Axial TIP Distribution

1609	34.1	55.9	72.6	94.2	108.3	119.4	127.8	136.0	123.0	116.2	115.1	115.6
	94.7	93.0	85.5	81.1	69.9	66.4	60.1	52.4	46.9	38.7	26.6	15.4
2409	29.0	51.0	73.1	95.9	120.3	142.9	167.0	178.7	180.0	166.0	168.2	165.5
	156.0	145.8	134.4	131.7	115.3	109.1	102.6	93.8	89.2	79.1	53.9	33.9
3209	32.7	55.2	75.3	96.5	117.3	127.3	136.0	141.3	134.0	136.8	146.6	146.2
	141.6	132.7	120.9	115.9	99.9	101.8	93.4	81.9	79.7	65.5	46.1	29.3
4009	30.7	48.7	63.4	84.8	101.5	119.4	138.4	142.0	149.1	130.2	133.2	127.3
	115.3	110.9	108.0	97.2	86.6	83.6	74.8	65.9	60.5	48.2	33.7	20.1
4809	37.4	57.5	72.3	93.2	103.9	111.0	111.6	122.3	113.6	104.5	101.1	95.7
	83.4	78.8	72.1	67.6	60.5	54.9	53.2	42.4	39.2	31.9	22.6	14.7
0817	37.3	59.5	74.7	94.6	107.4	113.1	121.4	124.1	119.0	107.8	110.4	105.1
	85.8	86.5	80.4	74.4	66.2	62.9	55.5	47.2	41.7	33.4	23.2	12.8
1617	34.5	55.3	70.2	91.5	111.8	132.8	149.2	158.2	152.8	147.8	147.2	138.1
	134.3	127.7	119.0	114.4	101.5	101.6	91.2	83.4	77.6	59.1	41.2	22.9

Figure 3-11. Example Data Set

Source: "Core Design and Operating Data for Cycles 1 and 2 of Quad Cities 1," EPRI NP-240, Electric Power Research Institute.

Figure 3-11 also contains an example control rod map. The control rod positions are measured in notches, with one notch equal to three inches. The convention is to describe the rod position by the number of notches withdrawn. Thus, a control rod at notch position 00 is fully inserted and a notch position of 48 is fully withdrawn. The total length of an inserted control rod is 144 inches, corresponding to the active fuel height. The physical notches of the control blades are six inches apart, therefore only even numbered notch positions are possible.

4.0 CORE DEPLETION MODELING

4.1 Overview

Accurate predictions of the nodal fuel prcperties at various core exposures are needed for calculations of core power distributions and reactivity. As a result, the depletion calculations provided a basis for all other calculations performed in the study. Inaccurate depletion modeling can result in significant errors in power distribution and reactivity calculations through a cycle.

The simulation of the core exposure accumulation was performed using the forward step depletion method described in section 2.5. The measured operating parameters contained in Tables 3-3 and 3-4, together with the corresponding control rod patterns, were used to simulate core operation using a series of depletion steps.

4.2 Depletion Steps

The core was depleted using the depletion steps suggested in Reference 7 and 8. The exposure intervals, rod sequences, and TIP data availability are shown in Table 4-1 and 4-2. These steps were suggested based on TIP measurement points and control rod sequence changes. Additional steps were added near the end-of-cycles 1 and 2 to update the Ba-140 distribution for the gamma scan comparisons.

The operating parameters provided at each exposure correspond to the core conditions at the time of TIP measurements. This allows improved power distribution comparisons by calculating simulated TIP

Table 4-1

Cycle 1 Depletion Step Information

Depletion Step	Exposure Interval (MWd/MT)	Control Rod Sequence	Operating Data Set #	TIP Data Available
1	0 to 272	A	1	Yes
2	272 to 712	A	2	Yes
3	712 to 882	A	3	Yes
4	882 to 1052	A	3	
5	1052 to 1470	B	4	Yes
6	1470 to 2239	B	5	Yes
7	2239 to 2727	B	5	
8	2727 to 3190	A	6	Yes
9	3190 to 3749	A	6	
10	3749 to 3836	B	7	Yes
11	3836 to 4074	B	8	Yes
12	4074 to 4737	B	9	Yes
13	4737 to 5301	B	10	Yes
14	5301 to 5654	B	10	
15	5654 to 6031	B	11	Yes
16	6031 to 6558	A	12	Yes
17	6558 to 6807	A	13	Yes
18	6807 to 7205	A	13	
19	7205 to 7397	B	14	Yes
20	7397 to 7628	B	14	
21	7628 to 7659	A	15	Yes
22A	7659 to 7980	A	16	
22B	7980 to 8049	A	16	

Table 4-2

Cycle 2 Depletion Step Information

Depletion Step	Exposure Interval (MWd/MT)	Control Rod Sequence	Operating Data Set #	TIP Data Available
23	7286 to 7303	A	17	Yes
24	7303 to 7532	A	18	Yes
25	7532 to 7964	A	19	Yes
26	7964 to 8337	A	19	
27	8337 to 8423	B	20	Yes
28	8423 to 8789	B	21	Yes
29	8789 to 9141	B	22	Yes
30	9141 to 9585	B	22	
31	9585 to 10173	A	23	Yes
32	10173 to 10658	A	23	
33	10658 to 11238	B	24	Yes
34	11238 to 11593	B	24	
35	11593 to 11935	B	25	Yes
36	11935 to 12399	B	25	
37	12399 to 12896	B	26	Yes
38	12896 to 13198	ARO*	27	Yes
39	13198 to 13611	ARO	28	Yes
40	13611 to 13741	ARO	29	Yes

*All Rods Out

responses based on the same core conditions as the measurements. However, the core depletion modeling may not be optimized.

Representative operating data for each exposure interval are difficult to quantify due to the large fluctuation in the operating parameters throughout both cycles. An example reactor histogram showing typical fluctuations in the operating parameters is shown in Figure 4-1.

Comparisons of the operating histograms during each exposure interval and the corresponding state point data suggested for that interval show that only slight improvements in determining representative conditions can be made. Due to the inaccuracy of determining core exposures and operating data based on the operating histograms, no attempt was made to refine the depletion steps.

The depletion calculations were performed by first calculating the core power distribution at the beginning of each depletion step using the operating conditions for that exposure interval. The nodal fuel histories were then advanced based on the calculated power distribution and the incremental core exposure. If TIP measured readings were available, updated power distributions and effective multiplication factors were recalculated at the end of the depletion step using the same operating conditions.

The cycle 1 operation continued for five days past the last TIP measurement. Therefore an additional depletion step (step 22B) was added to update the end-of-cycle conditions for the gamma scan comparison, and to update nodal histories of the assemblies to be

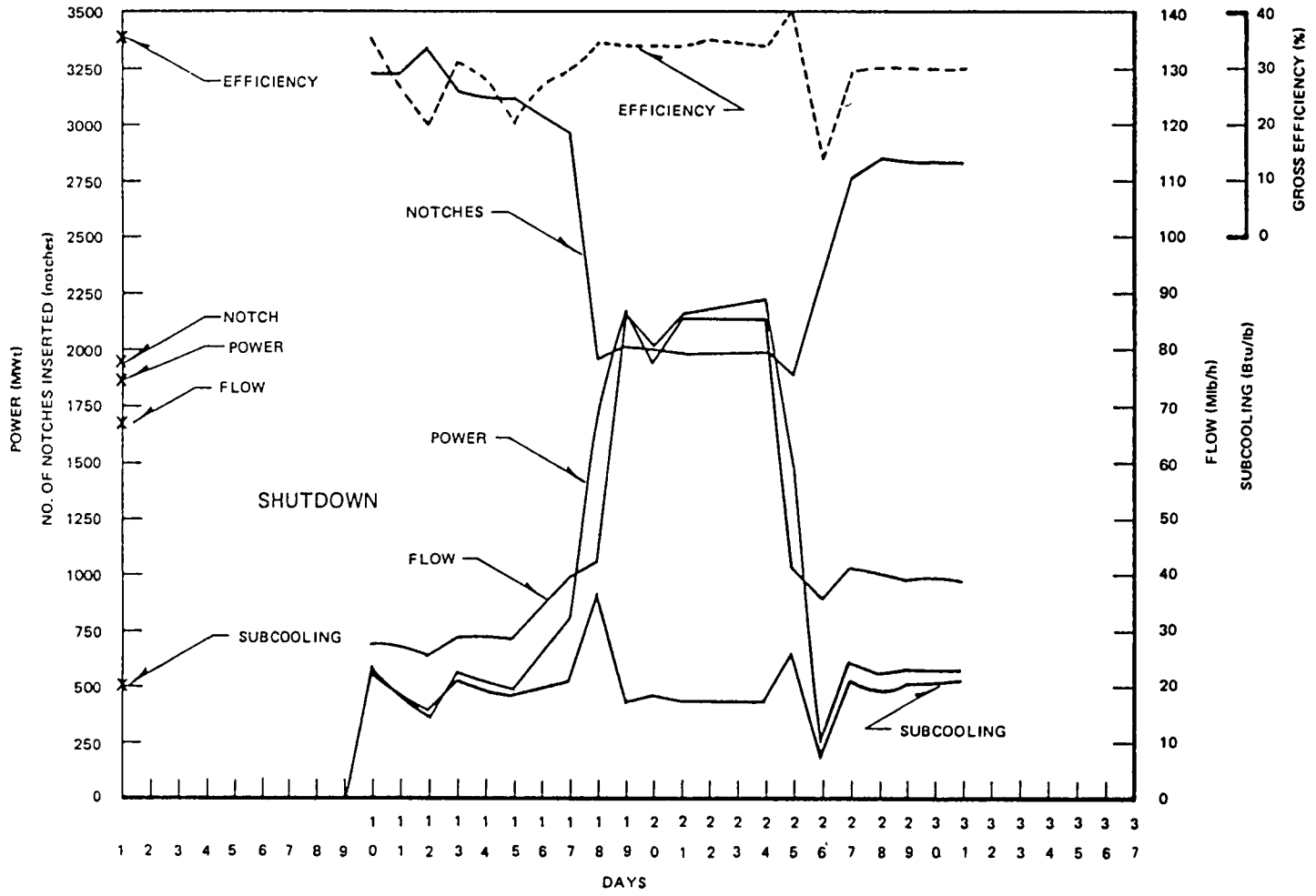

Figure 4-1. Example Operating Histogram

Source: "Core Design and Operating Data for Cycles 1 and 2 of Quad Cities 1," EPRI NP-240, Electric Power Research Institute.

loaded in cycle 2. For cycle 2, the last TIP measurement was made just prior to shutdown and no depletion extension was required.

4.3 Core Simulator Restart Files

Core simulator restart files containing nodal history properties (exposure, control history, moderator density history), nodal operating conditions (power, moderator density, temperatures, etc.), predicted TIP readings, and nodal Ba-140 concentrations were written at the end of each depletion step. These files were used as input to the depletion and cold critical calculations to pass nodal history properties and to provide initial power distribution guesses. To continue the core depletion after cycle 1, nodal history properties contained on the end-of-cycle 1 restart file were shuffled according to the cycle 2 loading pattern. Finally, restart files were used to pass calculated TIP and nodal Ba-140 concentrations to auxiliary programs for comparisons with measured data.

5.0 REACTIVITY COMPARISONS

5.1 Overview

Reactor design analyses rely on the ability to accurately predict the core reactivity over a wide range of operating conditions. Design calculations such as cycle length determination, shutdown margin, hot excess reactivity, rod withdrawal error, misloaded assembly, and standby liquid control system worth require the prediction of core reactivity throughout the cycle.

In general, even theoretically well-founded reactor analysis methods cannot reproduce a k-effective of unity for known critical core configurations. Consequently, the calculational bias of reactivity calculations must be determined prior to performing predictive calculations. While the calculational bias must be known for predictive calculations, the actual value (within limits) of the bias often has little significance. However, the consistency of the calculational bias is very important. Large uncertainties in predicting criticality result in less than optimum core designs and operating strategies since the uncertainties must be incorporated in the design analyses.

A large quantity of benchmark data are available from Quad Cities-1 to evaluate reactivity calculations. Each state point used in the depletion modeling represents a high power critical reactor configuration. The k-effective values from these calculations are presented in section 5.2 to assess reactivity calculations for hot operating reactor conditions.

Critical configuration data from eight cold, xenon-free distributed rod pattern startups are reported in Reference 7. Supplemental information describing four additional in-sequence criticals performed during cycle 1 was obtained from Pennsylvania Power and Light (PP&L). The data from PP&L also included corrections to data reported in Reference 7. The in-sequence critical data are used in section 5.3 to evaluate reactivity calculations under cold zero-power reactor conditions.

A series of local critical experiments was performed during startup testing and at two exposures in cycle 1. These experiments involved two to four adjacent control rods being withdrawn until a critical configuration was achieved. Thirty-two of these criticals were calculated using data obtained from the Commonwealth Edison Company and PP&L. Calculated results from these experiments are examined in section 5.4 to determine the capability of the TGBLA/CORE-II methods to calculate cold zero-power reactivity induced in very localized regions.

Comparisons of calculated k-effective values from in-sequence and local criticals are made in section 5.5. This comparison is made to determine the accuracy of the physics methods for in-sequence shutdown margin demonstration calculations.

5.2 Hot Operating Reactivity Predictions

k-effective values from the cycle depletion calculations represent reactivity calculations at high power, steady-state core conditions. The calculated k-effective values from cycles 1 and 2 are plotted in

Figures 5-1 and 5-2, respectively. The results are also tabulated in Table 5-1. The k-effectives are taken directly from CORE-II output without adjustment. For comparison purposes, results from previous LATTICE/CORE calculations[13] for the Quad Cities-1 reactor have been included.

The fluctuations exhibited in the curves are reasonable, given that the reactor experienced frequent deviations from rated conditions during both cycles. The uncertainties of lattice physics parameters such as Doppler reactivity change with core operating condition, resulting in a calculation bias which is often a function of the core condition. In addition, fluctuations at several exposures are expected due to core conditions being reported while the reactor was not at steady-state, equilibrium xenon conditions.

For cycle 1, CORE-II calculated an average k-effective value of 1.00805 with a standard deviation of 0.00173. This is slightly more consistent than the standard deviation of 0.0022 calculated using the LATTICE/CORE methods. The trend of increasing k-effectives near end of cycle is less prevalent in the CORE-II results. The k-effective distributions are less fluctuating if the low power and flow data sets at exposures of 0.27 GWd/MT and 6.03 GWd/MT are not included.

A noticeable improvement is seen in the trend of k-effective values calculated by CORE-II during the cycle 2 depletion. CORE-II results shown in Figure 5-2 show very little dependence on cycle exposure. The corresponding LATTICE/CORE results indicate a general trend of increasing k-effective values with increased cycle exposure. K-effective values using the new methods maintain a relatively stable

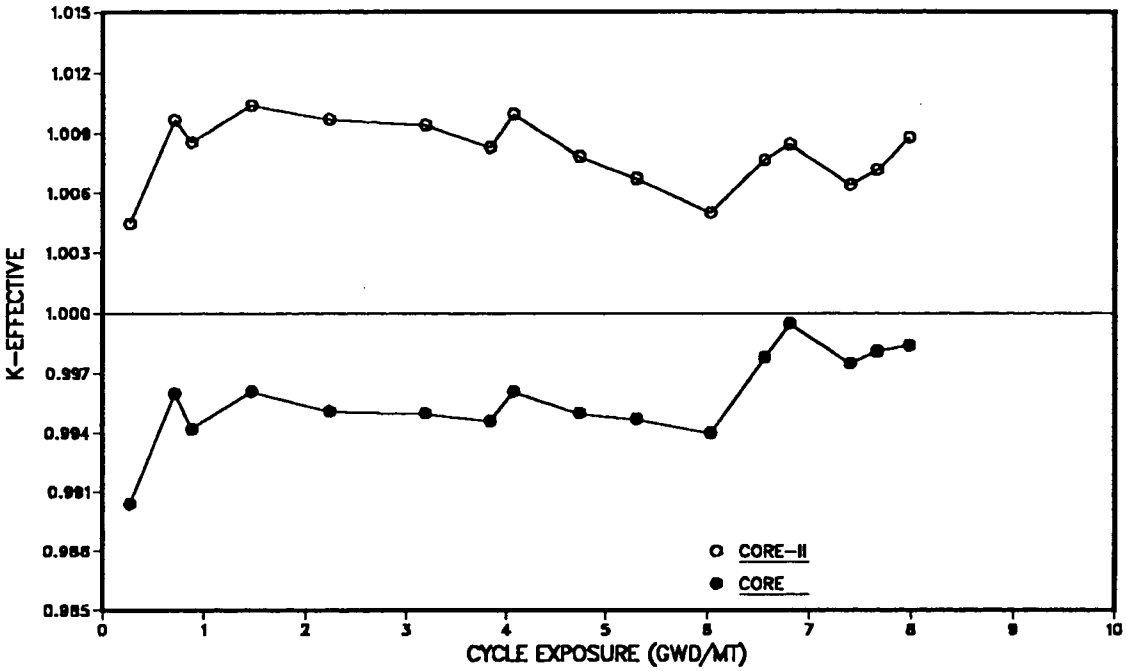

Figure 5-1. Hot Operating Critical K-effective Versus Cycle 1 Exposure

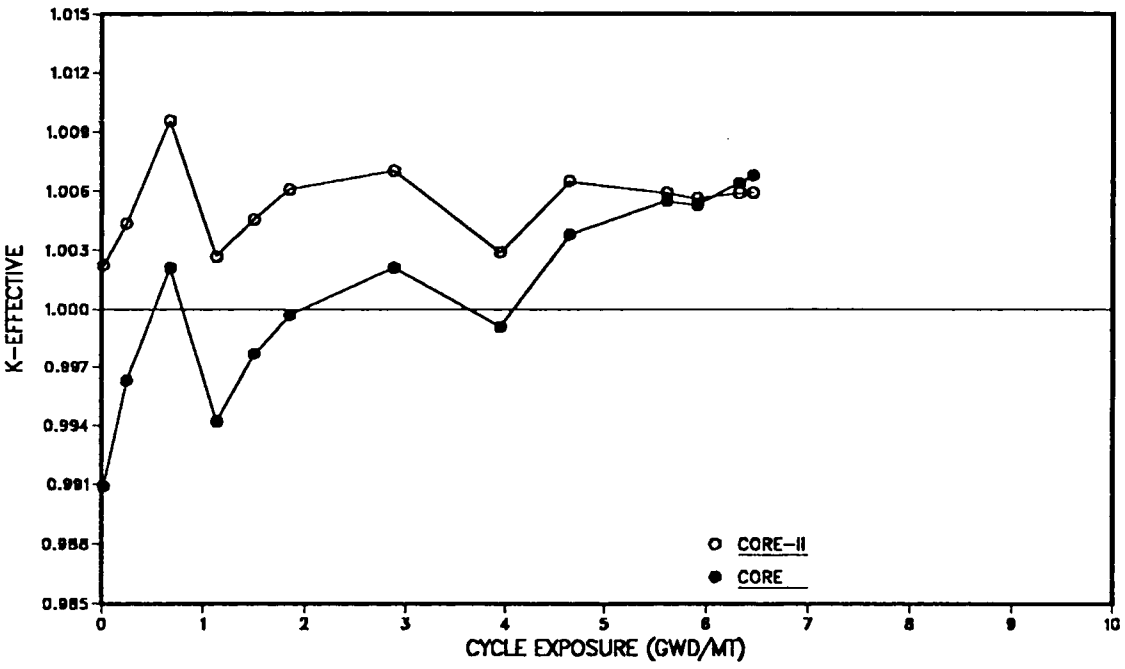

Figure 5-2. Hot Operating Critical K-effective Versus Cycle 2 Exposure

Table 5-1

Hot Operating K-effective from Cycles 1 and 2

Core Average Exposure (GWD/MT)	Fraction of Rated Power	Fraction of Rated Flow	LATTICE/ CORE K-effective	TGBLA/ COREII K-effective
0.272	0.870	0.861	0.9904	1.00448
0.712	0.897	1.016	0.9960	1.00969
0.882	0.892	0.966	0.9942	1.00857
1.471	0.875	0.996	0.9961	1.01042
2.239	0.976	1.000	0.9951	1.00973
3.190	0.961	0.972	0.9950	1.00945
3.837	0.875	0.968	0.9946	1.00832
4.075	0.924	0.967	0.9961	1.00999
4.738	0.947	0.948	0.9950	1.00786
5.301	0.931	0.928	0.9947	1.00675
6.031	0.802	0.750	0.9940	1.00504
6.558	0.886	0.999	0.9978	1.00768
6.807	0.880	0.961	0.9995	1.00846
7.397	0.903	0.976	0.9975	1.00643
7.660	0.871	0.997	0.9981	1.00718
7.980	0.878	0.979	0.9984	1.00881
Cycle 1 Average			0.9958	1.00805
Standard Deviation			0.0022	0.00173
7.303	0.567	0.503	0.9909	1.00225
7.532	0.865	0.855	0.9963	1.00438
7.964	0.859	0.898	1.0021	1.00956
8.424	0.835	0.837	0.9942	1.00268
8.790	0.960	0.994	0.9977	1.00456
9.142	0.996	0.987	0.9997	1.00608
10.174	0.981	0.992	1.0021	1.00702
11.239	0.985	0.980	0.9991	1.00291
11.936	0.858	1.002	1.0038	1.00651
12.897	0.682	0.960	1.0055	1.00592
13.199	0.682	0.960	1.0053	1.00565
13.612	0.616	0.977	1.0064	1.00590
13.742	0.592	0.968	1.0068	1.00591
Cycle 2 Average			1.0008	1.00533
Standard Deviation			0.0050	0.00199

average of 1.00533 with a standard deviation of 0.00199. This result is improved relative to the LATTICE/CORE average k-effective of 1.0008 with a standard deviation of 0.0050.

A common problem with reactor physics methods is a dependence of the calculational bias on exposure. This is particularly true with high energy fuel containing large gadolinum loadings. In each cycle, the dependence of TGBLA/CORE-II k-effective values on cycle exposure has been decreased relative to the LATTICE/CORE methods. This indicates improved modeling using the new methods, possibly due to improved treatments of the gadolinium burnup and fission product buildup. Although these cycles did not contain high energy fuel, the decrease in the exposure dependence of the k-effective values indicates that improvements may be expected when used with high energy fuel.

5.3 In-Sequence Cold Critical Predictions

Critical configuration data are available from Quad Cities-1 to model 14 in-sequence criticals performed during cycles 1 and 2. These criticals correspond to startup rod patterns in which the rods are withdrawn in a distributed pattern throughout the core. This type of critical produces a more uniform core-wide flux distribution and avoids operational problems associated with core configurations which yield high rod worths. Appendix A contains data sheets describing each of the 14 in-sequence criticals.

The critical configuration data were recorded after a sustained reactor period was observed. Therefore, the reactor was actually super-critical (k-effective > 1.0) at the time of the reported core

conditions. The actual k-effective can be calculated by adding the reactivity equivalent of the measured reactor period to unity. This k-effective value could then be compared directly with the calculated k-effective value.

However, the common practice in reporting results from reactivity calculations is to assume that the reactor was exactly critical at the time criticality was measured. This approach is equivalent to the above method and requires that the calculated k-effective value be adjusted by subtracting the reactivity equivalent of measured reactor period. The difference between the adjusted k-effective value and unity is then the calculational bias.

The calculated results for each in-sequence critical are shown in Table 5-2. The tabulated k-effective values have been adjusted for the reactivity equivalent of measured reactor periods using the in-hour equation. The core average delayed neutron fraction of each core configuration for use in the in-hour equation was calculated using CORE-II. The period adjustment to k-effective ranged from 0.0002 for a 300 second period to 0.0010 for a 45 second period.

The average CORE-II k-effective for all criticals is 1.00193 with a standard deviation of 0.00503. For comparison, results in Reference 13 from LATTICE/CORE calculations of eight of the fourteen criticals have an average k-effective of 0.9963 with a standard deviation of 0.0027. Results from both reactor physics methods are plotted in Figure 5-3. While both methods exhibit an exposure dependence, the CORE-II trend of decreasing k-effective with increased exposure is more pronounced. This behavior is possibly due to an under prediction of

Table 5-2

In-Sequence Cold Critical K-effective
from Cycles 1 and 2

Date	Exposure (GWD/MT)	Coolant Temp (°F)	Reactor Period (SEC)	Controlled Notches	Corrected[1] K-effective
03/14/72	0.0	152	180	6390	1.00662
03/15/72	0.0	159	160	6344	1.00731
03/15/72	0.0	161	150	6324	1.00724
03/16/72	0.0	157	125	6336	1.00741
03/16/72	0.0	160	65	6318	1.00708
04/06/72	0.0	155	120	6412	1.00628
02/09/73	2.866	163	300	6698	1.00319
05/04/73	3.748	120	300	7118	1.00087
05/08/73	3.748	178	181	6830	1.00040
08/05/73	4.938	120	45	6936	0.99679
01/06/74	6.911	179	300	6415	0.99608
*10/06/74	8.276	185	100	6224	0.99563
12/16/74	9.138	160	45	2520	0.99650
05/04/75	10.603	190	130	5928	0.99565
			Average		1.00193
			Standard Deviation ...		0.00503

[1]The corrected k-effective has the reactivity equivalent of the measured reactor period subtracted from the calculated k-effective.

*First critical in cycle 2

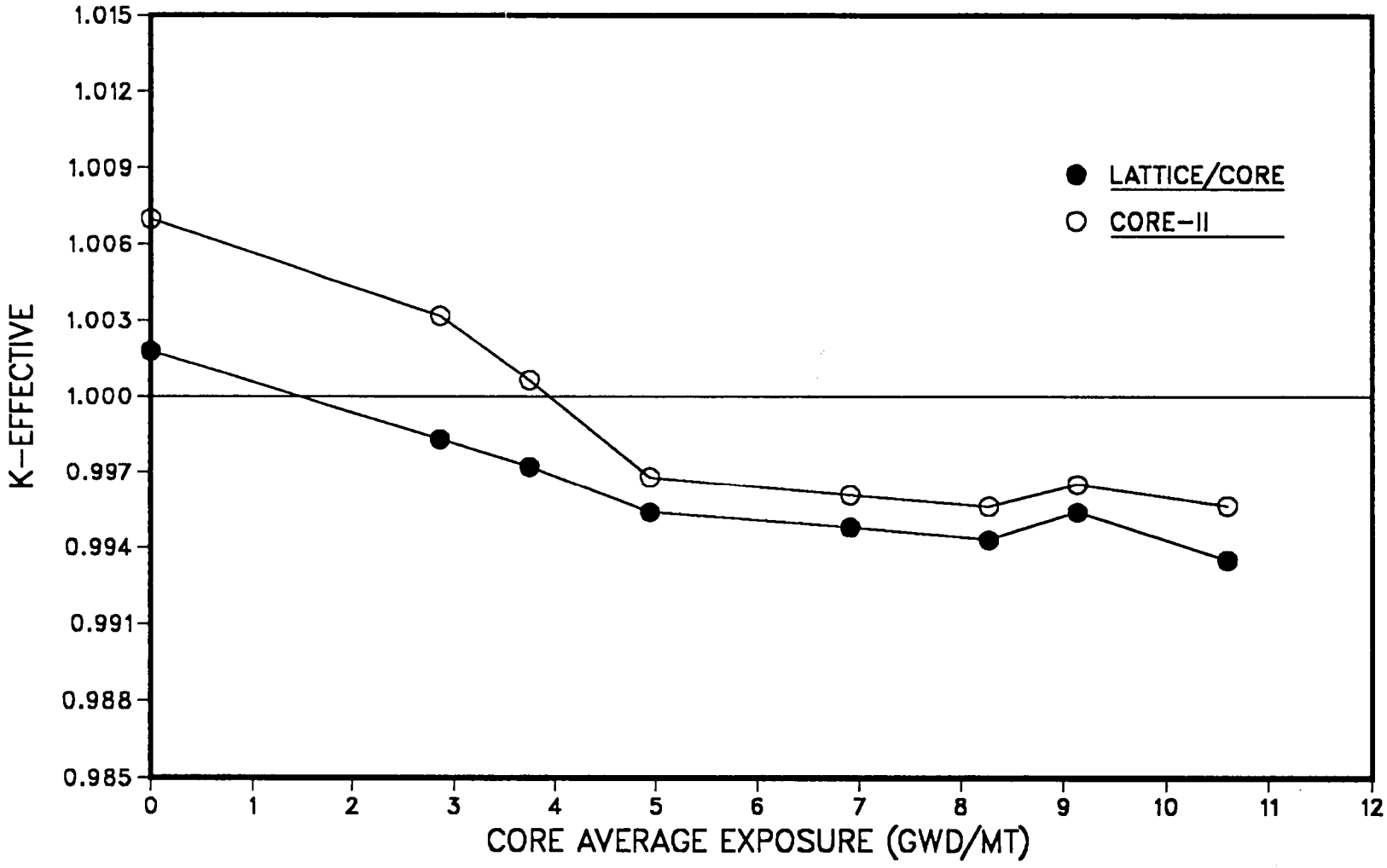

Figure 5-3. In-Sequence Cold Critical K-effective Versus Core Exposure

the gadolinium, xenon, and/or samarium worth at low exposures under cold conditions. Note that whenever more than one critical was performed at the same exposure point, the average values have been plotted.

5.4 Local Cold Critical Predictions

Two to four rod criticals were modeled to verify the capability of CORE-II to predict very localized reactivity configurations typical of shutdown margin calculations. Calculated results for a total of 32 local criticals are shown in Table 5-3. Many of the zero exposure local criticals are very similar since they were performed in symmetric locations. Since the reactor temperature was essentially constant, the differences in rod positions between similar criticals may be due to a variation in detector readings or assembly manufacturing tolerances. As discussed in section 5.3, the tabulated results have been corrected for the measured reactor period. Note that Table 5-3 contains a complete description of the critical configurations for benchmark calculations.

The average k-effective value for all 32 criticals from CORE-II is 1.00257 with a standard deviation of 0.00245. If only the 25 criticals performed at BOC 1 are considered the standard deviation of the average k-effective value is reduced to 0.00054.

Because a complete set of critical configurations was not previously available, a comparison with LATTICE/CORE results is only possible for 10 of the 32 local criticals. The average k-effective reported in Reference 13 for the first 10 criticals listed in Table 5-3

Table 5-3

Local Cold Critical K-effective from Cycle 1

Exposure (GWD/MT)	Control Rods Fully Withdrawn	Partially Withdrawn Rod	Notch	Coolant Temp (°F)	Reactor Period (Sec)	Corrected* K-effective
0.0	30-47; 30-43	26-43	06	156	160	1.00369
0.0	30-47; 34-37			158	45	1.00319
0.0	34-43; 34-37	30-43	06	158	60	1.00304
0.0	26-43; 26-47	30-43	06	157	148	1.00361
0.0	18-35; 22-35	18-31	06	159	238	1.00270
0.0	18-35; 18-39	22-35	08	158	25	1.00391
0.0	14-39; 18-39			159	260	1.00366
0.0	14-35; 18-35	18-31	06	159	350	1.00371
0.0	22-23; 26-23	26-27	08	160	30	1.00362
0.0	14-35; 14-39			160	175	1.00410
0.0	46-19;	46-23	44	160	50	1.00333
0.0	18-11;	22-11	46	157	65	1.00377
0.0	26-27; 30-27	30-31	08	159	245	1.00482
0.0	46-19;	50-19	46	159	32	1.00335
0.0	38-11; 42-11			160	60	1.00378
0.0	38-11;	38-15	44	159	75	1.00365
0.0	50-23;	50-19	46	158	78	1.00382
0.0	46-23;	50-23	46	158	90	1.00444
0.0	26-31; 26-35	30-31	08	159	41	1.00373
0.0	26-27; 26-31	30-31	08	159	332	1.00490
0.0	26-23; 26-27	30-27	08	160	38	1.00378
0.0	22-39;	22-35	24	158	42	1.00355
		26-35	08			
0.0	22-39; 26-39	26-35	08	159	39	1.00392
0.0	42-39;	42-35	38	158	39	1.00415
		38-35	08			
0.0	38-39; 38-35	34-35	06	158	169	1.00261
3.748	50-27;	50-23	22	108	54	0.99584
3.748		26-11	38	70	43.7	1.00041
		22-11	20			
3.748	22-11;	22-15	18	77	280	0.99961
3.748	26-11;	22-11	20	75	47.5	1.00031
3.748	26-15; 22-11	18-15	22	120	157	0.99925
3.748	14-27; 10-23	14-19	22	125	140	0.99909
6.911	22-11; 22-15	26-11	06	182	100	0.99483
				Average		1.00257
				Standard Deviation		0.00245

*The corrected k-effective has the reactivity equivalent of the measured reactor period subtracted from the calculated k-effective.

is 1.0009 with a standard deviation of 0.0006, compared to a corresponding TGBLA/CORE-II average of 1.00352 with a standard deviation of 0.00042. This indicates that for the same criticals and core exposure, CORE-II is slightly more consistent.

5.5 In-Sequence Versus Local Critical Comparison

BWR cores are designed to provide sufficient control of reactivity with control rods such that the core can be made subcritical at the most reactive core state with the highest worth rod stuck in the full out position. BWR technical specifications require that the margin to criticality in this configuration be measured prior to operation of each cycle.

The most definitive method to demonstrate that sufficient shutdown margin exists is to withdraw the analytically determined highest worth rod and then withdraw adjacent rods until criticality is achieved. This demonstrates that the reactor is subcritical with the strongest rod withdrawn and allows a determination of the actual margin to criticality. However, this method has been shown to be operationally difficult due to extremely high rod worths.

The most widely used method for verifying shutdown margin is based on normal startup criticals combined with calculated results for the stuck rod configuration (in-sequence method).

Differences in calculated k-effective values from in-sequence and locals criticals are expected due to the variation in flux distributions and localized exposure mispredictions. Therefore, to employ the in-sequence method of demonstrating shutdown margin, the

difference in predictions of in-sequence criticals versus local criticals is considered in the analyses.

A comparison of k-effective values from in-sequence cold criticals and local cold criticals is shown in Table 5-4 and Figure 5-4. As expected, the in-sequence k-effective values exceed the local critical k-effectives. This is due to the fuel rod spacers being neglected in the core model. The spacers have a larger reactivity worth when the neutron flux is distributed over a larger core area. K-effective values are compared only at like exposures in Table 5-4 since the k-effective differences are most meaningful when the in-sequence and local criticals are performed under the same core conditions.

The difference in average k-effectives from in-sequence and local criticals at core exposures of 3.748 and 6.911 GWd/MT are 0.00156 and 0.00125, respectively. These differences show excellent agreement and demonstrate that CORE-II can consistently predict in-sequence and local criticality of an irradiated core.

However, the k-effective difference of 0.00328 at zero exposure is unexpectedly high. The k-effective comparison at zero exposure should be more consistent than comparisons with irradiated fuel due to the lack of uncertainties associated with local exposure mispredictions.

To illustrate the magnitude of this difference, current Browns Ferry Technical Specifications require that a minimum shutdown margin of 0.38 $\%\Delta k$ be demonstrated. This margin is the uncertainty of predicting the highest worth control rod. The shutdown margin requirement is based on two components of uncertainty: (1) a manufacturing tolerance uncertainty, and (2) a calculational

Table 5-4

In-Sequence Cold Critical K-effective Bias Relative to Local Cold Criticals for Cycle 1

Exposure (GWD/MT)	Average In-Sequence K-effective	Average Local K-effective	Bias (%ΔK)
0.000	1.00699 (6)[1]	1.00371 (25)	0.328
2.866	1.00319 (1)		
3.748	1.00064 (2)	0.99908 (6)	0.156
4.938	0.99679 (1)		
6.911	0.99608 (1)	0.99483 (1)	0.125

[1]Numbers in parentheses indicate the number of k-effective values used to obtain each average.

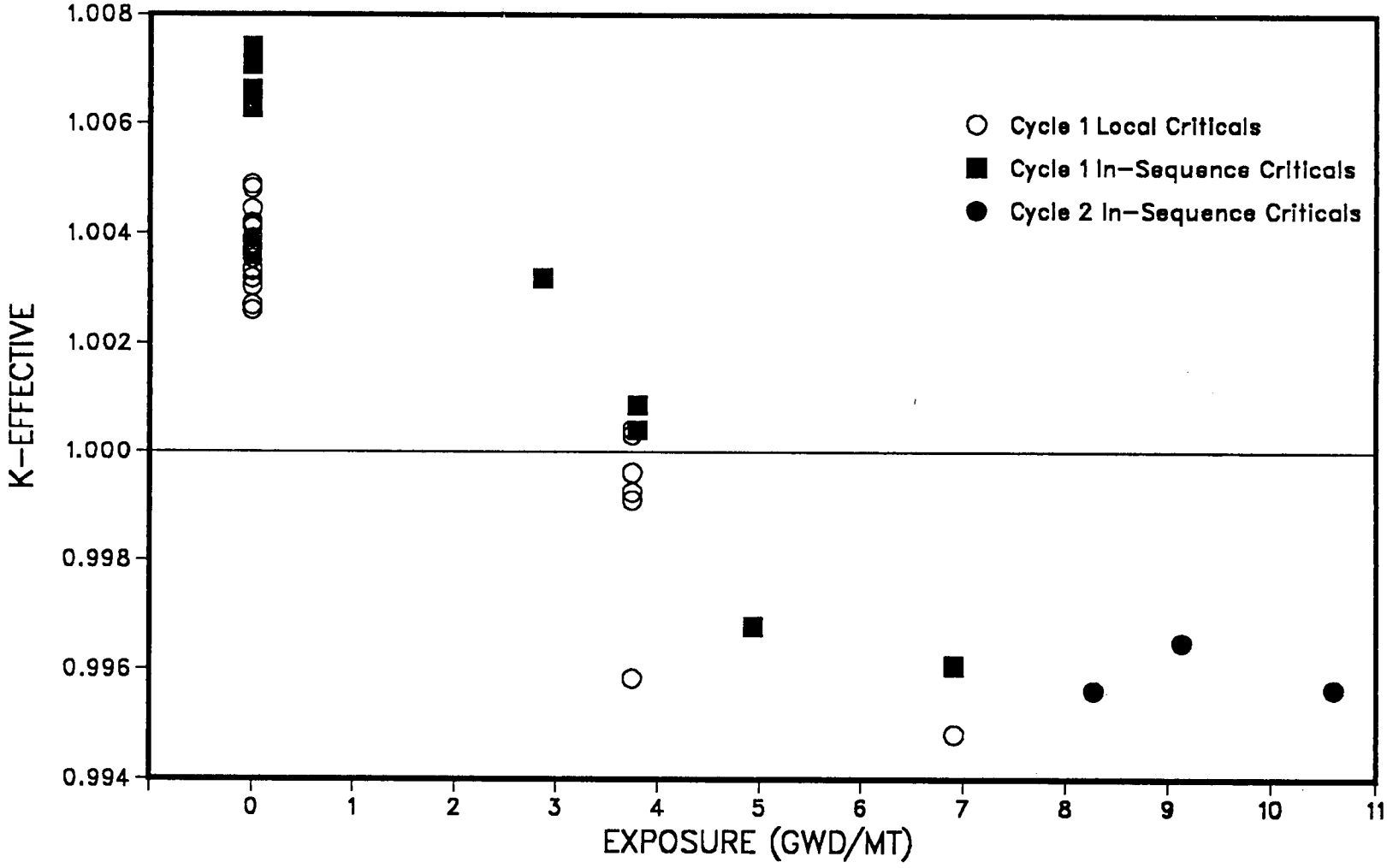

Figure 5-4. In-Sequence And Local Cold Critical K-effective Versus Core Exposure

uncertainty. The manufacturing uncertainty has been determined by General Electric Company based on the stack-up of manufacturing tolerances for fuel assemblies and control blades. The calculational uncertainty was based on tne local critical comparison using LATTICE/CORE methods. Reference 13 reports a LATTICE/CORE difference of 0.0009 between in-sequence and local critical k-effectives at zero exposure. This difference is exceptionally small considering that these codes are less sophisticated and may be the fortuitous result of modeling error cancellations.

The increased bias of the in-sequence criticals at low exposures indicates that the problem may be related to the in-sequence critical calculations. This is shown by considering the difference between CORE-II and CORE in-sequence k-effective values versus exposure (Figure 5-3). If the bias between the codes at low exposures were consistent with the higher exposure points, the difference between CORE-II in-sequence and local criticals would be similar to the CORE difference of 0.0009.

The cause of the increased k-infinity difference at zero exposure relative to LATTICE/CORE calculations is not readily explained. A discussion of future work to investigate this problem is included in section 8.

6.0 TRAVERSING IN-CORE PROBE COMPARISONS

6.1 Overview

Calculated power distributions provide the basis for thermal limit calculations and are the primary input to the forward step depletion calculations used to track exposure accumulation. Consequently, the accuracy of all core design analyses are dependent on the ability to predict core power distributions through an operating cycle.

Comparison to in-core detector measurements is a primary means of quantifying the accuracy of calculated power distributions. A large number of TIP measurements at near rated power and flow were made at Quad Cities-1 during operation of cycles 1 and 2. Complete TIP reading sets for 15 exposures through cycle 1 and 13 exposures through cycle 2 are reported in References 7 and 8. A correct TIP set is unavailable for data set 16.

The Quad Cities TIP detectors are small movable fission chambers which measure the thermal neutron flux in the narrow water gap corner between four fuel assemblies. Thimble tubes for TIP traversing are located in the 41 radial locations shown in Figure 2-2. To remove differences due to detector sensitivity, each TIP machine was calibrated to read an average of 100 when inserted into the common TIP thimble (location 32-33). Both calculated and measured TIP readings represent the average TIP reading over six inch intervals, with the elevations of the measured TIP readings corresponding directly to the core simulator nodal midpoints.

Power distributions from the depletion calculations were used to construct simulated TIP readings for comparison with each measured TIP set. The core simulator converted the calculated power distribution to effective TIP readings using the procedure outlined in section 2.5. An auxiliary program was written to perform nodal, radial, and symmetric location comparisons of measured versus calculated TIP readings. Prior to the comparisons, the calculated TIP responses were normalized such that the core average response was the same as the average measured response.

The nodal comparisons were made by calculating the percent difference between the measured and calculated nodal TIP readings. This type of comparison provides an assessment of the accuracy of the calculated nodal power distribution, which affects thermal limits calculations such as LHGR. For the nodal comparisons, the percent difference between calculated and measured data is determined as:

$$\%\Delta_{m,k} = \left[\frac{(C_{m,k} - M_{m,k})}{(C_{m,k} + M_{m,k})/2}\right] 100 \qquad (6\text{-}1)$$

where

$\%\Delta_{m,k}$ = percent difference of the nodal measured versus calculated values at radial location m, and axial location k,

$M_{m,k}$ = measured TIP reading at radial location m, and axial location k,

$C_{m,k}$ = calculated TIP reading at radial location m, and axial location k.

The standard deviation of the nodal percent differences is calculated as:

$$\sigma_{node} = \sqrt{\frac{\sum_{i=1}^{n} (\%\Delta_{m,k} - \%\Delta_{node})^2}{(n - 1)}} \qquad (6\text{-}2)$$

where

σ_{node} = standard deviation of the nodal percent differences,

$\%\Delta_{m,k}$ = percent difference at radial location m, and axial location z,

$\%\Delta_{node}$ = core average measured versus calculated percent difference,

n = total number of nodal TIP readings (41x24).

The radial comparisons were made using the axially integrated TIP values at each of the 41 radial locations. This type of comparison provides an assessment of the accuracy of the assembly averaged power distribution, which affects thermal limit calculations such as Critical Power Ratio (CPR). For the integrated comparisons, the percent difference between measured and calculated data are determined as:

$$\%\Delta_m = \left[\frac{(C_m - M_m)}{(C_m + M_m)/2}\right] 100 \qquad (6\text{-}3)$$

where

$\%\Delta_m$ = percent difference of integrated measured versus calculated values at radial location m,

M_m = axial averaged measured TIP response at radial location m,

C_m = axial averaged calculated TIP response at radial location m.

The standard deviation of the integrated percent differences is calculate as:

$$\sigma_{int} = \sqrt{\frac{\sum_{i=1}^{n} (\%\Delta_m - \%\Delta_{int})^2}{(n - 1)}} \qquad (6\text{-}4)$$

where

σ_{int} = standard deviation of integrated percent difference,

$\%\Delta_m$ = percent difference of measured versus calculated values at radial location m,

$\%\Delta_{int}$ = core average measured versus calculated percent difference,

n = Total number of radial TIP locations (41).

6.2 Results

Table 6-1 summarizes the nodal and integrated comparison of measured versus calculated TIP readings for each of the 28 TIP sets. Since the calculated TIP readings were normalized to the average of the measured TIP readings, the average nodal and integrated percent differences are small. Therefore, the standard deviation of the percent differences is used to show the accuracy of the calculated results. Results from Reference 13 for LATTICE/CORE calculations of the same core conditions have been included in Table 6-1 for

Table 6-1

Measured Versus Calculated TIP Comparison from Cycles 1 and 2

Core Average Exposure (GWd/MT)	Standard Deviation (%)					
	TGBLA/COREII		LATTICE/CORE		TGBLA/COREII[1]	
	Integrated	Nodal	Integrated	Nodal	Integrated	Nodal
0.272	6.47	12.04	5.21	10.28	5.35	11.46
0.712	6.99	12.96	5.49	8.22	5.70	14.17
0.882	7.01	12.96	5.60	8.50	5.73	13.50
1.471	7.17	13.64	5.73	8.60	6.24	14.66
2.239	7.01	12.05	5.75	8.38	6.46	12.97
3.190	7.28	11.60	6.02	8.95	6.66	12.07
3.837	6.86	11.37	6.04	9.55	6.69	13.26
4.075	7.21	12.58	6.25	10.48	7.04	14.93
4.738	6.48	11.46	5.82	9.44	6.33	12.76
5.301	6.33	11.83	5.85	10.82	6.09	11.40
6.031	5.97	11.24	5.21	12.59	5.35	8.84
6.558	6.96	11.69	5.62	10.62	5.51	10.71
6.807	6.84	11.07	5.44	10.70	5.22	9.56
7.397	6.01	9.76	5.46	10.43	5.43	8.45
7.660	6.58	10.72	5.41	11.14	5.26	9.08
7.980	-	-	-	-	-	-
7.303*	6.23	14.04	4.38	13.37	4.30	9.59
7.532	6.36	15.15	5.11	13.49	5.00	10.79
7.964	5.70	10.11	4.78	11.66	4.78	8.10
8.424	6.02	13.68	5.21	11.84	5.16	10.34
8.790	5.64	12.10	5.04	11.03	5.15	9.45
9.142	5.68	11.17	5.22	10.85	5.44	9.01
10.174	5.34	8.67	5.76	11.30	5.69	9.03
11.239	4.57	9.06	4.79	12.78	4.59	7.72
11.936	4.98	9.36	5.60	12.17	5.11	11.63
12.897	4.82	8.51	-	-	5.45	10.53
13.199	4.34	7.35	4.76	11.74	4.74	8.41
13.612	4.21	9.36	4.62	14.12	4.71	8.80
13.742	4.70	10.96	5.11	14.95	5.18	10.17
Average	6.06	11.30	5.40	11.24	5.51	10.76

[1]Calculated using LATTICE Detector Activation Rate/Power table sets
*First TIP set in cycle 2

comparison. The last two columns of this table are discussed later in this section.

Due to control rod movements, power and/or flow changes, several of the TIP measurements were taken before an equilibrium xenon distribution was achieved. Although this has a negative impact on the comparisons due to equilibrium xenon concentrations being assumed in the calculations, results for all TIP sets are included.

The average standard deviation for all 28 data sets is 11.30% and 6.06% for nodal and integrated values respectively. The TGBLA/CORE-II results are slightly less consistent than the corresponding LATTICE/CORE results of 11.04% and 5.38%. The CORE-II results are improved during the last half of cycle 2. This period of operation was characterized by a decreasing control rod inventory until all rods were withdrawn at end-of-cycle.

The loading patterns for cycles 1 and 2 are half-core symmetric about the TIP diagonal line of symmetry. The A-sequence control rod patterns, which are also symmetric about the TIP diagonal, were in use during 15 of the 28 TIP measurements. Under these conditions, TIP detectors not located directly on the symmetry line will have nearly the same neutron flux conditions. The only non-symmetric effect is due to depletion steps with rod patterns which retained only rotational symmetry. This results in slightly non-symmetric exposure accumulation during B-sequence depletion steps.

An estimate of the TIP measurement uncertainty can be made by comparing calculated and measured TIP readings with their symmetric locations. Table 6-2 contains a comparison of calculated and measured

Table 6-2

Symmetric TIP Location Comparison from Cycles 1 and 2

Core Average Exposure (GWd/MT)	Data Set	Rod Sequence	Standard Deviation (%) Symmetric Calculated Integrated	Symmetric Calculated Nodal	Symmetric Measurement Integrated	Symmetric Measurement Nodal
0.272	1	A	0.01	0.03	5.54	10.51
0.712	2	A	0.11	0.64	8.56	11.69
0.882	3	A	0.01	0.03	8.83	12.12
1.471	4	B	-	-	-	-
2.239	5	B	-	-	-	-
3.190	6	A	0.86	1.58	8.77	12.43
3.837	7	B	-	-	-	-
4.075	8	B	-	-	-	-
4.738	9	B	-	-	-	-
5.301	10	B	-	-	-	-
6.031	11	B	-	-	-	-
6.558	12	A	1.15	2.01	8.37	12.02
6.807	13	A	1.30	2.22	8.49	12.97
7.397	14	B	-	-	-	-
7.660	15	A	1.39	2.71	8.21	10.86
7.980	16	A	1.43	2.46	8.66	10.41
7.303*	17	A	1.10	2.08	5.64	11.05
7.532	18	A	1.09	2.06	7.41	12.17
7.964	19	A	1.05	2.33	6.36	10.85
8.424	20	B	-	-	-	-
8.790	21	B	-	-	-	-
9.142	22	B	-	-	-	-
10.174	23	A	1.47	3.33	6.36	10.04
11.239	24	B	-	-	-	-
11.936	25	B	-	-	-	-
12.897	26	B	-	-	-	-
13.199	27	ARO[1]	1.59	2.76	6.44	9.73
13.612	28	ARO	1.57	2.74	5.71	9.11
13.742	29	ARO	1.57	2.73	5.62	9.01
Average			1.05	1.98	7.26	11.00

[1]All Rods Out
*First TIP set in cycle 2

symmetric TIP readings. An estimate of the asymmetry introduced due to asymmetric exposure accumulation is shown in the comparison of symmetric calculated readings. For this comparison, the calculated results are 1.05% and 1.98% for nodal and integrated values respectively.

The average standard deviation of the measured percent differences for nodal and integrated values are 11.00% and 7.26% respectively. Thus, the standard deviation of the percent differences between measured and calculated TIP readings was approximately the same as the symmetric measurements. This indicates that the uncertainty in predicted TIP readings is similar to the measurement uncertainty.

The ability to predict gross axial power distributions through cycle 1 operation is shown in Figures 6-1 through 6-15. These figures show good agreement between measured and calculated core average TIP readings as a function of core height. CORE-II slightly over predicted the axial peak throughout the cycle.

Figures 6-16 through 6-28 show similar plots for the cycle 2 TIP readings. The peak of calculated TIP readings was significantly overestimated early in the cycle, during operation with a strong bottom peaked power shape. The agreement with the measured data improved as control rods were withdrawn and the power shape flattened through the cycle.

It should be noted that the depressions shown in Figures 6-1 through 6-28 for the measured data are due to fuel rod spacers. Rod spacers are located at seven axial levels in each assembly and shield

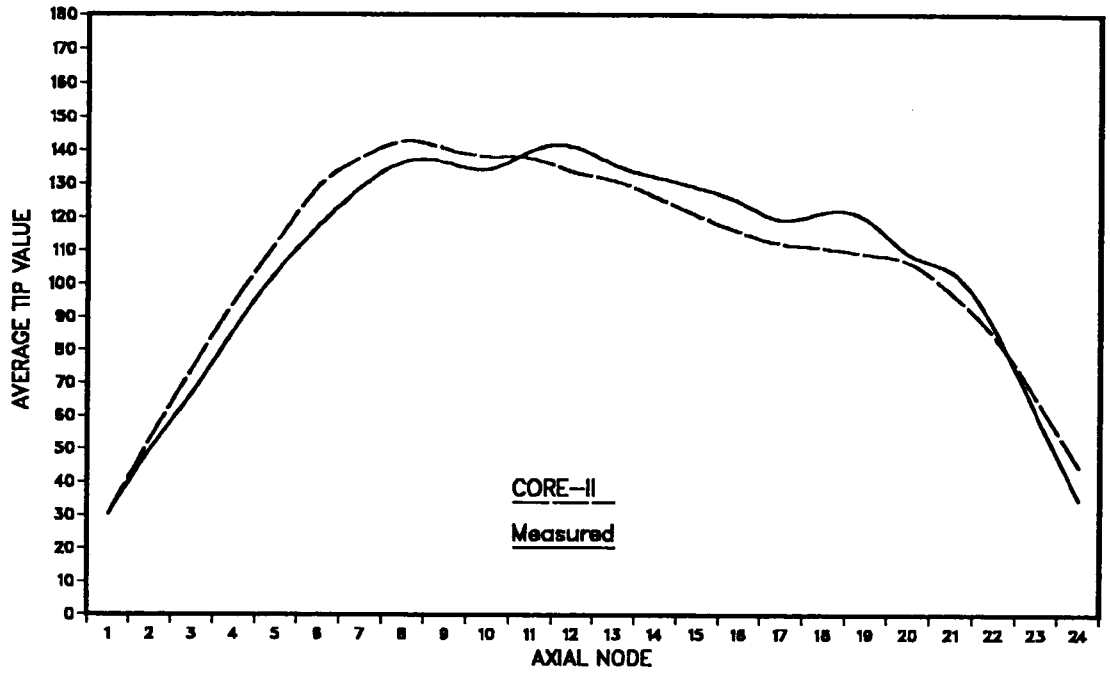

Figure 6-1. Cycle 1 Core Average Axial TIP Comparison at 272 MWd/MT

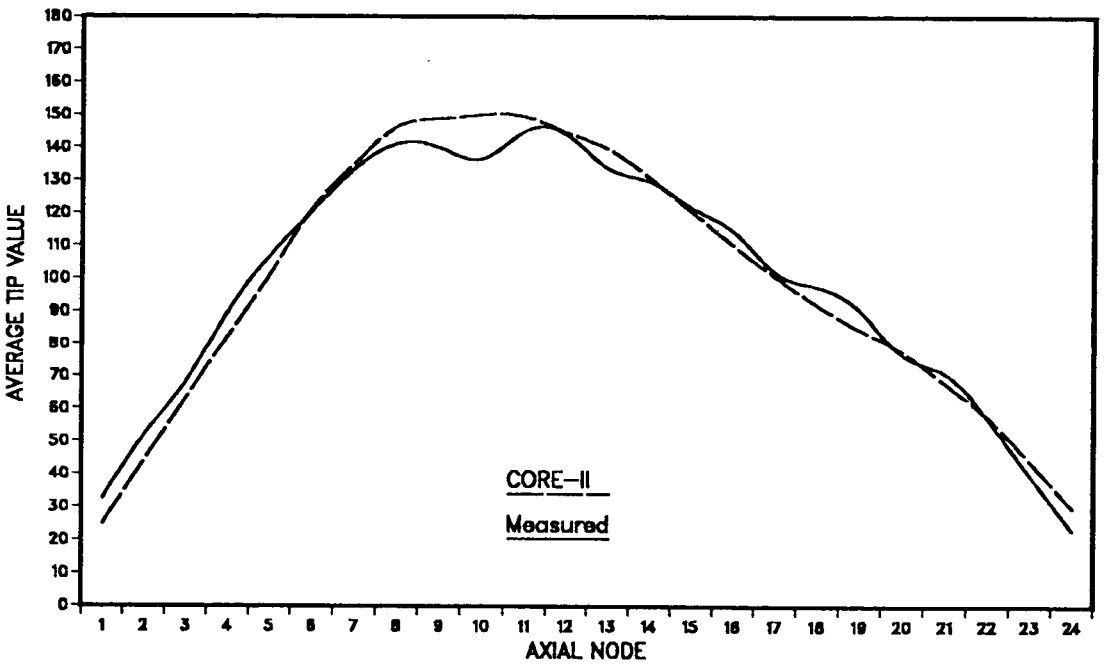

Figure 6-2. Cycle 1 Core Average Axial TIP Comparison at 712 MWd/MT

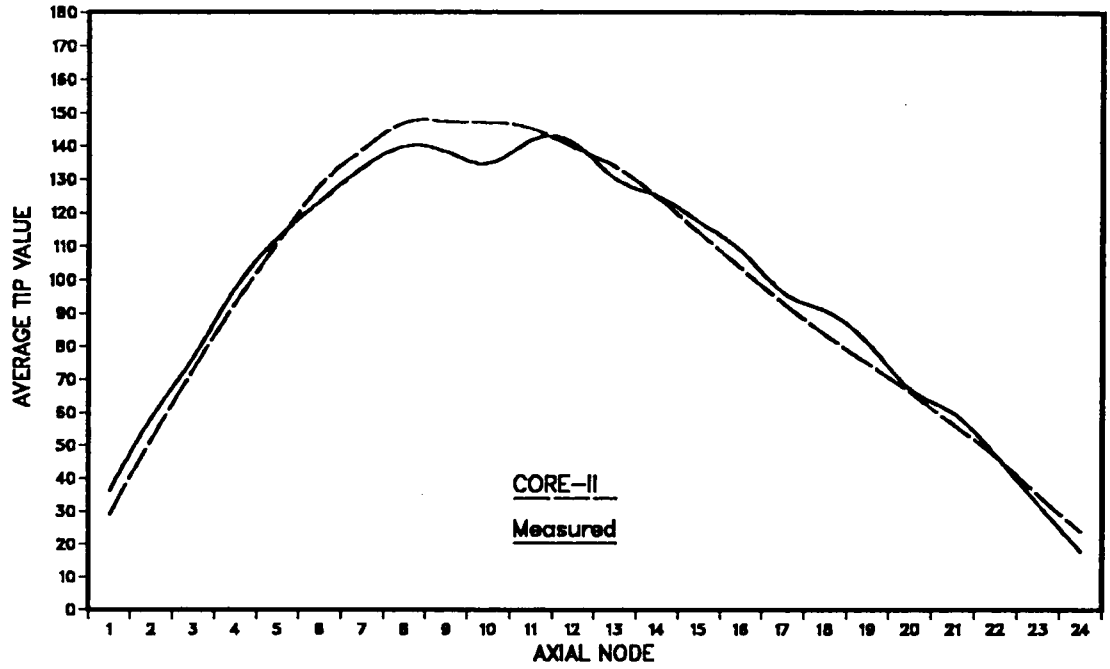

Figure 6-3. Cycle 1 Core Average Axial TIP Comparison at 882 MWd/MT

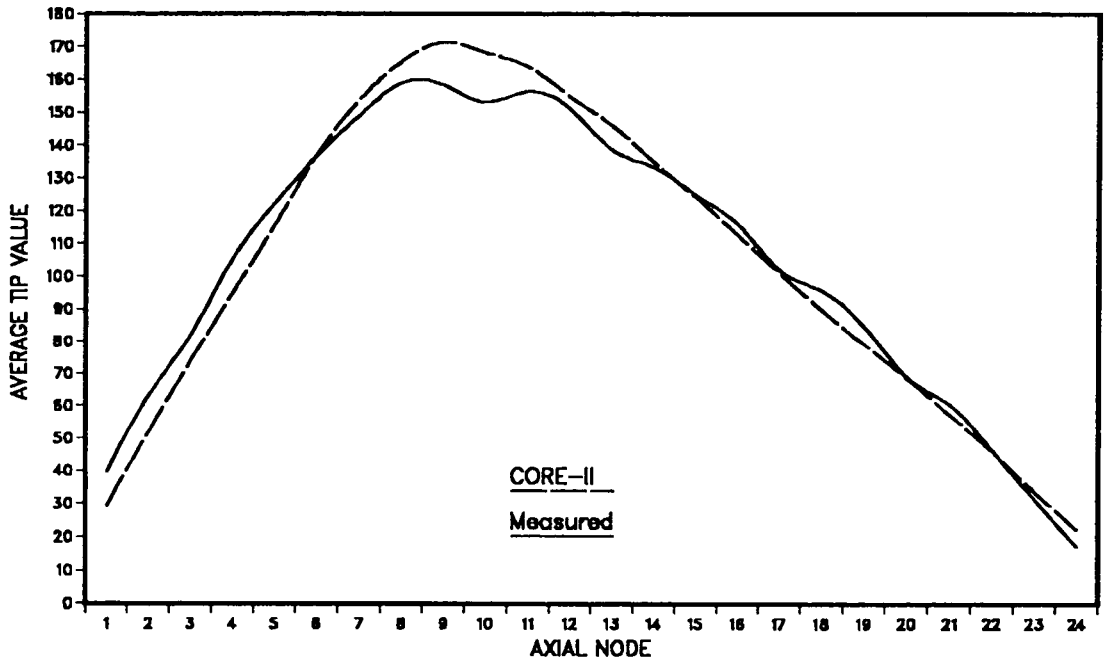

Figure 6-4. Cycle 1 Core Average Axial TIP Comparison at 1471 MWd/MT

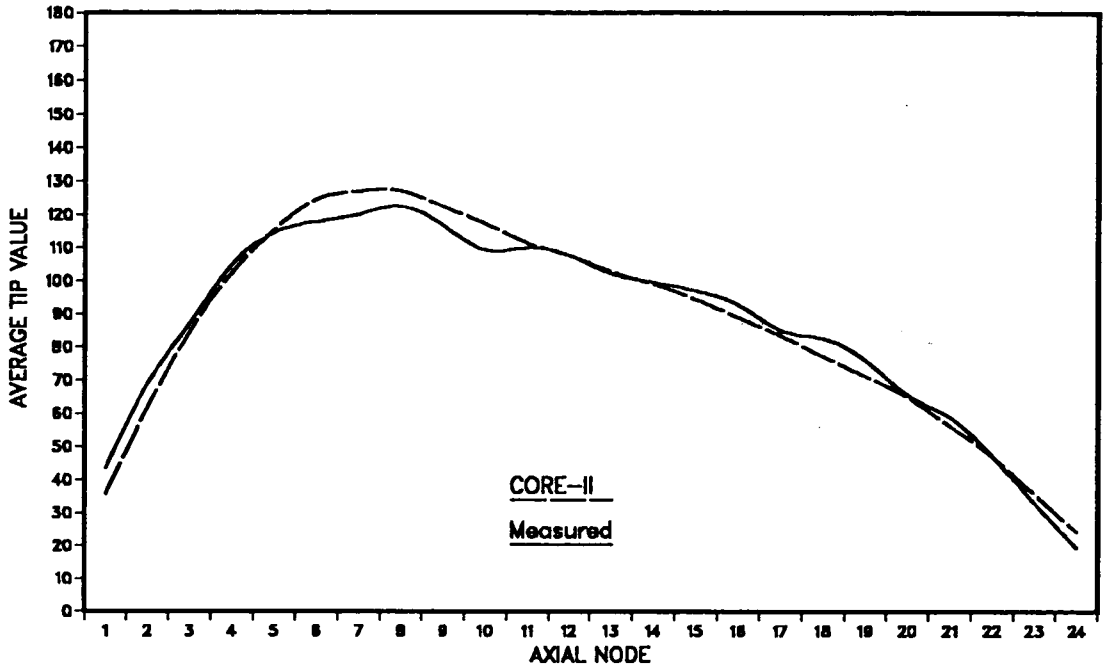

Figure 6-5. Cycle 1 Core Average Axial TIP Comparison at 2239 MWd/MT

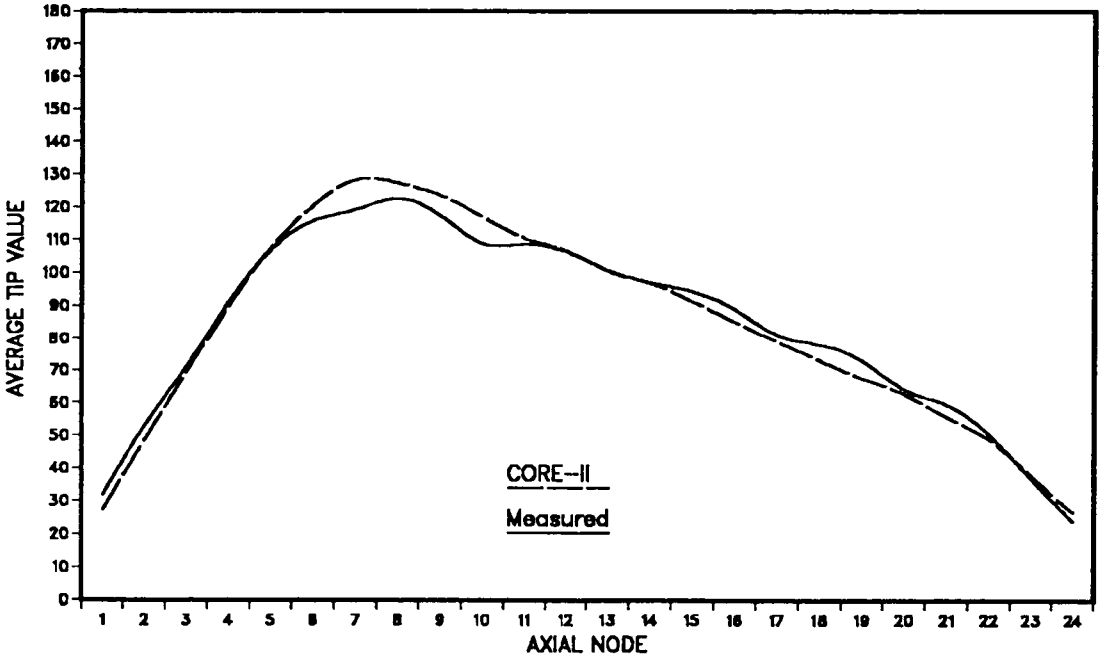

Figure 6-6. Cycle 1 Core Average Axial TIP Comparison at 3190 MWd/MT

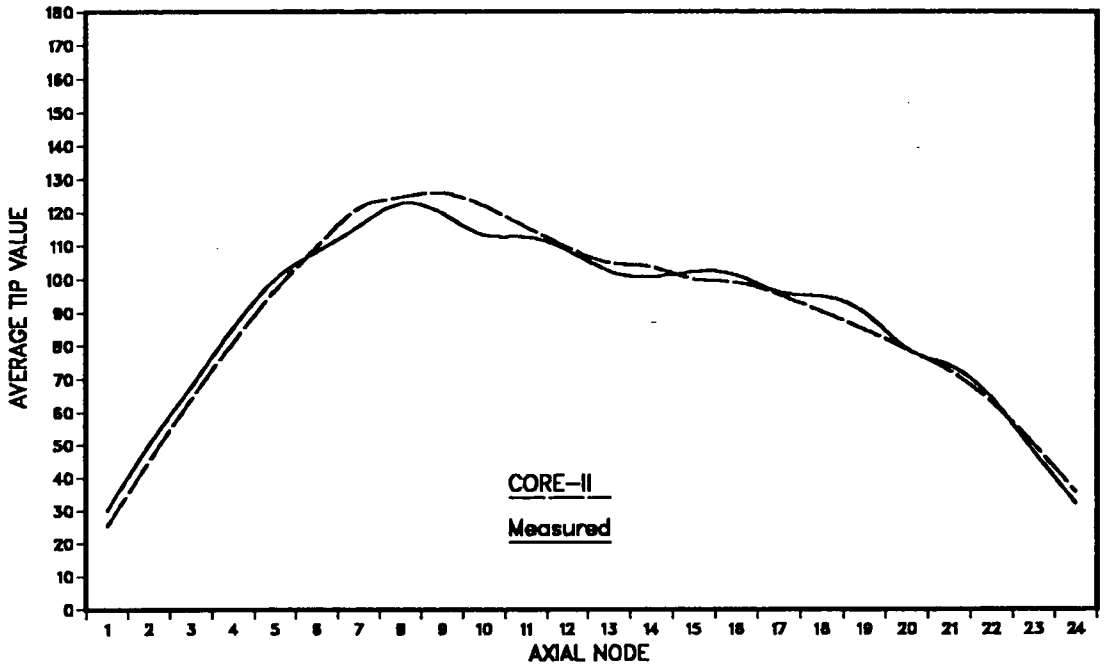

Figure 6-7. Cycle 1 Core Average Axial TIP Comparison at 3837 MWd/MT

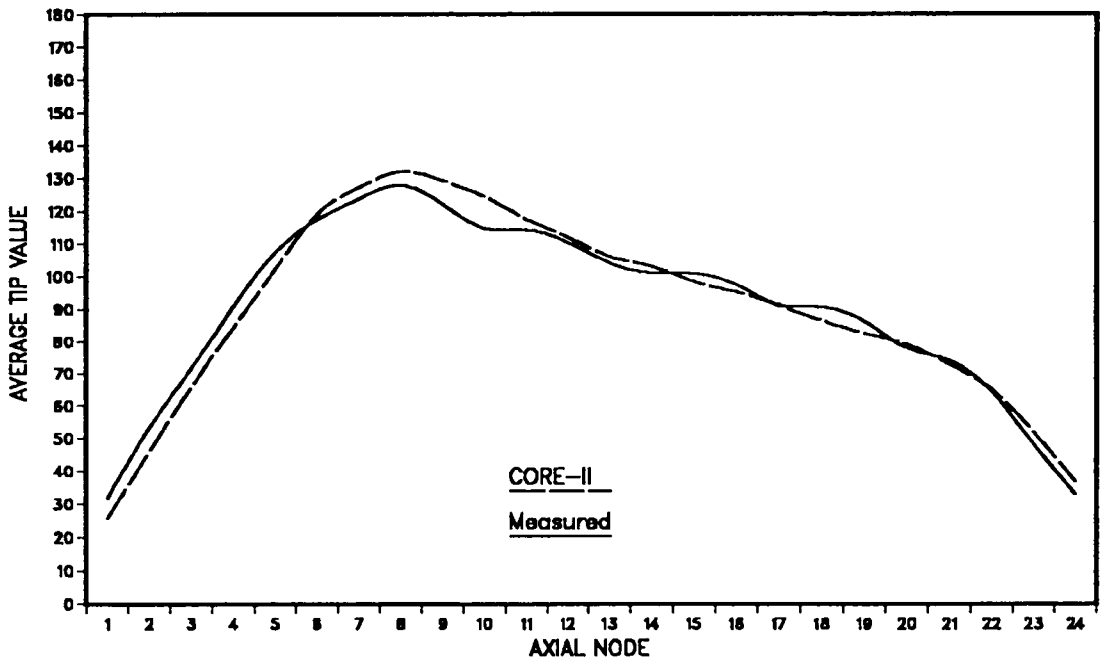

Figure 6-8. Cycle 1 Core Average Axial TIP Comparison at 4075 MWd/MT

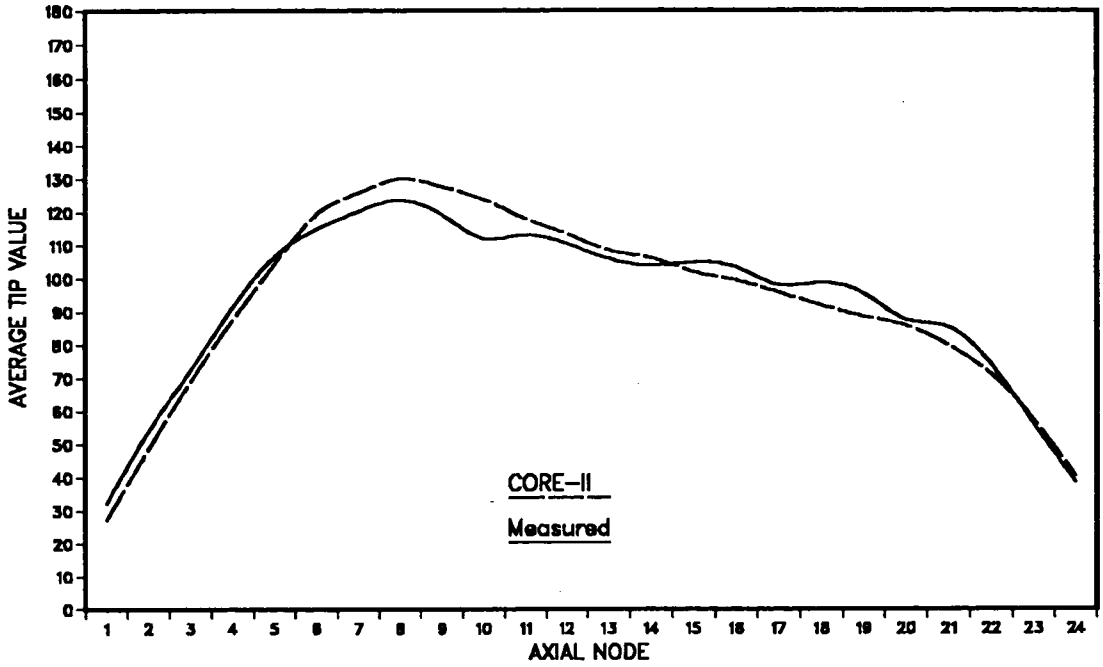

Figure 6-9. Cycle 1 Core Average Axial TIP Comparison at 4738 MWd/MT

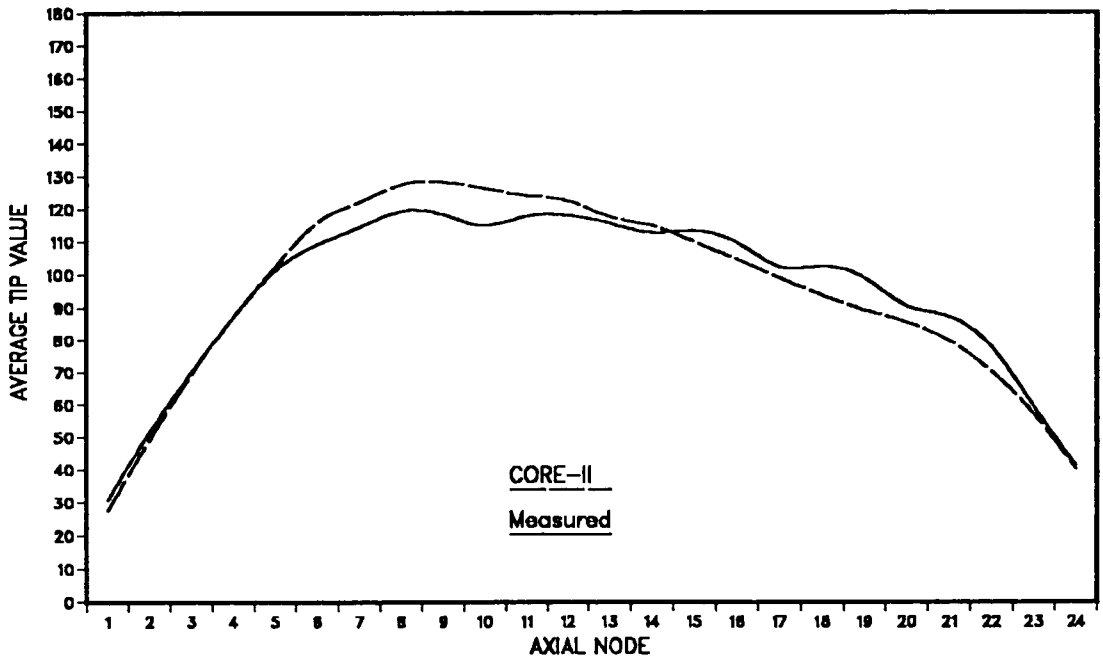

Figure 6-10. Cycle 1 Core Average Axial TIP Comparison at 5301 MWd/MT

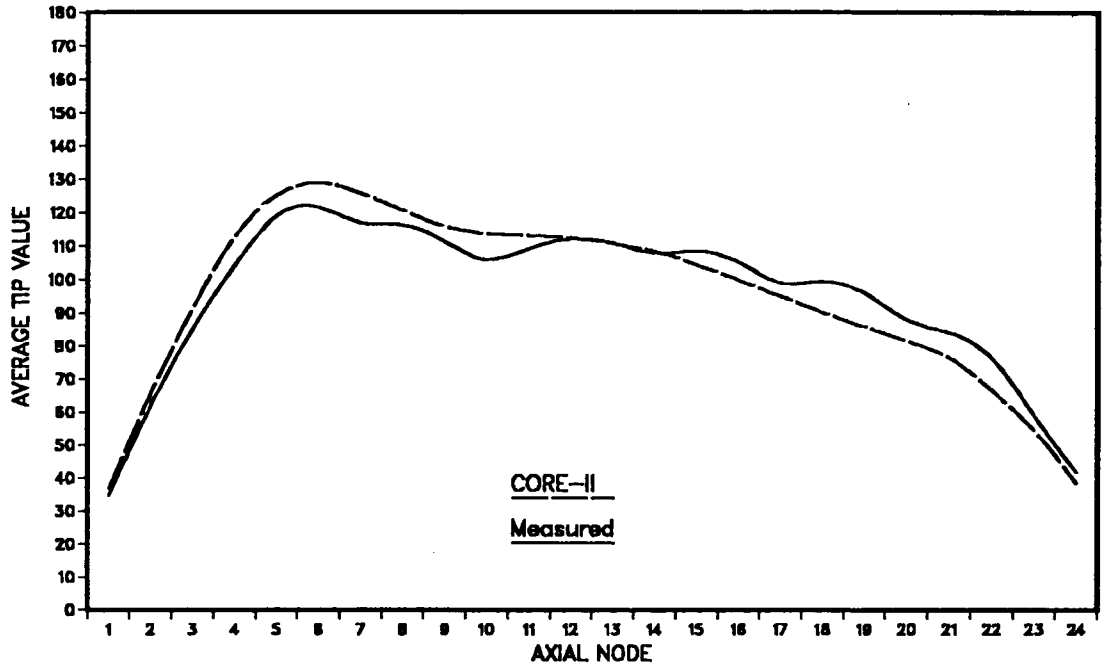

Figure 6-11. Cycle 1 Core Average Axial TIP Comparison at 6031 MWd/MT

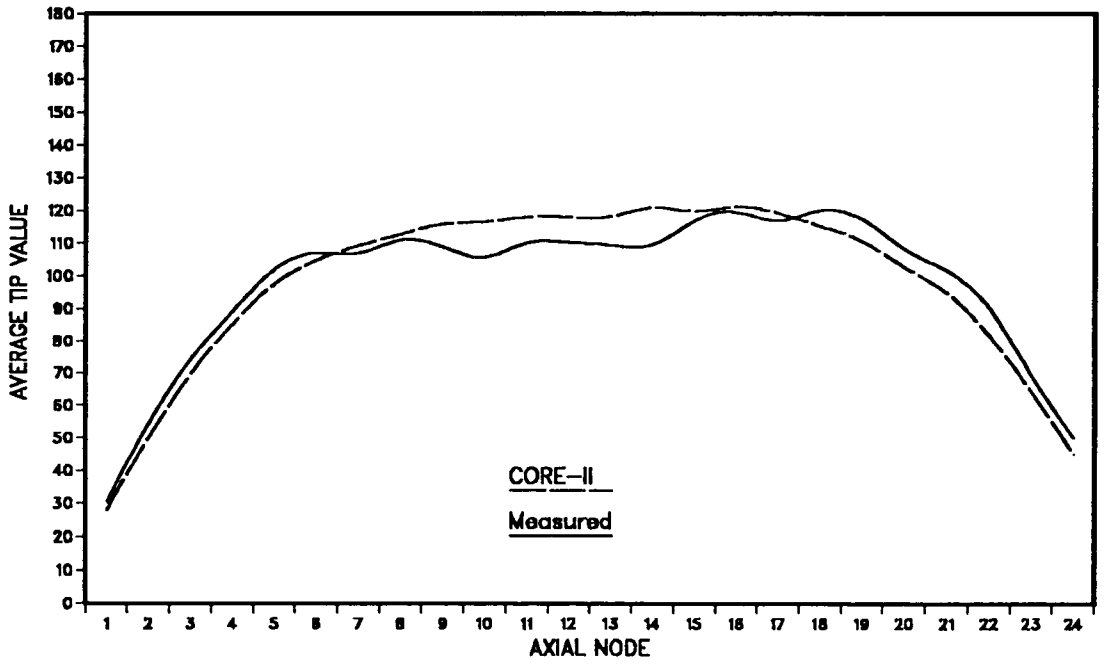

Figure 6-12. Cycle 1 Core Average Axial TIP Comparison at 6558 MWd/MT

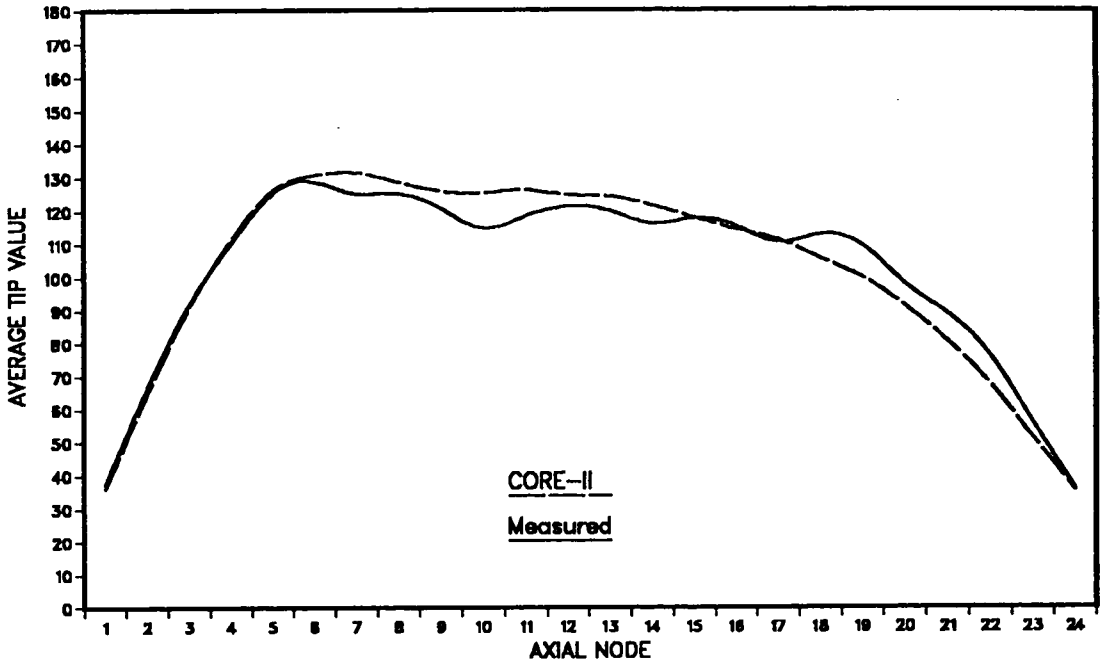

Figure 6-13. Cycle 1 Core Average Axial TIP Comparison at 6807 MWd/MT

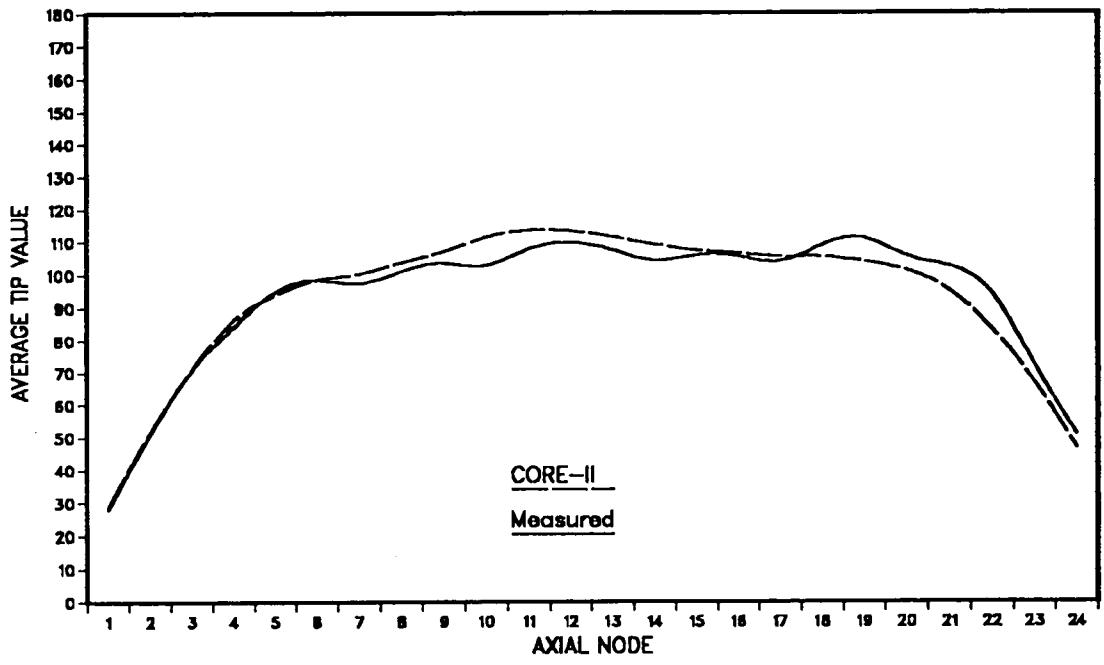

Figure 6-14. Cycle 1 Core Average Axial TIP Comparison at 7397 MWd/MT

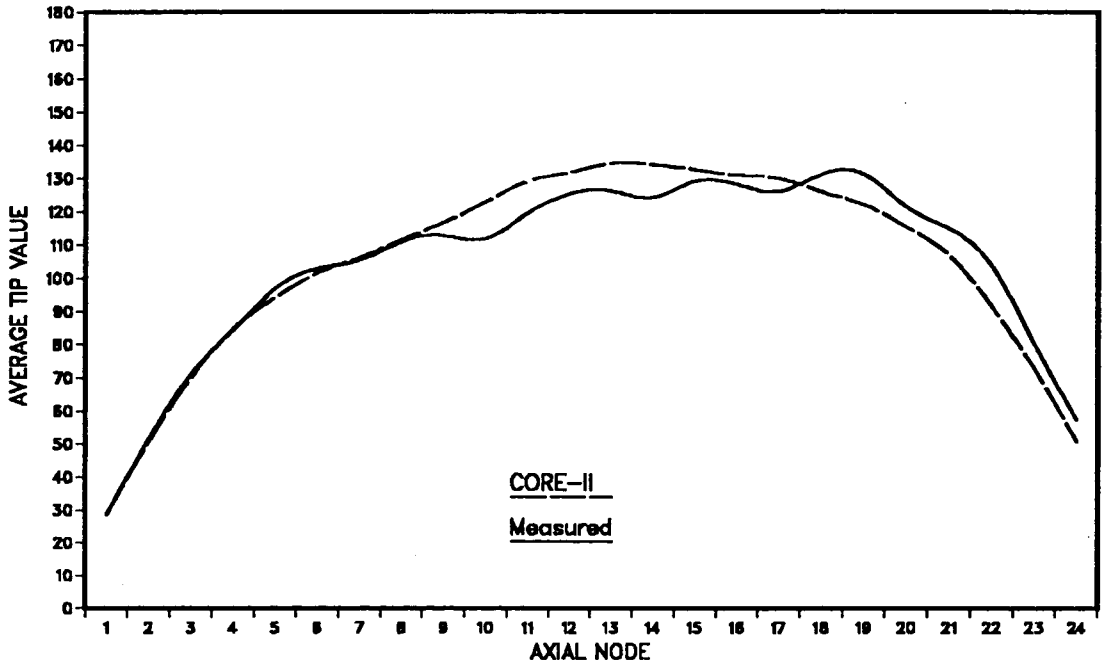

Figure 6-15. Cycle 1 Core Average Axial TIP Comparison at 7660 MWd/MT

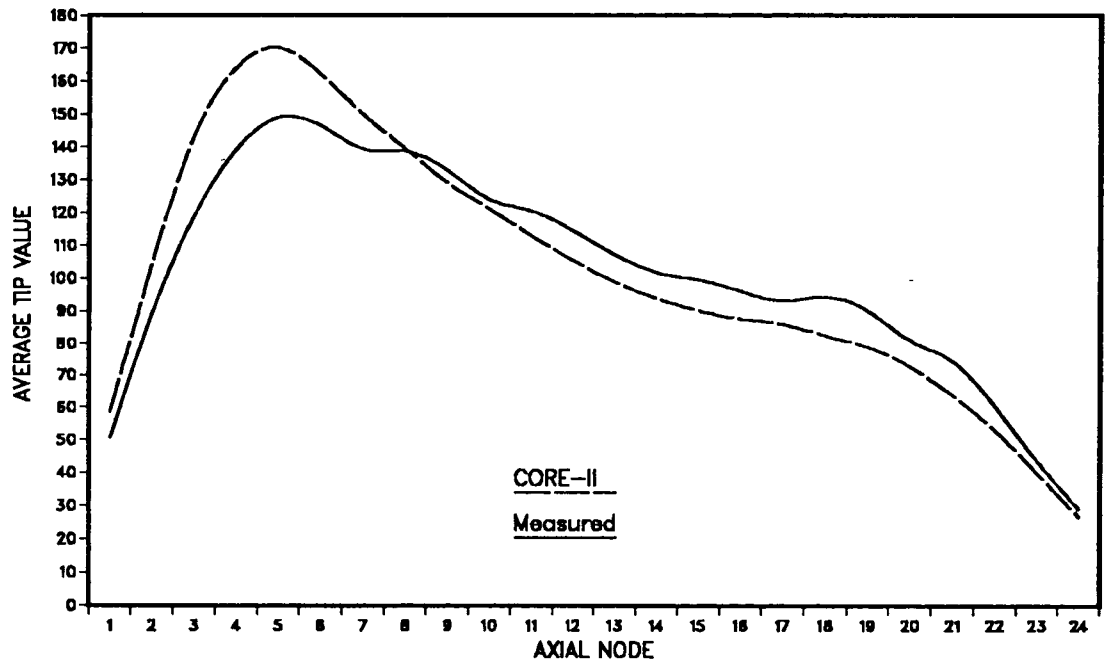

Figure 6-16. Cycle 2 Core Average Axial TIP Comparison at 7303 MWd/MT

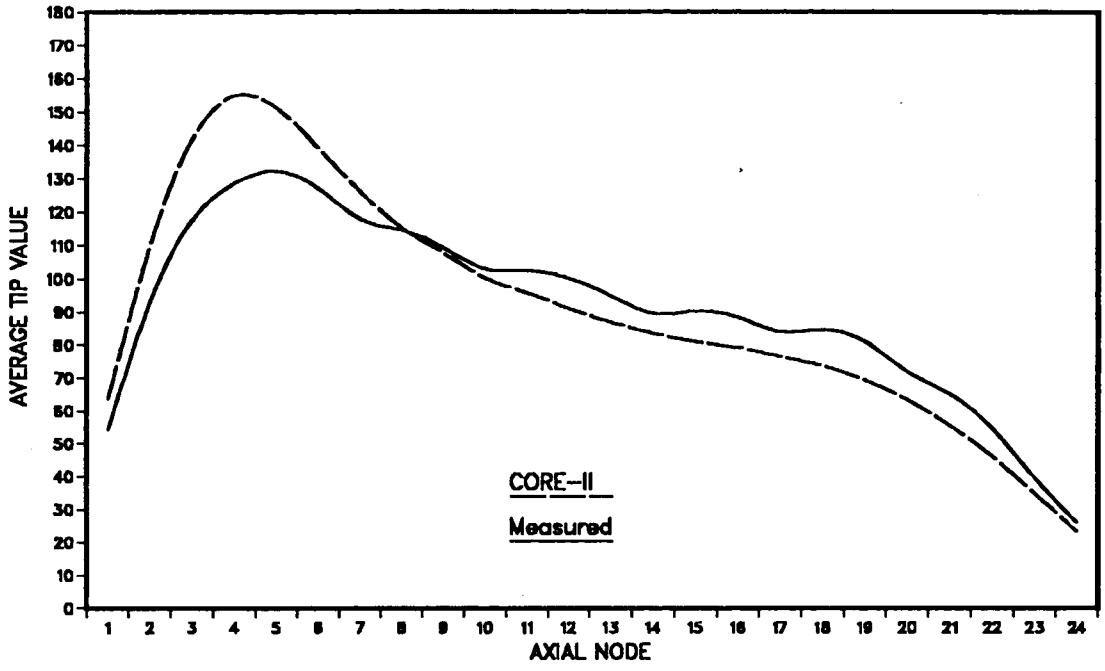

Figure 6-17. Cycle 2 Core Average Axial TIP Comparison at 7532 MWd/MT

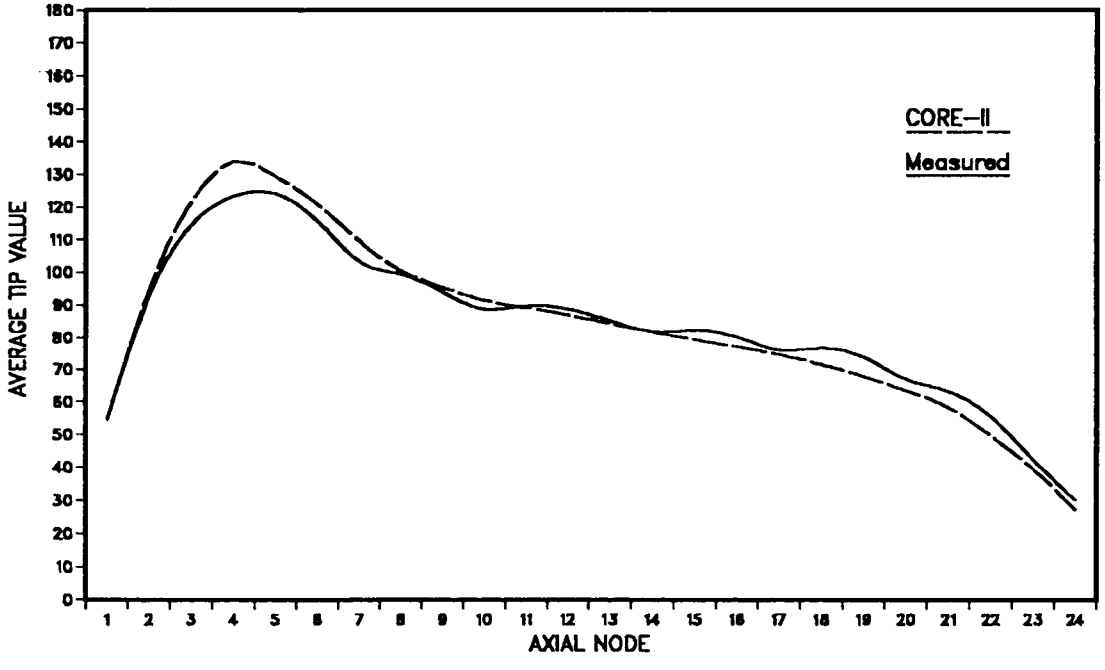

Figure 6-18. Cycle 2 Core Average Axial TIP Comparison at 7964 MWd/MT

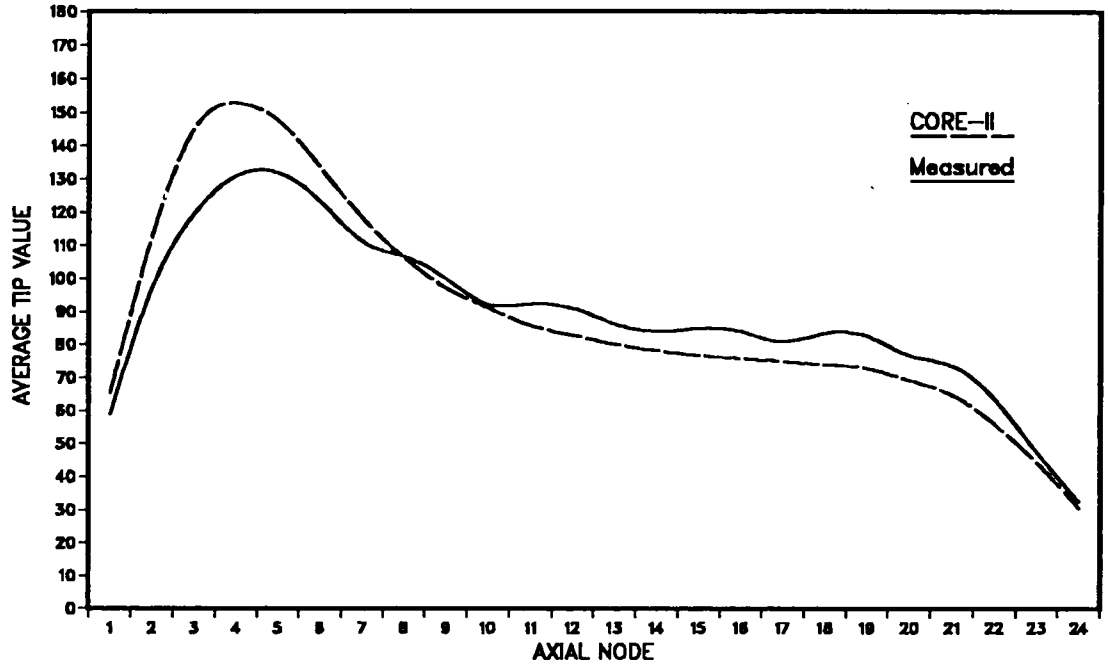

Figure 6-19. Cycle 2 Core Average Axial TIP Comparison at 8424 MWd/MT

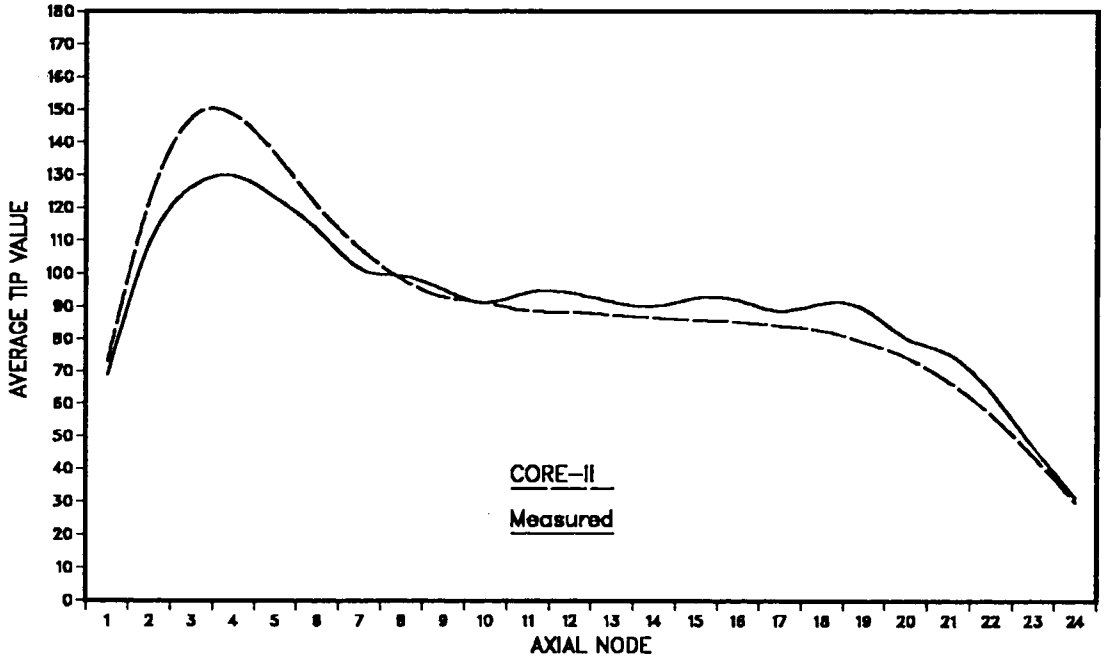

Figure 6-20. Cycle 2 Core Average Axial TIP Comparison at 8790 MWd/MT

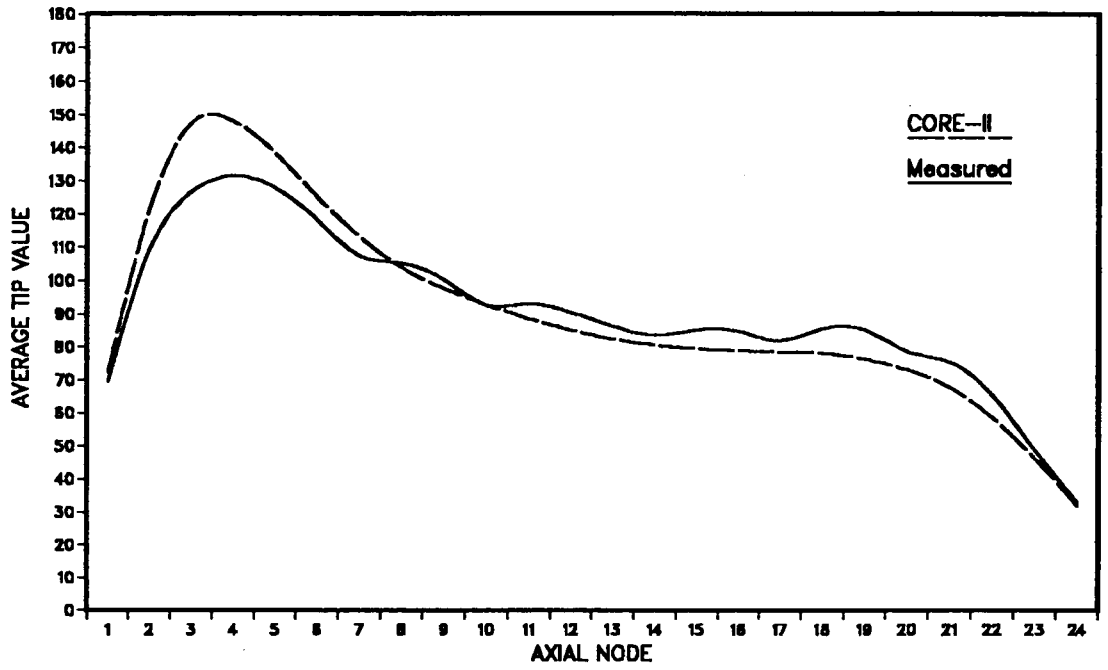

Figure 6-21. Cycle 2 Core Average Axial TIP Comparison at 9142 MWd/MT

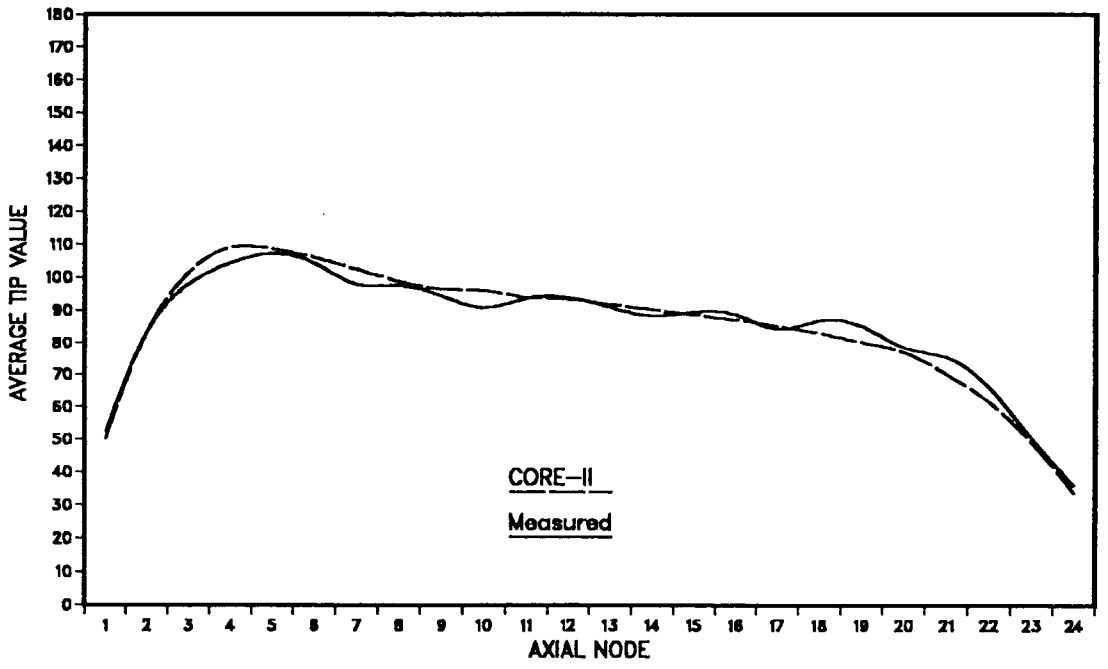

Figure 6-22. Cycle 2 Core Average Axial TIP Comparison at 10174 MWd/MT

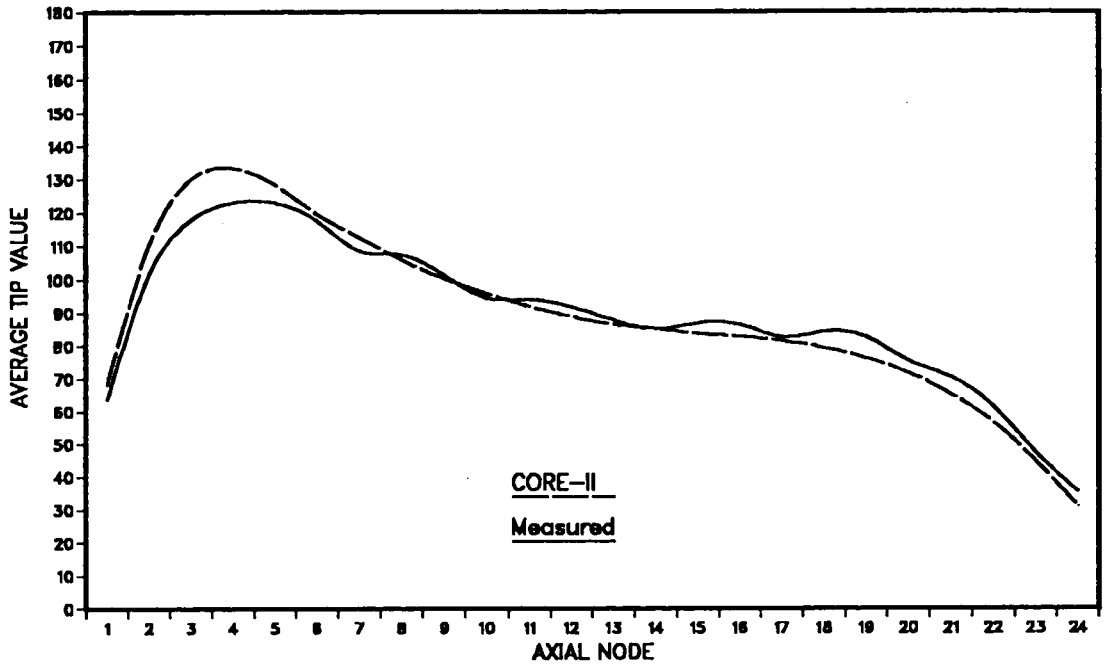

Figure 6-23. Cycle 2 Core Average Axial TIP Comparison at 11239 MWd/MT

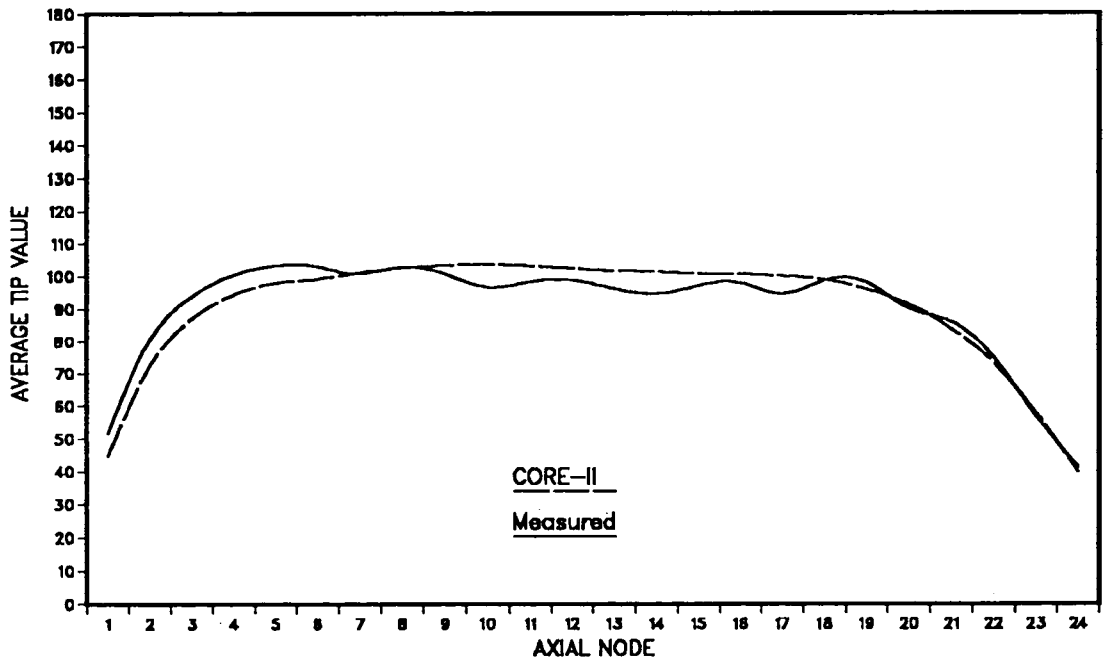

Figure 6-24. Cycle 2 Core Average Axial TIP Comparison at 11936 MWd/MT

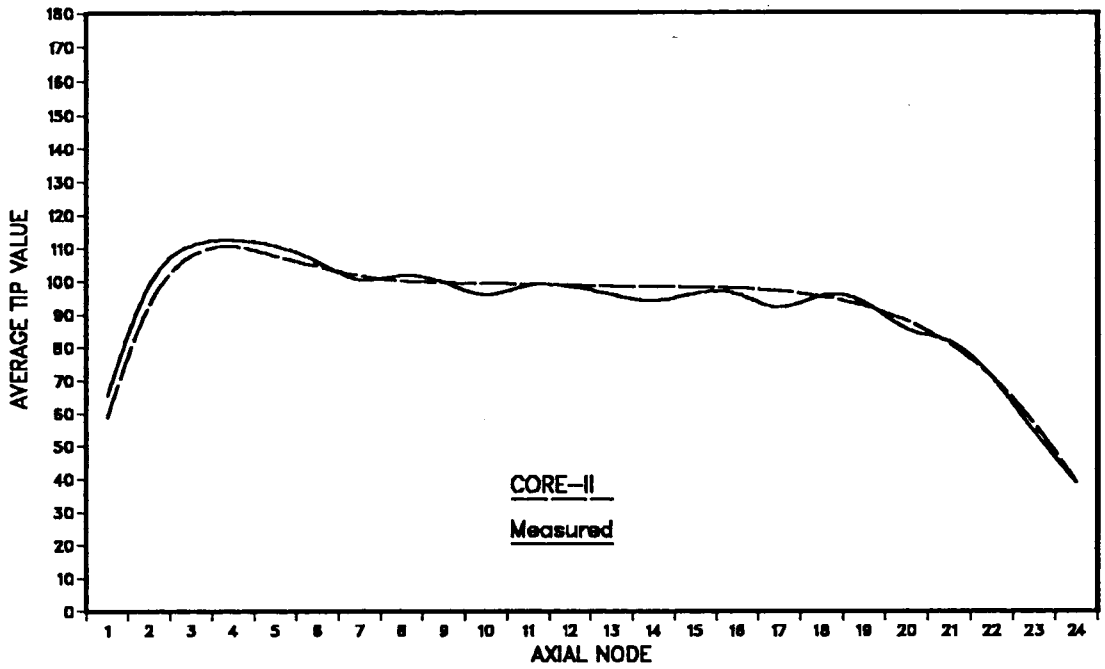

Figure 6-25. Cycle 2 Core Average Axial TIP Comparison at 12897 MWd/MT

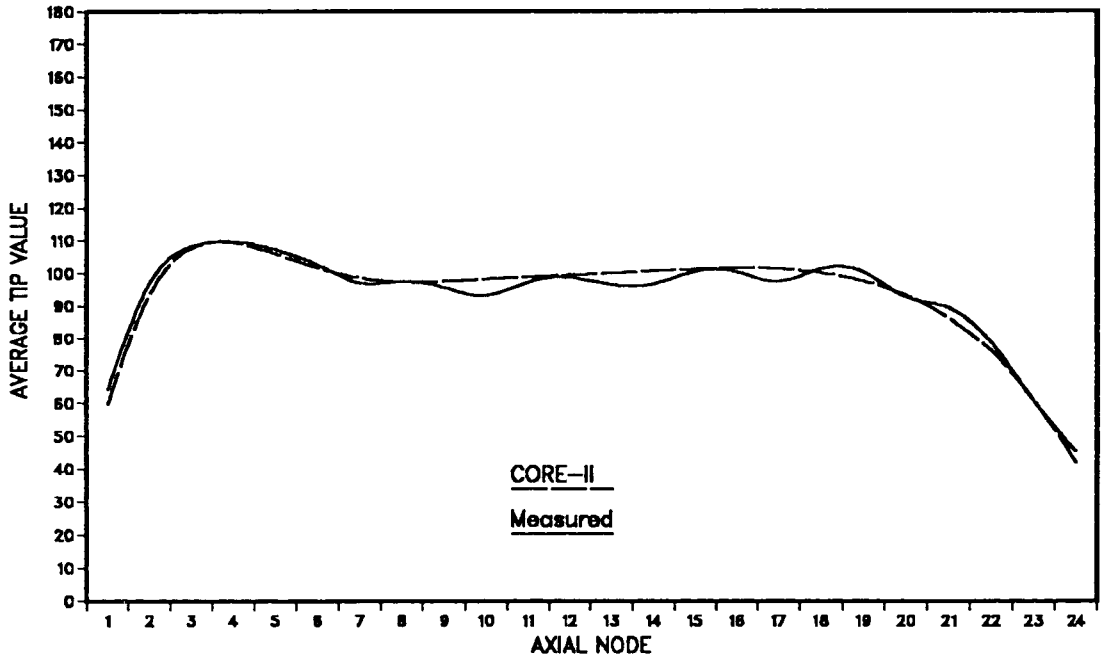

Figure 6-26. Cycle 2 Core Average Axial TIP Comparison at 13199 MWd/MT

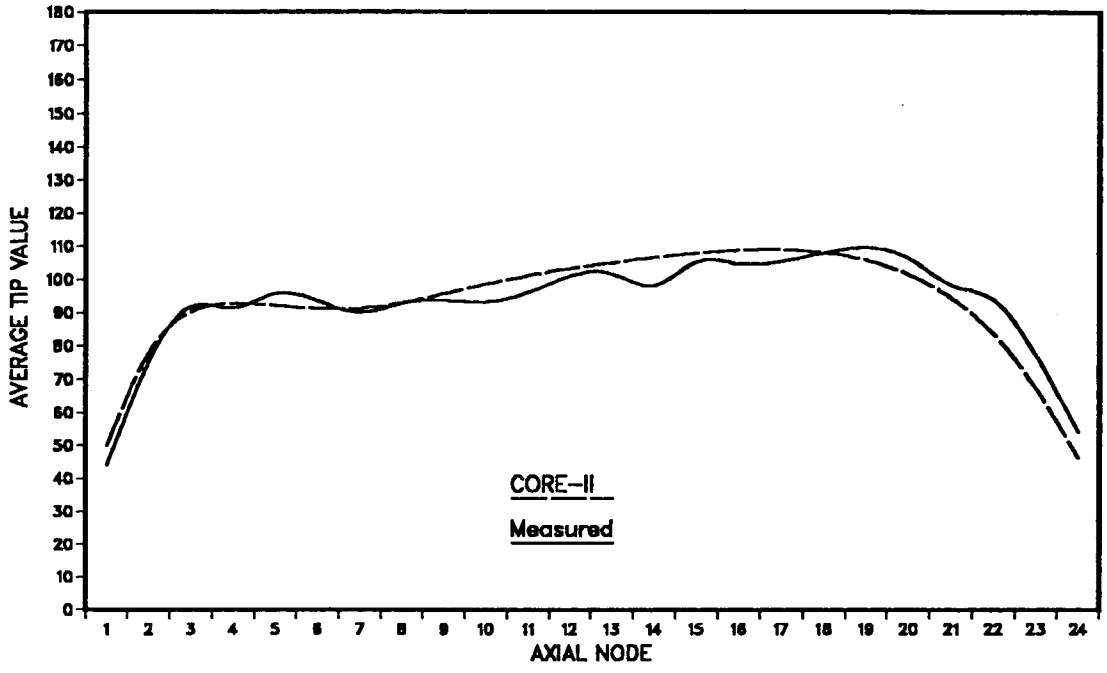

Figure 6-27. Cycle 2 Core Average Axial TIP Comparison at 13612 MWd/MT

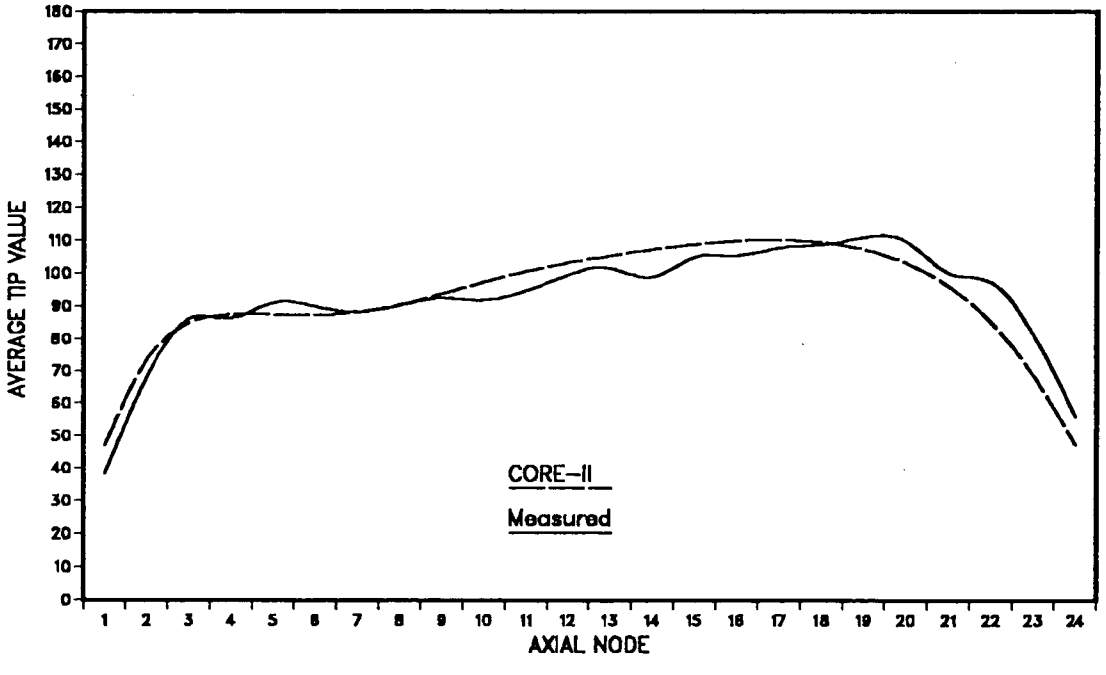

Figure 6-28. Cycle 2 Core Average Axial TIP Comparison at 13742 MWd/MT

the TIP detector from the neutron flux. The effect of spacers was ignored in the calculated TIP readings, as shown in the smooth CORE-II distributions.

6.3 Investigation of TIP Prediction Problems

The TIP predictions presented in the previous section were generally good with uncertainties comparable to the uncertainties of symmetric measurements. However, results contained in section 7 for the gamma scan comparisons indicate that improvements in the CORE-II calculated TIP readings are possible. In addition, the over prediction of the axial peak early in cycle 2 is of concern due to the possibility of being overly conservative in design thermal limit calculations.

Two possible causes of the CORE-II TIP mispredictions were investigated. The first area examined was the TGBLA calculation of the power-to-TIP conversion factor. Many lattice physics codes, such as LATTICE, place a small amount of U-235 in the narrow gap corner. This allows the microscopic fission cross section for the detector to be evaluated based on a neutron spectrum similar to that of the detector location. However, an investigation showed that TGBLA uses the assembly averaged U-235 microscopic fission cross section to calculate the detector fission rate used in the power-to-TIP calculation.

The neutron energy spectrum in the detector locations tends to be constant through operation due to the non-boiling exchannel water. Therefore, this approximation causes the power-to-TIP conversion factor to be sensitive to the assembly moderator density and control state.

In particular, the in-channel neutron energy spectrum is hardened significantly at low moderator densities. From zero void fraction to 80% void fraction conditions, the assembly microscopic fission cross section can vary by as much as a factor of three. The assembly control state has a lesser effect on the assembly averaged spectrum and fission cross section.

The neutron energy spectrum is generally thermal at the detector location. Therefore, the assembly averaged detector fission cross section is only a good estimate of the detector fission cross section when the in-channel moderator density is high. At low moderator densities the actual detector fission cross section is underestimated. The simulated TIP readings are directly proportional to the detector microscopic fission cross section. Thus, the TIP readings of nodes located in the upper core, which is characterized by a low moderator density, are underestimated. Since the simulated TIP distribution is normalized, this causes the simulated TIP readings in the core bottom to be overestimated. This is consistent with the general trend of CORE-II over-predicting the bottom axial TIP peak.

The problem with the power-to-TIP conversion factor from TGBLA prompted the use of LATTICE equivalent factors to be used as input to CORE-II. The results are shown in the last two columns of Table 6-1. The average standard deviation of the percent differences for nodal and integrated comparisons are 5.51% and 10.76% respectively. Although the use of selected LATTICE data in a TGBLA lattice physics library is not consistent, these results show that improvements are possible by redefining the power-to-TIP conversion factor.

The second area examined as part of the TIP mispredictions involved the possibility of control rod pattern effects on the power-to-TIP conversion factors. The method described in section 2.6 for the calculation of simulated TIP readings shows that the power-to-TIP conversion factors of the four surrounding nodes are weighted by nodal power. No other weighting is applied in determining the composite TIP reading. Due to the infinite lattice assumption inherent in the lattice physics calculations, the power-to-TIP conversion factors for controlled nodes are determined based on the four assemblies surrounding the TIP detector being controlled. Under these conditions, a large flux gradient away from the control rods and toward the detector is produced. Since the power-to-TIP conversion factors are directly proportional to the flux at the detector location, they are over estimated for nodes in TIP cells that have less than four controlled nodes. The converse is true for uncontrolled nodes, the TIP readings are underestimated if any of the four control rods are inserted.

The TIP mispredictions during cycle 1 and early in cycle 2 are consistent with this reasoning. These operation periods were characterized by relatively large control rod inventories.

Individual axial TIP reading plots are contained in Appendix B. These plots show that the TIP readings in controlled zones are generally over predicted. To estimate the magnitude of this problem, an auxiliary program was written to calculate the TIP readings independent of CORE-II. The results confirmed that the TIP readings in controlled nodes were being over predicted. Considering only TIP cells

with a surrounding control rod inserted, the largest assembly TIP reading used to determine the four assembly composite TIP reading was from controlled nodes with a frequency of 80% averaged over all 28 TIP sets. Although the power-to-TIP conversion factor is expected to be higher for controlled nodes due to the large flux tilt away from the control rod, the relatively low power of the controlled nodes should compensate this, resulting in less contribution to the composite TIP reading relative to uncontrolled nodes.

The control rod pattern effects were quantified by empirically weighting the four nodal TIP readings to improve agreement with the measured TIP readings. The results showed that a 1% to 2% reduction in the standard deviation of the percent differences could be realized if the control rod pattern dependence of the power-to-TIP factor was accounted for.

Suggestions for future work to improve the TIP reading predictions are discussed in discussed in section 8.

7.0 GAMMA SCAN COMPARISONS

7.1 Overview

The most accurate data available for verification of calculated power distributions are from La-140 gamma scan measurements. La-140 gamma scanning can measure the power history of individual fuel segments and is therefore more detailed than TIP measurements. In addition, the uncertainty in gamma scan measurements is significantly less than TIP measurements.

Gamma scan projects were performed at Quad Cities-1 following operation of cycles 1 and 2. These measurements provide detailed power distribution data for a large number of assemblies. Measured gamma intensity data for selected assemblies from end-of-cycle 1 and 2 are contained in References 9 and 10 respectively. This section contains comparisons of calculated results with measured gamma scan data to quantify the accuracy of predicted power distributions. Since the gamma scan comparisons are more definitive than TIP comparisons in verifying power distribution calculations, the calculated results are examined in more detail.

7.2 La-140 Gamma Scan Technique

The La-140 gamma scan technique involves scanning the La-140 gamma activity at the four corners of selected irradiated assemblies and averaging the results at each level. The gamma emitted during the beta decay of La-140 is chosen for power distribution gamma scan measurements for four reasons: (1) La-140 and its parent isotope Ba-140

have relatively short half lives, (2) Ba-140 has a high fission yield (6.29%) from U-235 fissions, (3) within several weeks following shutdown, La-140 is the most prominent gamma emitting isotope in fuel, and (4) the La-140 gamma peak is relatively isolated from other peaks. Since the half lives of La-140 and Ba-140 are relatively short, the Ba-140 concentration distribution is representative of the integrated power distribution over approximately the last 1-2 months prior to shutdown. Alternatively, isotopes with relatively long half lives can be used in exposure distribution measurements.

The Ba-140 nuclide beta decays to La-140 with a half life of 12.79 days. The La-140 nuclide then beta decays to Cs-140 with a half life of 40.23 hours and emits a high energy gamma ray of 1.596 MeV. After approximately 10 to 15 days following shutdown, a transient equilibrium decay scheme is established between Ba-140 and La-140 as a result of the differences in half lives. During transient equilibrium, the decay rate of La-140 is determined by the half-life of Ba-140 and is proportional to the Ba-140 concentration. Therefore, the measured relative La-140 activity can be compared to the calculated relative Ba-140 concentration. A calculation of the actual La-140 concentration is not required for this comparison. Figures 7-1 and 7-2 illustrate the Ba-140 decay chain and relative Ba-140 importance versus time following shutdown, respectively.

Since the end-of-cycle Ba-140 concentration distribution is dependent on the power distribution during the last 1 to 2 months of operation, the calculated end-of-cycle power shape can not be used to

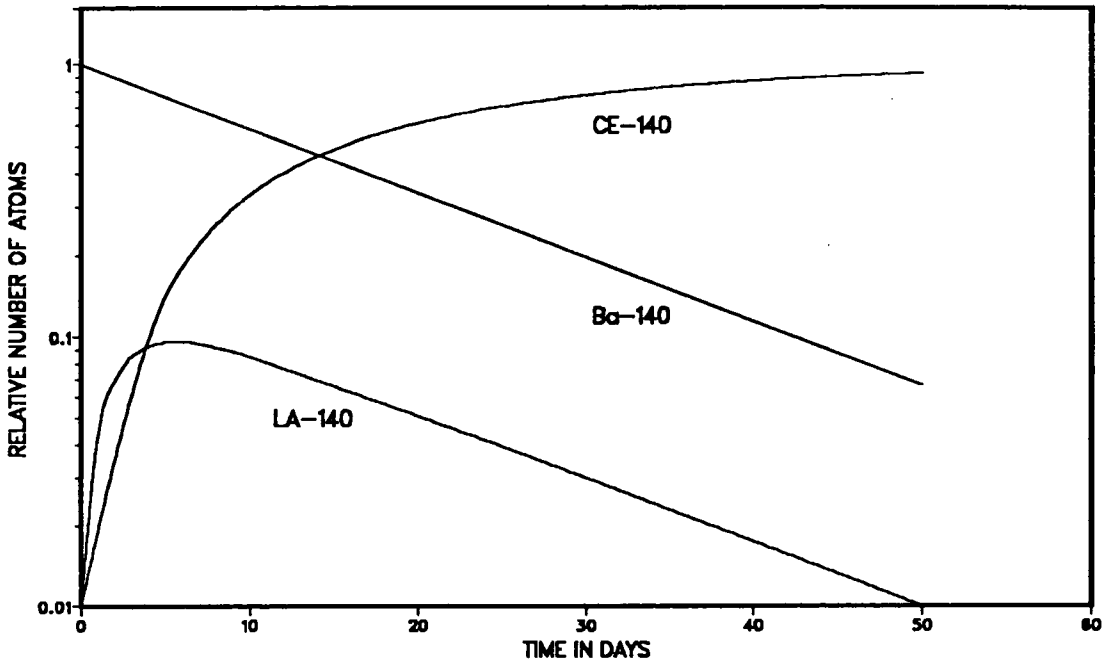

Figure 7-1. Decay of Radioactive Ba-140

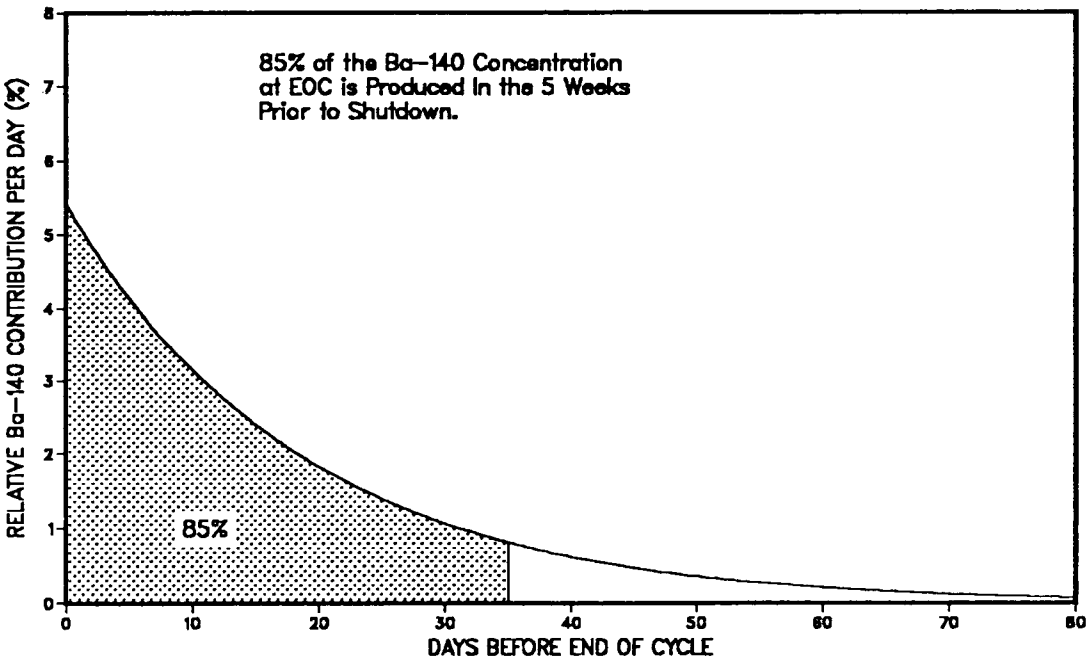

Figure 7-2. Relative Ba-140 Importance Versus Shutdown Time

calculate the end-of-cycle Ba-140 distribution. The nodal Ba-140 concentrations must be tracked with the core simulator over the final few months of operation. This incorporates the production and decay of Ba-140 during periods when the power shape changes. The decay rate equation for La-140 can be used to calculate the amount of time the Ba-140 concentrations should be tracked. The relative Ba-140 importance versus shutdown time is plotted in Figure 7-2. This figure shows that 85% of the end-of-cycle Ba-140 is generated within the last 35 days of operation.

The Ba-140 tracking for Quad Cities was performed during the depletion calculations by first setting the Ba-140 distribution to equilibrium concentrations approximately three months prior to shutdown. This three month lead time ensured that the end-of-cycle Ba-140 was correctly accounted for. The nodal Ba-140 concentrations were then tracked to the end-of-cycle based on the calculated power distribution for each depletion step and the time associated with each step.

7.3 End-of-Cycle 1 Gamma Scan

The Quad Cities-1 end-of-cycle 1 gamma scan project involved 31 assemblies distributed in groups of 3-4 neighboring assemblies from each octant of the core. Figure 7-3 shows the locations of assemblies selected for scanning. The reactor was operated with a sizable control rod inventory during the last few months prior to shutdown. Fourteen of the scanned bundles were operated during the last month with

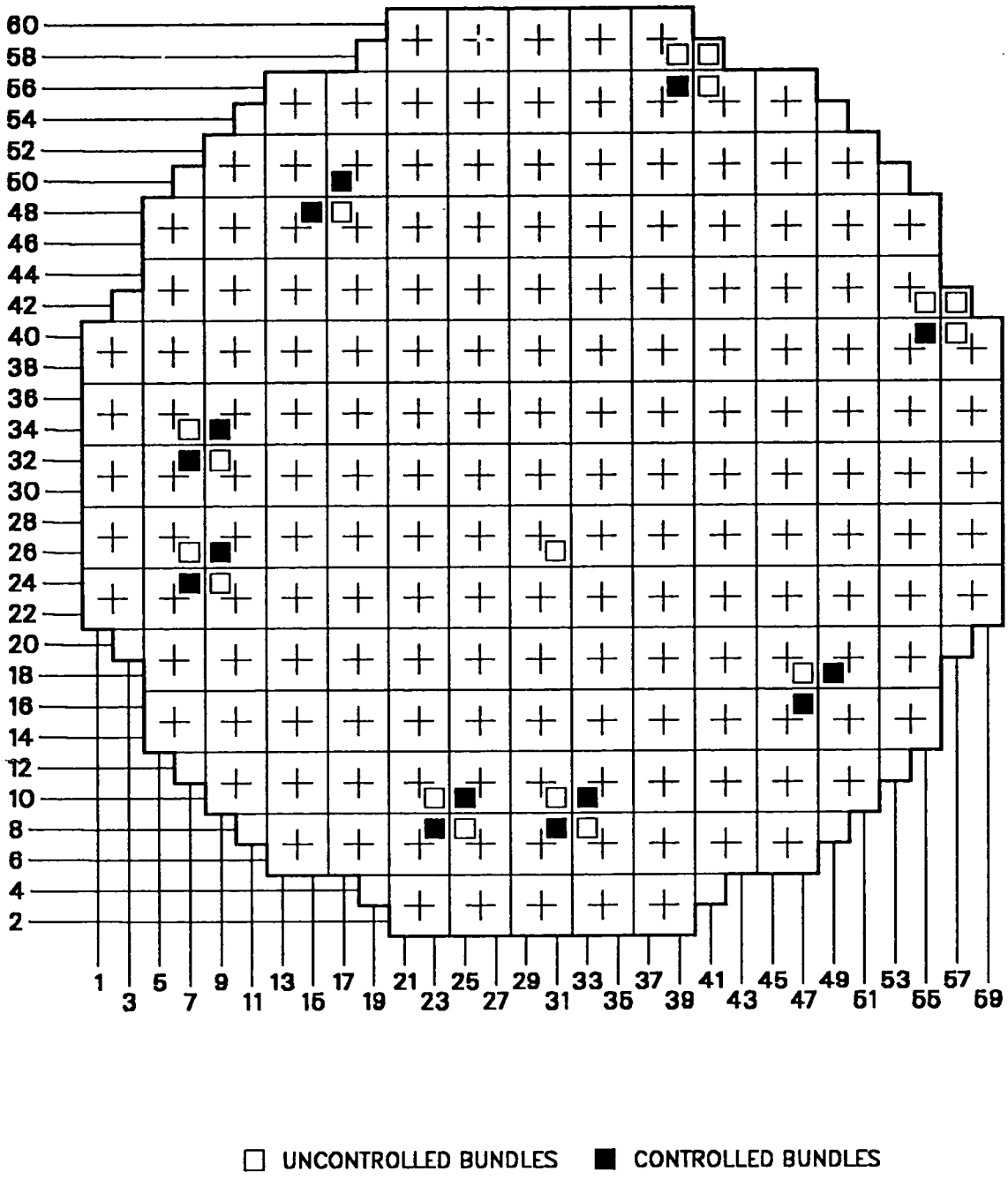

Figure 7-3. Bundles Selected for La-140 Gamma Scan Following Cycle 1

adjacent control rods partially inserted while the remaining assemblies were operated uncontrolled. The operating conditions were held nearly constant during the final months of operation to generate a consistent integrated Ba-140 distribution. Data from this gamma scan project are used to verify CORE-II's capability to predict axial peaking factors and axial power shapes. Radial comparison are not possible due to instrument calibration only being performed between readings of symmetric assemblies.

Axial comparisons. The 31 bundle averaged calculated and measured Ba-140 axial distributions are shown in Figure 7-4. Both calculated and measured data were normalized such that the average is 1.0. The axial shapes are in excellent agreement. Figures 7-5 and 7-6 show typical uncontrolled and partially controlled assembly La-140 distributions respectively. The overall agreement between the measured and calculated distributions is good for both assemblies, with CORE-II overpredicting the nodal Ba-140 concentration above the partially inserted control rod in Figure 7-6. The measured data for Figures 7-4 thru 7-6 were only available in graphical form in Reference 9. Therefore, no statistics are reported for these comparisons.

Accurate predictions of peaking factors are vital in performing reload core design analyses. This aspect of the power distribution calculation was examined by comparing calculated axial peaking factors for each of the 31 scanned bundles with the measured values tabulated in Reference 9.

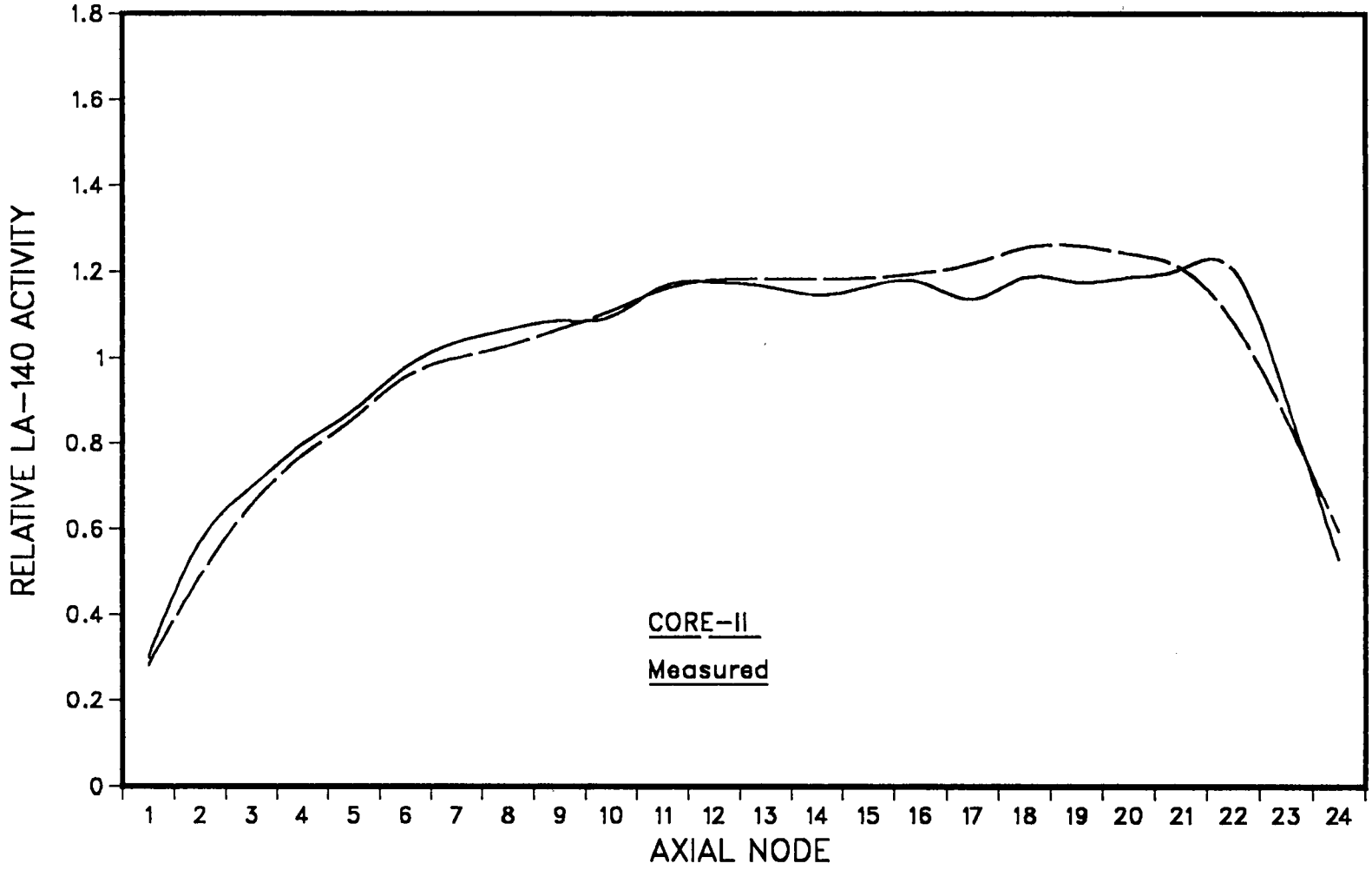

Figure 7-4. Thirty-one Assembly-Averaged Axial La-140 Distribution from End-of-Cycle 1 Gamma Scan

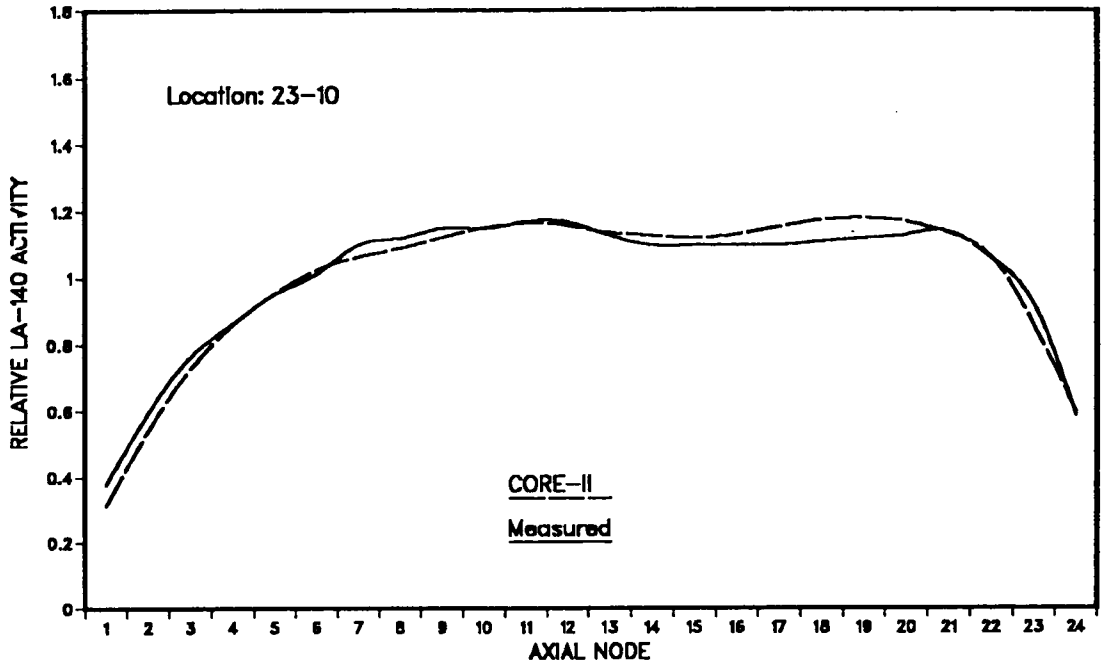

Figure 7-5. Axial La-140 Distribution of an Uncontrolled Assembly from End-of-Cycle 1 Gamma Scan

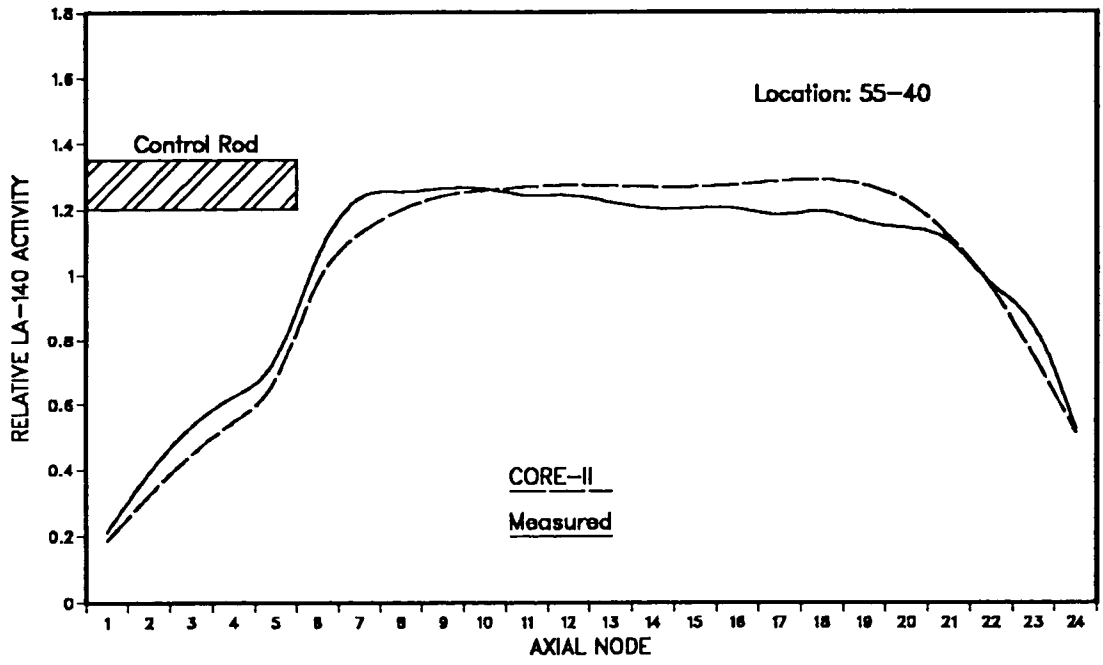

Figure 7-6. Axial La-140 Distribution of a Controlled Assembly from End-of-Cycle 1 Gamma Scan

This comparison measures CORE-II's ability to predict assembly axial power shapes, since any radial calculational bias is removed in the determination of these values. Table 7-1 summarizes the axial peaking factor comparison. The percent differences are calculated as:

$$\%\Delta = \left[\frac{(C - M)}{(C + M)/2}\right] 100 \qquad (7\text{-}1)$$

where

$\%\Delta$ = measured versus calculated peak-to-average percent difference,

M = measured peak-to-average ratio

C = calculated peak-to-average ratio.

For all 31 scanned bundles, CORE-II overpredicted the assembly axial peaking factor by an average of 3.10% with a standard deviation of 2.66%. CORE-II's ability to predict the large flux gradients associated with control blade insertions is demonstrated by considering only the fourteen controlled assemblies. For this comparison, CORE-II overestimated the assembly axial peaking factor by an average of 3.54% with a standard deviation of 2.56%. CORE-II also overpredicted the assembly axial peaking factor for the seventeen uncontrolled bundles by an average difference of 2.74% with a standard deviation of 2.76%. Examination of the results from CORE in Table 7-1 shows that the average CORE-II percent difference for each comparison is improved, with the standard deviations being nearly the same.

Table 7-1

Axial Peaking Factor Comparison from
End-of-Cycle 1 Gamma Scan

Rod Notch	Location IX-JY	Measured Peak/Ave	LATTICE/ CORE Peak/Ave	TGBLA/ COREII Peak/Ave	Percent Difference LATTICE/ CORE	Percent Difference TGBLA/ COREII
48	39-58	1.2712	1.3210	1.2663	3.84	-0.39
48	41-58	1.2125	1.3035	1.2208	7.23	0.68
48	41-56	1.2236	1.2594	1.2178	2.88	-0.47
48	17-48	1.2870	1.3288	1.3259	3.20	2.98
48	55-42	1.1854	1.2579	1.2694	5.93	6.85
48	57-42	1.1913	1.2992	1.2580	8.66	5.45
48	57-40	1.2452	1.3154	1.2552	5.48	0.80
48	7-34	1.1763	1.2096	1.2476	2.79	5.88
48	9-32	1.1476	1.1944	1.2101	4.00	5.31
48	7-26	1.1696	1.1958	1.2336	2.22	5.33
48	9-24	1.1859	1.2338	1.2424	3.96	4.66
48	31-26	1.3543	1.3765	1.4318	1.63	5.56
48	47-18	1.2498	1.3135	1.2939	4.97	3.47
48	23-10	1.1784	1.2013	1.1786	1.92	0.02
48	25- 8	1.2390	1.2286	1.2146	-0.84	-1.99
48	31-10	1.1718	1.1935	1.1888	1.83	1.44
48	33- 8	1.2212	1.2553	1.2335	2.75	1.00
38	39-56	1.2815	1.3353	1.2755	4.11	-0.47
14	17-50	1.6087	1.7427	1.7043	8.00	5.77
38	15-48	1.2800	1.3285	1.3386	3.72	4.48
38	55-40	1.2688	1.3316	1.2889	4.83	1.57
8	9-34	1.4180	1.5151	1.4876	6.62	4.79
28	7-32	1.3225	1.4142	1.3583	6.70	2.67
8	9-26	1.3660	1.5130	1.4865	-0.21	8.45
38	7-24	1.2313	1.2803	1.2637	3.90	2.60
14	49-18	1.6017	1.7366	1.6911	8.08	5.43
38	47-16	1.2829	1.3161	1.3175	2.55	2.66
8	25-10	1.3579	1.4936	1.4394	9.52	5.82
38	23- 8	1.2512	1.2814	1.2424	2.38	-0.71
8	33-10	1.3851	1.5044	1.4523	8.26	4.74
28	31- 8	1.3693	1.4366	1.3935	4.80	1.75
All 31 Bundles			Average		4.71	3.10
			Standard Dev		2.64	2.66
17 Uncontrolled Bundles			Average		3.67	2.74
			Standard Dev		2.28	2.76
14 Controlled Bundles			Average		5.98	3.54
			Standard Dev		2.56	2.56

7.4 End-of-Cycle 2 Gamma Scan

Following the completion of Quad Cities-1 cycle 2 operation, an extensive gamma scan project was performed which provides detailed benchmark data for 89 fuel assemblies. The measurements provide an excellent measure of several aspects of CORE-II's power distribution calculations. Axial, radial, and core wide measured versus calculated comparisons are made. Relative to the end-of-cycle 1 gamma scan project, the end-of-cycle 2 gamma scan included larger exposure gradients and a variety of different fuel types. This provides an opportunity to access power distribution calculations under more typical core conditions.

The scanned bundles encompassed nearly a complete octant of the core and 12 additional symmetric locations. Figure 7-7 shows the locations of the 89 assemblies selected for scanning. Measurements were made at 12 axial levels for 73 assemblies and 24 axial levels for the remaining 16 assemblies. The reactor was operated with constant operating conditions and all control rods withdrawn for the final two months of operation, producing a consistent Ba-140 distribution. A measurement uncertainty of 3.0% was estimated in Reference 10 by periodic rescanning of the same fuel assembly.

Axial comparisons. Figure 7-8 shows the 89 assembly averaged axial distributions of measured and calculated values. The calculated results are in excellent agreement, with the maximum value calculated by CORE-II 2.42% higher than measured. For the axial distribution,

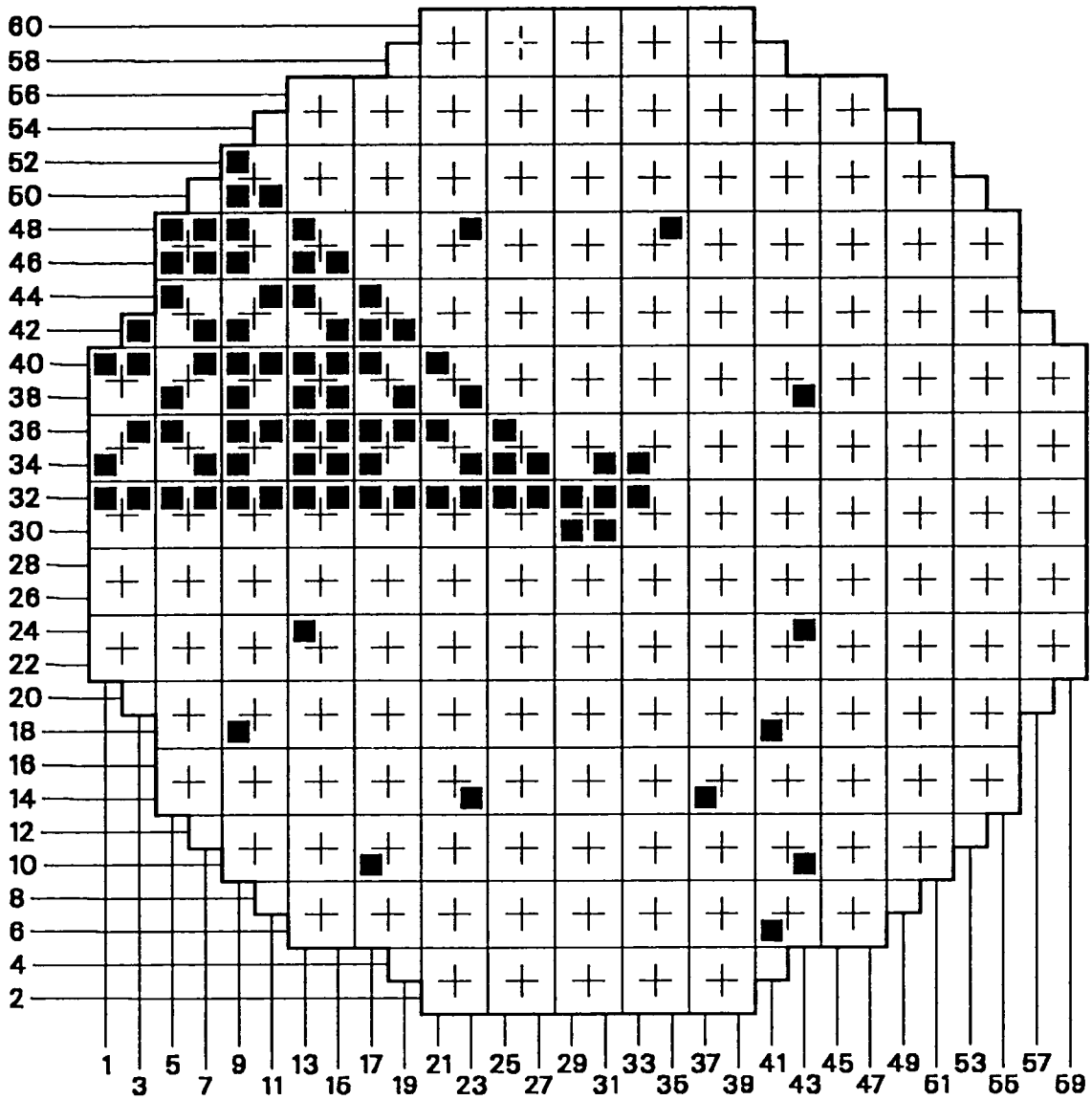

Figure 7-7. Bundles Selected for La-140 Gamma Scan Following Cycle 2

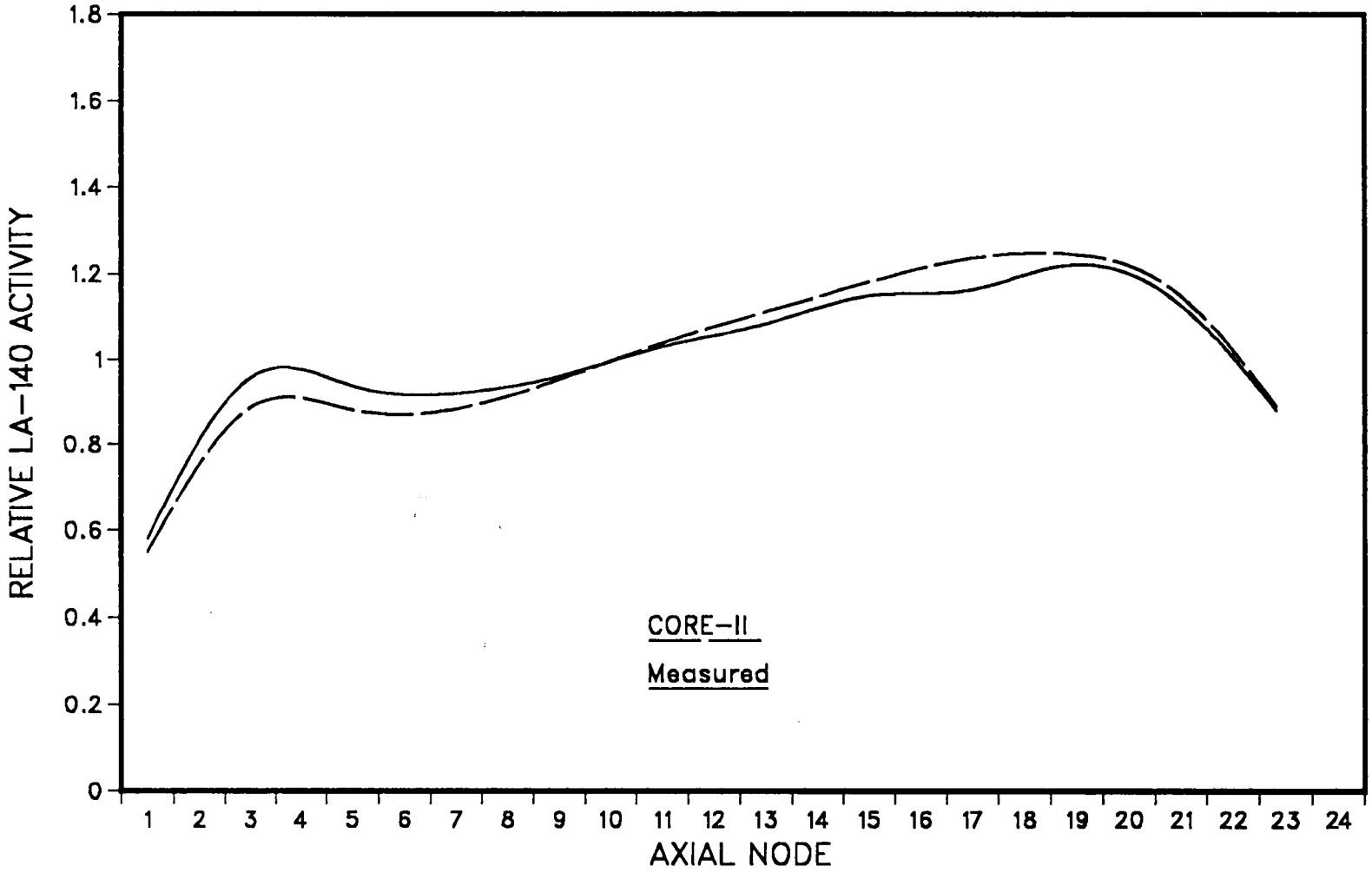

Figure 7-8. Eighty-nine Assembly Average Axial La-140 Distribution from End-of-Cycle 2 Gamma Scan

CORE-II overestimated the Ba-140 concentration by an average of 1.18% with a standard deviation 4.63%. The individual assembly axial distribution comparisons are similar to the 89 assembly average, as shown in Figures 7-9 through 7-12 for typical assemblies.

Figure 7-13 is an eighth core map showing measured versus calculated individual assembly axial peaking factors for 71 assemblies within the octant that was scanned. Results for the 18 assemblies not shown on this figure are similar to their symmetric pairs. This type of comparison evaluates CORE-II's ability to predict assembly axial power shapes since any radial calculational bias is removed. The results show that CORE-II over predicted the axial peaking factors for all 89 assemblies by an average of 2.40% with a standard deviation of 1.64%. This result is more consistent relative to the average difference of 1.47% with a standard deviation of 1.89% from LATTICE/CORE calculations. The over prediction of assembly axial peaking factors is consistent with the over prediction for the end-of-cycle 1 comparisons. The lower average percent difference for the end-of-cycle 2 comparison may be explained by the absence of control rods, which yields smoother assembly power shapes.

Radial comparisons. CORE-II's ability to predict assembly powers is demonstrated in Figure 7-14. This figure compares the relative radial values by averaging the nodal values at the measured locations in each assembly. The TGBLA/CORE-II standard deviation of the differences is 2.79%, which is more consistent then the corresponding LATTICE/CORE standard deviation of 3.82%. The most notable difference

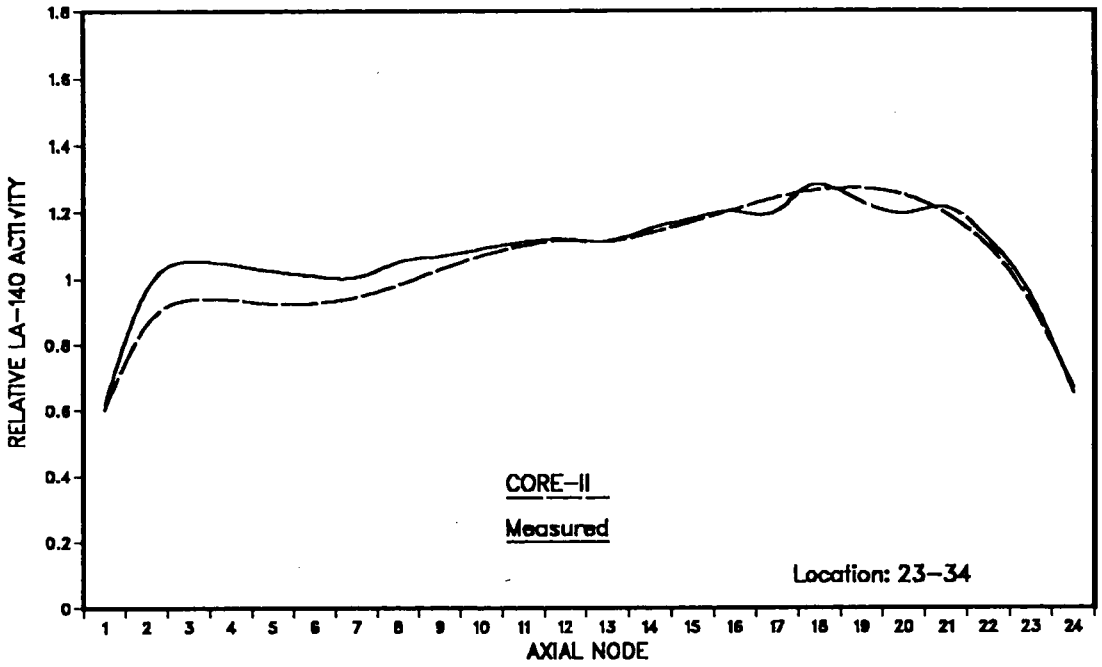

Figure 7-9. Axial La-140 Distribution for an Initial Core 7x7 UO2 Central Assembly from End-of-Cycle 2 Gamma Scan

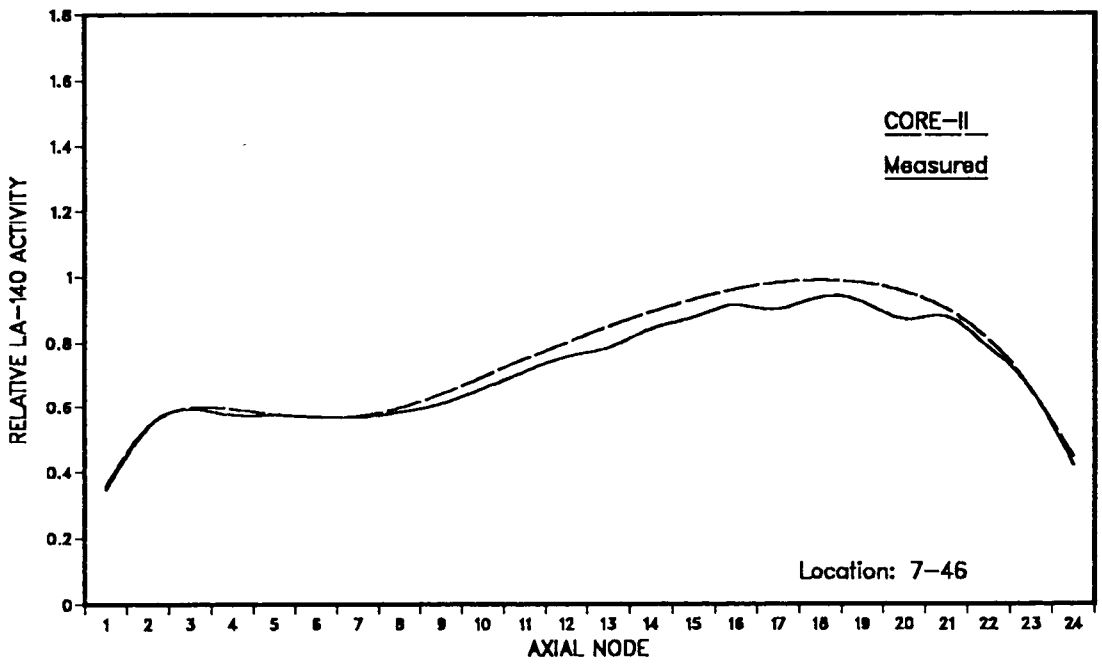

Figure 7-10. Axial La-140 Distribution for an Initial Core 7x7 UO2 Peripheral Assembly from End-of-Cycle 2 Gamma Scan

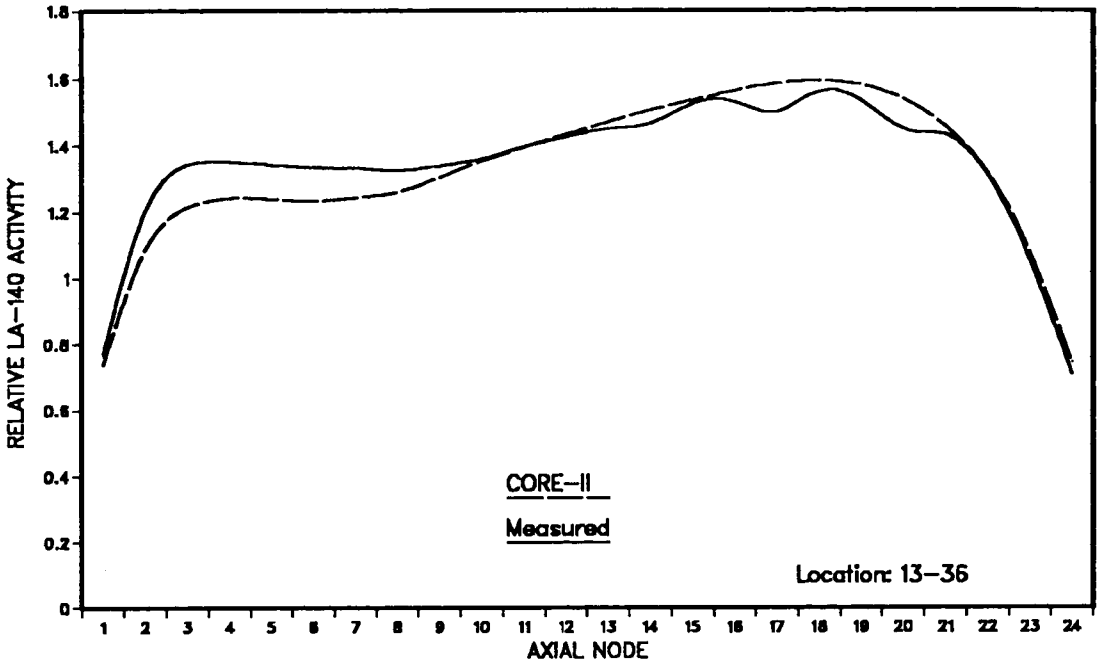

Figure 7-11 Axial La-140 Distribution for a Reload 8x8 UO2 Assembly from End-of-Cycle 2 Gamma Scan

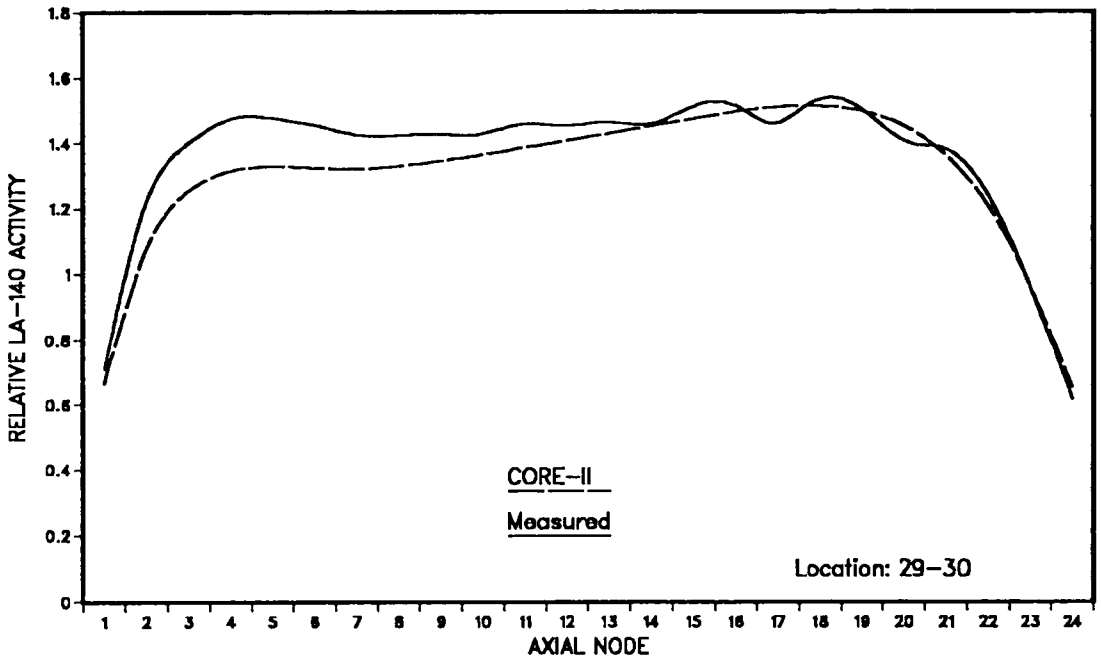

Figure 7-12. Axial La-140 Distribution for a Reload 7x7 Mixed Oxide Assembly from End-of-Cycle 2 Gamma Scan

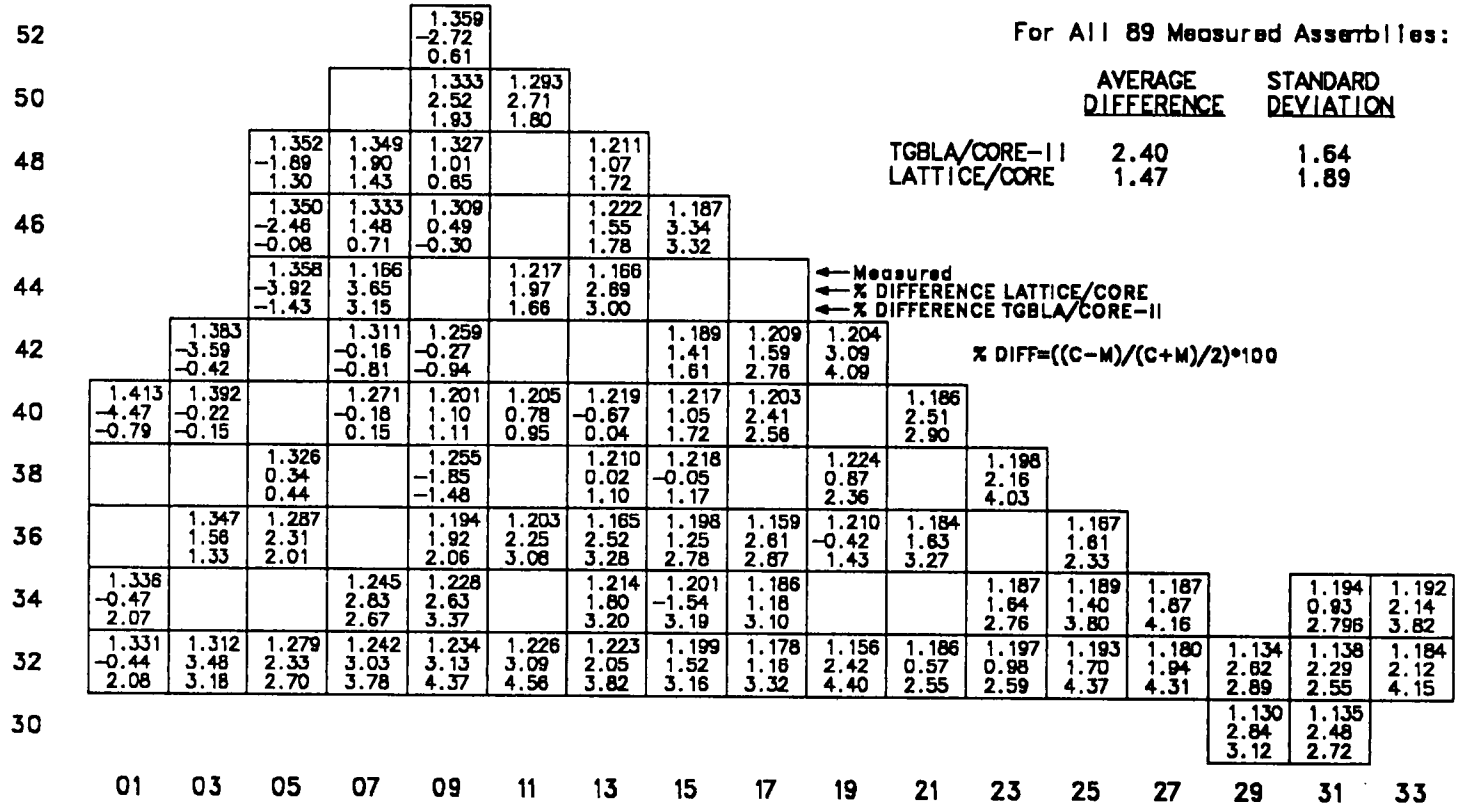

Figure 7-13. Assembly La-140 Activity Axial Peaking Factor from End-of-Cycle 2 Gamma Scan

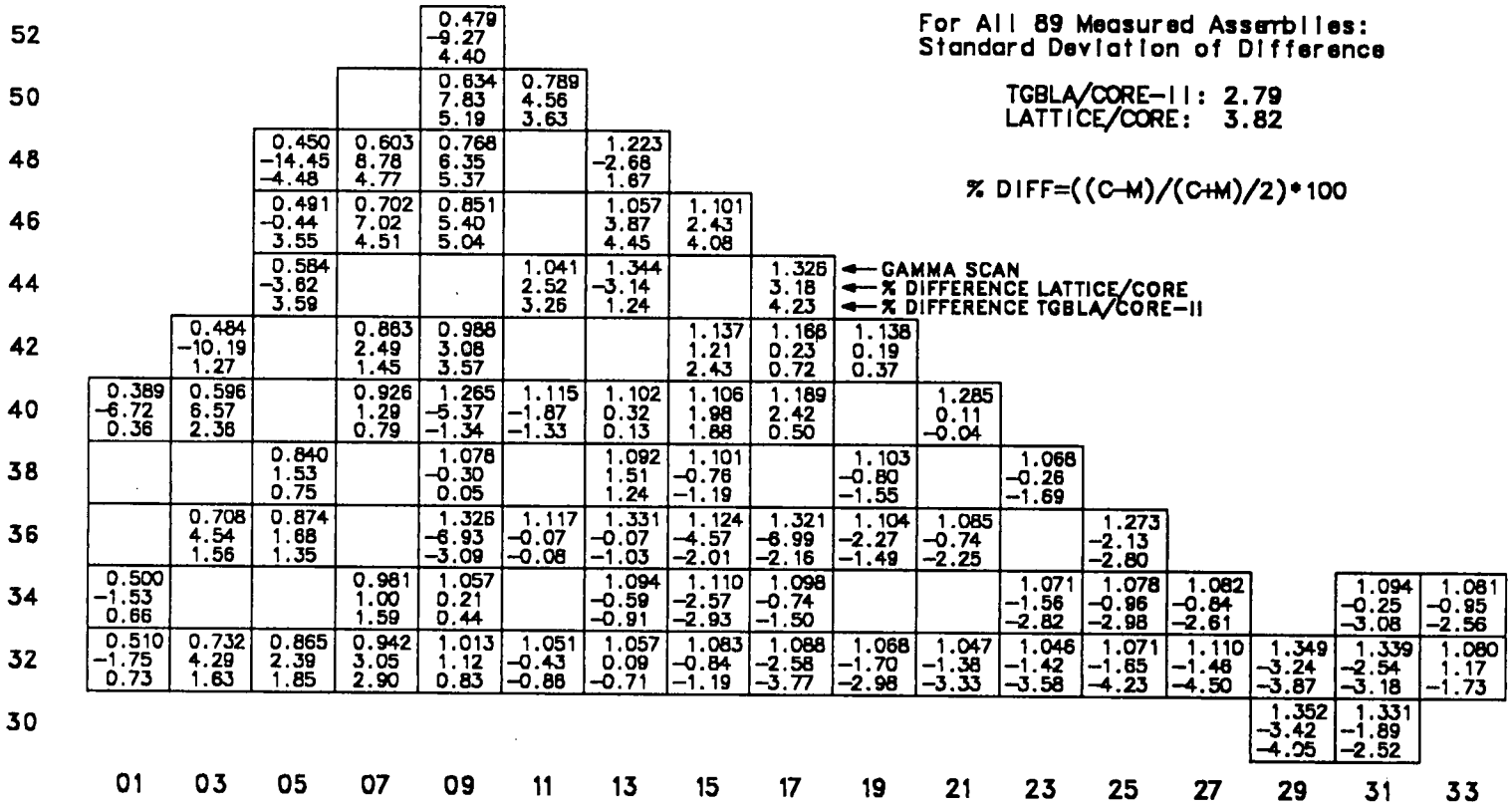

Figure 7-14. Assembly Average Radial La-140 Distribution from End-of-Cycle 2 Gamma Scan

between the two methods is the improved CORE-II results for peripheral assemblies. This improvement in the radial comparison can be primarily attributed to CORE-II's treatment of the flux gradients near the reactor core periphery. While CORE-II errors have been increased (relative to CORE results) within the high power regions, the magnitude is not significant and is well within the bounds of the uncertainty of the calculation and the 3% error associated with the measuring technique.

A radial comparison with any axial bias removed is presented in Table 7-2. This table compares the standard deviation of the nodal differences for the 89 assemblies at each measured axial level. Measured and calculated nodal values were normalized to 1.0 at each level prior to comparison. The average of the planar standard deviations is 3.68% with a standard deviation of 1.01%. Results in Table 7-2 from the CORE code show that the CORE-II results are improved at each axial level, particularly in the lower levels. The CORE-II results show a trend of improved radial errors with increased core height. This suggests a dependence of the radial power distribution on the moderator density. Axial shapes for the interior assemblies shown in Figures 7-9, 7-10, and 7-11 also show that the CORE-II errors increase in the bottom of the core.

The improved CORE-II results for the planar comparisons are consistent with the assembly power comparisons. This is further evidence of the improved treatment by CORE-II of the boundary flux gradients.

Table 7-2

Nodal Standard Deviation for the 12 Axial Planes from End-of-Cycle 2 Gamma Scan

Axial Plane		Percent Planar Standard Deviation LATTICE/ CORE	TGBLA/ COREII
23	.... (Top)	5.61	3.03
21	.....	4.04	2.64
19	.....	3.41	2.62
17	.....	3.79	2.62
15	.....	4.09	3.29
13	.....	4.19	3.31
11	.....	4.15	3.43
9	.....	4.51	3.69
7	.....	4.60	4.18
5	.....	5.30	4.57
3	.....	6.59	5.19
1	... (Bottom) ...	7.96	5.64
	Average	4.85	3.68
	Standard Dev	1.31	1.01

For each axial plane, the 89 measured and calculated nodal values are normalized to an average of 1.0.

Core wide comparisons. An overall improvement in the TGBLA/CORE-II calculated Ba-140 distribution is demonstrated by comparing the measured versus calculated values for all measured nodes. The standard deviation of the nodal differences is 5.45% for the TGBLA/CORE-II calculations, which is significantly less than the corresponding value of 10.72% for LATTICE/CORE results.

8.0 SUMMARY AND CONCLUSIONS

8.1 Summary

The capability of the TGBLA/CORE-II reactor physics methods to predict core behavior was evaluated by modeling the Quad Cities-1 reactor through cycle 2 and comparing calculated results with measured benchmark data. The results were compared to previous calculations made using the LATTICE/CORE reactor physics methods for the same Quad Cities benchmarks. These comparisons identified areas which are improved and other areas in which further refinements are warranted. This section contains a summary of the results.

The prediction of reactivity under hot operating conditions was evaluated by calculating the k-effective value at each of the 29 exposure points in the core depletion calculations. The results verified that CORE-II accurately predicts core reactivity through a reactor cycle. The average k-effective from cycles 1 and 2 was 1.00805 $\pm$ 0.00173 and 1.00533 $\pm$ 0.00199 respectively. The CORE-II k-effectives showed less variation with core exposure than the corresponding CORE values. This was particularly evident in the k-effective response during cycle 2.

Predictions of cold zero power reactivity were investigated by modeling 14 in-sequence startup criticals and 32 local critical experiments. For the 14 in-sequence criticals performed during cycles 1 and 2 CORE-II calculated an average k-effective of 1.00193 $\pm$ 0.00503. A larger variation in the CORE-II k-effectives relative to CORE results was due primary to an over prediction of low exposure in-sequence

criticals, resulting in a stronger trend of decreasing bias with increased exposure.

Results from the 32 local criticals demonstrated that CORE-II accurately calculates reactivity under conditions consistent with the stuck rod shutdown margin core configuration. For all 32 criticals performed during cycle 1, the average CORE-II k-effective was 1.00257 $\pm$ 0.00245. A comparison of calculations for similar zero exposure local criticals showed that CORE-II k-effectives were slightly more consistent than CORE calculated k-effectives.

Comparisons of in-sequence versus local critical k-effectives were performed to determine the bias associated with in-sequence shutdown margin demonstrations. The difference in k-effective between in-sequence and local criticals at zero exposure was 0.00328. This value is significantly higher than the k-effective difference of 0.0009 from similar CORE comparisons. The in-sequence versus local critical k-effective differences of 0.00156 at 3.748 GWd/MT and 0.00125 at 6.911 GWd/MT were very reasonable and indicate that a solution to the poor result at zero exposure is possible.

The ability of CORE-II to predict power distributions during high power reactor operation was investigated by comparing simulated TIP readings with 28 measured TIP sets. Over both cycles, the CORE-II simulated TIP comparison statistics were comparable to corresponding CORE results. The standard deviation of differences between measured and calculated nodal and integrated TIP readings were approximately the same as symmetric measured readings. However, the differences in simulated TIP readings increased during cycle 1 and early in cycle 2.

An investigation of the power-to-TIP conversion factor calculation suggests that improvements in the simulated TIP readings are possible. The possibility for improved TIP readings is further supported by the improved gamma scan results discussed below.

A more detailed evaluation of the power distribution calculations was performed by comparing calculated end-of-cycle Ba-140 distributions with end-of-cycles 1 and 2 measured La-140 activities. The end-of-cycle 1 comparison showed that the assembly axial peaking factors were over predicted by 3.10 $\pm$ 2.66%. The corresponding end-of-cycle 2 peak-to-average values were similarly over predicted by an average of 2.40 $\pm$ 1.64%. Results from both gamma scans were comparable to previous CORE results and to the 3% measurement uncertainty. For both gamma scan projects, the average and individual assembly relative Ba-140 distributions agreed well with the measured data.

Additional comparisons were performed with the end-of-cycle 2 gamma scan data. A comparison of the radial distributions showed that CORE-II predicted the assembly averaged values with a standard deviation of 2.79%. Another radial comparison performed by normalizing nodal values at each axial level to 1.0 showed that CORE-II predicted the relative values with a standard deviation of 3.68%. Finally, the overall improvement in CORE-II results was demonstrated by considering the standard deviation of differences in measured and calculated relative values for all available nodal activities. CORE-II predicted the nodal activities with a standard deviation of 5.45%, while previous calculations using CORE had a standard deviation of 10.72%.

8.2 Future Work

Based on the Quad Cities benchmark calculations, investigations beyond the scope of this thesis can be suggested to improve the TGBLA/CORE-II reactor physics methods. As discussed in previous sections, the results from the cold critical comparisons and simulated TIP readings were less accurate than desired. This section contains a discussion of possible investigations which would provide insight into these problems. In addition, a brief description of benchmark data available from Quad Cities-1 cycles 3 and 4 is presented. Comparisons with measured data from these cycles would be beneficial in the overall methodology qualification effort.

Cold criticals. The in-sequence critical results at low core exposures had a relatively large positive calculational bias. This resulted in a strong trend of decreasing k-effective with increased core exposure. The local critical results at zero exposure did not exhibit the same bias and the difference between in-sequence and local critical k-effectives was large. The reason for this result is not clear without further investigation.

The QUANDRY neutronic algorithm incorporated in CORE-II has been successfully tested using one and two-dimensional benchmark problems with large flux gradients. This suggests that the flux gradients produced in the local criticals are being modeled correctly. Given this, the core simulator input is suspect. Examination of TGBLA predictions of k-infinity, control rod worths, gadolinium worth, and xenon worth at low exposures may provide some insight. Errors in these

variables may be amplified in the in-sequence critical calculations due to the flux being spread over a larger core area.

The possibility of a control rod pattern effect on the assembly discontinuity factors should also be investigated. The large flux gradients produced in the local criticals may cause the infinite lattice assumption used to determine these factors to break down. This effect is present, to a lesser degree in the in-sequence criticals due to the highly controlled control rod configurations. Calculations based on a four assembly TIP cell model could be used to determine correction factors as a function of the configuration of the four surrounding control rods.

A more detailed investigation to prove that CORE-II does not have a calculational bias due to large flux gradients could be performed by setting up a large core model with a higher order method such as KENO. Reactivity calculations could then be compared under uniform and gradient flux shapes.

Power-to-TIP conversion. As discussed in section 6.3, the TGBLA detector activation rate for power-to-TIP conversion factor is incorrectly calculated using the assembly averaged U-235 microscopic cross section. The simplest solution to this problem would be to process the power-to-TIP conversion factor external to TGBLA. The power-to-TIP factors could be calculated based on the one group flux at the detector location. Since the neutron energy spectrum at the detector location is relatively constant, a constant microscopic U-235

fission cross section based on a thermal spectrum could be used to calculated the detector reaction rate.

A more involved solution to this problem would be to modify the TGBLA code to include a small amount of U-235 in the detector location. This would allow the fission cross section for the detector to be determined based on the calculated neutron spectrum at the actual detector location.

The power-to-TIP conversion factor may also require a correction for the control rod configuration around the TIP cell. As discussed previously, the infinite lattice calculation assumes that the surrounding assemblies have the same control state. As a result, a large flux gradient toward the detector is produced in the calculation of controlled power-to-TIP conversion factors. The power-to-TIP conversion factor is then over predicted when all the surrounding control rods are not inserted. An investigation using a four assembly TIP cell model to calculate correction factors based on the control rod configuration may improve the simulated TIP readings.

Additional Quad Cities-1 benchmark data. Benchmark data for Quad Cities-1 cycles 3 and 4 have been published which could be used to provide additional verification of the TGBLA/CORE-II physics methods. The incremental work involved in performing these calculations would be small since a significant amount of the model development work was performed during this project. Much of the reload fuel for these cycles is identical to previous fuel. As a result, lattice physics data for only one additional lattice type are required to model

operation through cycle 4. The operating and design data needed to model the operation during cycles 3 and 4 are contained in References 8 and 14 respectively.

The cycle 3 data includes eight TIP sets through the cycle and end-of-cycle gamma scan data for 11 assemblies. This gamma scan project was performed as part of the plutonium recycle program. The results of La-140 activity measurements for the five cycle 2 MOX reloads and six adjacent UO2 assemblies are contained in Reference 15. These data would provide additional verification of the power distribution calculations.

A large gamma scan project similar to the end-of-cycle 2 project was performed following the operation of cycle 4. La-140 gamma activity data are reported in Reference 16 for nearly a complete octant of the core. Comparisons with this gamma scan data would be more applicable to current Browns Ferry cycle designs due to the more typical exposure mismatches and large 8x8 assembly type inventory.

The first detailed measurement of fast and thermal spatial flux shapes in a commercial BWR was also performed at the end-of-cycle 4[17]. This measurement was performed by withdrawing two adjacent control rod in the central region of the core. Two full length axial flux wire assemblies, each containing a nickel and a copper wire, were inserted into the core prior to the critical to obtain a measure of the fast and thermal flux axial distributions at two different radial positions. One flux wire assembly was located adjacent to the two withdrawn control rods and the other was located in the controlled fuel region several bundles away. These measured data would provide an excellent

opportunity to benchmark CORE-II's calculation of flux distributions produced during local criticals.

8.3 Conclusions

Methods less sophisticated than those of TGBLA/CORE-II have been shown to be acceptable in modeling the first two cycles of Quad Cities-1. These cycles were not high energy cycles and therefore less demanding of the physics methods. In this respect, significant improvements relative to the LATTICE/CORE results were not anticipated.

The results of the Quad Cities-1 comparisons indicate that improvements in future Browns Ferry core designs and analyses can be expected using the TGBLA/CORE-II methods. The gamma scan results show a large improvement in power distribution predictions. The exposure dependence of steady-state reactivity also was shown to be improved. The in-sequence and local critical k-effectives at higher exposures were in good agreement. Future work was suggested to resolve problems with cold critical calculations and the calculation of TIP readings.

In conclusion, the successful completion of this project contributed greatly to the methodology development and toward its ultimate qualification for production use.

REFERENCES

REFERENCES

1. B. L. DARNELL, T. D. BEU, and G. W. PERRY, "Methods for the Lattice Physics Analysis of LWR's," TVA-TR78-02-A (1978).

2. S. L. FORKNER, G. H. MERIWETHER, and T. D. BEU, "Three-Dimensional LWR Core Simulator Methods," TVA-TR78-03-A (1979).

3. A. F. ANSARI, R. R. GAY, and B. J. GITNICK, "FIBWR - A Steady-State Core Flow Distribution Code for Boiling Water Reactors," EPRI NP-1923, Electric Power Research Institute (1981).

4. "Steady-State Nuclear Methods," NEDO-30130-A, General Electric Company (1985).

5. S. L. FORKNER, "The CORE-II Version @0487 Input Description," TVA-MDS-803 (1987).

6. K. S. SMITH, "An Analytic Nodal Method for Solving the Two-Group, Multidimensional, Static and Transient Neutron Diffusion Equations," Nuclear Engineering Thesis, Department of Nuclear Engineering, M.I.T., Cambridge, MA (1979).

7. N. H. LARSEN, G. R. PARKOS and O. RAZA, "Core Design and Operating Data for Cycles 1 and 2 of Quad Cities 1," EPRI NP-240, Electric Power Research Institute (1976).

8. N. H. LARSEN, "Core Design and Operating Data for Quad Cities 1 Cycle 3," EPRI NP-552, Electric Power Research Institute (1983).

9. G. R. PARKOS, "BWR Simulator Methods Verification," General Electric Company, NEDO-20946-A (1977).

10. M. B. CUTRONE, G. F. VALBY, "Gamma Scan Measurements at Quad Cities Nuclear Power Station Unit 1 Following Cycle 2," EPRI NP-214, Electric Power Research Institute (1976).

11. M. YAMAMOTO, H. MIZUTA, "Development and Validation of TGBLA BWR Lattice Physics Methods," Topical Meeting on Reactor Physics and Shielding, Chicago, Ill., 364 (1984).

12. M. YAMAMOTO, H. MIZUTA, K. MAKINO, R. T. CHIANG, S. P. CONGDON, "Validation of the TGBLA BWR Bundle Design Methods," Trans. Am. Nucl. Soc., 43, 698 (1982).

13. "Verification of TVA Steady-State BWR Physics Methods," TVA-TR79-01-A (1979).

14. M. R. ALKOWNI, J. T. MA, "Core Design and Operating Data for Quad Cities 1 Cycle 4," NEDC-25490, General Electric Company (1981).

15. D. W. MERTH, "Gamma Scan Measurements at Quad Cities Nuclear Power Station Unit-1 Following Cycle 3," EPRI NP-2302-LD, Electric Power Research Institute (1982).

16. H. D. KOSANKE, "Gamma Scan Measurements at Quad Cities 1 Following Cycle 4,", NEDC-25492, General Electric Company (1981).

17. G. D. GALLOWAY, G. C. MARTIN, R. A. WOLTERS, "Cold Critical Measurement Performed Prior to Cycle-4 Startup of the Quad Cities-1 Reactor," EPRI NP-2303-LD, Electric Power Research Institute (1982).

BIBLIOGRAPHY

BIBLIOGRAPHY

Alkowni, M. R. and J. T. Ma, "Core Design and Operating Data for Quad Cities 1 Cycle 4," NEDC-25490, General Electric Company (1981).

Ansari, A. F., R. R. Gay, and B. J. Gitnick, "FIBWR - A Steady-State Core Flow Distribution Code for Boiling Water Reactors," EPRI NP-1923, Electric Power Research Institute (1981).

Cutrone, M. B. and G. F. Valby, "Gamma Scan Measurements at Quad Cities Nuclear Power Station Unit 1 Following Cycle 2," EPRI NP-214, Electric Power Research Institute (1976).

Darnell, B. L., T. D. Beu, and G. W. Perry, "Methods for the Lattice Physics Analysis of LWR's," TVA-TR78-02-A (1978).

Dyszel, A. and K. C. Knoll, "Qualification of Steady State Core Physics Methods for BWR Design and Analysis," PL-NF-87-001, Pennsylvania Power & Light Company, (1987).

Forkner, S. L., "The CORE-II Version @0487 Input Description," TVA-MDS-803 (1987).

Forkner, S. L., G. H. Meriwether, and T. D. Beu, "Three-Dimensional LWR Core Simulator Methods," TVA-TR78-03-A (1979).

Galloway, G. D., G. C. Martin, and R. A. Wolters, "Cold Critical Measurement Performed Prior to Cycle-4 Startup of the Quad Cities-1 Reactor," EPRI NP-2303-LD, Electric Power Research Institute (1982).

Kosanke, H. D., "Gamma Scan Measurements at Quad Cities 1 Following Cycle 4,", NEDC-25492, General Electric Company (1981).

Larsen, N. H., "Core Design and Operating Data for Quad Cities 1 Cycle 3," EPRI NP-552, Electric Power Research Institute (1983).

Larsen, N. H., G. R. Parkos and O. Raza, "Core Design and Operating Data for Cycles 1 and 2 of Quad Cities 1," EPRI NP-240, Electric Power Research Institute (1976).

Merth, D. W., "Gamma Scan Measurements at Quad Cities Nuclear Power Station Unit-1 Following Cycle 3," EPRI NP-2302-LD, Electric Power Research Institute (1982).

Parkos, G. R., "BWR Simulator Methods Verification," General Electric Company, NEDO-20946-A (1977).

Smith, K. S., "An Analytic Nodal Method for Solving the Two-Group, Multidimensional, Static and Transient Neutron Diffusion Equations," Nuclear Engineering Thesis, Department of Nuclear Engineering, M.I.T., Cambridge, MA (1979).

"Steady-State Nuclear Methods," NEDO-30130-A, General Electric Company (1985).

"Verification of TVA Steady-State BWR Physics Methods," TVA-TR79-01-A (1979).

Yamamoto M.and H. Mizuta, "Development and Validation of TGBLA BWR Lattice Physics Methods," Topical Meeting on Reactor Physics and Shielding, Chicago, Ill., 364 (1984).

Yamamoto, M., H. Mizuta, K. Makino, R. T. Chiang, and S. P. Congdon, "Validation of the TGBLA BWR Bundle Design Methods," Trans. Am. Nucl. Soc., 43, 698 (1982).

APPENDICES

APPENDIX A

IN-SEQUENCE CRITICAL DATA SHEETS

Date: 3/14/72
Core Exposure: 0 MWd/MT
Period: 180 Seconds
Temperature: 152 °F

0 (BLANK): FULL IN
48: FULL OUT

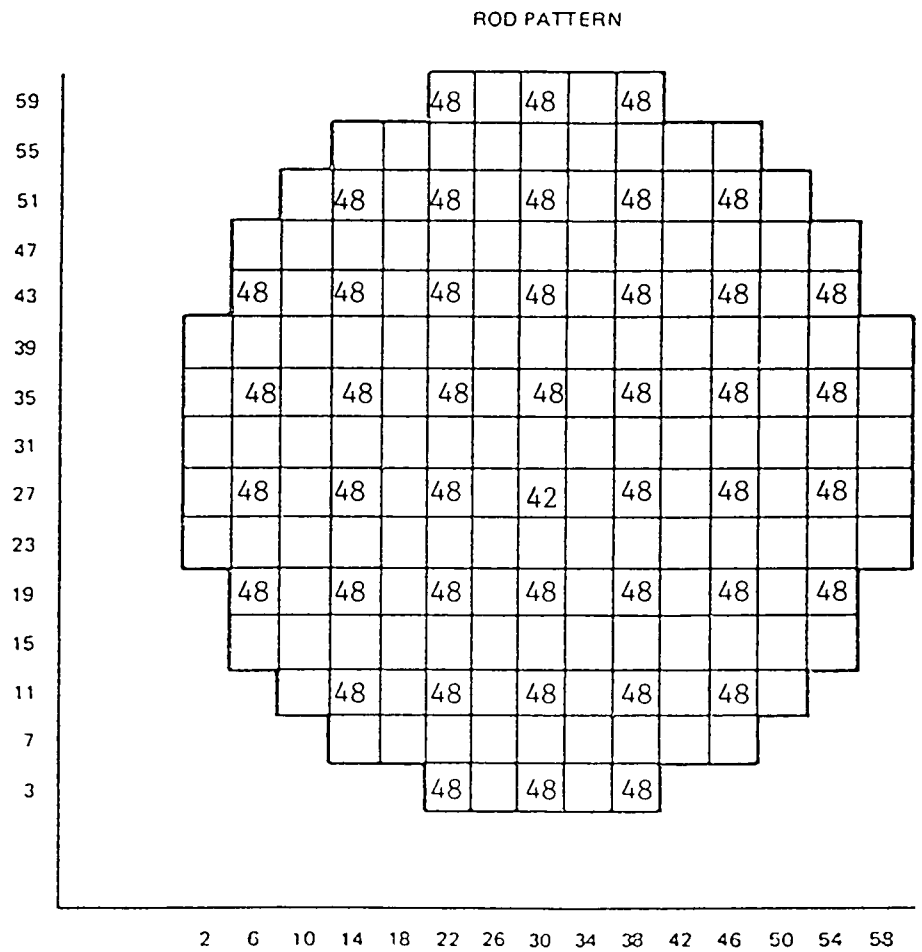

In-Sequence Critical #1 (Cycle 1), March 14, 1972

Date: 3/15/72
Core Exposure: 0 MWd/MT
Period: 160 Seconds
Temperature: 159 °F

0 (BLANK): FULL IN
48: FULL OUT

ROD PATTERN

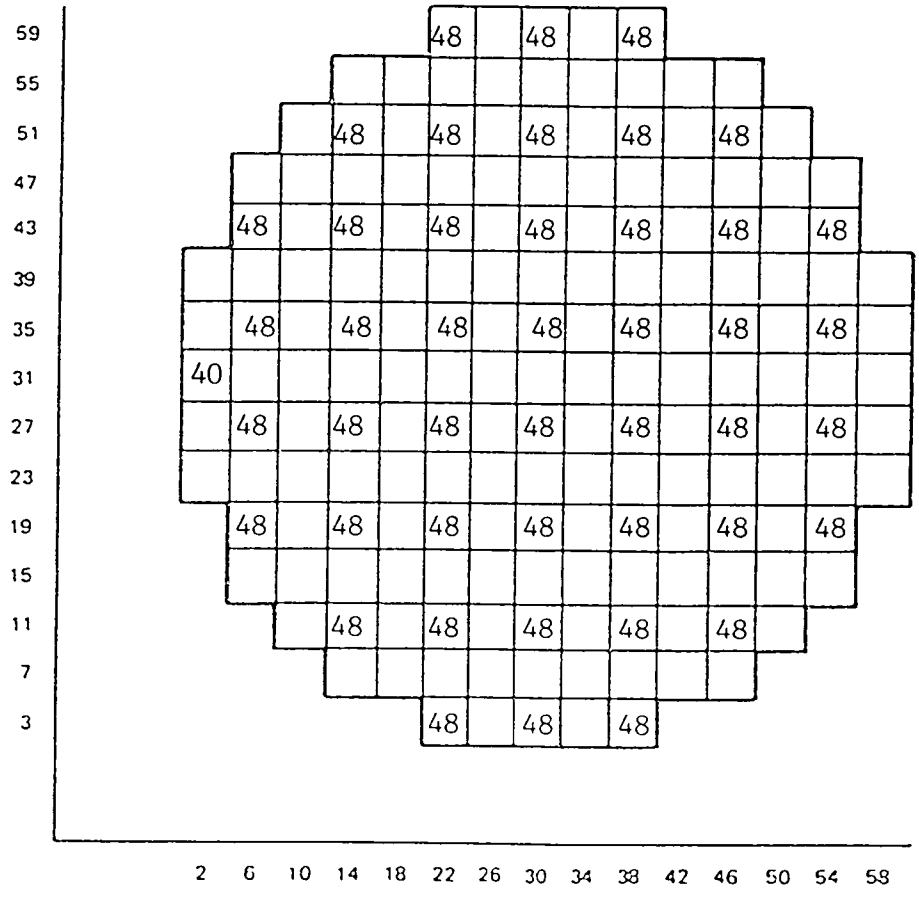

In-Sequence Critical #2 (Cycle 1), March 15, 1972

Date: 3/15/72
Core Exposure: 0 MWd/MT
Period: 150 Seconds
Temperature: 161 °F

0 (BLANK): FULL IN
48: FULL OUT

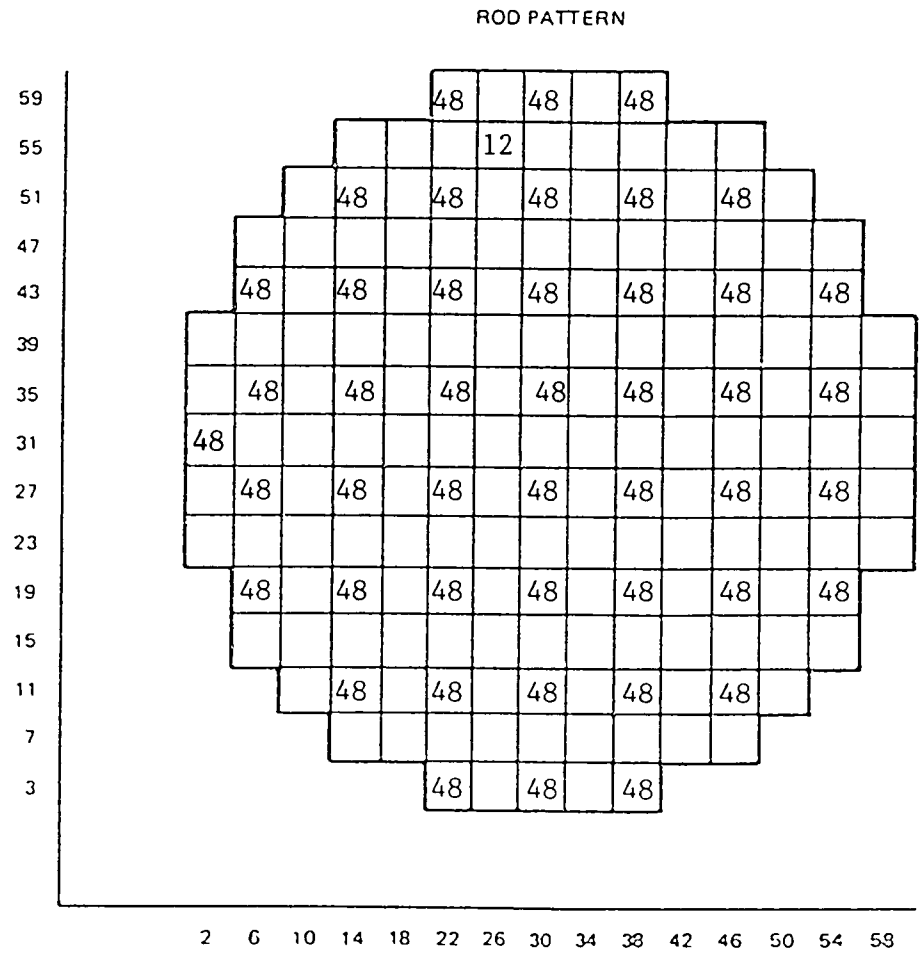

In-Sequence Critical #3 (Cycle 1), March 15, 1972

Date: 3/16/72
Core Exposure: 0 MWd/MT
Period: 125 Seconds
Temperature: 157 °F

0 (BLANK): FULL IN
48: FULL OUT

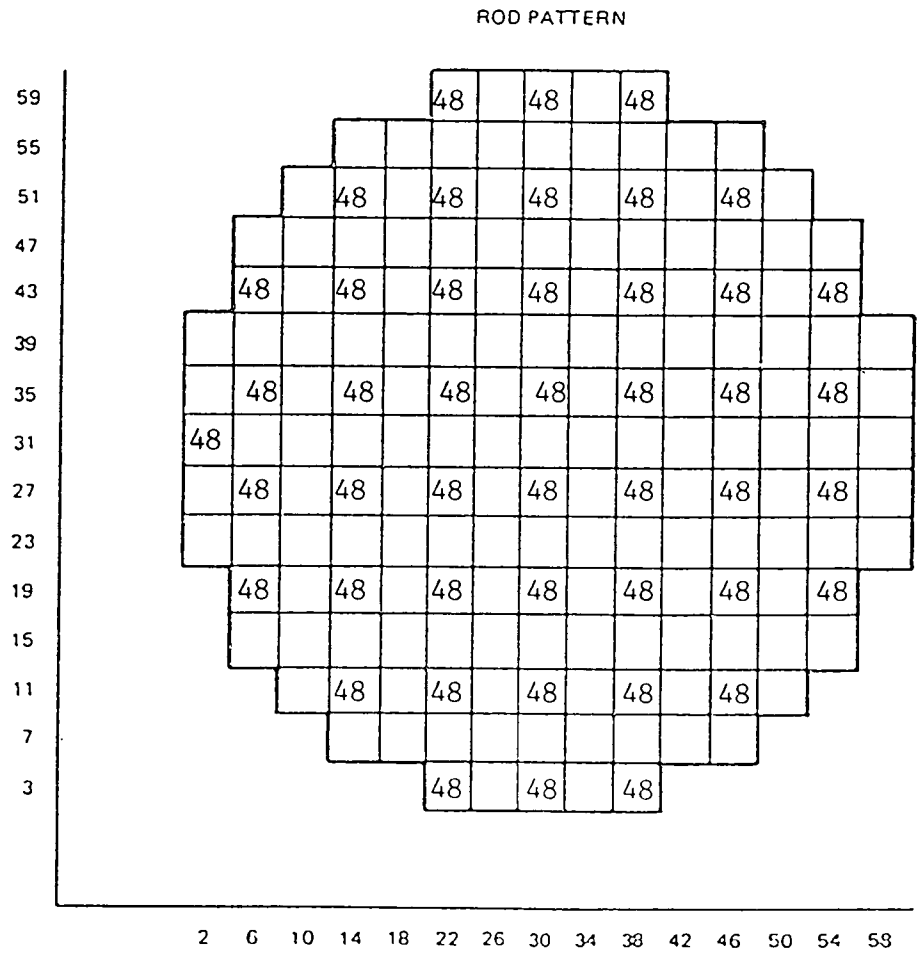

In-Sequence Critical #4 (Cycle 1), March 16, 1972

Date: 3/16/72
Core Exposure: 0 MWd/MT
Period: 65 Seconds
Temperature: 160 °F

0 (BLANK): FULL IN
48: FULL OUT

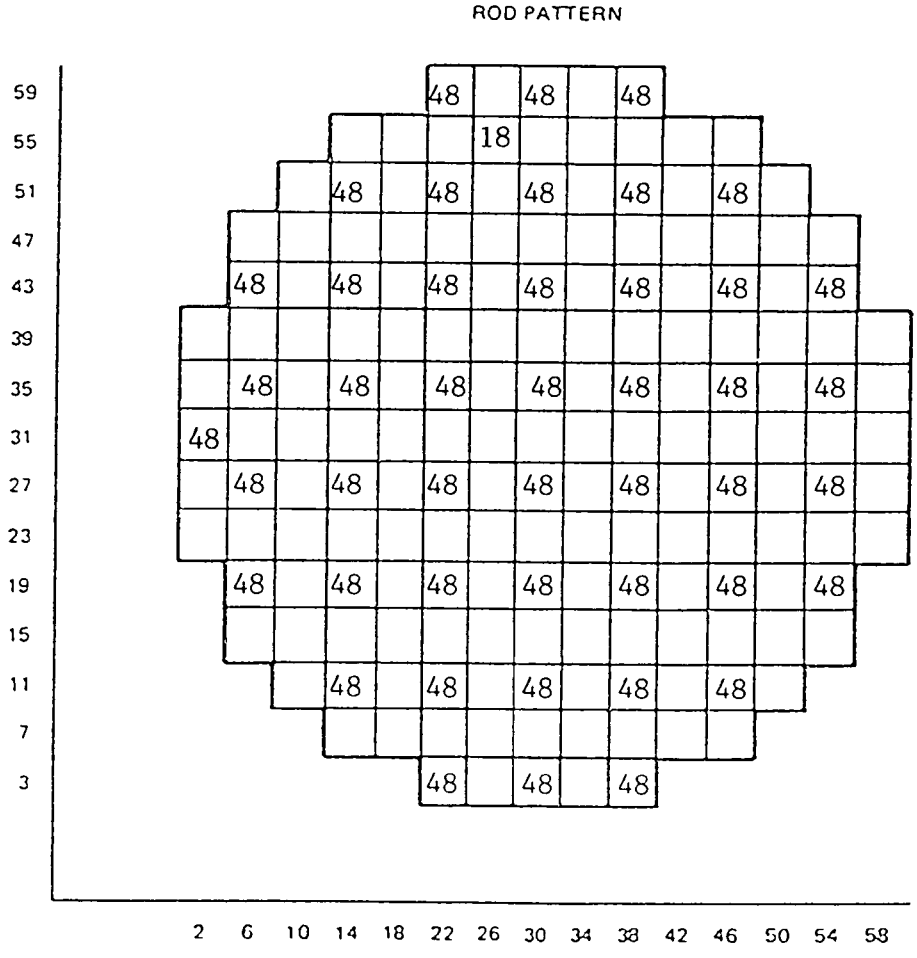

In-Sequence Critical #5 (Cycle 1), March 16, 1972

Date: 4/6/72
Core Exposure: 0 MWd/MT
Period: 120 Seconds
Temperature: 155 °F

0 (BLANK): FULL IN
48: FULL OUT

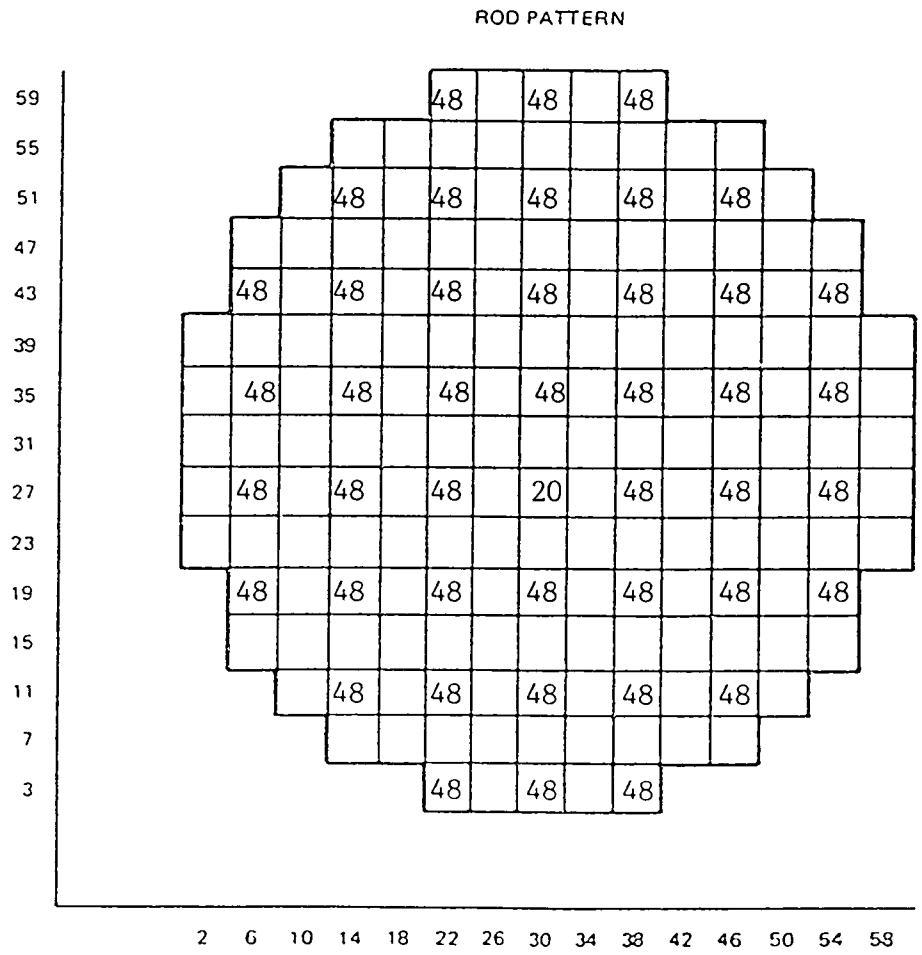

In-Sequence Critical #6 (Cycle 1), April 6, 1972

Date: 2/9/73
Core Exposure: 2,866 MWd/MT
Period: 300 Seconds
Temperature: 163 °F

0 (BLANK): FULL IN
48: FULL OUT

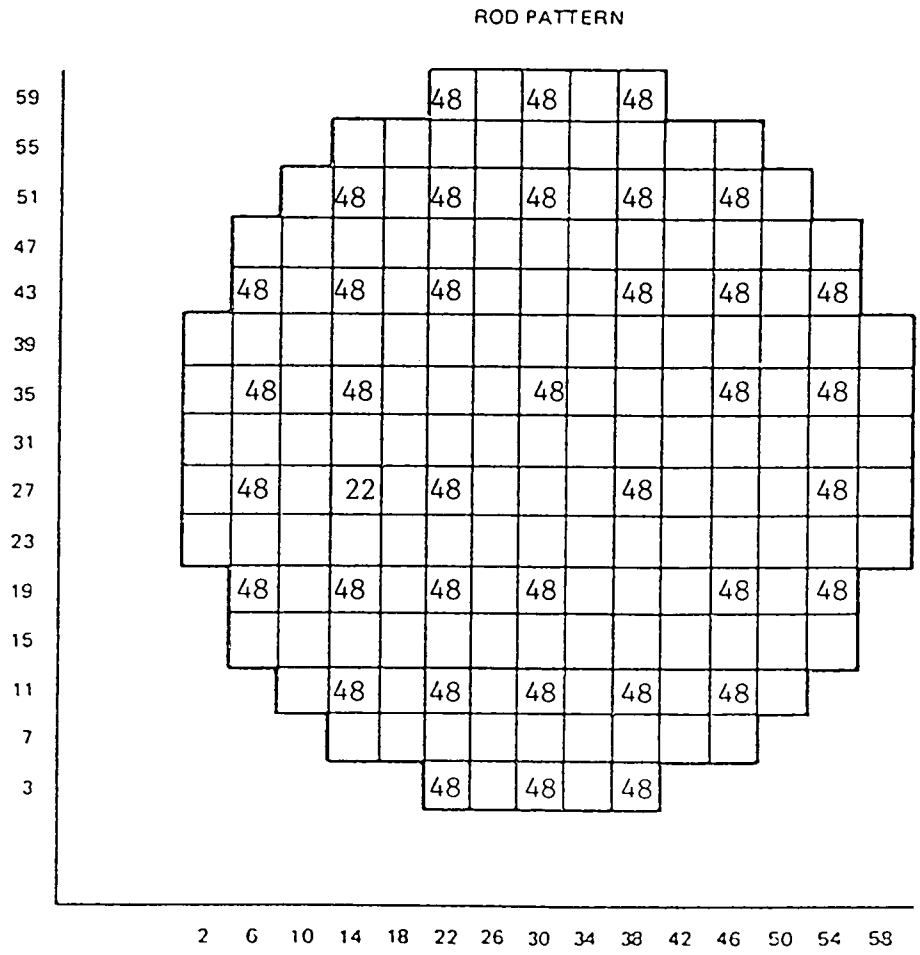

In-Sequence Critical #7 (Cycle 1), February 9, 1973

Date: 5/4/73
Core Exposure: 3,748 MWd/MT
Period: 300 Seconds
Temperature: 120 °F

0 (BLANK): FULL IN
48: FULL OUT

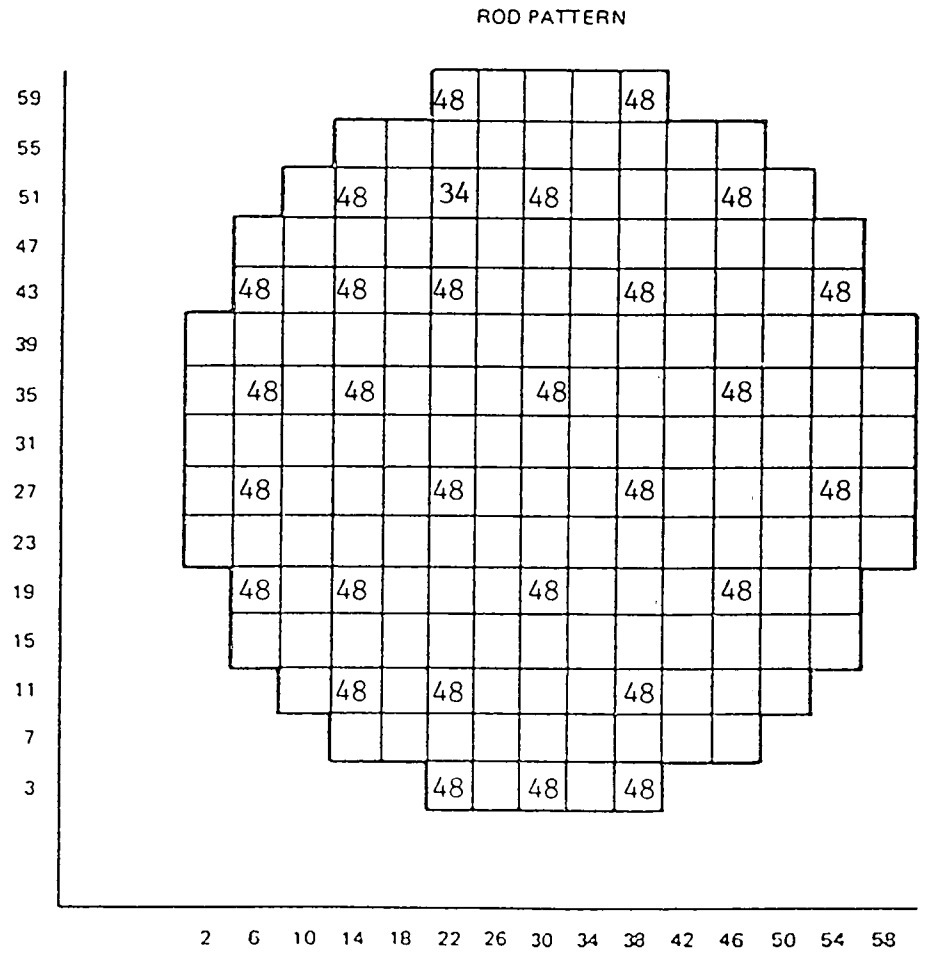

In-Sequence Critical #8 (Cycle 1), May 4, 1973

Date: 5/8/73
Core Exposure: 3,748 MWd/MT
Period: 181 Seconds
Temperature: 178 °F

0 (BLANK): FULL IN
48: FULL OUT

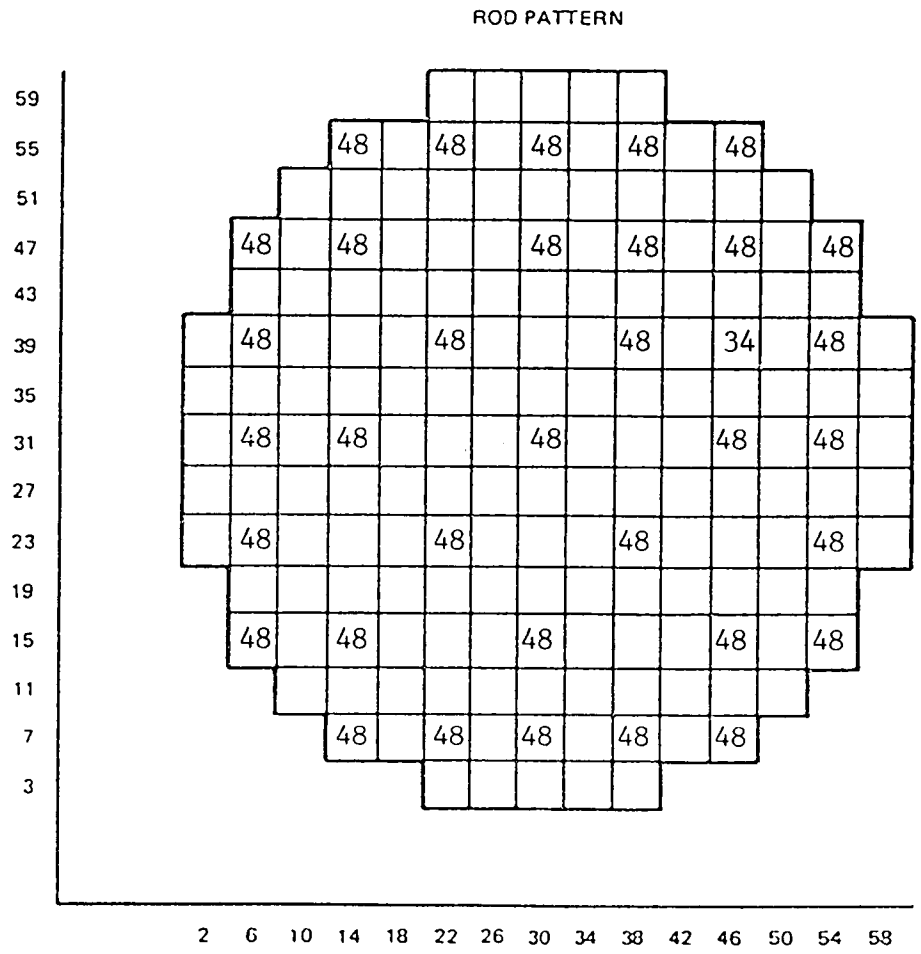

In-Sequence Critical #9 (Cycle 1), May 8, 1973

Date: 8/5/73
Core Exposure: 4,938 MWd/MT
Period: 45 Seconds
Temperature: 120 °F

0 (BLANK): FULL IN
48: FULL OUT

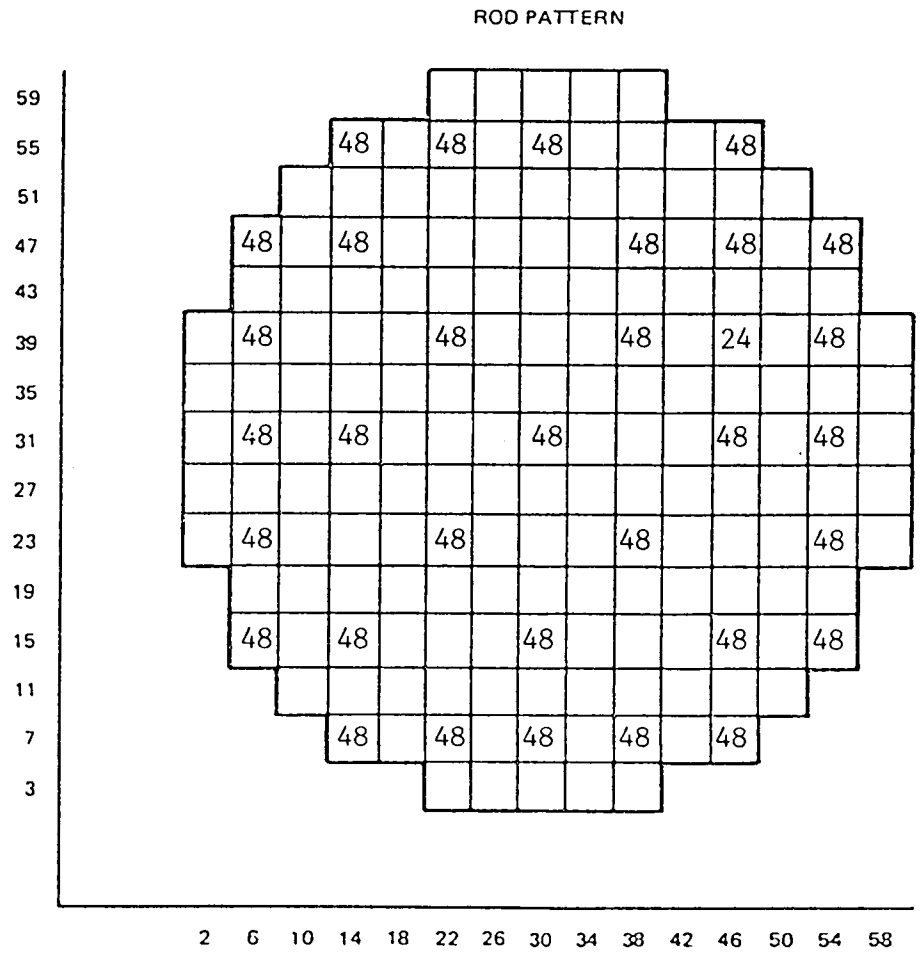

In-Sequence Critical #10 (Cycle 1), August 5, 1973

Date: 1/6/74
Core Exposure: 6,911 MWd/MT
Period: 300 Seconds
Temperature: 179 °F

0 (BLANK): FULL IN
48: FULL OUT

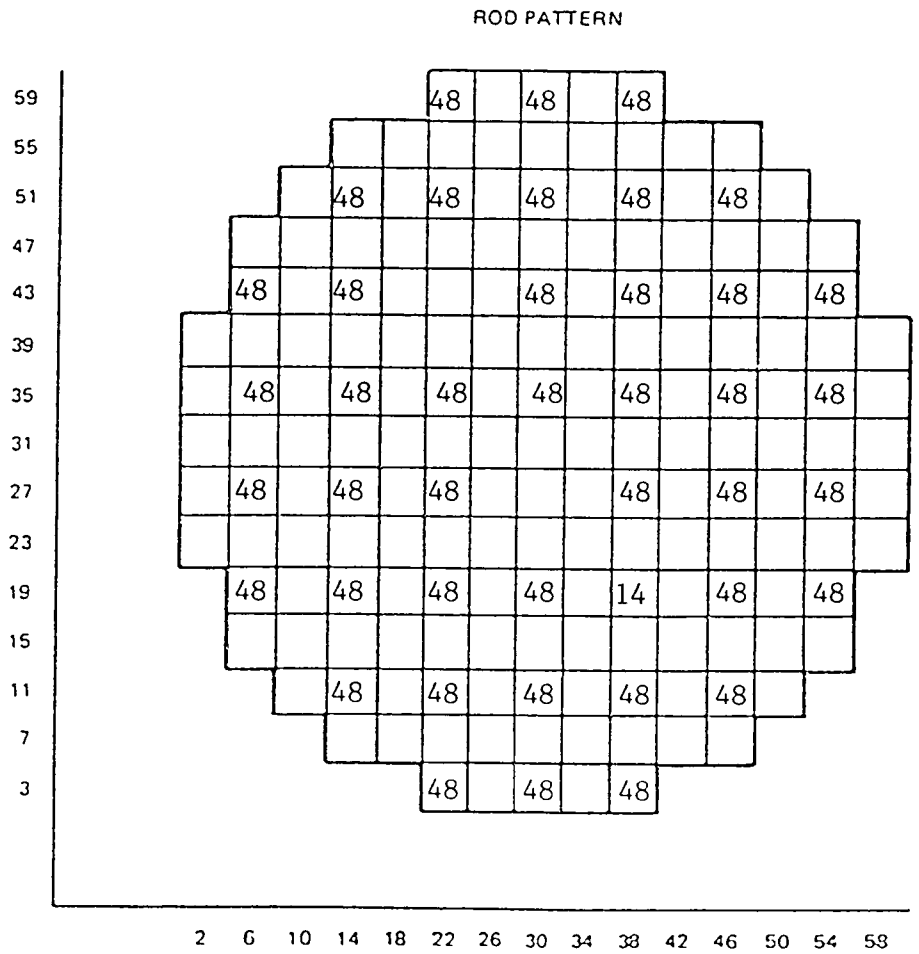

In-Sequence Critical #11 (Cycle 1), January 6, 1974

Date: 10/6/74
Core Exposure: 8,276 MWd/MT
Period: 100 Seconds
Temperature: 185 °F

0 (BLANK): FULL IN
48: FULL OUT

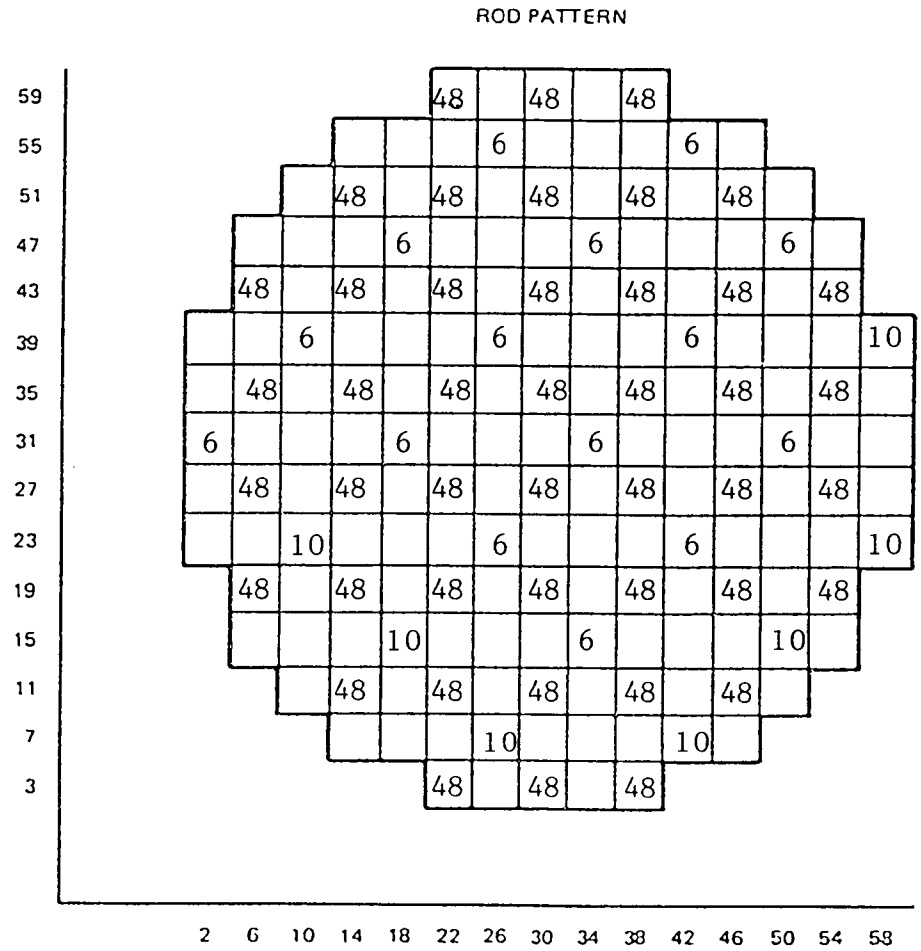

In-Sequence Critical #12 (Cycle 2), October 6, 1974

Date: 12/16/74
Core Exposure: 9,138 MWd/MT
Period: 45 Seconds
Temperature: 160 °F

0 (BLANK): FULL IN
48: FULL OUT

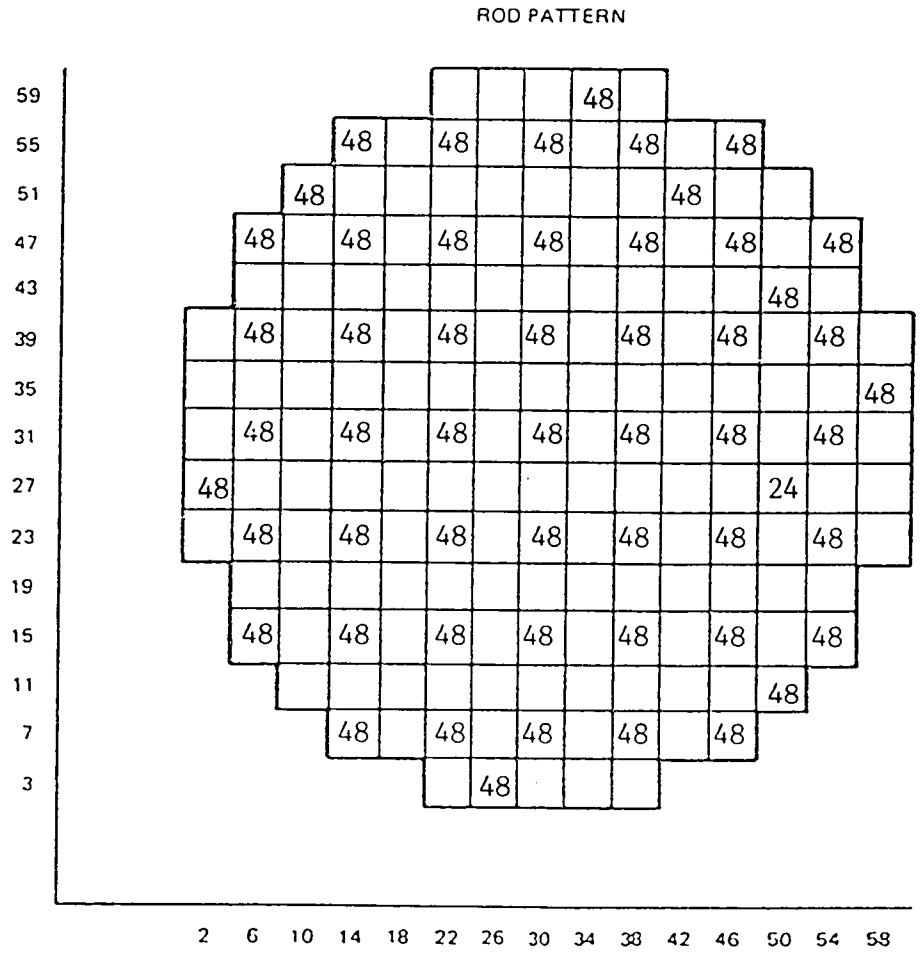

In-Sequence Critical #13 (Cycle 2), December 16, 1974

Date: 5/4/75
Core Exposure: 10,603 MWd/MT
Period: 130 Seconds
Temperature: 190 °F

0 (BLANK): FULL IN
48: FULL OUT

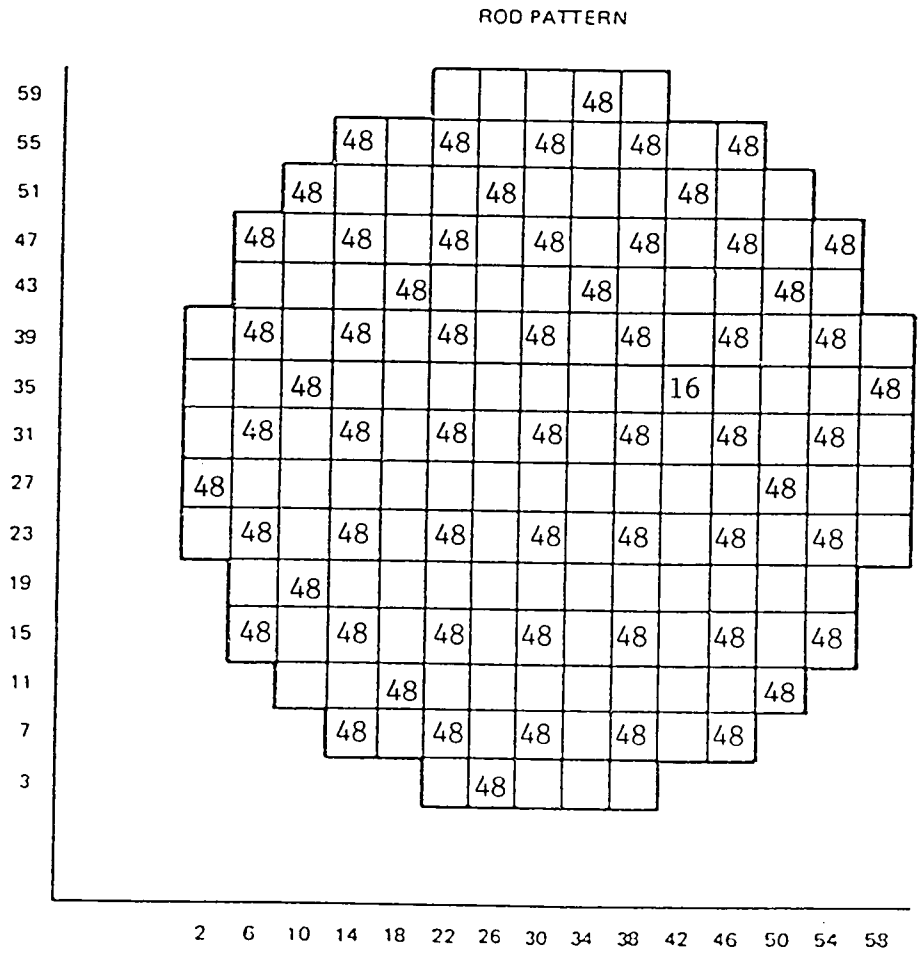

In-Sequence Critical #14 (Cycle 2), May 5, 1974

APPENDIX B

INDIVIDUAL AXIAL TIP COMPARISON PLOTS

The figures contained in this Appendix present TIP comparisons for each detector location in the core at a given core average exposure. The x-y assignments indicated on each subplot correspond to the numbering system used previously in this thesis. The layout of the subplots matches the relative core location. For example, the subplot for detector location 24-57 is located in the upper left corner of each figure, and detector location 48-9 is located in the lower right corner.

Solid vertical bars are used in the subplots to indicate the position of control rods adjacent to the detector. Note that in normal operation no more than two control rods are inserted adjacent to a four assembly TIP cell.

Each TIP distribution contains 24 axial points. The data is normalized such that the core average of TIP values from the core simulator matches the core average TIP value from measurement.

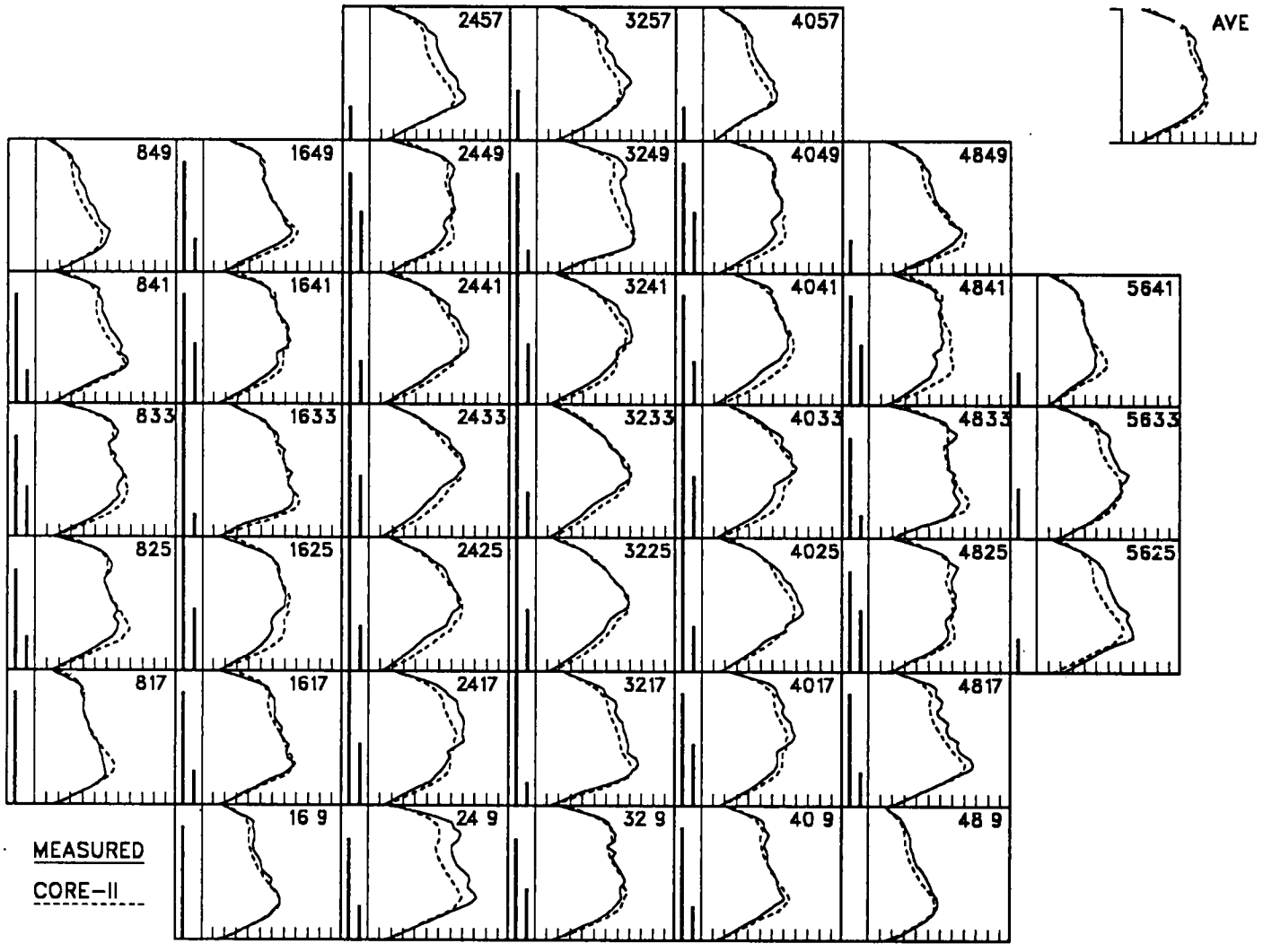

Cycle 1 Individual Axial TIP Comparison at 272 MWd/MT

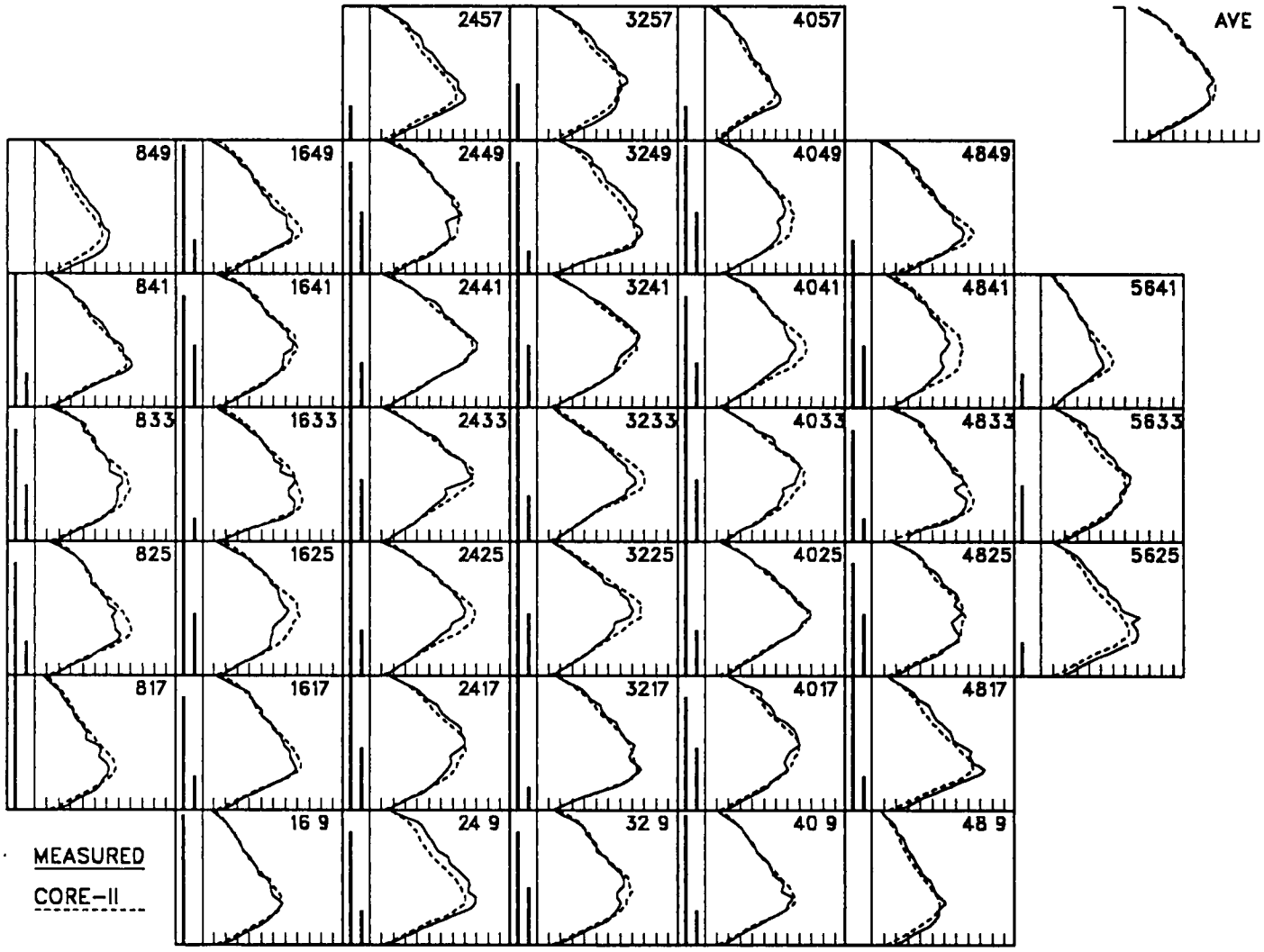

Cycle 1 Individual Axial TIP Comparison at 712 MWd/MT

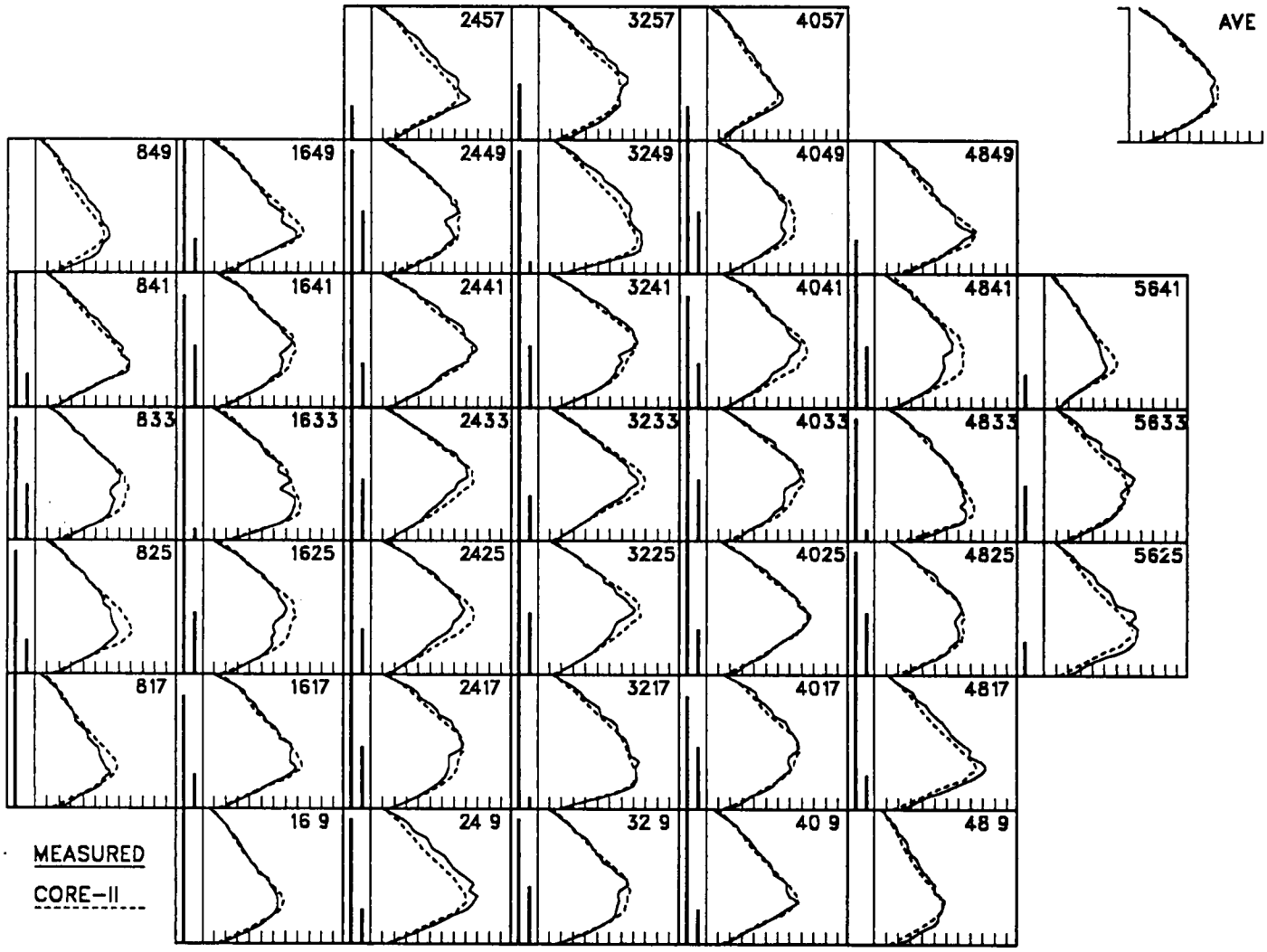

Cycle 1 Individual Axial TIP Comparison at 882 MWd/MT

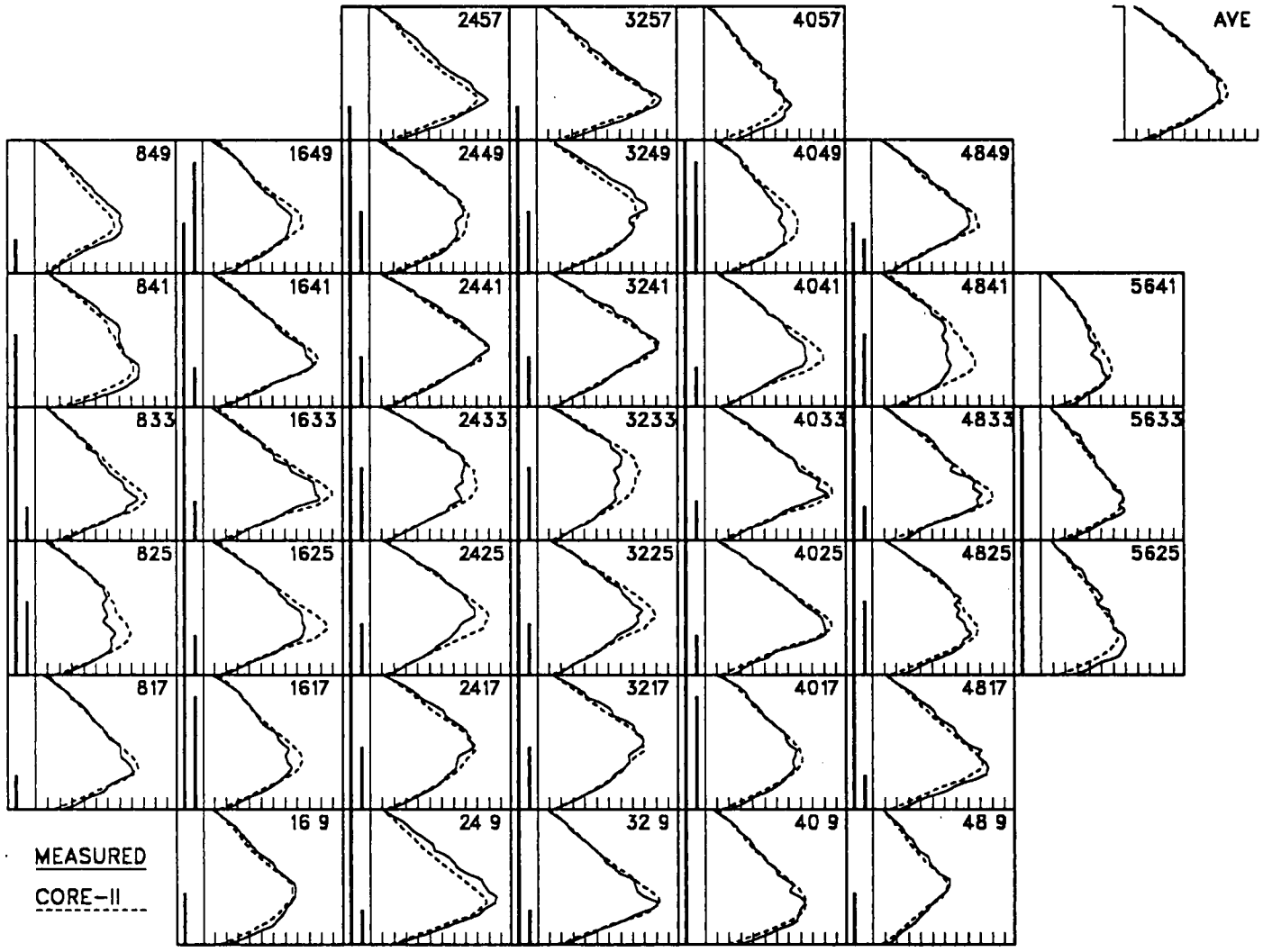

Cycle 1 Individual Axial TIP Comparison at 1471 MWd/MT

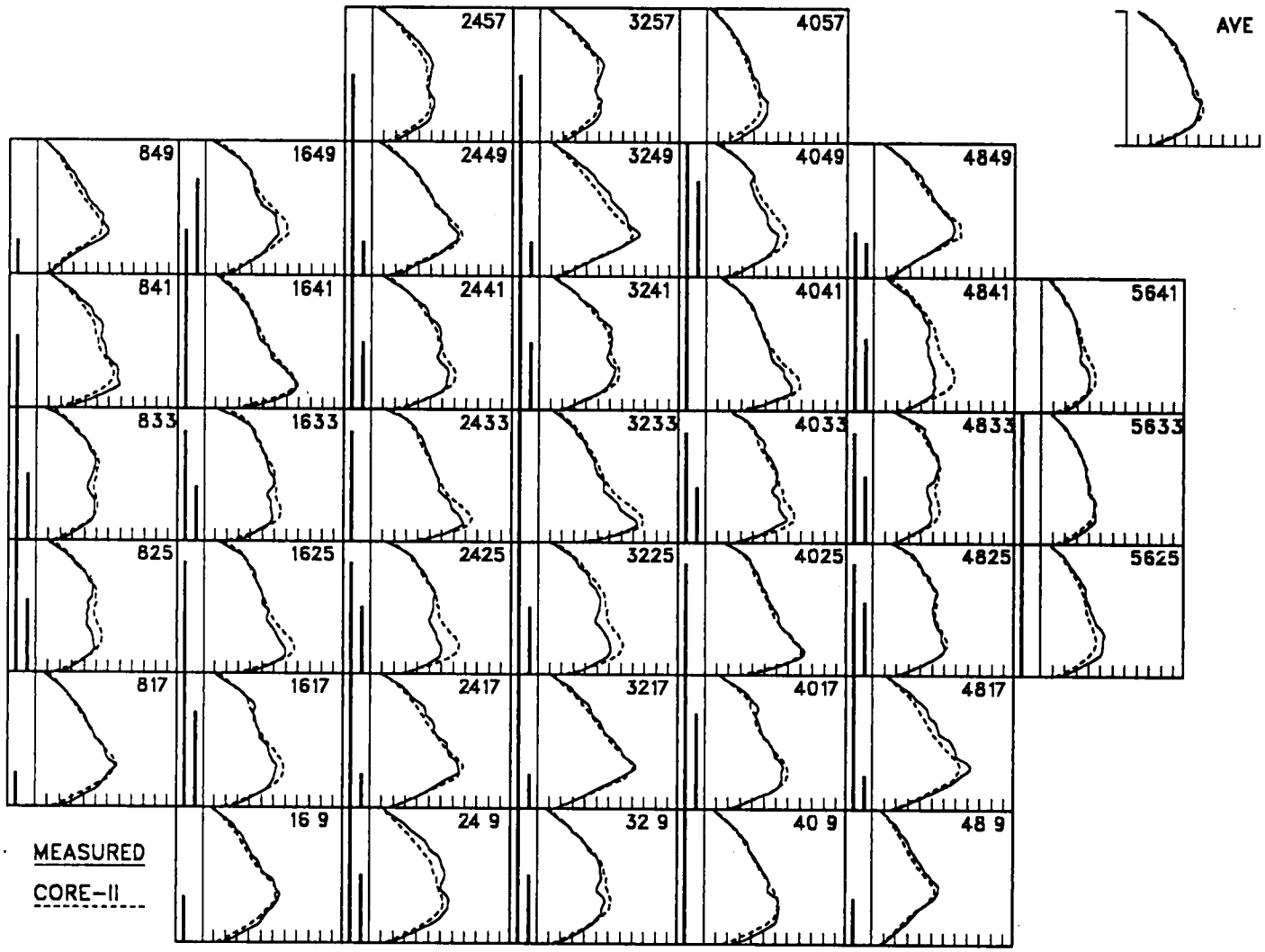

Cycle 1 Individual Axial TIP Comparison at 2239 MWd/MT

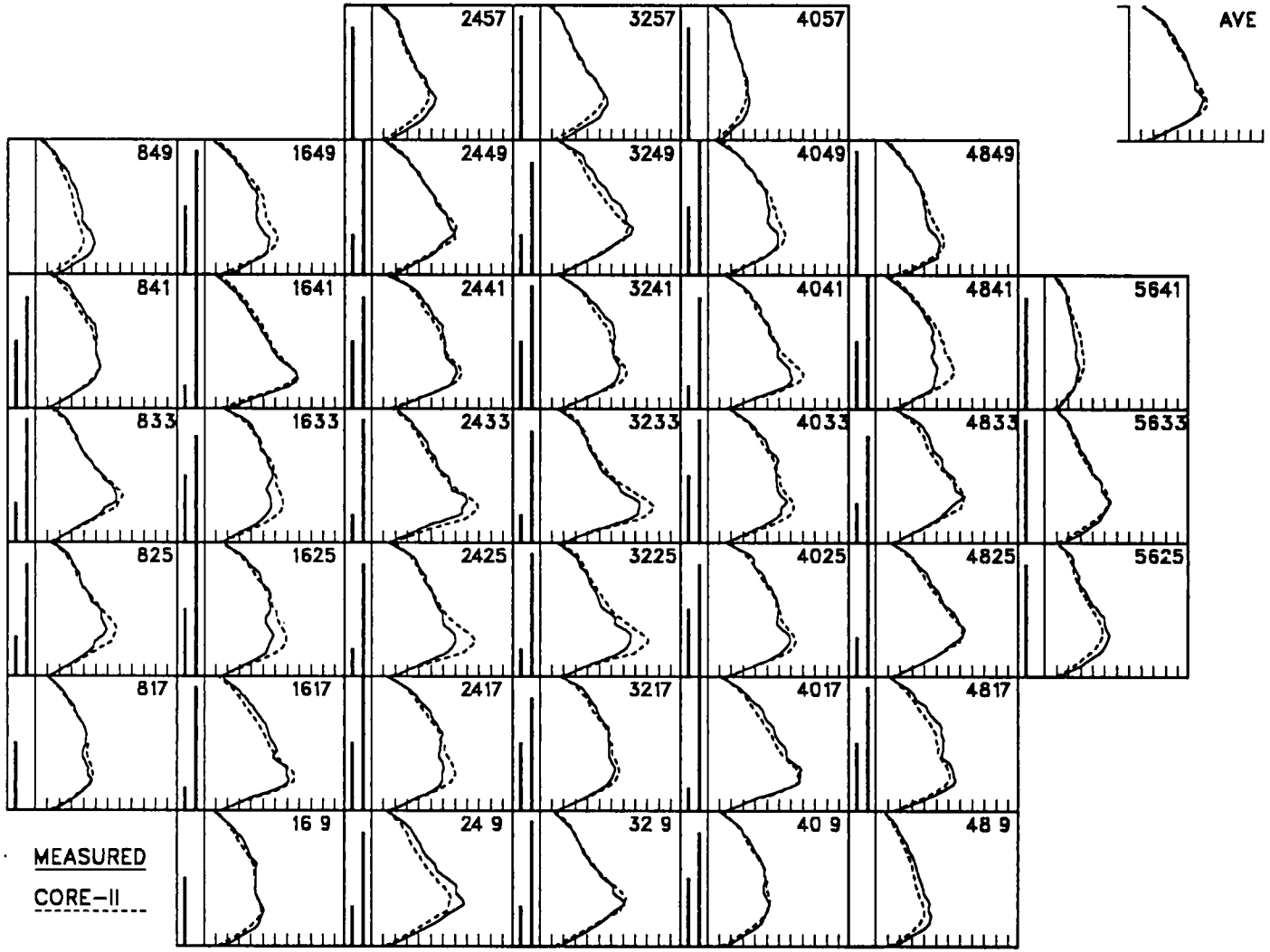

Cycle 1 Individual Axial TIP Comparison at 3190 MWd/MT

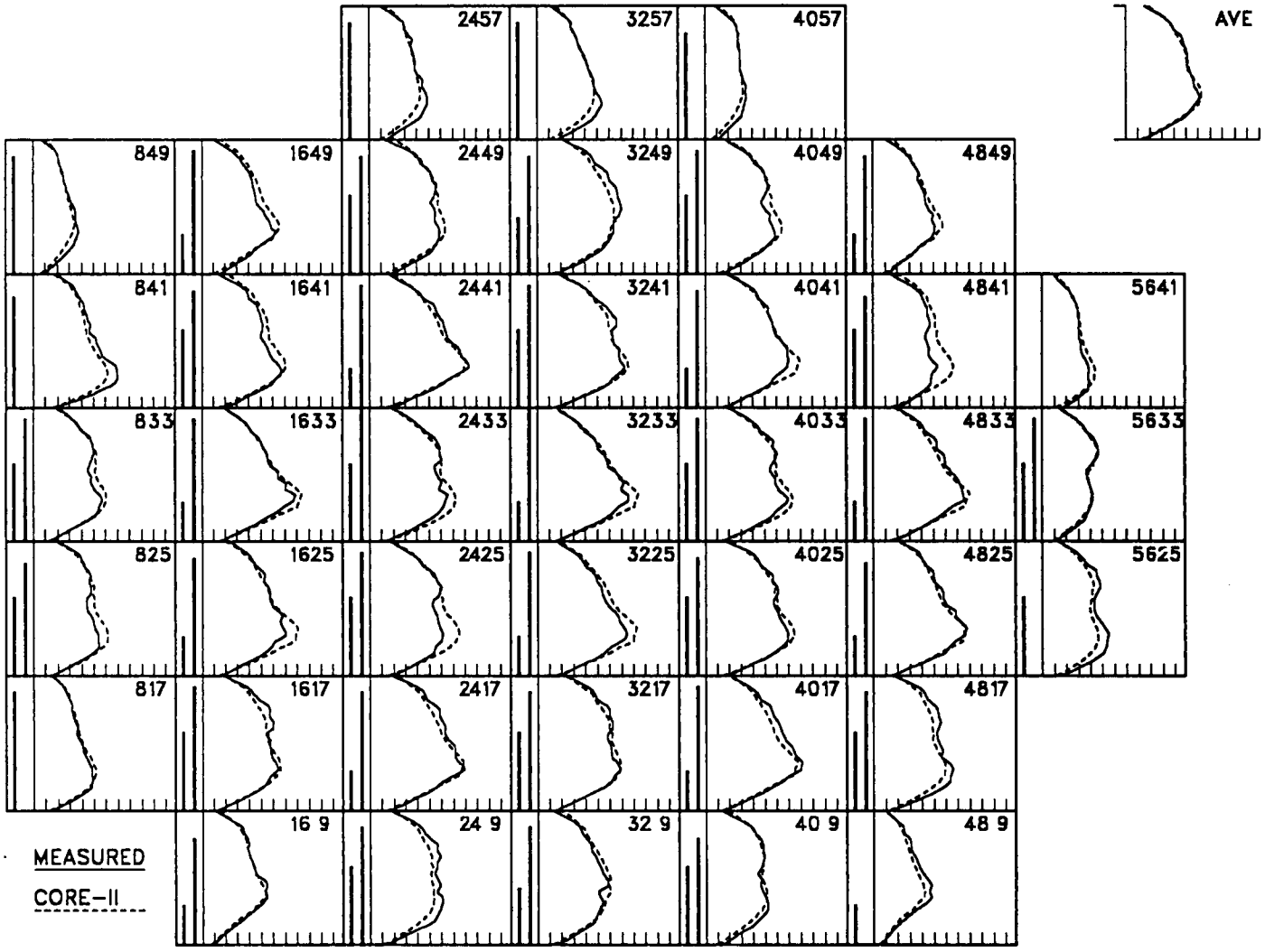

Cycle 1 Individual Axial TIP Comparison at 3837 MWd/MT

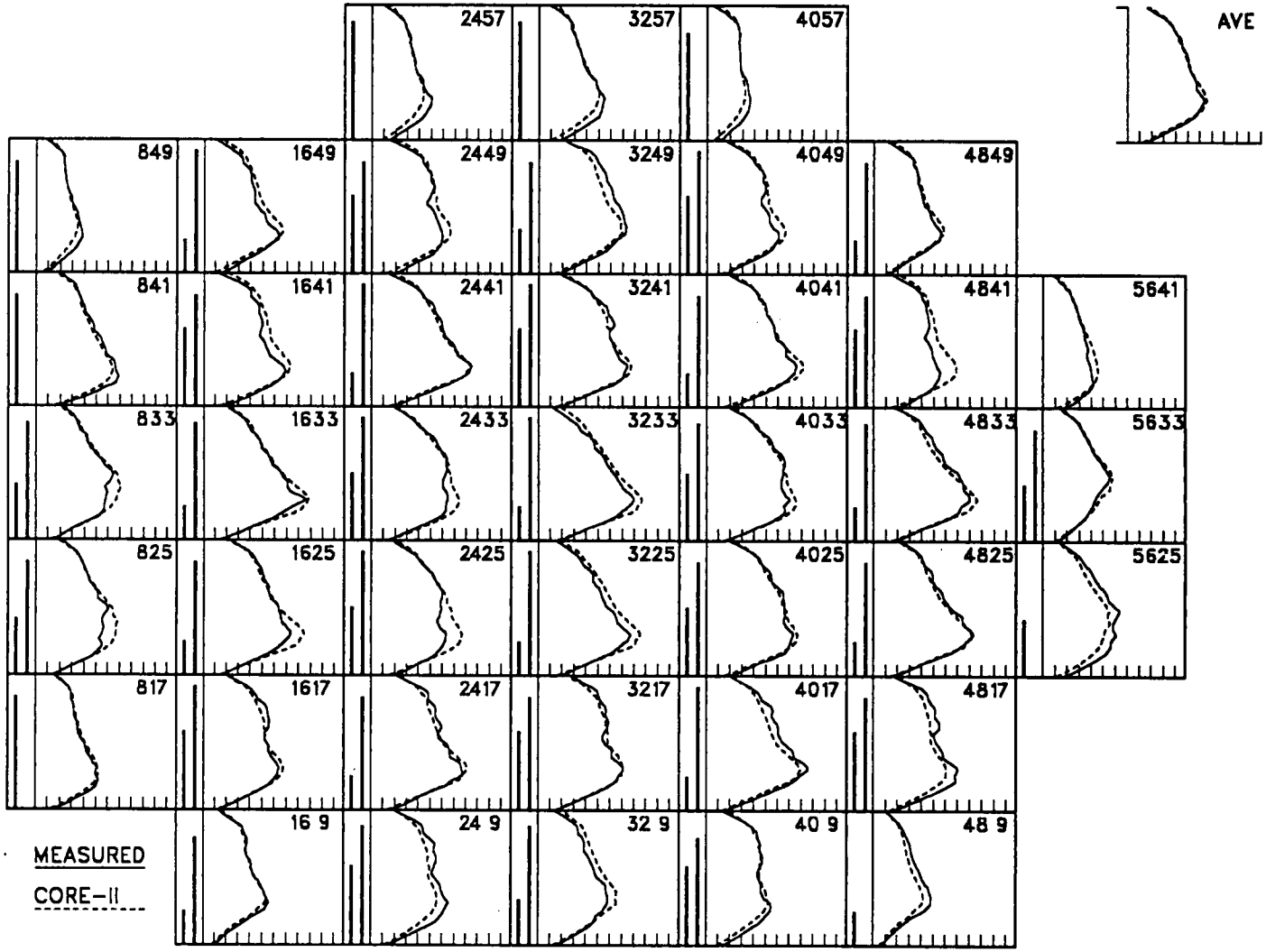

Cycle 1 Individual Axial TIP Comparison at 4075 MWd/MT

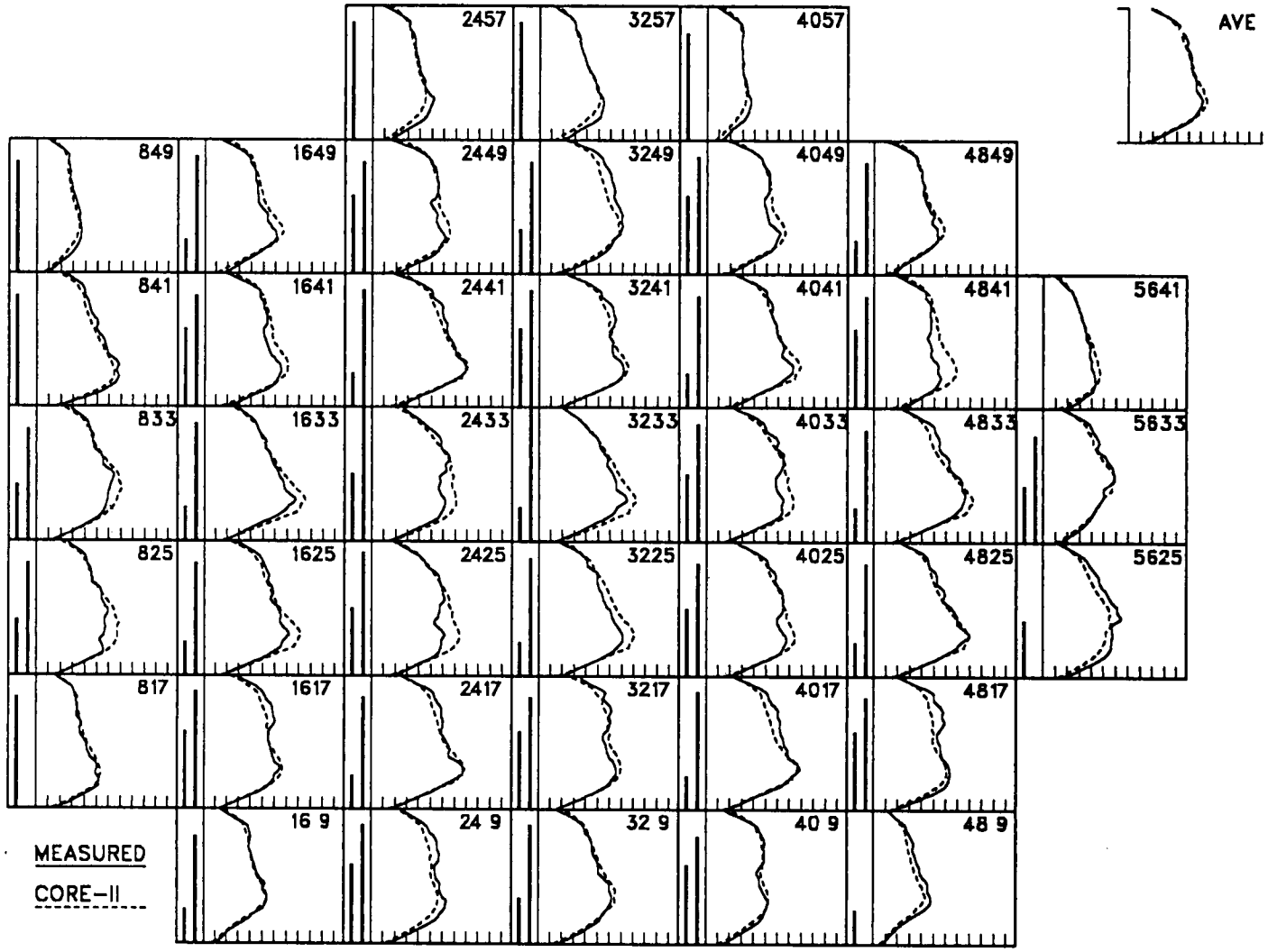

Cycle 1 Individual Axial TIP Comparison at 4738 MWd/MT

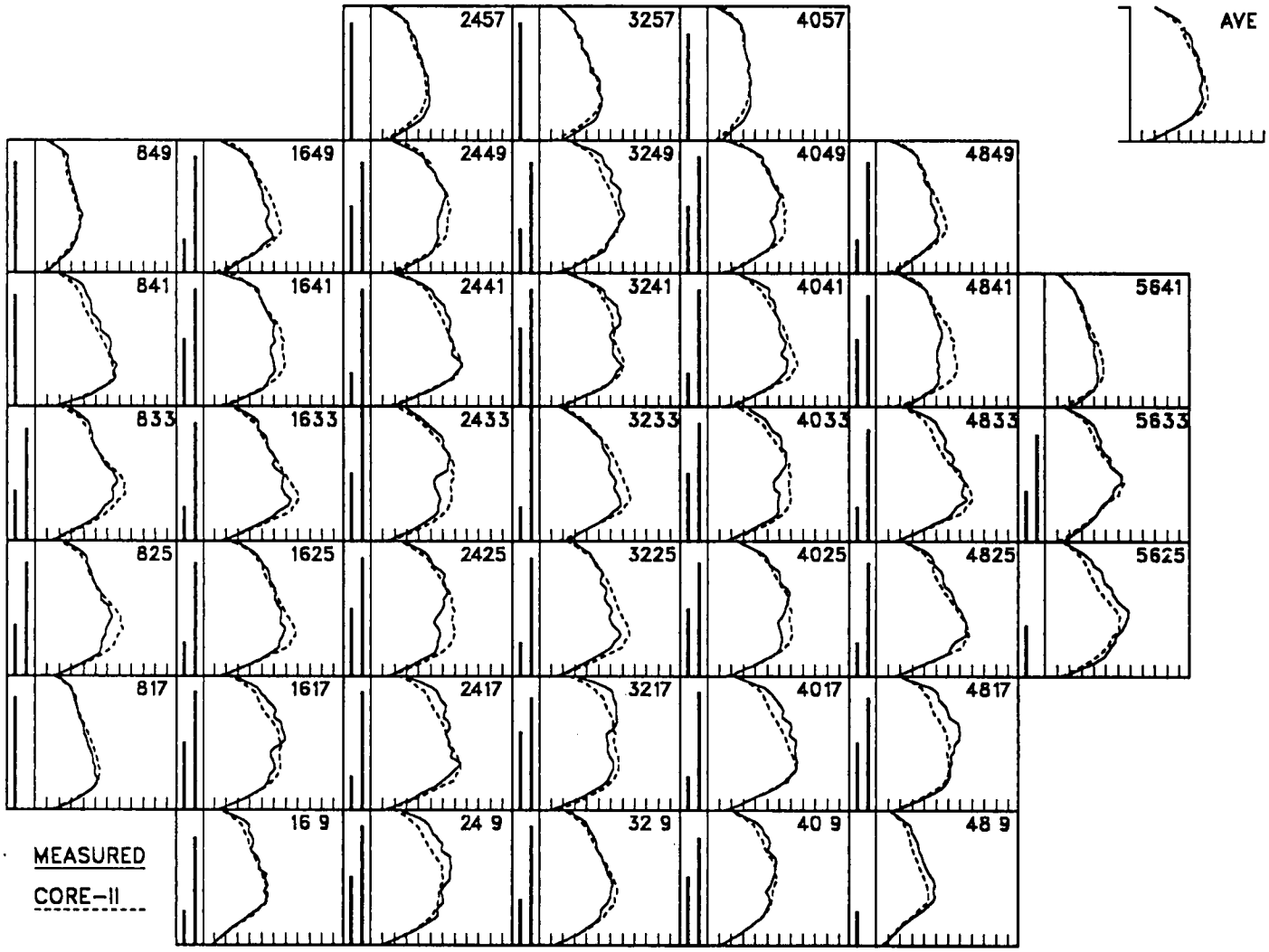

Cycle 1 Individual Axial TIP Comparison at 5301 MWd/MT

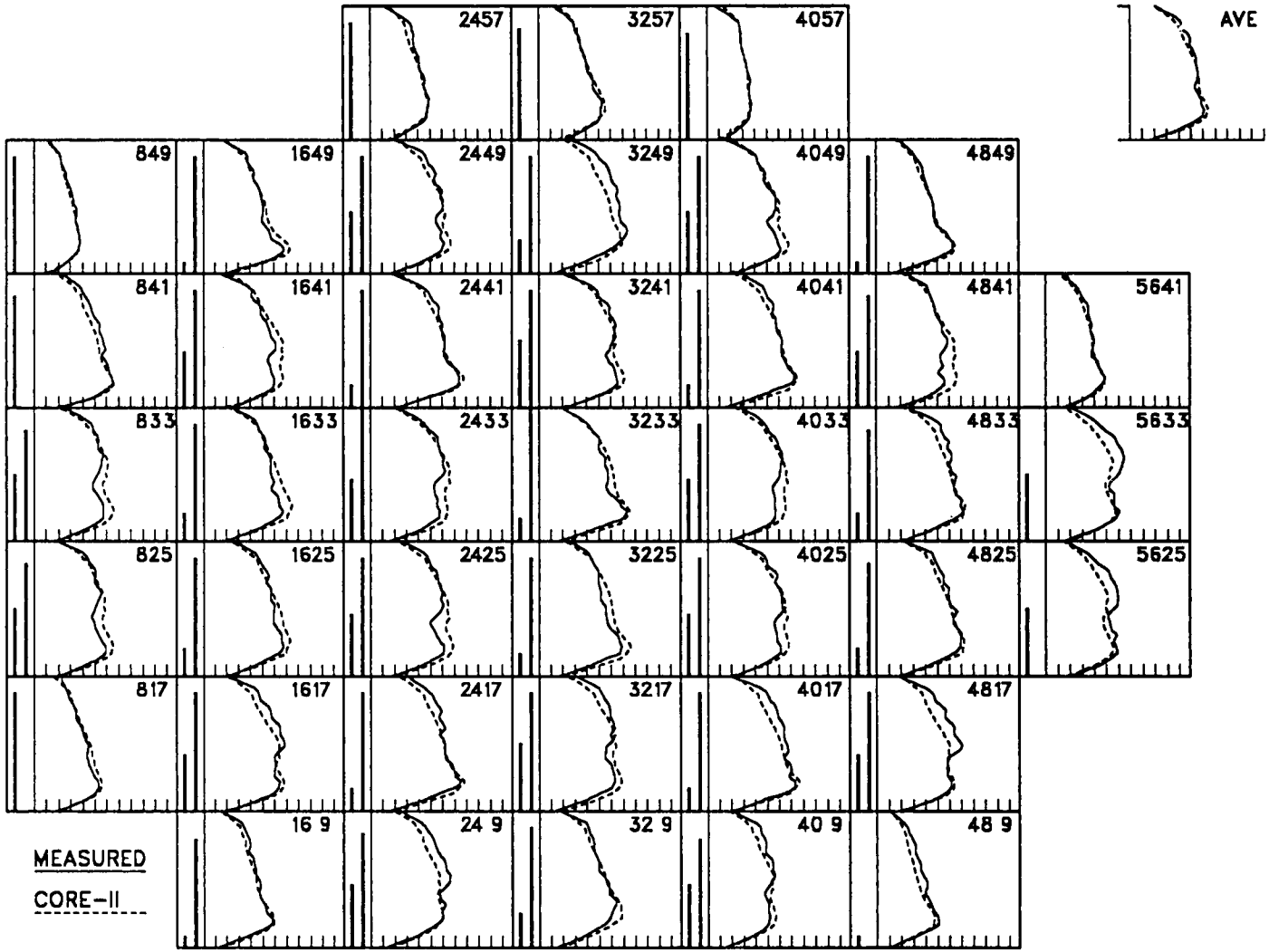

Cycle 1 Individual Axial TIP Comparison at 6031 MWd/MT

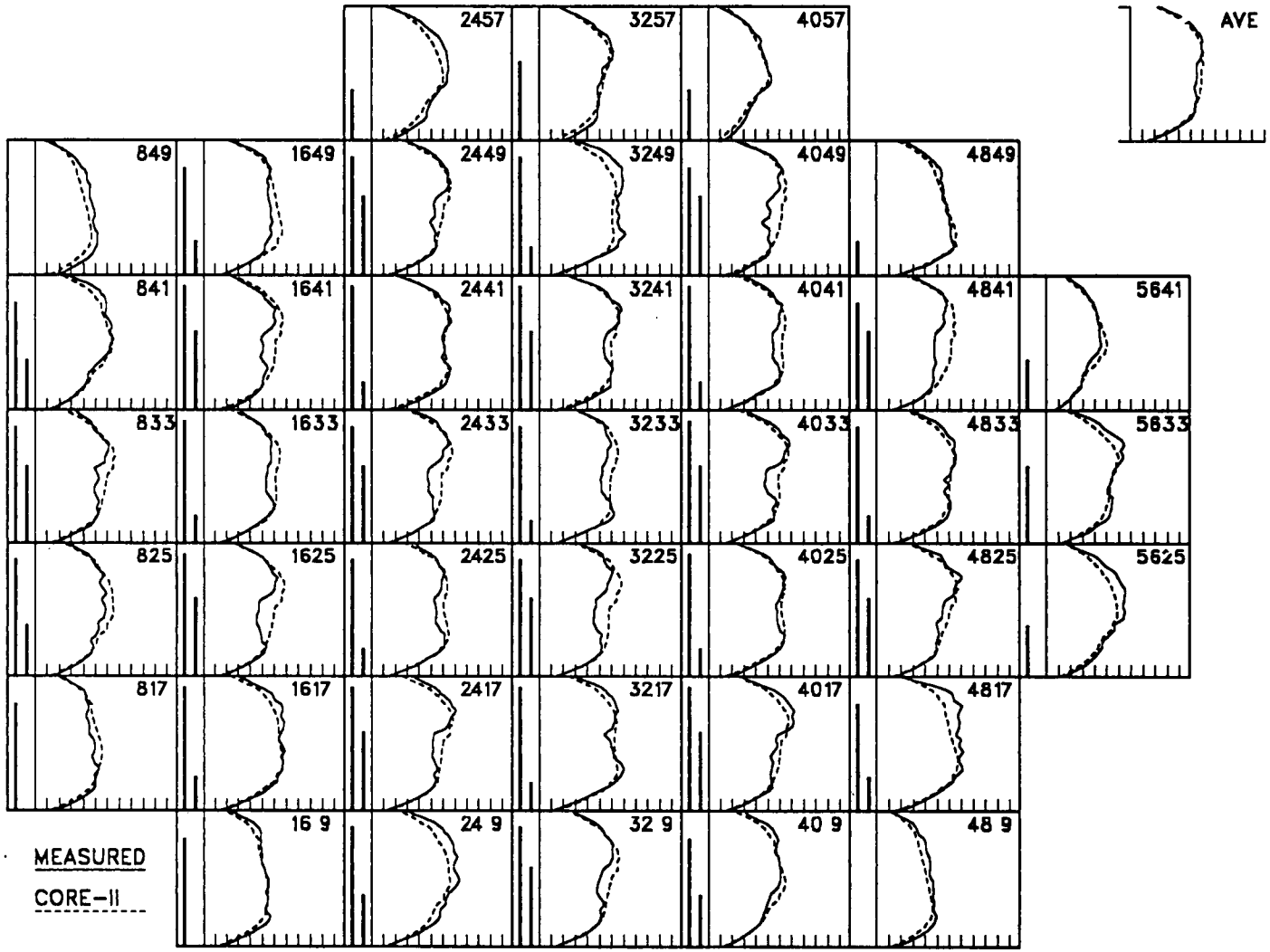

Cycle 1 Individual Axial TIP Comparison at 6558 MWd/MT

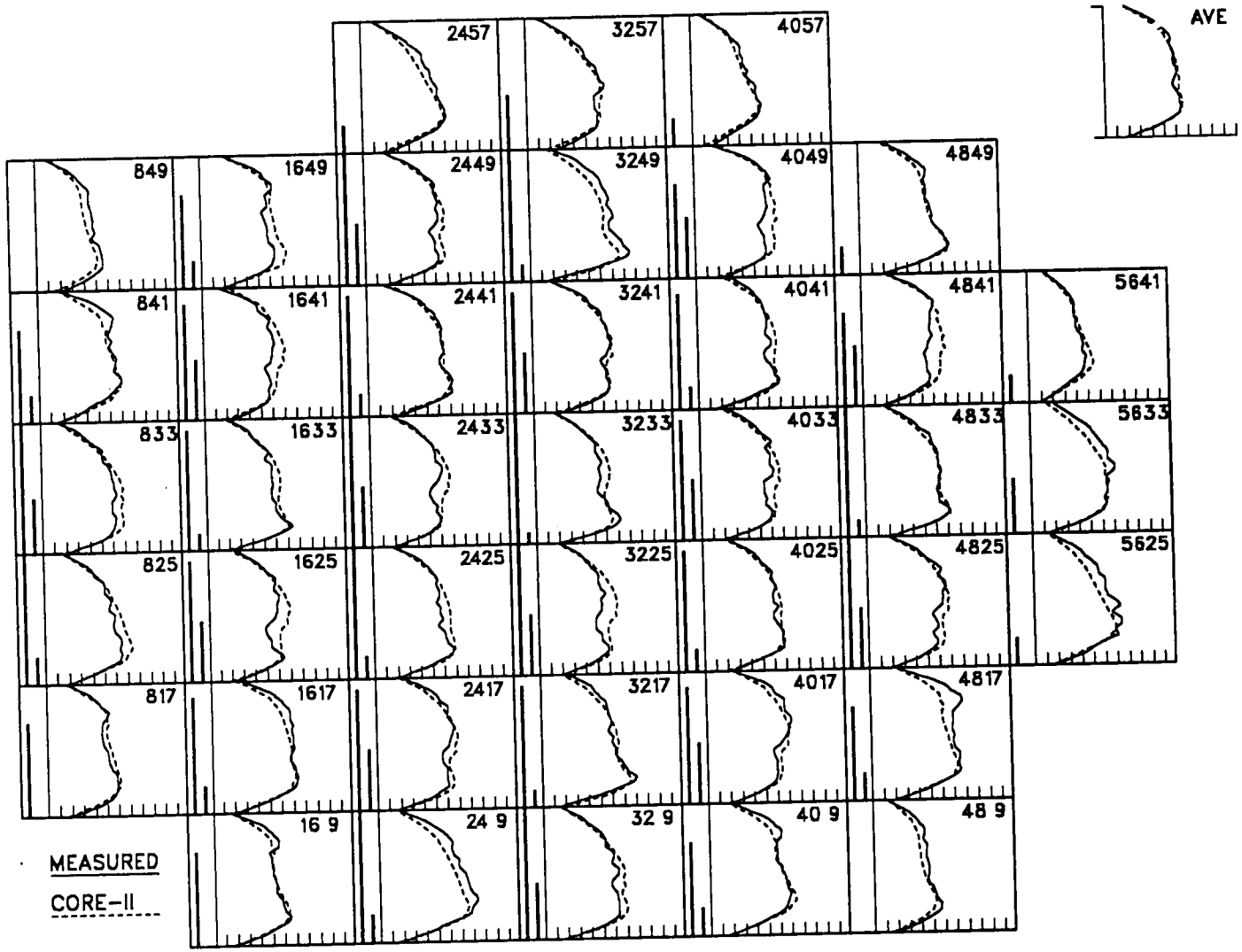

Cycle 1 Individual Axial TIP Comparison at 6807 MWd/MT

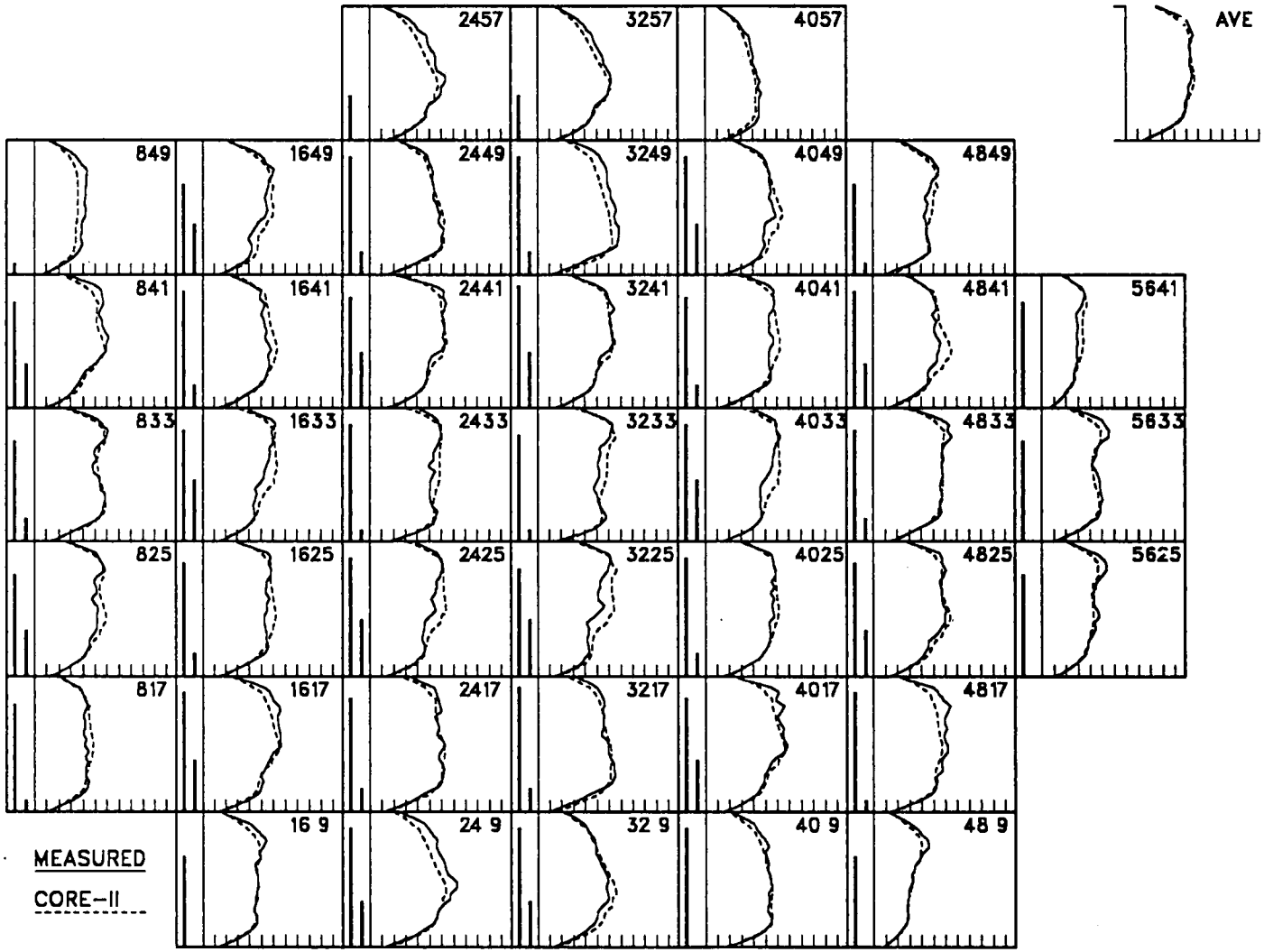

Cycle 1 Individual Axial TIP Comparison at 7397 MWd/MT

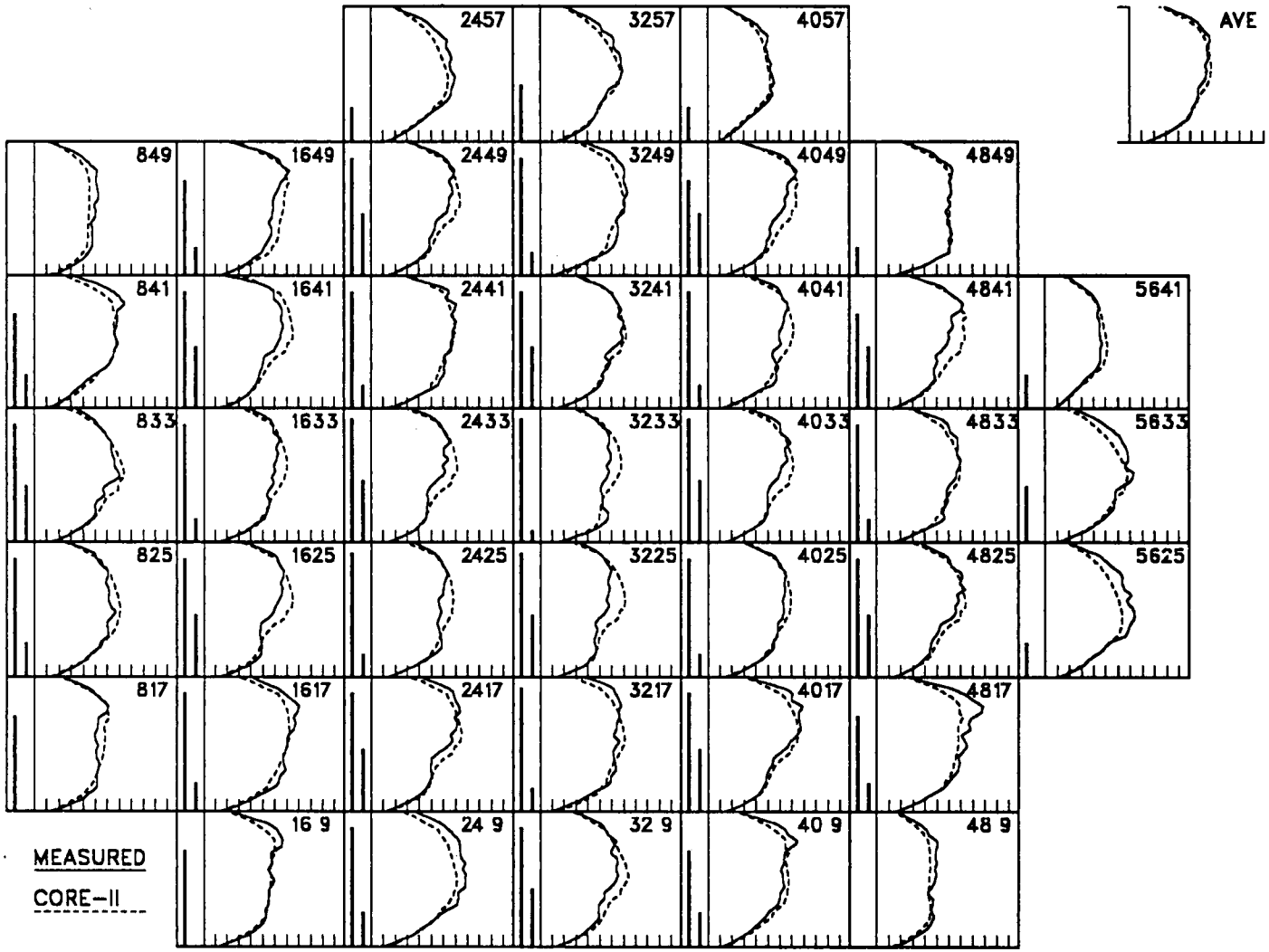

Cycle 1 Individual Axial TIP Comparison at 7660 MWd/MT

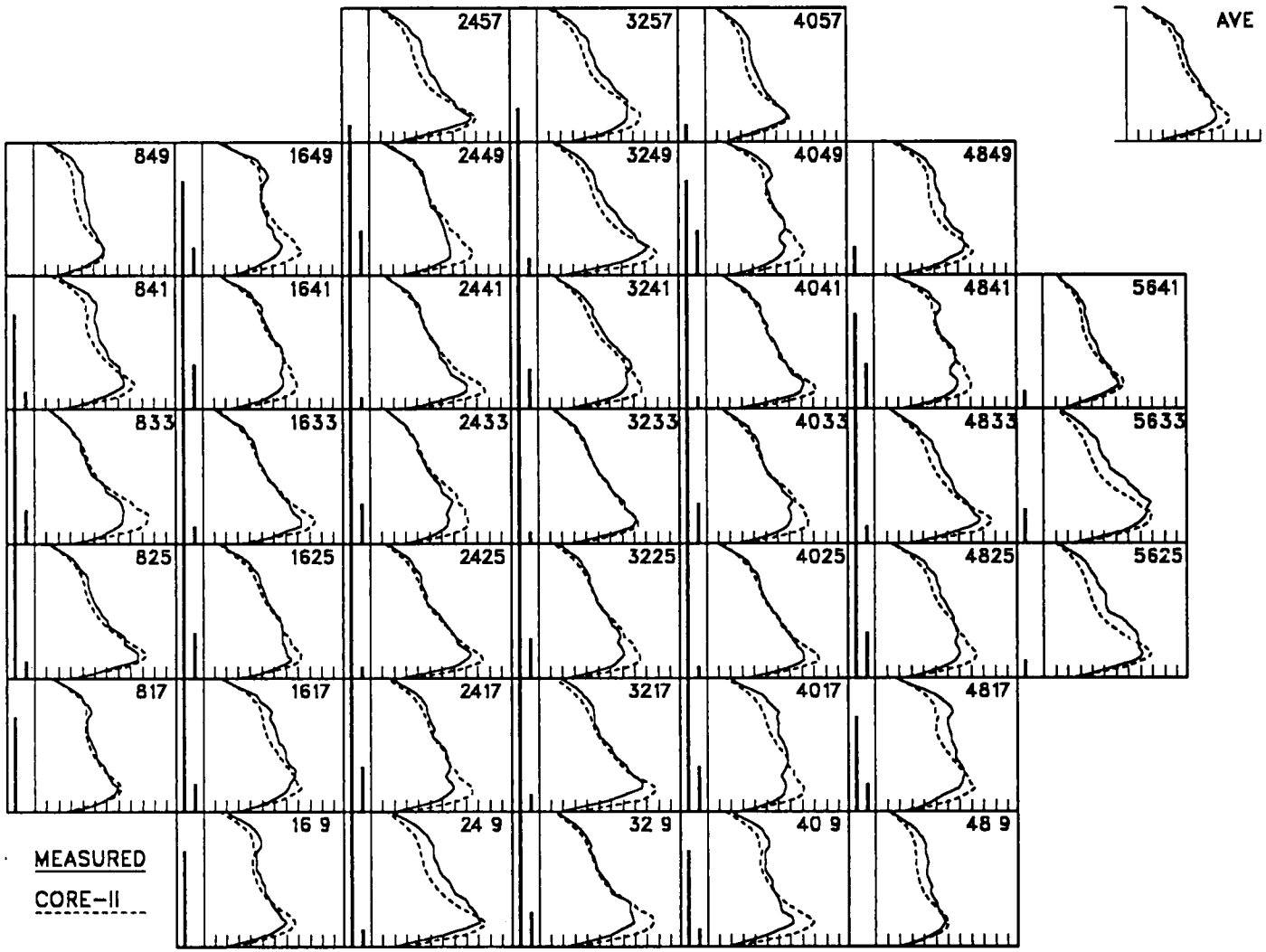

Cycle 2 Individual Axial TIP Comparison at 7303 MWd/MT

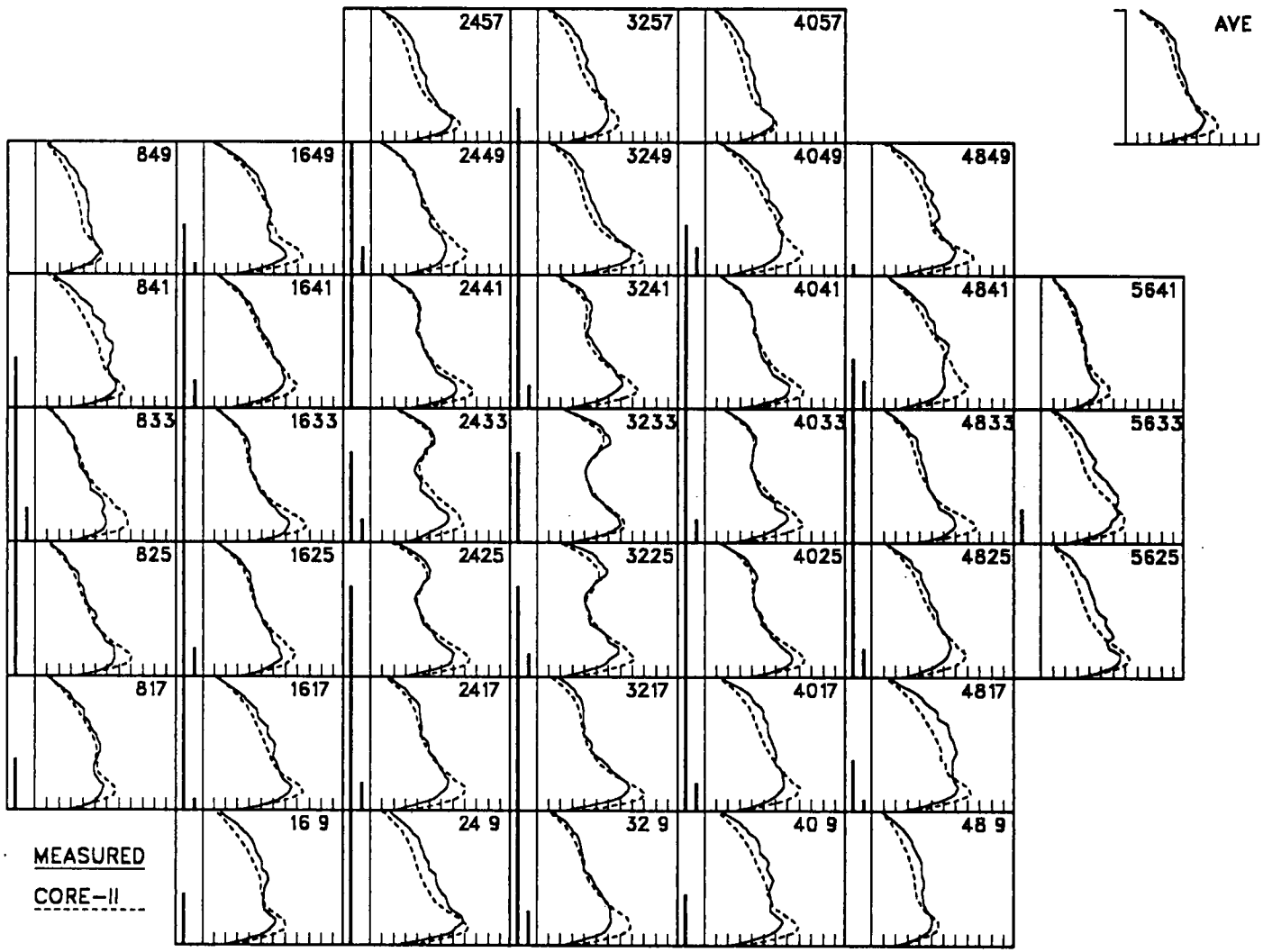

Cycle 2 Individual Axial TIP Comparison at 7532 MWd/MT

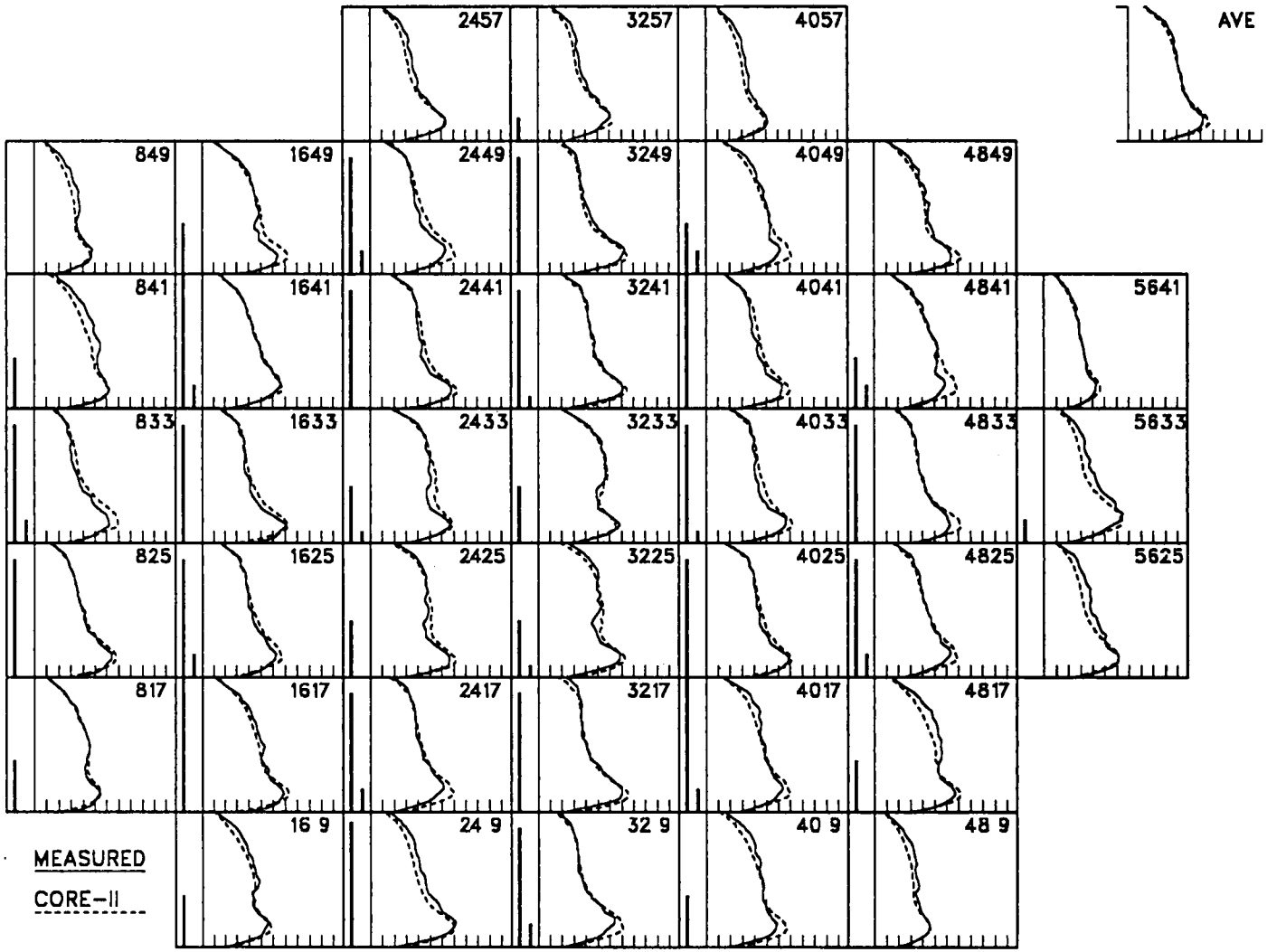

Cycle 2 Individual Axial TIP Comparison at 7964 MWd/MT

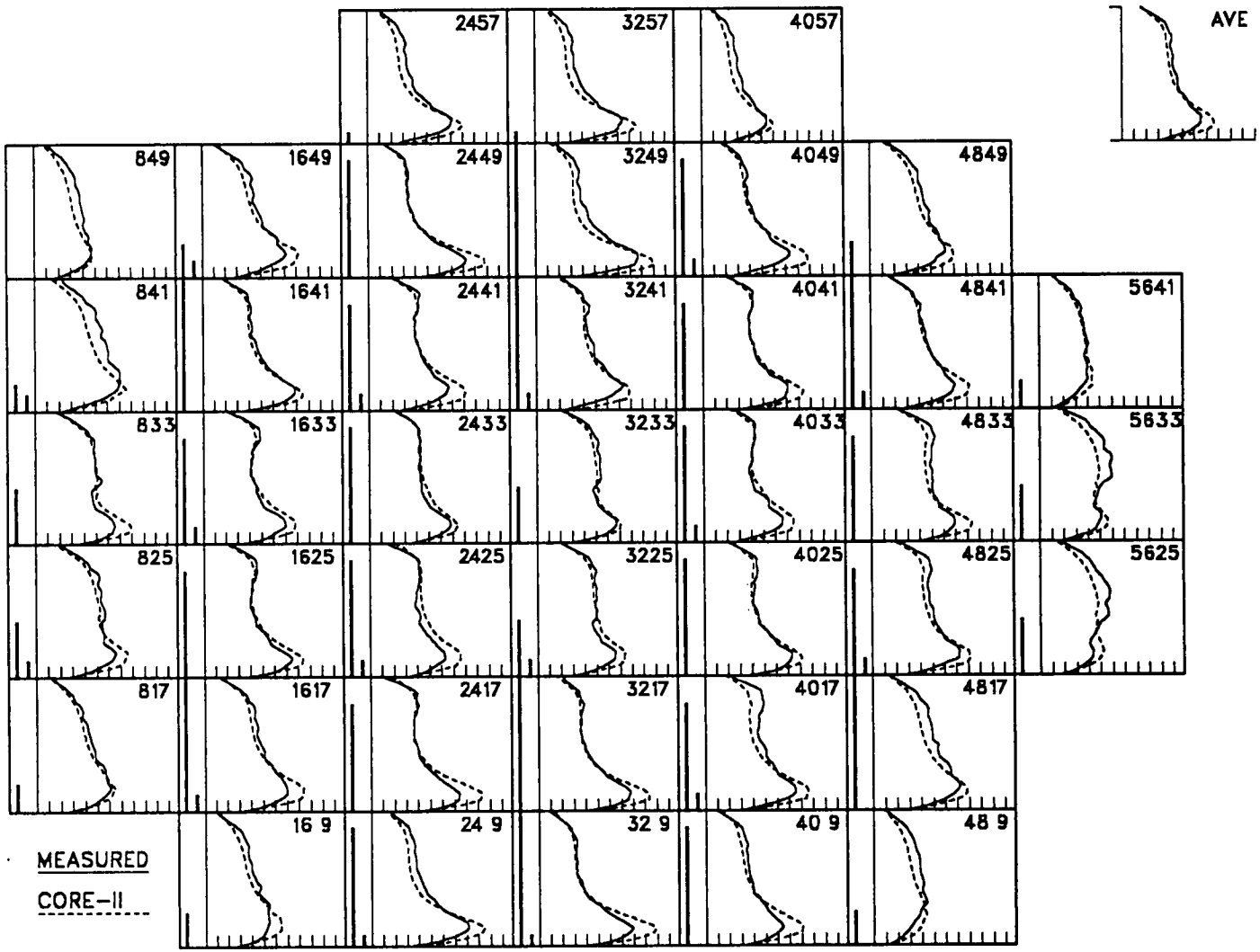

Cycle 2 Individual Axial TIP Comparison at 8424 MWd/MT

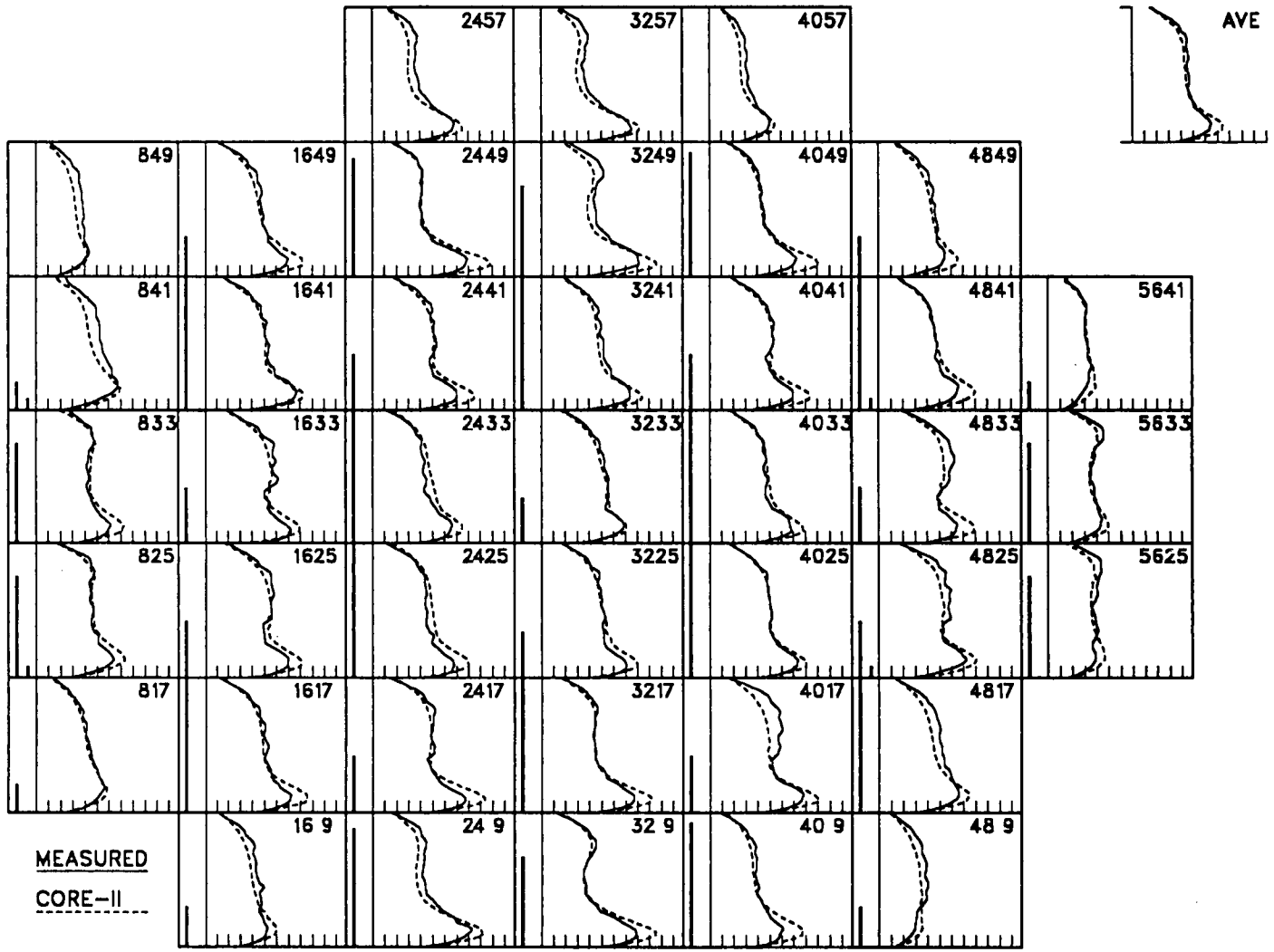

Cycle 2 Individual Axial TIP Comparison at 8790 MWd/MT

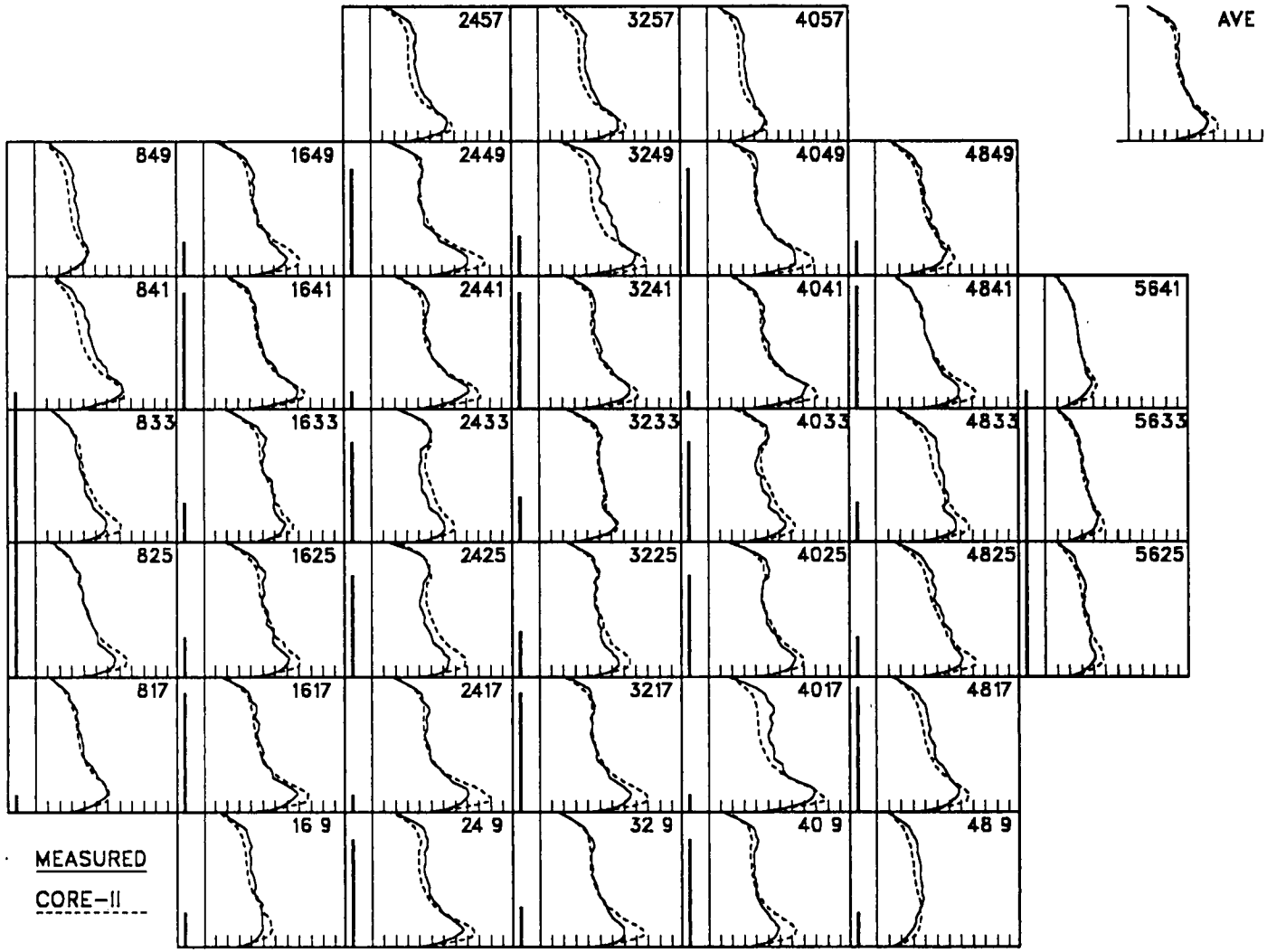

Cycle 2 Individual Axial TIP Comparison at 9142 MWd/MT

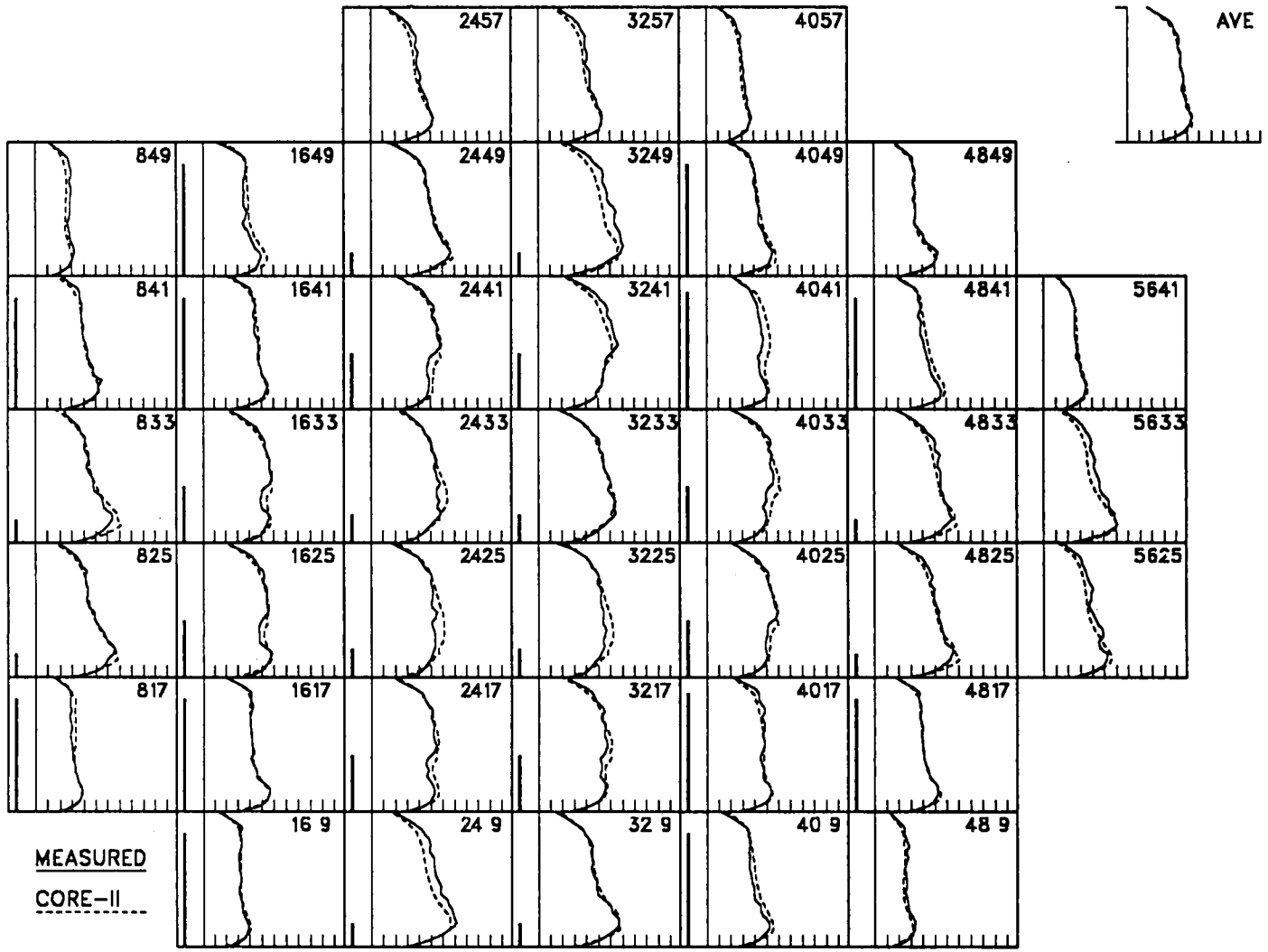

Cycle 2 Individual Axial TIP Comparison at 10174 MWd/MT

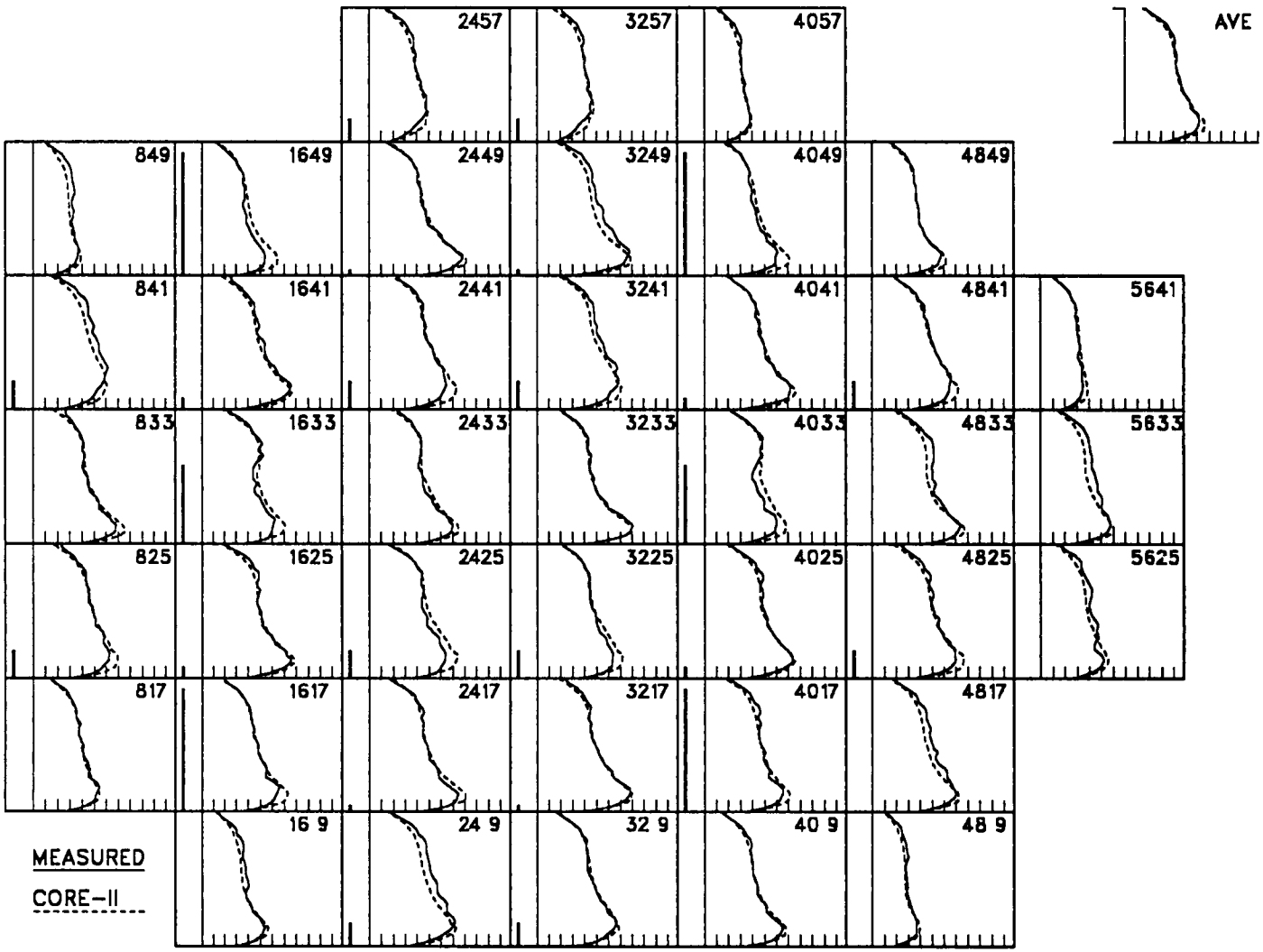

Cycle 2 Individual Axial TIP Comparison at 11239 MWd/MT

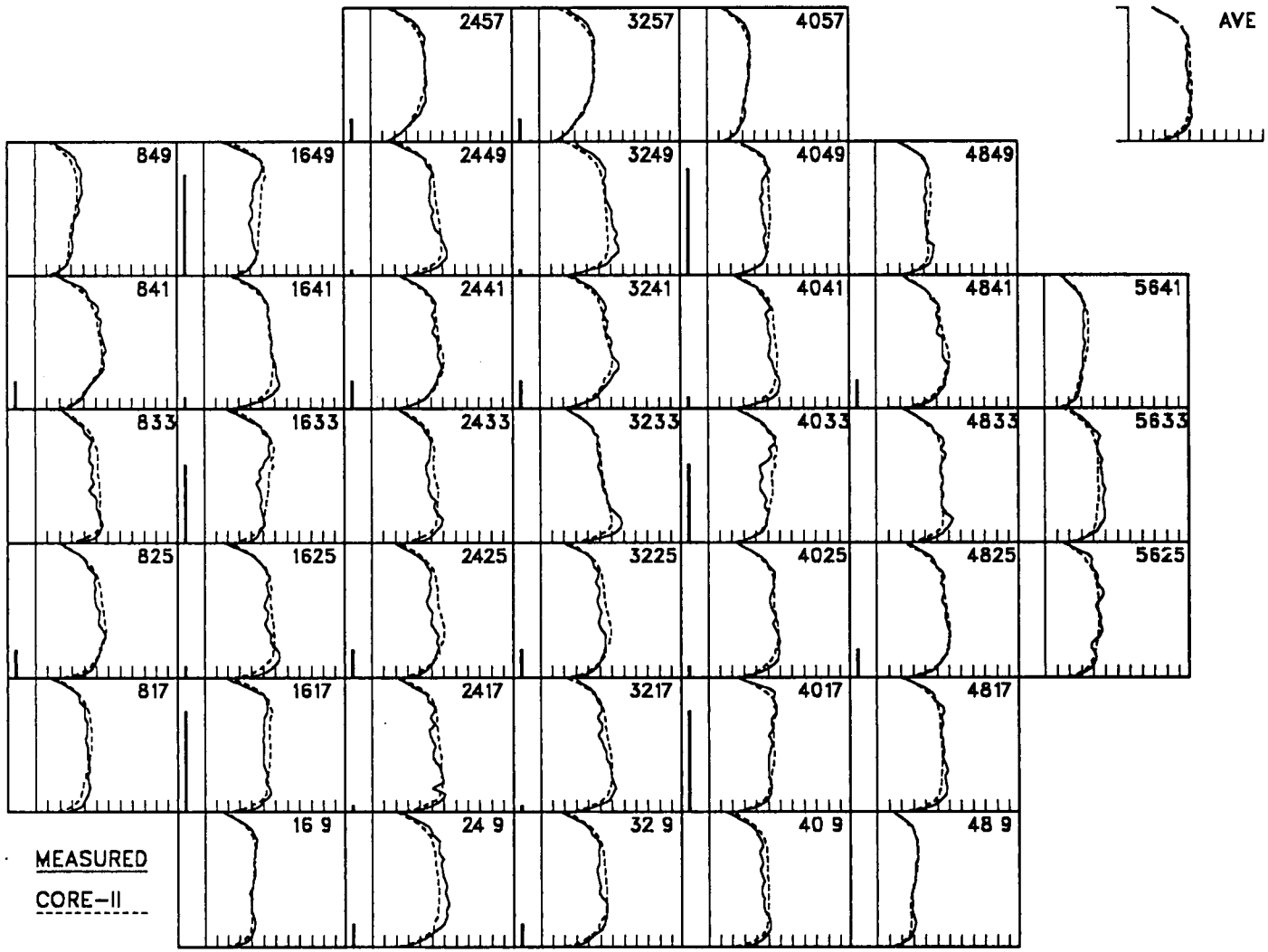

Cycle 2 Individual Axial TIP Comparison at 11936 MWd/MT

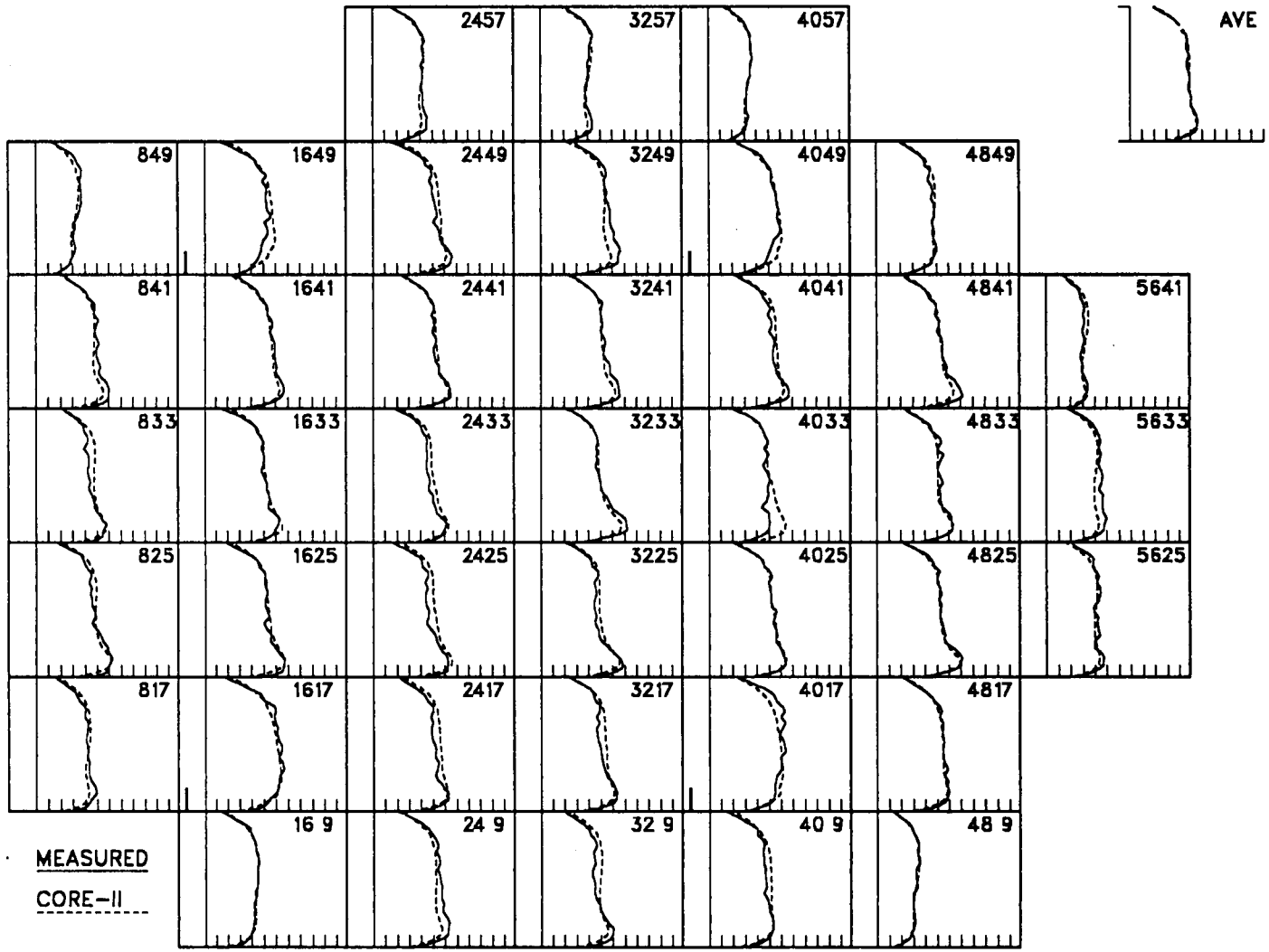

Cycle 2 Individual Axial TIP Comparison at 12897 MWd/MT

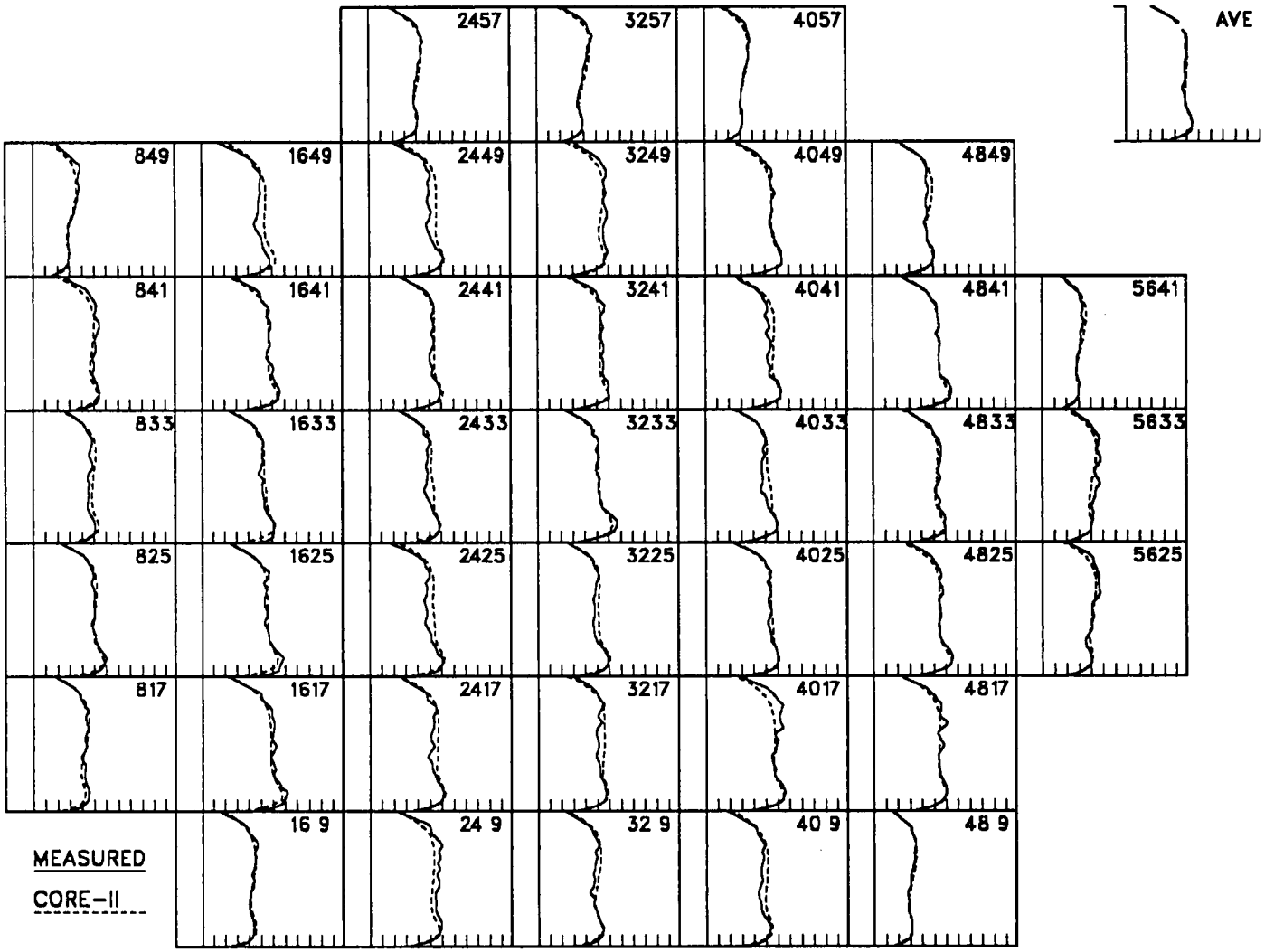

Cycle 2 Individual Axial TIP Comparison at 13199 MWd/MT

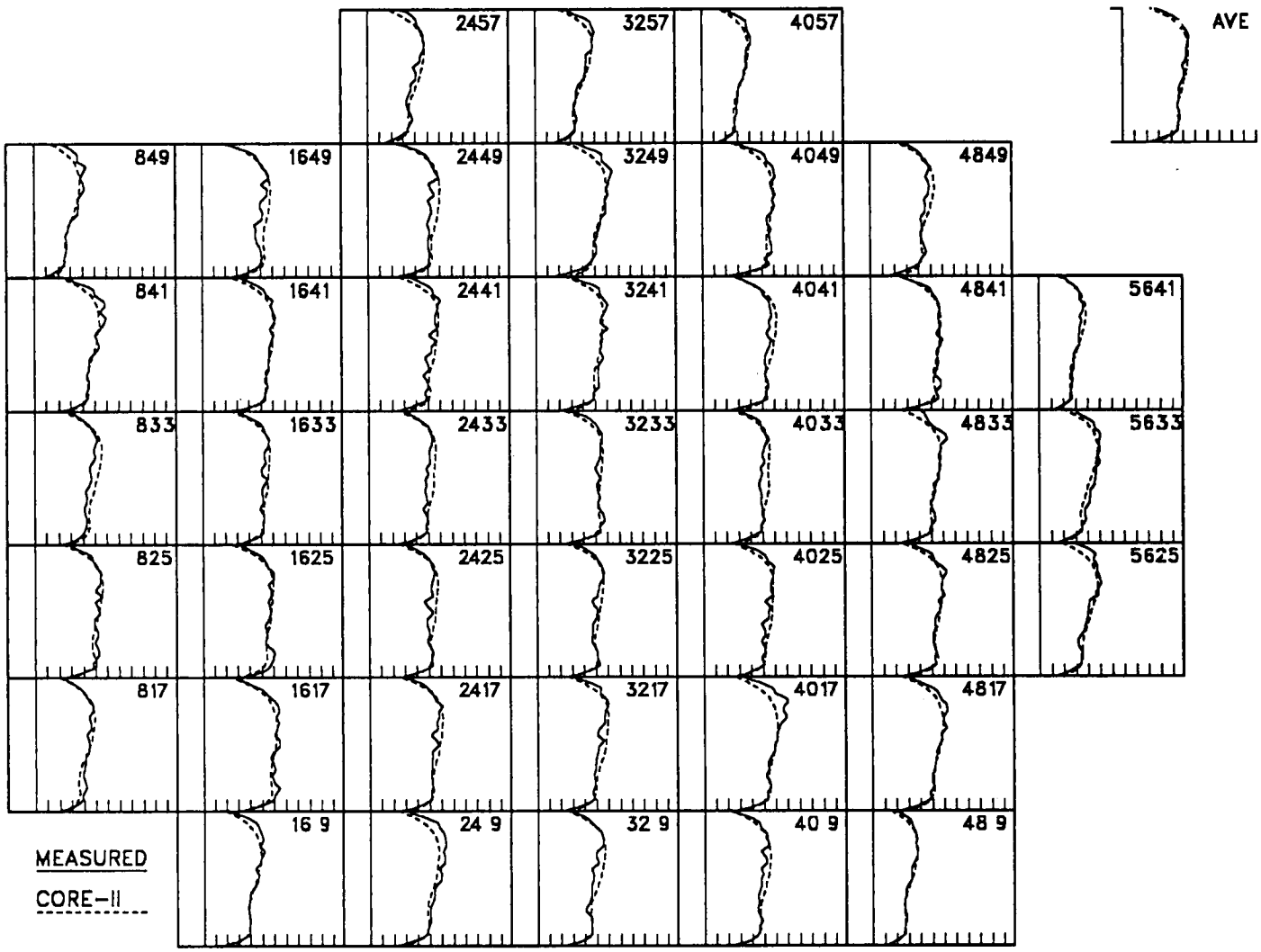

Cycle 2 Individual Axial TIP Comparison at 13612 MWd/MT

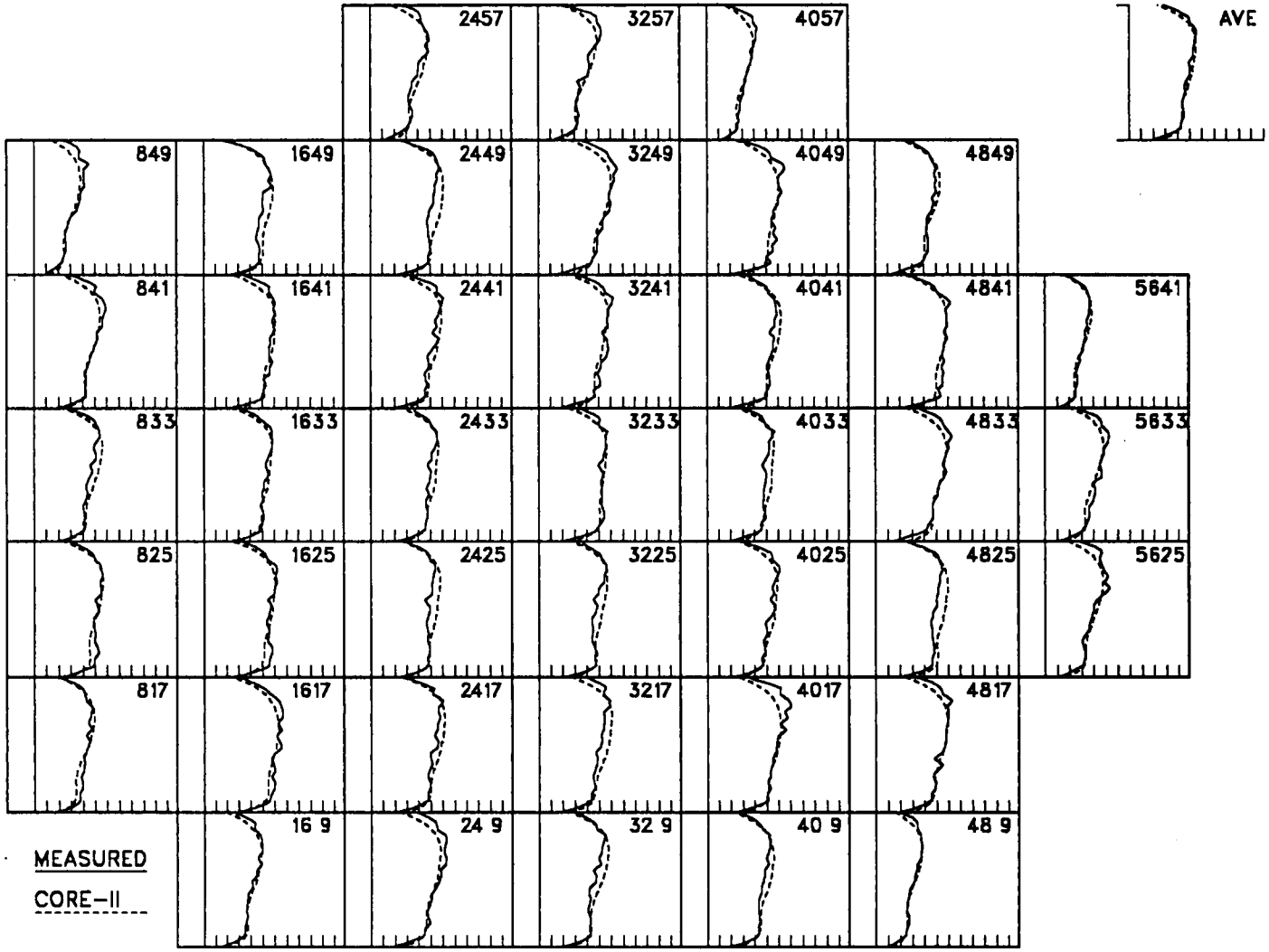

Cycle 2 Individual Axial TIP Comparison at 13742 MWd/MT

VITA

Scott B. Thomas was born January 16, 1963 in Syracuse, New York. He spent most of his youth in southern Ohio, and graduated from Waverly High school in June 1981. The following September he entered Ohio Northern University. In September 1983 he transferred to the University of Tennessee, Knoxville to complete his undergraduate studies. The author graduated with honors and received the degree of Bachelor of Science in Nuclear Engineering in the spring of 1986.

The author accepted a research assistantship at the University of Tennessee, Knoxville and began working toward a Masters of Science in Nuclear Engineering. He is a member of Tau Beta Pi, the American Nuclear Society and is the recipient of a Hilton A. Smith scholarship.

The author received the degree of Masters of Science in Nuclear Engineering in the fall of 1989. Mr. Thomas has worked in the area of Boiling Water Reactor Core Design with the Tennessee Valley Authority since October 1987.